



Investigation of High-Performance Millimetre-Wave and Terahertz Beam- Shaping Devices for Next Generation Communication Systems

by Jianfeng Zhu

Thesis submitted in fulfilment of the requirements for
the degree of Doctor of Philosophy

under the supervision of
Principal Supervisor: Dr Yang Yang
Co-Supervisor: Prof. David McGloin

University of Technology Sydney
Faculty of Engineering and Information Technology

November 2020

CERTIFICATE OF ORIGINAL AUTHORSHIP

I, Jianfeng Zhu declare that this thesis, is submitted in fulfilment of the requirements award of the Doctoral Degree, in the School of Electrical and Data Engineering, Faculty of Engineering and Information Technology at the University of Technology Sydney.

This thesis is wholly my own work unless otherwise referenced or acknowledged. In addition, I certify that all information sources and literature used are indicated in the thesis.

I certify that the work in this thesis has not previously been submitted for a degree nor has it been submitted as part of the requirements for a degree at any other academic institution except as fully acknowledged within the text. This thesis is the result of a Collaborative Doctoral Research Degree program with Beijing University of Posts and Telecommunications.

This research is supported by the Australian Government Research Training Program.

Signature: Production Note:
Signature removed prior to publication.

Date: 2021/1/12

Acknowledgement

Throughout my Ph.D. studies in Sydney, Australia, I have enjoyed learning new knowledge, exploring interesting things, and experiencing exciting moments with wonderful persons. I'm so glad that I can show my gratitude to everyone here.

I would like to express my sincere gratitude to my Ph.D. supervisor and mentor Dr. Yang Yang. I am grateful that Dr. Yang Yang brought me the opportunity and guided me throughout my Ph.D. career by providing a comfortable research environment for us. I am also thankful for his support at all stages of my research at UTS both at the academic and personal levels.

I would also like to express my warmest gratitude to my co-supervisor Prof. McGloin for his support in my academic research. Prof. McGloin's views on optics and photonics inspired me a lot in my research area of mm-wave and THz beam shaping. I am also grateful to Prof. McGloin for his mentorship and guidance on the development of novel ideas and research impact. Dr. Alex McKnight also assisted by proofreading the final draft for grammatical and stylistic errors.

I would like to thank Prof. Shufang Li from Beijing University of Posts and Communications (BUPT) and Prof. Quan Xue and Prof. Shaowei Liao from South China University of Technology (SCUT) for their full support for my research career pathway.

Finally, I would like to thank my parents and family members for their everlasting love, patience, and support.

Published and Under Review Papers Related to This Thesis

- [1] **J. Zhu**, Y. Yang, D. McGloin, R. Unnithan, S. Li, S. Liao, and Q. Xue, “3-D Printed Planar Dielectric Linear-to-Circular Polarization Conversion and Beam Shaping Lenses Using Coding Polarizer,” *IEEE Transactions on Antennas and Propagation*, vol. 68, no. 6, pp. 4332-4343, June 2020, doi: 10.1109/TAP.2020.2972625. **[Chapter 2, Section 2.2]**
- [2] **J. Zhu**, Y. Yang, D. McGloin, S. Liao and Q. Xue, “Sub-Terahertz 3-D Printed All-Dielectric Low-Cost Low-Profile Lens-Integrated Polarization Beam Splitter,” *IEEE Transactions on Terahertz Science and Technology*, vol. 11, no. 4, pp. 433-442, July 2021, doi: 10.1109/TTHZ.2021.3064209. **[Chapter 2, Section 2.3]**
- [3] **J. Zhu**, Y. Yang, D. McGloin, S. Liao and Q. Xue, “3-D Printed All-Dielectric Dual-Band Broadband Reflectarray with a Large Frequency-Ratio,” *IEEE Transactions on Antennas and Propagation*, early access doi: 10.1109/TAP.2021.3076528. **[Chapter 2, Section 2.4]**
- [4] **J. Zhu**, Y. Yang, S. Li, S. Liao, and Q. Xue, “Single-Ended-Fed High-Gain LTCC Planar Aperture Antenna for 60 GHz Antenna-in-Package Applications,” *IEEE Transactions on Antennas and Propagation*, vol. 67, no. 8, pp. 5154-5162, Aug. 2019 **[Chapter 3, Section 3.2]**
- [5] **J. Zhu**, Y. Yang, C. Chu, S. Li, S. Liao, and Q. Xue, “Low-Profile Wideband and High-Gain LTCC Patch Antenna Array for 60 GHz Applications,” *IEEE Transactions on Antennas and Propagation*, vol. 68, no. 4, pp. 3237-3242, April 2020. **[Chapter 3, Section 3.2]**
- [6] **J. Zhu**, Y. Yang, D. McGloin, S. Liao and Q. Xue, “Dual-Band Dual-Sense Circularly Polarized High Gain Antenna with a Single Linearly-Polarized Feed,”

submitted to *IEEE Transactions on Antennas and Propagation*, [Chapter 4, Section 4.2]

[7] **J. Zhu**, Y. Yang, S. Liao, and Q. Xue, “Large Frequency-Ratio, High Aperture Reuse efficiency, Dual-Band Antenna for Millimeter-Wave and Sub-6 GHz Applications,” submitted to *IEEE Antennas and Wireless Propagation Letters* (*Major revision*) [Chapter 4, Section 4.3]

Abstract

The shortage of global bandwidth has motivated the exploration of the underutilized millimetrewave (mm-wave) and terahertz (THz) spectrum for future broadband communication networks. Nevertheless, one of the fundamental challenges is the huge propagation loss. To tackle this problem, antennas at the front-end of transceivers should be capable of shaping the mm-wave/THz wavefront to achieve high-directivity radiation and large spatial coverage. Meanwhile, the print circuit board (PCB) cannot fully satisfy the demand due to the deterioration of electrical performance at high frequencies. Therefore, new fabrication technologies need to be exploited to build highly-efficient and highly-integrated mm-wave/THz beam shaping devices. In this thesis, taking advantage of PCB, 3-D printing, and low-temperature co-fire ceramics (LTCC), beam shaping devices including lenses, reflectarrays, antennas operating in the mm-wave and low THz region are proposed for next-generation communication systems applications. The main contents are as follows:

1. 3-D printed polarization manipulation and beam-shaping devices. First, we present a new 3-D printed lens, which achieves linear to circular polarization conversion and beam collimation in transmission mode simultaneously with a planar configuration. Next, we demonstrate a 3-D printed THz Fresnel-Rochon prism, which has the potential to replace conventional expensive prism. Finally, a new all-dielectric broadband dual-band reflectarray operating in K-band and V-band is demonstrated using low-cost 3-D printing. To the best of our knowledge, this is the first type of all dielectric reflectarray that has ever been reported.

2. Highly-integrated and high gain LTCC antenna array for 60-GHz antenna-in-package applications. Firstly, single-ended-fed planar aperture antennas fabricated using LTCC technology are demonstrated, which not only inherits the merits of the aperture antennas but also exhibits advantages of low-profile and compact size. Then, we demonstrate a low-profile wideband and high gain patch antenna array. The antenna achieves good radiation performances, which are comparable to those of the differential-driven patch antenna without a differential feeding network.

3. Dual-band beam-shaping antennas. First, a new kind of dual-band high gain antenna is proposed by folding a reflectarray into a Fabry-Perot cavity. The high gains of the two bands are achieved by exploiting the collimating reflectarray and Fabry-Perot resonant principles, respectively. Next, an aperture-shared dual-band antenna is proposed by integrating a high-band Fabry-Perot cavity antenna into a low-band patch antenna. Because of the FP resonance, the antenna can achieve a peak gain of 16 dBi at 28 GHz band without a feeding network.

Keywords: Millimetre-wave, THz, beam shaping, polarization, 3-D printing, LTCC

CONTENTS

Abstract	VI
Chapter I Introduction.	1
1.1 Research Background	1
1.2 Literature Review	3
1.2.1 Mm-wave and THz High Gain Antennas	3
1.2.1.1 Aperture antennas and Yagi-Uda antennas	3
1.2.1.2 Reflectarray	6
1.2.1.3 Fabry-Pérot cavity (FPC) antennas	10
1.2.1.4 High gain surface wave antenna	12
1.2.2 Mm-wave and THz Multi-beam Devices (MBDs)	18
1.2.2.1 MBDs based on reflectors/reflectarrays	18
1.2.2.2 MBDs based on lenses	21
1.2.2.3 MBDs based on beamforming circuits	22
1.2.3 Fabrication Technology for Mm-wave and THz Beam-Shaping Devices	24
1.2.3.1 Low-temperature co-fired ceramic (LTCC) fabrication technique	24
1.2.3.2 3-D printing technique	25
1.3 Conclusion	27
References	28
Chapter II 3-D Printed Mm-wave and Sub-THz Polarization Manipulation and Beam-shaping Lenses, Prisms and Reflectarrays	38
2.1 Introduction	38
2.2 3-D Printed Planar Dielectric Linear-to-Circular Polarization Conversion and Beam-Shaping Lenses	39
2.2.1 Unit cells of the lens	40
2.2.2 LP-to-CP conversion lens	48
2.2.3 Wollaston-prism-like and Rochon-prism-like planar circularly polarized beam-shaping lenses	52
2.3 0.14 THz 3-D Printed All-Dielectric Low-Cost Low-Profile Lens-Integrated Fresnel Rochon Prism	57
2.3.1 3-D printed Rochon prism design	59
2.3.2 3-D Printed Fresnel Rochon Prism design	63
2.4 Low-Cost 3-D Printed All-Dielectric Dual-Band Broadband Reflectarray with a Large Frequency-Ratio	72
2.4.1 Dielectric mirror	73
2.4.2 Reflectarray design	77
2.5 Conclusion	81
2.6 References	81
Chapter III High Gain LTCC Antenna-in-Package for 60-GHz Applications	91
3.1 Introduction	91
3.2 Single-Ended-Fed High-Gain LTCC Planar Aperture Antenna for 60 GHz Antenna-in-Package Applications	92
3.3 Low-Profile Wideband and High-Gain LTCC Patch Antenna Array for 60 GHz	

Applications	103
3.4 Conclusion	113
3.5 References.....	114
Chapter IV Dual-Band Mm-Wave Polarization Manipulation and Beam-shaping Devices	117
4.1 Introduction.....	117
4.2 Folding Reflectarray Into Fabry-Perot Cavity Makes Dual-Band Dual Polarized High Gain Antenna	118
4.2.1 Antenna design.....	119
4.2.2 Design guidelines	124
4.2.3 Fabrication, measurement, and discussion.....	125
4.3 Large Frequency-Ratio, High Aperture Reuse Efficiency, Dual-Band Antenna for Millimetre-Wave and Sub-6 GHz Applications	129
4.3.1 Antenna design.....	132
4.3.2 Measurement and discussion.....	136
4.4. Conclusion	139
4.5 References.....	139
Chapter V Conclusion and Future Work	145
5.1 Conclusion	145
5.2 Future work.....	147
Publications.	149

Chapter I Introduction

1.1 Research Background

The wireless industry faces overwhelming transmission speed and capacity demands because of continuing increased advances and discoveries in communications. An approximately 1000-fold increase in capacity demand will be encountered in the next decades and the current nearly exhausted microwave spectrum cannot fully support this demand obviously [1-2]. Generally, approaches to the enhancement of the system capacity include shrinking the cell-area, advanced signal processing techniques, and exploiting a new communication spectrum for cellular networks. The first two methods can improve spectral efficiency but not by orders of magnitudes [3]. Therefore, they are combined with the allocating new frequency spectrum (millimetre-wave (mm-wave) frequency band and lower terahertz (THz) frequency range) to enormously increase communication capacity and speed, given that the technology in the mm-wave bands can be practically implemented. Because of the broad bandwidths, shrinking cell sizes, and advanced signal processing techniques, the transmission capacity, and speed demands can be fulfilled for the next decade or so.

The mm-wave frequency band and lower THz frequency band (30 GHz to <1 THz), which are still underutilized, are important spectra for post-fifth-generation and sixth-generation communication systems to meet the escalating demand for capacity. The general hurdles of this frequency range are the tremendous losses and the quasi-optical propagation path of communication links [4-6]. Recalling the Friis transmission formula [7]:

$$P_r = P_t + G_t + G_r + 20 \log_{10} \left(\frac{c}{4\pi r f} \right) \quad (1-1)$$

where P_r , P_t , G_t , G_r are receiver power (dBW), transmitter output power (dBW), gain of the transmitter antenna (dB), and gain of the receiver antenna (dB),

respectively, c is the speed of light, r is the distance between the transmitter (meter) and receiver and f is the frequency, the attenuation is increased with larger r and f . Moreover, the strongly polar molecule H_2O aggravates the attenuation. For example, the 60 GHz band has a lossy channel with an excess loss of up to approximately 15 dB/km due to oxygen absorption. Fig. 1.1 shows the attenuation versus frequency, where certain transmission windows located at 80, 140, 200, 300 GHz, and 350 GHz with minimum attenuation can be identified. However, it is demonstrated that for an indoor distance of 10 m at 300-GHz, the overall attenuation is still too high, reaching 102 dB [8]. To tackle this high attenuation, one can only use high gain antennas in the front-end of the transceiver. In fact, the mm-wave and THz antennas, lenses, etc. that can shape the beams of electromagnetic (EM) waves will play an important role in future communication applications. The following section presents a literature review and discusses the state-of-art studies of beam-shaping devices operating in the mm-wave and THz bands.

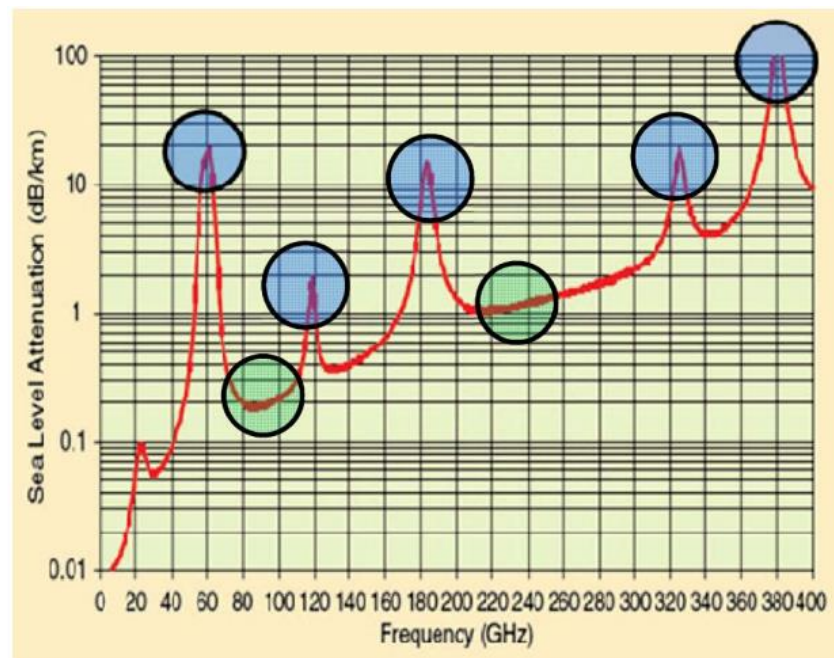


Fig.1.1 Atmospheric absorption across mm-wave/sub-THz frequencies in dB/km ^[1]. (The 120-, 183-, 325-, and 380-GHz bands (blue circles) are very likely allocated for short-range communications.)

1.2 Literature Review

1.2.1 Mm-wave and THz High Gain Antennas

1.2.1.1 Aperture antennas and Yagi-Uda antennas

As stated previously, due to the high path loss at mm-wave and low THz bands, the most important feature of the mm-wave/THz antenna is the gain and aperture efficiency. As for the antenna gain for mm-wave communications, a higher gain can be a better choice though no specific requirement for antenna gain. It usually depends on different communication scenarios and their requirements. As for the aperture efficiencies, we always want that the antenna has a higher aperture efficiency because a higher aperture efficiency means a higher gain can be achieved in a more compact size. Thus, the higher the aperture efficiency, the better. To enhance the antenna gain, one can increase the effective radiating aperture size of the antenna or improve the aperture efficiency of the antenna [9]. Using an array antenna with multiple radiating elements is an effective approach to increasing the

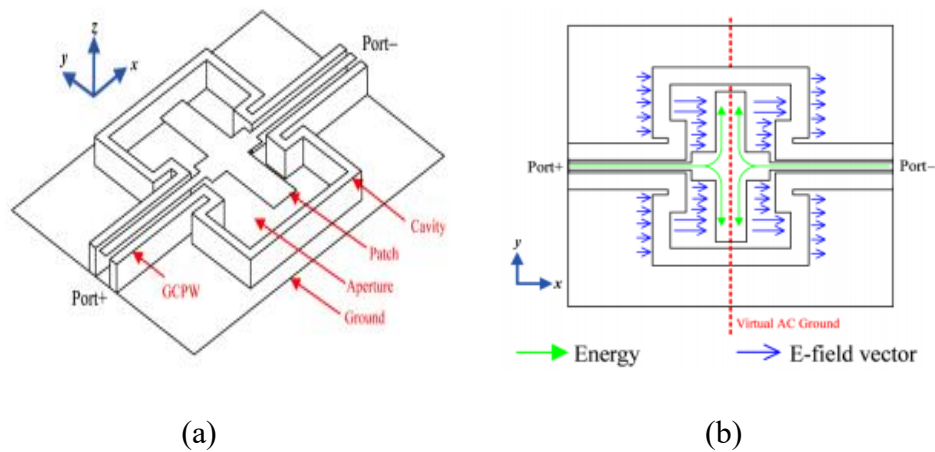


Fig. 1.2. (a) Basic configuration of PAA element ^[21]. (b) Working principle demonstration ^[21].

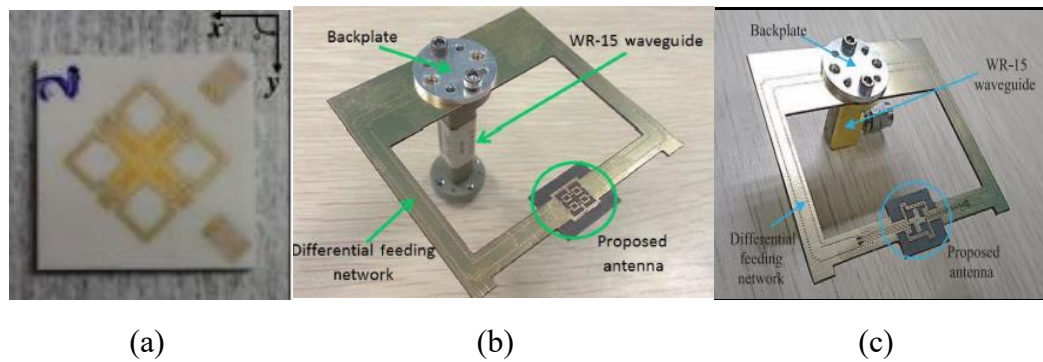


Fig. 1.3. (a) Dual polarized PAA antenna [22]. (b) Circularly polarized PAA [23]. (c) Circularly polarized PAA [24].

radiating aperture [10-14]. Commonly used elements include slots, dipoles, patches. To achieve high aperture efficiency, it is necessary to first determine the geometry of the radiating element and then carefully optimize it to obtain a uniform E-field distribution at the aperture. Aperture antennas, such as horn [15] and parabolic reflector antennas [16] are good examples of high aperture efficiency antennas. Nevertheless, in the mm-wave and THz regions, the high profile limits their integration in the front-end of transceivers for consumer-level applications. Cavity-backed aperture antennas have been demonstrated as an efficient approach to achieve high gain with a planar low-profile [17-20]. For example, Liao *et.al* demonstrated a kind of cavity-backed aperture antenna [21] with a simple patch feeding. It is called a planar aperture antenna (PAA) because it achieves a uniform aperture field distribution in its physical aperture, which is similar to the conventional aperture antenna, as shown in Fig. 1.2. The gain of this PAA can reach 15.3 dBi with aperture efficiency larger than 41.3%. The authors then extended this principle to realize several other high gain antennas, such as dual-polarized [22] and circularly polarized PAA [23,24], as shown in Fig. 1.3.

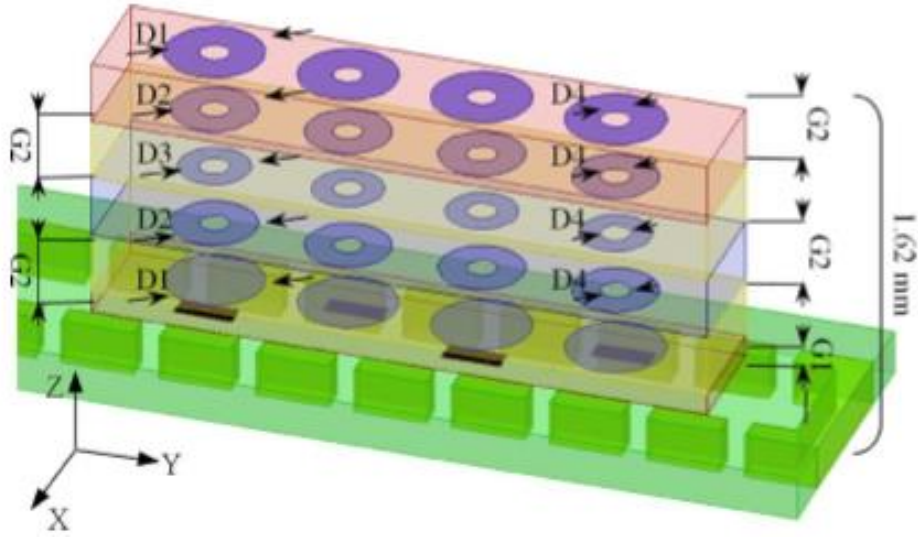


Fig. 1.4. W-band high gain Yagi-Uda antenna array^[25].

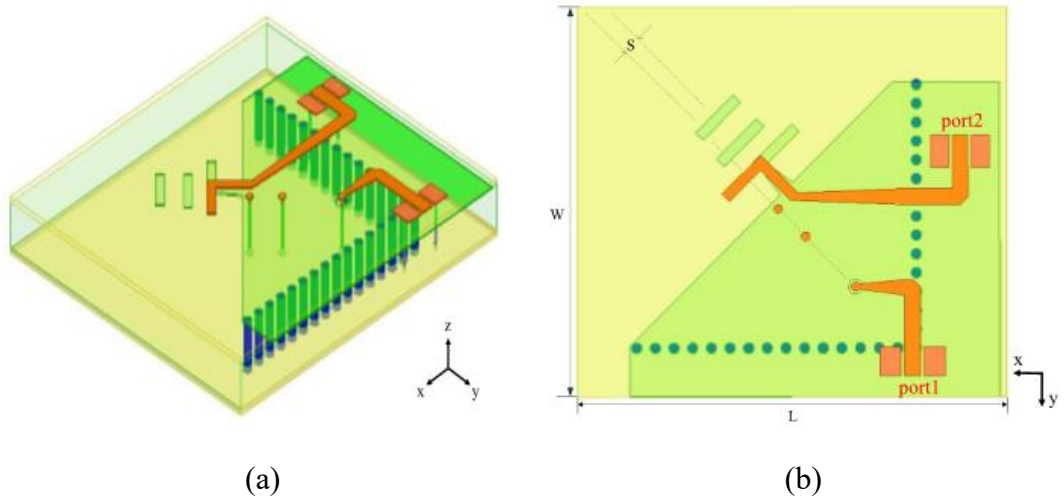


Fig. 1.5. End-fire dual-polarized Yagi-Uda antenna^[26]. (a) 3D view. (b) Top view.

By introducing directors and a reflector, the Yagi-Uda antenna is widely used to achieve high directivity. Many high gain Yagi antennas or quasi-Yagi antennas that can be used in mm-wave communication have been demonstrated. Fig. 1.4 shows the design of a W-band Yagi-like antenna [25]. By introducing a multilayer dielectric plate and a circular patch, the gain of the 4×4 antenna array can reach 19 dBi. As for the end-fire radiation, Hsu *et al.* demonstrated a dual-polarized antenna with end-fire radiation [26], as shown in Fig. 1.5. For the vertical polarization, both the driver and two directors consist of vias with about quarter-wavelength. For the horizontal polarization, half-wavelength differential-fed metal arms are adopted as the driver.

The truncated ground is used as the reflector and two short metal strips as directors. By using this configuration, the peak gain of the element can reach 6.5 dBi.

1.2.1.2 Reflectarray

A reflectarray is another kind of high gain antenna combining many favourable features of both printed array antennas and reflector antennas with a low profile and low mass [27-31]. The direct phase control of each pixel on the aperture without a complicated feeding network makes it even more attractive [32]. Its flexibility of generating independent beams at different frequencies with different polarizations can be used to fulfill independent requirements in different channels. Generally, the elements used to control the phase on the reflectarray aperture can be categorized into three [31]:

- 1) element (uniform size) with different lengths of phase delay line,
- 2) element with different sizes,
- 3) element (uniform size) with different rotation angles.

1) and 2) are called propagation phases, and they work for both linearly- and circularly-polarized EM-waves. 3) is called a geometrical phase, or Berry phase. It is a very interesting phase-tuning method. One can control the transmit/reflect phase by simply rotating the angles of the element without changing its size.

Without loss of generality, considering a right-hand circularly polarized wave along -z direction impinged on a reflection-type phasing element, as shown in Fig. 1.6, can be expressed as:

$$\hat{E}_i = E_0(\hat{x} + j\hat{y})e^{jk_0z}e^{j\omega t} \quad (1-2)$$

where, k_0 is the wavenumber, and ω is the angular frequency. Then, because the propagation direction changes, the reflected wave will be left-hand circularly polarized.

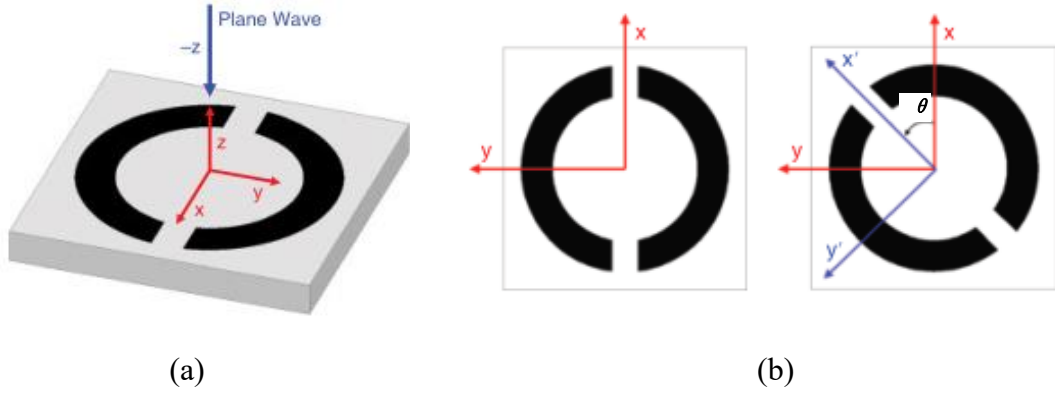


Fig. 1.6. (a) Right-hand circularly polarized incident wave impinging on a reflection-type phasing element^[31]. (b) Reference element and rotated element at an angle of θ ^[31].

Nevertheless, the sense of polarization of the reflected wave can be maintained as long as the element can introduce a 180° phase difference between the two orthogonal components of the reflected field, *i.e.* $\phi_y = \phi_x + 180^\circ$, where ϕ_x and ϕ_y are the reflection phase of the incident waves along x - and y -direction. The 180° phase difference can be realized easily, such as by using a patch with phase-delay lines, or split ring resonator. For the reference element in Fig. 1.6 (a), the reflected field can be written as:

$$\hat{E}_r = E_0(\hat{x}e^{j\phi_x} + j\hat{y}e^{j\phi_y})e^{-jk_0z}e^{j\omega t} = E_0(\hat{x} - j\hat{y})e^{j\phi_x}e^{-jk_0z}e^{j\omega t} \quad (1-3)$$

Now if the element is rotated by θ , as shown in Fig. 1.6 (b), the incident and reflected fields can be correspondingly obtained in the new coordinate system (x', y') , which is aligned with the rotating element. The incident field is given by:

$$\begin{aligned} \hat{E}_i &= E_0((\hat{x}'\cos(\theta) - \hat{y}'\sin(\theta) + j(\hat{x}'\sin\theta + \hat{y}'\cos\theta))e^{jk_0z}e^{j\omega t}) \\ &= E_0((\hat{x}' + j\hat{y}')e^{j\theta}e^{jk_0z}e^{j\omega t}) \end{aligned} \quad (1-4)$$

In the new coordinate system, the incident wave can be expressed as:

$$\hat{E}_r = E_0(\hat{x}'e^{j\phi_{x'}} + j\hat{y}'e^{j\phi_{y'}})e^{j\theta}e^{-jk_0z}e^{j\omega t} = E_0(\hat{x}' - j\hat{y}')e^{j\phi_{x'}}e^{j\theta}e^{-jk_0z}e^{j\omega t} \quad (1-5)$$

In the new coordinate system, the condition $\phi_x = \phi_{x'}$, $\phi_y = \phi_{y'}$ is still maintained. Therefore, the reflected wave can be expressed as:

$$\hat{E}_r = E_0(\hat{x}' - j\hat{y}')e^{j\phi_{x'}}e^{j\theta}e^{-jk_0z}e^{j\omega t} \quad (1-6)$$

In the original coordinate system, the reflected wave can be further expressed as:

$$\begin{aligned}\hat{E}_i &= E_0(\hat{x}(\cos \theta + j \sin \theta) + \hat{y}(\sin \theta - j \cos \theta))e^{j\phi_x}e^{j\theta}e^{jk_0z}e^{j\omega t} \\ &= E_0((\hat{x} - j\hat{y})e^{j\phi_x}e^{j2\theta}e^{-jk_0z}e^{j\omega t}\end{aligned}\quad (1-7)$$

A comparison of (1-3) and (1-7) indicates that the reflected wave shows 2θ phase delay after the phasing element is rotated at an angle of θ in a counter-clockwise direction. It can be demonstrated in the same way that the reflected wave shows 2θ phase advance for the left-hand circularly polarized incident wave.

We can also use the Jones matrix to clarify the relationships between polarization and phase. Without loss of generality, for a birefringent transmission unit with rotation angle α , its scattering can be expressed by the Jones matrix as [33]:

$$\hat{M} = \hat{R}(-\alpha) \begin{bmatrix} t_o & 0 \\ 0 & t_e \end{bmatrix} \hat{R}(-\alpha) \quad (1-8)$$

$$\hat{R}(\alpha) = \begin{bmatrix} \cos(\alpha) & \sin(\alpha) \\ -\sin(\alpha) & \cos(\alpha) \end{bmatrix} \quad (1-9)$$

where t_o and t_e are scattering coefficients along two orthogonal planes and $\hat{R}(\alpha)$ is a rotation matrix. Considering the LHCP wave (E_I^L) impinged on the surface, the transmitted wave can be expressed as:

$$E_T = \hat{M} \cdot E_I^L = \frac{t_o + t_e}{2} E_I^L + \frac{t_o - t_e}{2} \exp(i2\alpha) E_I^R \quad (1-10)$$

If the RHCP wave (E_I^R) impinges on the surface, the transmitted wave can be expressed as:

$$E_T = \hat{M} \cdot E_I^R = \frac{t_o + t_e}{2} E_I^R + \frac{t_o - t_e}{2} \exp(-i2\alpha) E_I^L \quad (1-11)$$

The first term on the right of the equation shows the same polarization as that of the incident wave, and the second term on the right is orthogonal to the polarization of the incident wave. The second term is also accompanied by a Berry phase (twice the rotation angle). If we construct an element that satisfies the phase difference of 180 degrees between t_o and t_e , the incident wave will be completely transformed into the

transmission wave with orthogonal polarization with the corresponding phase change.

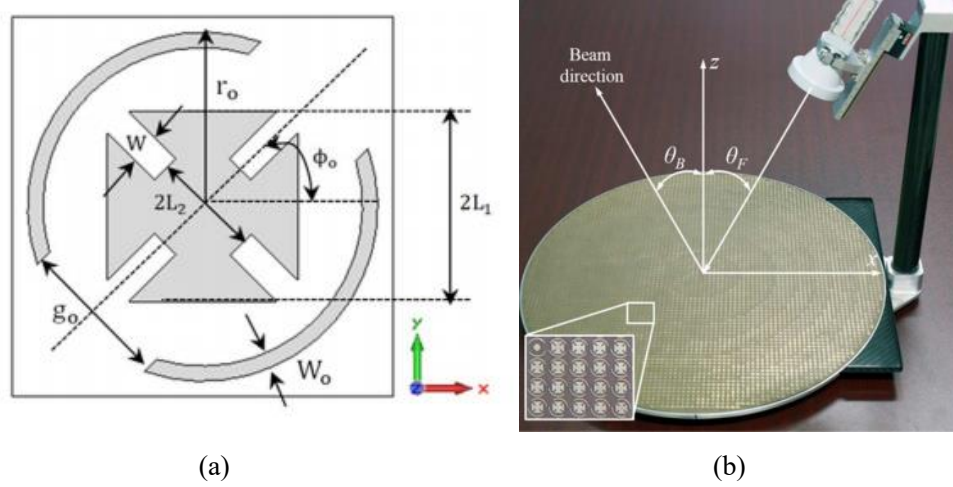


Fig. 1.7. Phasing element using Melta cross and split loop^[33]. (b) Dual circularly polarized reflectarray^[33].

Apart from collimating the beams, the reflectarray can also easily control the polarization of the EM-waves. Several dual-band dual-polarized reflectarrays have been demonstrated for different applications [34-39]. Generally, the strategies for achieving dual-band dual-polarization can be categorized into two types, as follows: (1) using different resonant cells operating at different bands and polarizations in a single substrate. For example, a dual-band dual-circularly-polarized (CP) reflectarray is demonstrated by combining Melta cross and split loop as the phasing elements [34]. The compensating phase is achieved by rotating the angle of the split loop and varying the size of the Melta cross for low- and high-band, respectively, as shown in Fig. 1.7. However, the challenge lies in the cross-talk between two resonant cells because it is difficult to guarantee that each cell operates only independently at its frequency. As for the dual-band dual-linearly-polarized reflectarray, the most common approach is arranging phasing elements, such as dipoles, along two orthogonal directions [35], [36]. Because the phasing elements are orthogonally interleaved on the reflectarray surface, the phase response in one polarization is only slightly affected by the other polarization. The disadvantage is that since the reflectarray itself cannot rotate the polarization, it requires two feeds with orthogonal polarizations or one dual-polarized feed. (2) using two different

reflectarray layers with a frequency selective surface (FSS) between them, where each layer works for one band [37-39]. The FSS works as the ground of the upper reflectarray while it allows low-band EM-wave to pass through. For example, a dual-band reflectarray has been developed by placing a Ka-band reflectarray on the top of an X-band reflectarray and a dual-screen FSS is used as a separator [39], as shown in Fig. 1.8 (a). The mutual coupling between the resonant cells can be greatly reduced. The blockage effect is another important issue to be considered for the reflectarray. A folded reflectarray (FR) has been demonstrated to eliminate the blockage effect of the feed [39]. The basic set-up of the FR is given in Fig. 1.8 (b). It consists of an LP feed, a polarizing grid, and a reflectarray. EM waves with an x-directed E-field are transmitted from the feed to the grid and are reflected by the grid toward the reflectarray. Then, the reflectarray collimates the EM-waves and twists their polarizations by 90° . Finally, the waves pass the grid and are radiated into free space with high gain. Although the FR eliminates the blockage effect and reduces the distance between the feed and reflectarray aperture, it only achieves high gain radiation over one polarization because the polarizing grid always reflects its orthogonal polarization back.

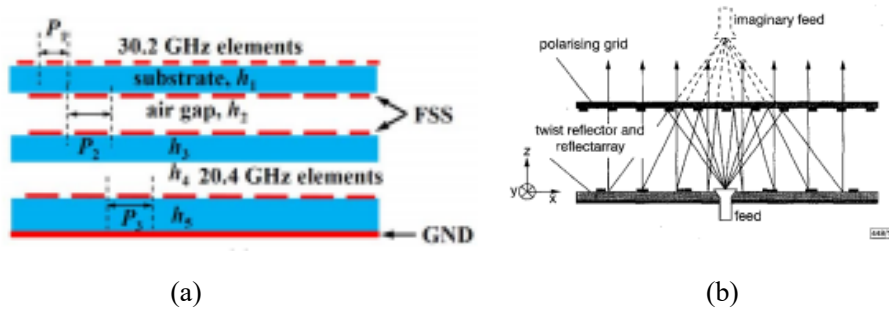


Fig. 1.8. (a) Multi-layer reflectarray configuration [38]. (b) Folded reflectarray [39].

1.2.1.3 Fabry-Pérot cavity (FPC) antennas

Fabry-Pérot cavity (FPC) antennas, employing a partially-reflective-surface (PRS) on top of a fully reflective surface with a low-directivity primary source, have been widely used to achieve high directivity radiation in various communication systems.

Since introduced by G. Von Trentini in 1956 [40], FPC antennas have been extensively investigated. In general, an FPC antenna is achieved by placing a partially reflecting surface (PRS) located approximately half a wavelength above the low-directivity primary source and its ground plane. Though the configurations of the folded reflectarray and FPC antenna are similar, the principles are different. For folded reflectarray, the EM wave is reflected by the polarizer atop first and directly collimated by the reflectarray. For the FPC antenna, the waves radiated from the source undergo multiple reflections, which interfere constructively in the broadside direction, resulting in a directive beam [42-45]. The thickness of the FPC cavity (h_{cavity}) should satisfy the Fabry-Perot resonant condition [40], given by

$$\frac{-4\pi h_{cavity}}{\lambda_0} + \varphi_{PRS} + \varphi_{ground} = 2n\pi \quad (1-12)$$

Where, φ_{PRS} and φ_{ground} are the reflection phases of the PRS and ground, respectively, λ_0 is the free space wavelength at the centre frequency and n is an integer. The relation between the directivity (D) of the FP resonator antenna and the reflection magnitude ($|\Gamma|$) of the PRS layer can be expressed as [46]:

$$D = 10 \log \frac{1+|\Gamma|}{1-|\Gamma|} \quad (1-13)$$

The higher the reflection of the PRS, the higher the gain of the FPC antenna can achieve. The PRS of the FPC antenna can be realized by dielectric slabs [47],[48], metal structures [49], and FSS [50],[51]. An artificial magnetic conductor (AMC) was also introduced to replace the conventional metal ground of an FPC to reduce the cavity height [52]. With its high directivity and simple configuration, the FPC antenna is an ideal candidate for wireless communications systems. However, the narrow bandwidth due to the strong resonance inside the cavity hinders its wide application. Over the last decade, many efforts have been devoted to improving the bandwidth of FPC antennas. One of the most popular techniques, PRS with positive reflection phase gradients, has been investigated to ensure resonant conditions inside the cavity are satisfied over a wide frequency band. This kind of PRS can be realized by means of multi-layered metasurfaces [53] or stacked dielectric substrates [54].

Other than these approaches, the use of a spherically-modified ground to obtain higher-order resonance inside the cavity [55], and using multiple sources instead of one to effectively increase the illumination efficiency of the radiating aperture [56], have also been demonstrated.

1.2.1.4 High gain surface wave antenna

Slow-wave

If a wave propagates along a surface with a phase velocity lower than the velocity of light, the wave can be trapped near the surface and can propagate without attenuation. We call a slow-wave or trapped surface wave. Specifically, we consider a slow wave propagating along z-direction in a dielectric slab of thickness d (relative permittivity of ϵ_1 and wavenumber of k_1) placed on a perfectly conducting plane (Fig. 1.9).

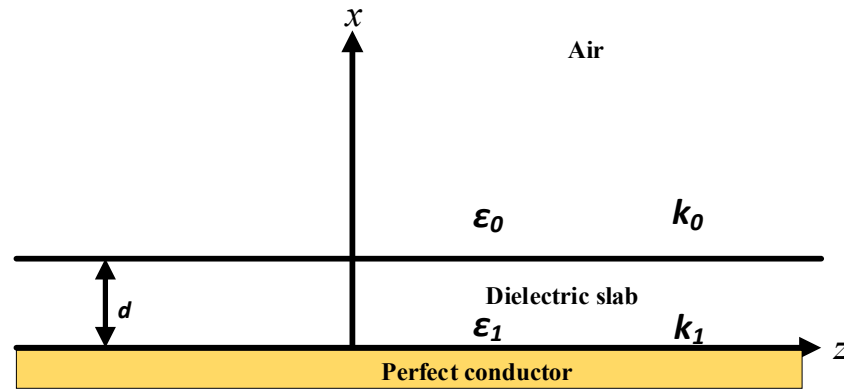


Fig. 1.9. Dielectric slab on perfect conducting plane.

For **TM waves**, the magnetic field H_y satisfies the wave equation:

$$\left(\frac{\partial^2}{\partial x^2} + \frac{\partial^2}{\partial z^2} + k^2\right)H_y = 0 \quad (1-14)$$

Solving the wave equation using boundary conditions, we have [57]:

$$H_{y1} = A e^{-\alpha_1 d} \frac{\cos px}{\cos pd} e^{-j\beta z} \quad (1-15)$$

$$H_{y0} = A e^{-\alpha_1 x - j\beta z} \quad (1-16)$$

$$E_{x0} = j \frac{1}{\omega \varepsilon} \frac{\partial}{\partial z} H_{y0} = \left(\frac{\beta}{k_1} \eta_0 \right) A e^{-\alpha_t x - j \beta z} \quad (1-17)$$

$$E_{x1} = j \frac{1}{\omega \varepsilon} \frac{\partial}{\partial z} H_{y1} = \left(\frac{\beta}{k_1} \eta_1 \right) A e^{-\alpha_t d - j \beta z} \frac{\cos px}{\cos pd} \quad (1-18)$$

The impedance is given by

$$\frac{E_z}{H_y} = j \frac{\alpha_t}{k_0} \eta_0 \quad (1-19)$$

This is purely inductive.

Similarly, for **TE waves**, the solution in the air region is:

$$E_{y0} = A e^{-\alpha_t x - j \beta z} \quad (1-20)$$

$$H_{x0} = \left(\frac{\beta}{k_0} \eta_0 \right) A e^{-\alpha_t x - j \beta z} \quad H_{z0} = -j \left(\frac{\alpha_t}{k_0 \eta_0} \right) A e^{-\alpha_t x - j \beta z} \quad (1-21)$$

The solution in the dielectric region is:

$$E_{y1} = A e^{-\alpha_t d - j \beta z} \frac{\sin px}{\sin pd} \quad (1-22)$$

$$H_{x0} = - \left(\frac{\beta}{k_1 \eta_1} \right) A e^{-\alpha_t d - j \beta z} \frac{\sin px}{\sin pd} \quad (1-23)$$

$$H_{z0} = j \left(\frac{p}{k_1 \eta_1} \right) A e^{-\alpha_t d - j \beta z} \frac{\cos px}{\sin pd} \quad (1-24)$$

Therefore, the surface supporting the trapped surface wave must be purely reactive. The TM mode requires a purely inductive surface, whereas the TE mode requires a purely capacitive surface. Taking advantage of this, Sievnepiper *et al.* demonstrated that energy can propagate along the boundary between PMC and PEC, as shown in Fig. 1.10.

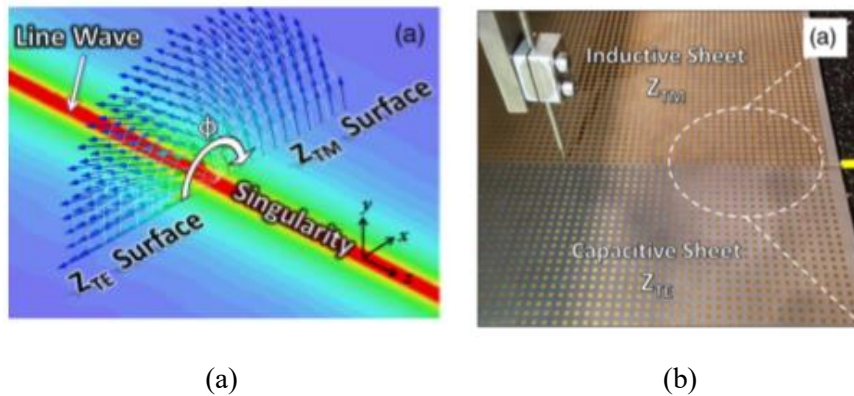


Fig.1.10. (a) Energy propagates efficiently along the boundary between PMC and PEC ^[58].
 (b) Using FSS to construct equivalent PEC and PMC plane ^[58].

Fast-wave:

Then, consider a fast wave propagating along the $+z$ direction along the surface. The amplitude of the fast wave increases exponentially in the $+x$ direction and decreases in the $+z$ direction, as shown in Figure 1.11. This type of wave is called a leaky wave because of the constant leakage of energy along the surface. Leaky waves can exist in a certain space. The most typical example is the radiation of energy along a waveguide slot. As shown in Figure 1.12, since the energy radiates outward continuously through the slot, the amplitude decreases continuously along the z direction. At the same time, the farther away from the surface along the $+x$ direction, the stronger the radiation amplitude in a certain space, (in fact, the amplitude along the $+x$ direction increases first and then decreases), and the radiation angle is determined by the propagation constant β_z .

$$\beta_z = k \sin \theta_c \quad (1-25)$$

Eq. (1-25) reveals that the radiation angle varies with the frequency. Therefore, we can use the leaky wave concept to design frequency scanning antennas. Conventionally, we can cut a slot in the waveguide, periodically short the microstrip line, or periodically modulated the slow-wave structure to achieve a leaky wave antenna, as shown in Fig. 1.13.

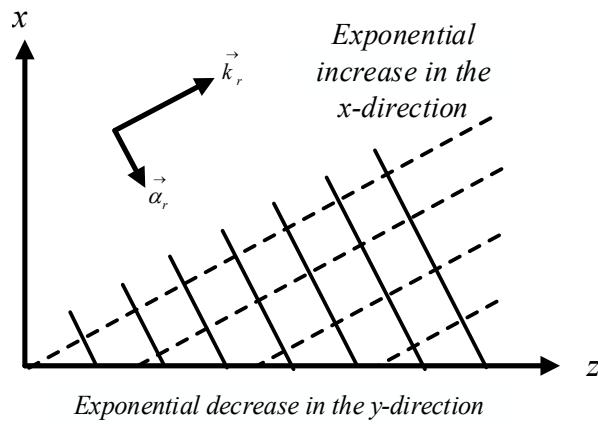


Fig. 1.11. Fast wave.

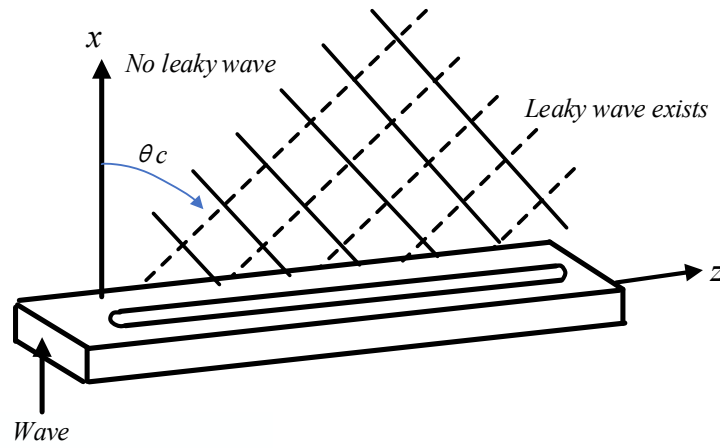


Fig. 1.12. Leaky wave was realized by cutting slot on the waveguide.

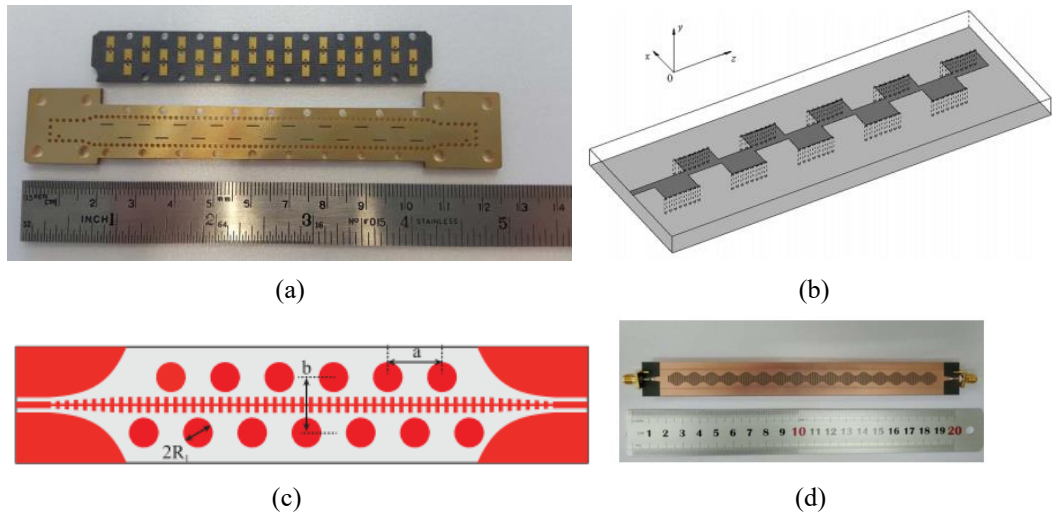


Fig. 1.13. Leaky wave antennas based on different structures. (a) Leaky wave antenna based on substrate-integrated waveguide ^[59]. (b) Leaky wave antenna based on periodically-shortened microstrip line ^[60]. (c) Leaky wave antenna based on spoof surface plasma polaritons ^[61]. (d) Leaky wave antenna based on periodically-modulated slow-wave structure ^[62].

Impedance modulated surface:

An impedance modulated surface is a method that combines impedance modulation and the leaky wave concept to control the propagation and radiation of surface waves [63]. By changing the physical dimensions of the surface element to modulate the equivalent impedance on the surface, the spatial beam can be adjusted arbitrarily. As shown in Fig. 1.15, suppose a scalar impedance modulated surface is located in the xoy plane. A dipole feed is used and placed at the surface origin. The dipole excites the excitation wave ψ_{ref} propagating along the surface, while the radiated target beam is ψ_{obj} , and the interference pattern of the excitation wave and the target beam is ψ_{intf} .

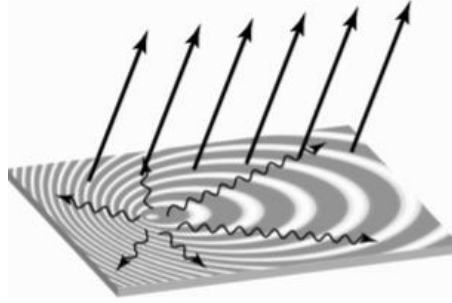


Fig. 1.14. Holographic leaky wave antenna concept [63].

The excitation wave can be expressed as [63]:

$$\Psi_{ref} = \exp(-jk_s \cdot r) \quad (1-26)$$

where, k_s is the wavenumber of the surface wave, and r represents an arbitrary position to the origin point $|r| = \sqrt{x^2 + y^2}$. The target beam can be expressed as:

$$\Psi_{obj} = \exp(-jk_0 x \sin \theta_l + j\phi) \quad (1-27)$$

where θ_l is the tilted angle of the target beam along x -direction, and ϕ is the initial phase at the origin point. Then the interference pattern can be expressed as:

$$\Psi_{int} = \Psi_{obj} \cdot \Psi_{ref}^* \quad (1-28)$$

When the interference pattern is illuminated by the reference wave, this term gives:

$$(\Psi_{obj} \cdot \Psi_{ref}^*) \cdot \Psi_{ref} = \Psi_{obj} |\Psi_{ref}|^2 \quad (1-29)$$

The expression of the target beam pointing to any angle in space is known, and the expression of the excitation is also clear. Therefore, the interference pattern of the surface and the impedance distribution of the surface can be obtained. The surface

impedance distribution is calculated according to the following formula [87]:

$$Z(x, y) = j[X + M \operatorname{Re} \Psi_{obj} \cdot \Psi_{ref}^*] \quad (1-30)$$

where
$$X = \left(\frac{Z_{\max} + Z_{\min}}{2} \right), \quad M = \left(\frac{Z_{\max} - Z_{\min}}{2} \right). \quad (1-31)$$

Different impedances can be realized by adjusting the structures of elements, and specific values can be directly extracted from HFSS. Based on the scalar impedance modulation surface, Sievnepiper *et al.* also demonstrated the tensor impedance modulation method, for example, changing the side lengths of each unit to realize a circularly polarized wave beam with different polarization. Minatti *et al.* later designed a variety of high-gain, large tilting angle, and multi-polarization surface antennas based on tensor impedance modulation surfaces [64], as shown in Fig. 1.15. In addition to achieving the target beam with any angle in space, surface antennas with impedance modulation have more advantages in the conformal antennas' community than traditional antennas.

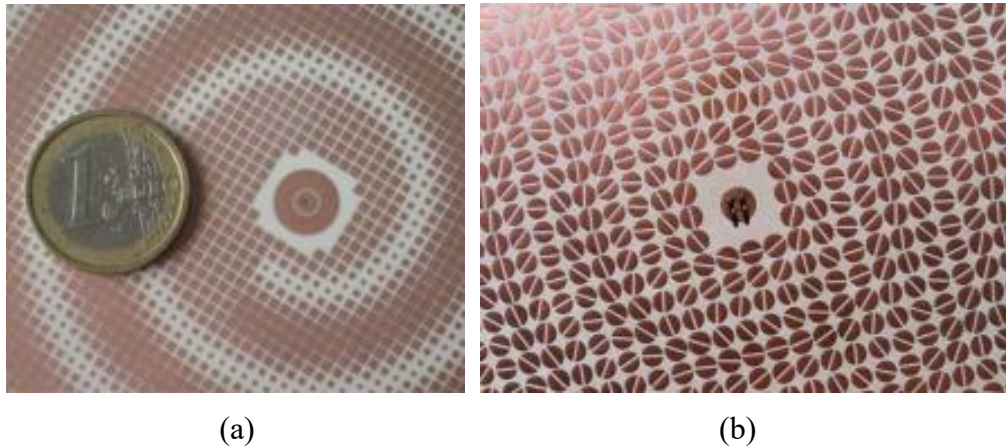


Fig. 1.15. Scalar and tensor holographic antennas. (a) Antenna based on scalar impedance surface [64]. (b) Circularly polarized antenna based on tensor impedance surface [64].

The disadvantage of high-gain antennas is that they have narrow beam-width coverage. Thus, they provide only limited spatial coverage, meaning that they are not good candidates for multi-user mobile communications [65]. Moreover, the

single-directional beam must be steered either mechanically or electronically to search for a reliable substitute link for non-LOS communications (mm-wave signals are also vulnerable to obstacles). To tackle this challenge, multi-beam devices (MBDs), which can generate several independent high-directive beams to cover a wide angular range, provide a good solution, as shown in Fig. 1.16.

1.2.2 Mm-wave and THz Multi-beam Devices (MBDs)

Generally, the technology to achieve MBDs can be categorized into three types: a) MBDs based on reflectors, b) MBDs based on lenses, c) MBDs based on beamforming circuits.

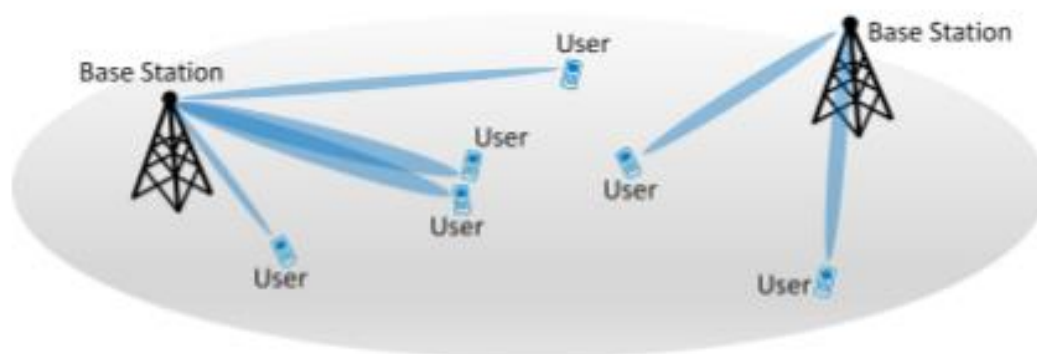


Fig. 1.16. Multibeam antennas used for base station application ^[65].

1.2.2.1 MBDs based on reflectors/reflectarrays.

Reflector-based MBDs are based on the ray-optics principle. Strictly speaking, the reflector performs the Fourier transform and redistributes energy from the impinging free-space propagating wave to the required aperture distribution [66]. The reflector can be single, such as the parabolic antenna [67] shown in Fig. 1.17, or dual-reflector-based, such as the Cassegrain antenna [68] shown in Fig. 1.18. In general, the scan coverage typically depends on the type of reflector, whereas scan speed and resolution depend on the choice of the feed system.

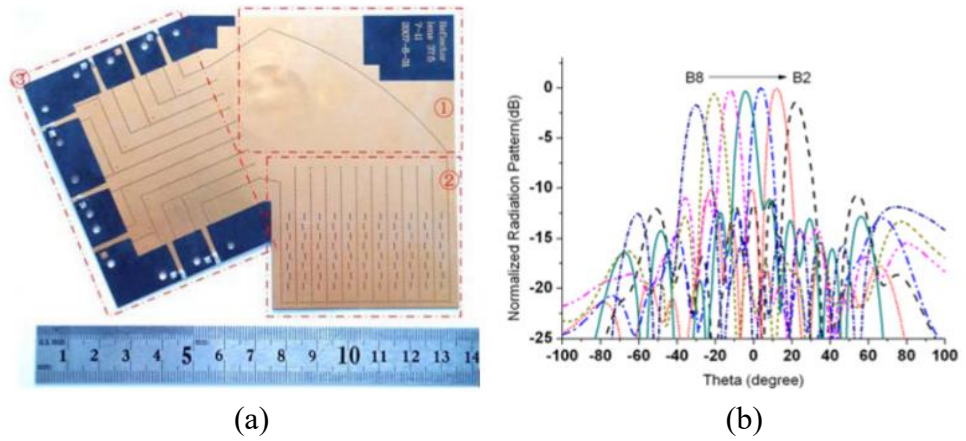


Fig.1.17. (a) Multibeam parabolic antennas ^[67]. (b) Scanning angle ^[67].

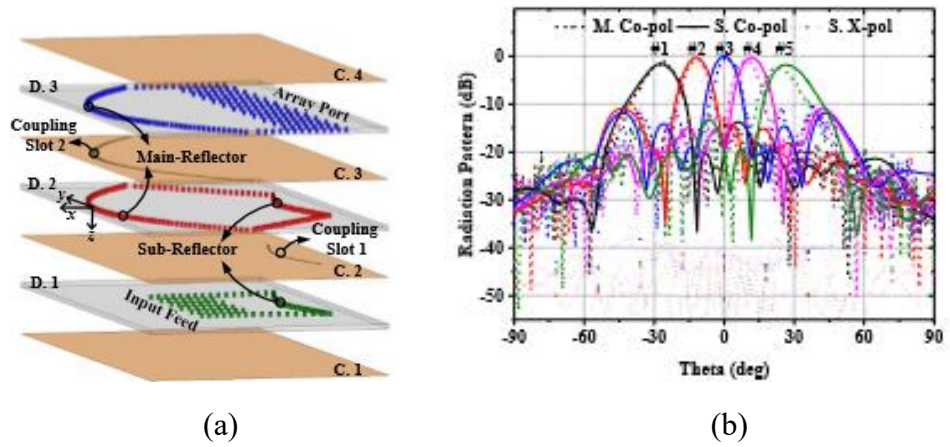


Fig 1.18. (a) Quasi-Cassegrain antenna with dual reflector ^[68]. (b) Scanning angle^[68].

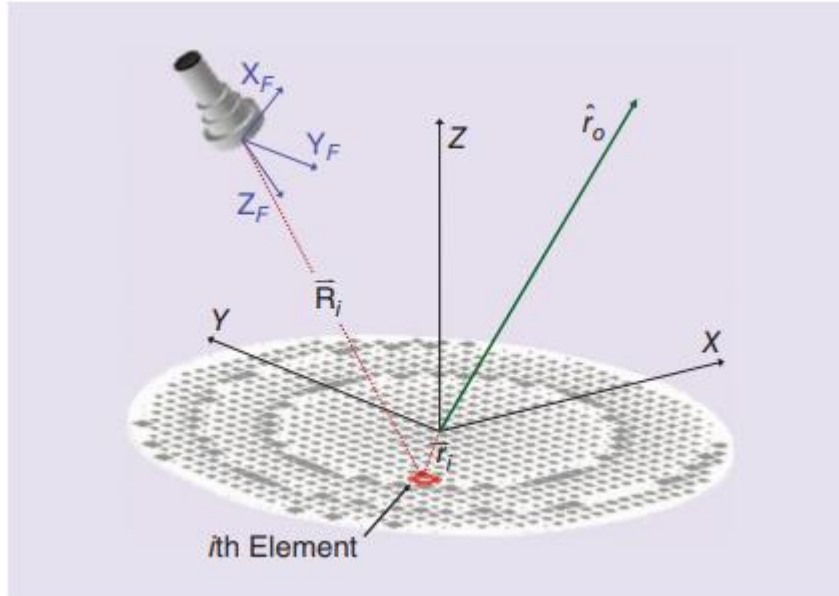


Fig. 1.19. Reflectarray with single feed ^[32].

Reflectarray antennas can be also used to achieve scanning beams. To dynamically control the beams, the phase distribution on the reflectarray aperture must be

predesigned corresponding to the direction of the scanned beams. Consider a reflectarray system that consists of a reflectarray with only a single feed, as shown in Fig. 1.19. The phase distribution for each element on the reflectarray aperture can be expressed as [32]:

$$\phi(x_i, y_i) = -k_0 R_i + \phi_R(x_i, y_i) \quad (1-32)$$

where k_0 is the free space wavenumber. The first component is the electrical distance between the phase centre of the feed and the phasing element on the array. The second term is the reflection phase of the i th element on the aperture. Because the two components are not related, they can be independently controlled. Therefore, the beam scanning approaches of the reflectarray can be categorized into two:

- Feed tuning
- Aperture phase tuning

For the feed-tuning technique, one tunes the spatial delay by dynamically changing the position of the feed system. For aperture phase tuning, the approaches can be varied. For example, one can use motors to dynamically rotate each phasing element [69] (shown in Fig. 1.20), use a pin diode switch [70], or use MEMS RF switches [71] (shown in Fig. 1.21).

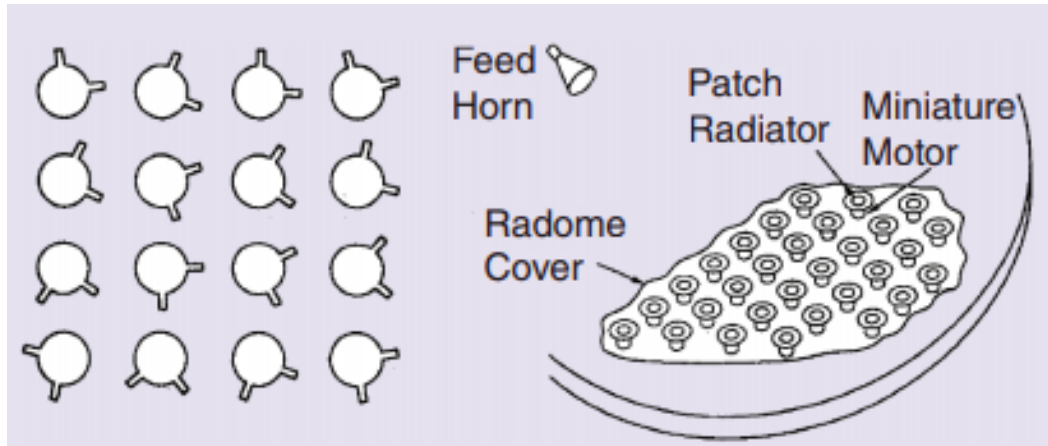


Fig. 1.20. Use motors to rotate the angle of each phasing element [61].

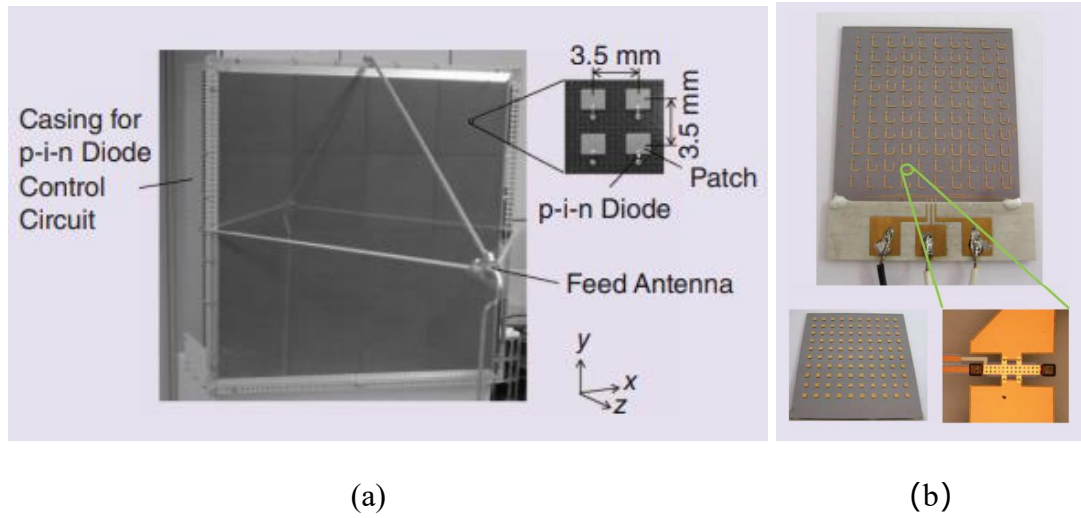


Fig. 1.21. (a) A beam-scanning reflectarray using pin diode to control the states of each phasing element ^[70]. (b) A beam-scanning reflectarray antenna using MEMS ^[71].

1.2.2.2 MBDs based on lenses

Different from reflector-based MBDs, lens-based MBDs are transmitting types that provide targeted multibeam radiation. Basically, one side of the lens is illuminated by multiple feeding antennas, while the other side of the lens serves as the radiating aperture [65]. Compared with the reflector-based MBDs, lens-based MBDs provide more compact system configurations without blockage effects from the feed antennas. Examples include the Rotman lens [72-74], the Luneburg lens [75-78], and the fisheye lens [79], as shown in Fig. 1.22.

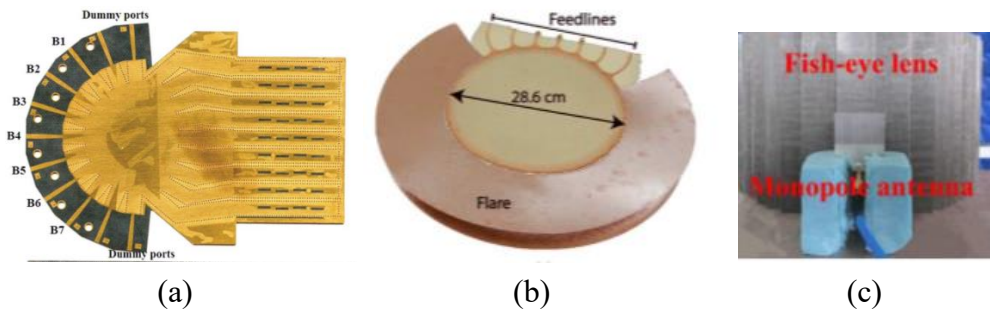


Fig. 1.22. (a) Rotman lens using SIW^[72]. (b) Luneburg lens^[75]. (c) fisheye lens ^[79].

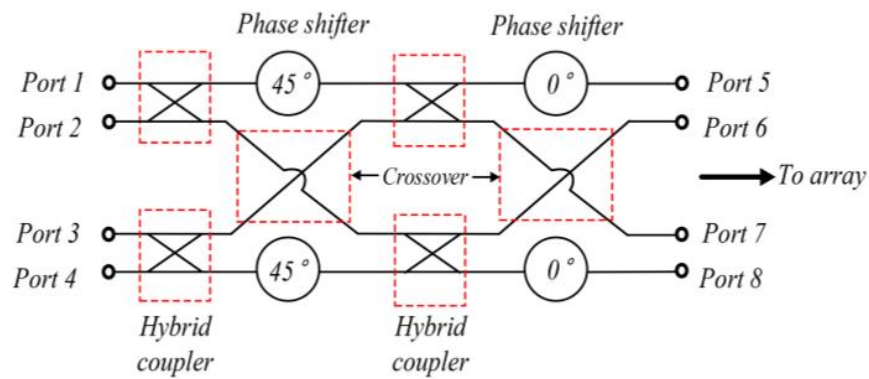


Fig. 1.23. Butler matrix.

1.2.2.3 MBDs based on beamforming circuits.

Unlike reflector-based and lens-based MBDs, which relies on the quasi-optics principle, a beamforming circuit is a versatile approach that integrates the feeding network into the array antennas [80]. Specifically, the phase distributions along the linear antenna array required to achieve beams pointing at different angles are obtained from phase-shifting transmission lines and directional couplers [81]. The most commonly used beamforming feeding network is the Butler matrix, the configuration of which is shown in Fig.1.23. One-dimensional beam scanning can be easily achieved by integrating radiators into the output of the Butler matrix. In order to achieve two-dimensional beam scanning, a dual Butler matrix is folded together to achieve 16-beams and 8-beams in two-dimensions [82-84], as shown in Fig. 1.24. Note that the Butler matrix occupies too large an area, which is difficult to integrate with circuits. Therefore, for multibeam antennas-in-package, we can also use chips to control the phase of each radiator to achieve electrical beam scanning [85], as shown in Fig. 1.25.

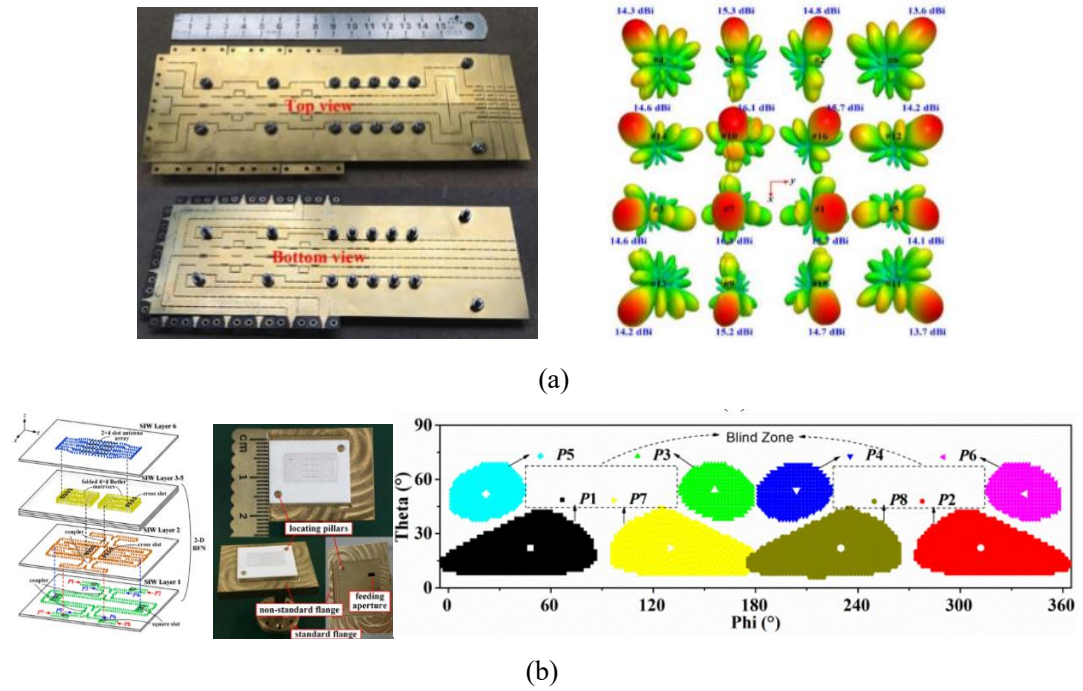


Fig. 1.24. (a) Two-dimensional MBD and its beam^[83]. (b) Two-dimensional MBD with folding Butler matrix and its beam scanning performance^[84].

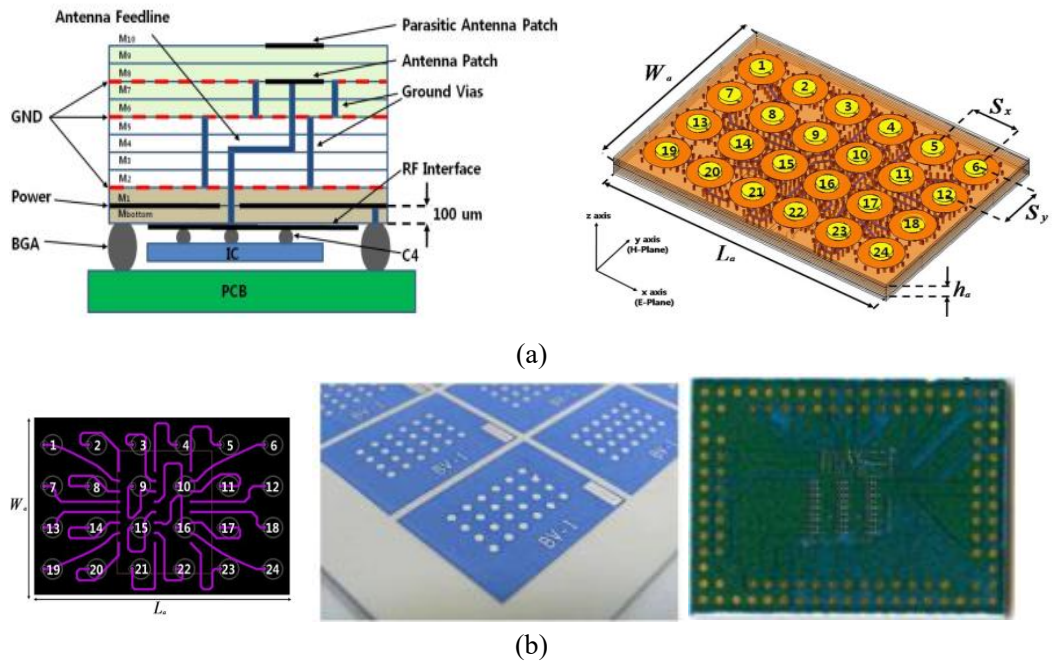


Fig. 1.25. Scanning beam antenna using chip^[77]. (a) Antenna element and its array view. (b) Prototype.

1.2.3 Fabrication Technology for Mm-wave and THz Beam-Shaping Devices:

The availability of fabrication for the mm-wave and THz devices also restricts the development of the mm-wave and THz fields. As the frequency increases, the fabrication tolerance and the losses from the materials become important issues and challenges for the designers. Though there are different fabrication solutions for mm-wave and THz devices, we will mainly introduce the low-temperature co-fired ceramic (LTCC) and 3-D printing fabrication, which are used for antenna fabrication in the thesis.

1.2.3.1 Low-temperature co-fired ceramic (LTCC) fabrication technique

Most planar beam-shaping devices operating in the microwave band are fabricated using PCB technology. In the mm-wave frequency band (<100 -GHz), PCB technology is still useful. For multilayer devices, each layer is fabricated independently and stacked in order using screw holes. Bonding should be used between PCB layers to remove the air between them. On the other hand, to achieve high gain to compensate for the high path loss in the mm-wave band, antennas are usually designed in an array form. To feed each element of the array, feeding work is required. Due to the high radiation loss of the microstrip line in the mm-wave frequency band, a SIW is commonly used as a feeding network. However, the SIW-based feeding network occupies too large an area. Therefore, the multilayer low-temperature co-fired ceramic (LTCC) fabrication technique was introduced and is now widely used in mm-wave consumer-level antenna designs, since the feeding structure and radiators can be integrated into the multi-layered substrate in a compact packaged form. The firing temperature of LTCC is about $900\text{ }^{\circ}\text{C}$. Therefore, gold, silver, and some other good conductive materials can be used instead of the molybdenum and tungsten which are commonly used in high-temperature co-fired ceramic (HTCC) fabrication [86]. The multi-step process is required for LTCC

fabrication, as shown in Fig. 1. 26. Before blanking, the sheets of ceramic (usually shipped in rolled form) are unrolled first and then cut carefully using a laser. After blanking, the via holes are drilled using a laser and the holes are then filled with the conductive paste using via filler. Conductors are also printed on the sheets. The sheets with printed conductors and via holes are laminated and exposed to fire at a temperature of about 900 °C. Additional circuit elements such as resistors and SMD components can be integrated on the top layer after cofiring is completed. Though high assembly yield, good crosstalk and radiation management, good stability and reliability can be achieved, LTCC technology is mainly used for fabricating devices operating at frequencies lower than 0.3 THz. This is because the loss of the dielectric and conductor layers would increase and the tolerance cannot meet the requirement for the frequency beyond 0.3 THz. For frequency higher than 0.3 THz, microfabrication would be a better solution.

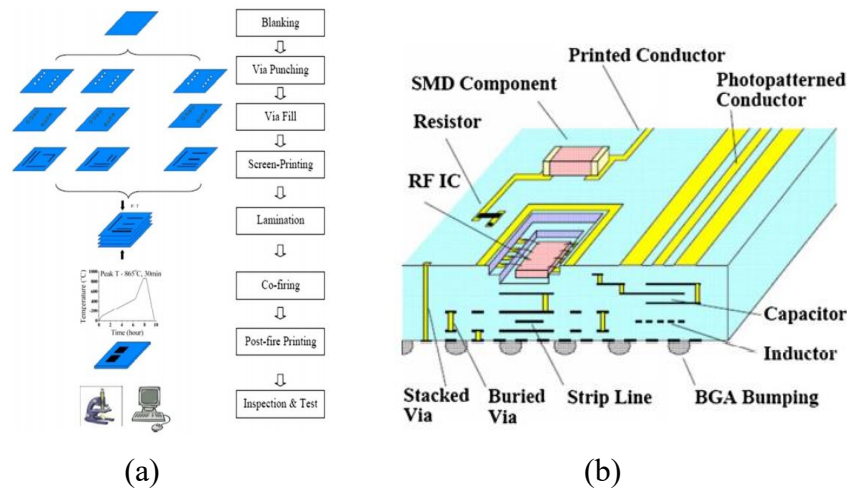


Fig. 1.26. (a) LTCC multilayer circuit processing steps ^[86]. (b) Schematic view of an LTCC module illustrating multiple embedded components ^[86].

1.2.3.2 3-D printing technique

As a low-cost and fast prototyping technology, 3-D printing has become a hot research subject in recent decades. The first 3-D printed antenna operating in the mm-wave band in the literature was reported in 2005 using dielectric powder as the

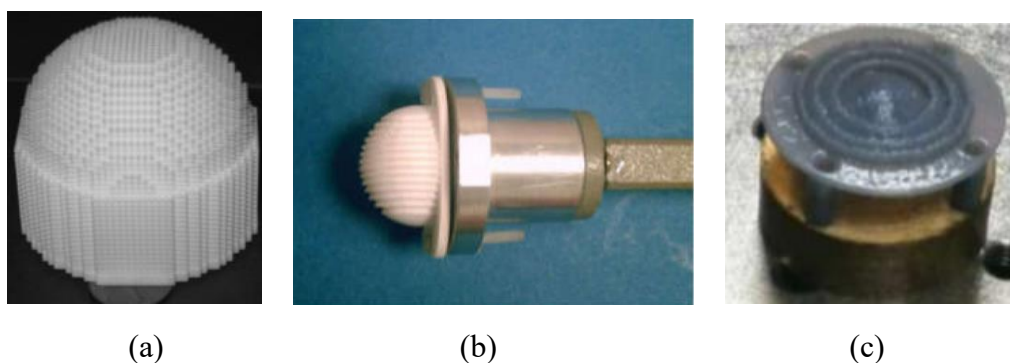


Fig. 1.27. (a) A CSLA Ka-band Luneburg lens using alumina ^[87]. (b) A 60-GHz lens by CSLA alumina ^[88]. (c) H-band lens ^[89].

printing material. Later, a Luneburg lens was printed using ceramic stereolithography apparatus (CSLA) in 2007 [87], as shown in Fig. 1. 27(a). After that, various kinds of passive components were printed and the operating frequency gradually moved to higher bands (mm-wave and low THz band). In 2010, a 60-GHz elliptical lens was reported, as shown in Fig. 1.27 (b) [88]. The lens was fabricated using the ceramic stereolithography apparatus. Its impedance bandwidth covered 55–65 GHz and the maximum gain reached 21 dBi at 64 GHz. In 2014, an H-band SLA lens was demonstrated [89], as shown in Fig. 1.27 (c). Its peak gain reached 26.5 dBi at 268 GHz. State-of-art work on the 3-D printed passive devices can be found in [90]. Generally, a 3D-printed passive device can be categorized as either dielectric-based or metal-based. For dielectric-based 3-D printing, the simplest case is that the device is printed first and assembled if the device has multiple parts, and the dielectric lens is an example. Devices that require metallization, such as filters and waveguides are usually printed first and then coated with metal. As shown in Fig. 1.28, an H-band (220–325GHz) stereolithography-based diagonal horn and waveguide were introduced [90]. The main parts are made of a non-conductive photopolymer and surfaces and waveguide flanges are metalized after printing. The diagonal horn has a maximum gain reaching 26 dBi at 320 GHz while the waveguide shows an average 0.4-dB insertion loss using Au and a 0.6-dB insertion loss using Alumina in the H-band.

Dielectric 3-D printing enjoys the benefits of low cost and light weight. However,

the disadvantages are obvious: first, the mechanical strength of the dielectric material is quite low, which limits its application in harsh environments and the life of the device; second, the additional processes such as metal coating and assembling increase the design complexity. In addition, the lossy filament of the dielectric printing also restricts the design of the devices operating at mm-wave and THz regions. Those disadvantages can be avoided by using metal printing. The mechanical strength of the metal is very high and no metal coating is required during the printing process. Furthermore, the thermal expansion problem that commonly appears in dielectric printing no longer exists. Zhang from the Chalmers University of Technology conducted a series of experiments on metallic 3-D-printed components, such as horns and waveguides to find the most appropriate material and process for device fabrication. Although various researchers are now exploring 3-D printing for the fabrication of mm-wave and THz devices, the fabrication tolerance, surface roughness, and cost of 3-D printing are still factors that restrict its wide use in commercial and consumer-level applications.

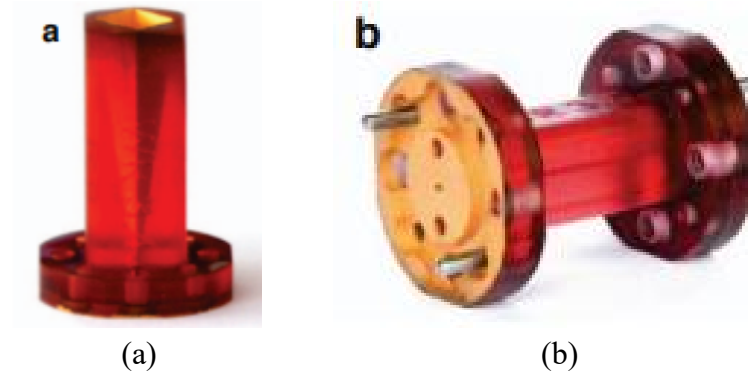


Fig. 1.28. (a) an H-band horn^[90]. (b) an H-band waveguide ^[90]. (Both are printed first and then electroplated).

1.3 Conclusion

In summary, high gain antennas are indispensable components for the mm-wave and sub-THz communication system. The commonly used high gain antennas, such as aperture antennas, reflectarray antennas, FPC antennas, and surface-wave antennas are investigated first. Because the high gain antennas can only provide

limited spatial coverage, mm-wave multi-beam antennas are then investigated. The common approaches to realized multi-beam can be categorized in general as a) MBDs based on reflectors, b) MBDs based on lenses, c) MBDs based on beamforming circuits. Each of three methods to realized multi-beam is discussed. Finally, the fabrication techniques used in the thesis including LTCC and 3-D printing are introduced with the state-of-the-art works discussed. Despite the enormous challenges, such as mm-wave/THz sources, circuits, antennas, system architecture, and fabrication that must be overcome, a new research area of mm-wave and THz technology is beginning to form.

References

- [1] X. Wang *et al.*, “Millimeter wave communication: a comprehensive survey,” IEEE Commun. Surv. Tutor, vol. 20, no. 3, pp. 1616-1653, third quarter 2018.
- [2] S. A. Busari, K.M.S. Huq, S. Mumtaz, *et al.*, “Millimeter-wave massive MIMO communication for future wireless systems: A survey,” IEEE Commun. Surv. Tutor, 20(2): 836-869 2017.
- [3] M. Agiwal, A. Roy and N. Saxena, “Next generation 5G wireless networks: a comprehensive survey,” IEEE Commun. Surv. Tutor, vol. 18, no. 3, pp. 1617-1655, third quarter 2016.
- [4] Z. Chen *et al.*, “A survey on terahertz communications,” China Commun., vol. 16, no. 2, pp. 1-35, Feb. 2019.
- [5] I. Akyildiz, J. Jornet, C. Han, “Terahertz band: next frontier for wireless communications,” Physical Commun., 12: 16-32, 2014.
- [6] K. Jha, G. Singh, “Terahertz planar antennas for future wireless communication: A technical review,” Infrared Physics & Technology, 60: 71-80, 2013.
- [7] Friis H T., “A note on a simple transmission formula,” Proceedings of the IRE, 34(5): 254-256, 1946.
- [8] T. Kleine-Ostmann, T. Nagatsuma, “A review on terahertz communications research,” Journal of Infrared, Millimeter, and Terahertz Waves, 32(2): 143-171. 2011.
- [9] J. Zhu, C. Chu, L. Deng, C. Zhang, Y. Yang and S. Li, “Mm-wave high gain

cavity-backed aperture-coupled patch antenna array,” IEEE Access, vol. 6, pp. 44050-44058, 2018.

[10] Petkov P Z, Simon P S. Antenna array with reduced mutual coupling between array elements: U.S. Patent 9,537,209[P]. 2017-1-3.

[11] B. Liu *et al.*, “Substrate integrated waveguide (SIW) monopulse slot antenna array,” IEEE Trans. Antennas Propag., vol. 57, no. 1, pp. 275-279, Jan. 2009.

[12] Y. Li and K. Luk, “A 60-GHz wideband circularly polarized aperture-coupled magneto-electric dipole antenna array,” IEEE Trans. Antennas Propag., vol. 64, no. 4, pp. 1325-1333, April 2016.

[13] H. Wang, X. B. Huang and D. G. Fang, “A single layer wideband U-slot microstrip patch antenna array,” IEEE Antennas Wireless Propag. Lett., vol. 7, pp. 9-12, 2008.

[14] H. Sun, Y. Guo and Z. Wang, “60-ghz circularly polarized u-slot patch antenna array on ltcc,” IEEE Trans. Antennas Propag., vol. 61, no. 1, pp. 430-435, Jan. 2013.

[15] Ohlsson M. Horn antenna: U.S. Patent 6,859,187[P]. 2005-2-22.

[16] Hart J W. Shrouded parabolic antenna structure: U.S. Patent 3,351,947[P]. 1967-11-7.

[17] Q. Wu, H. Wang, C. Yu and W. Hong, “Low-profile circularly polarized cavity-backed antennas using siw techniques,” IEEE Trans. Antennas Propag., vol. 64, no. 7, pp. 2832-2839, July 2016.

[18] J. Liu, A. Vosoogh, A. U. Zaman and J. Yang, “Design and fabrication of a high-gain 60-ghz cavity-backed slot antenna array fed by inverted microstrip gap waveguide,” IEEE Trans. Antennas Propag., vol. 65, no. 4, pp. 2117-2122, April 2017.

[19] Q. Wu, J. Yin, C. Yu, H. Wang and W. Hong, “Low-profile millimeter-wave SIW cavity-backed dual-band circularly polarized antenna,” IEEE Trans. Antennas Propag., vol. 65, no. 12, pp. 7310-7315, Dec. 2017.

[20] D. Guan, C. Ding, Z. Qian, Y. Zhang, Y. Jay Guo and K. Gong, “Broadband high-gain siw cavity-backed circular-polarized array antenna,” IEEE Trans. Antennas Propag., vol. 64, no. 4, pp. 1493-1497, April 2016.

[21] S. Liao, P. Wu, K. M. Shum and Q. Xue, “Differentially fed planar aperture antenna with high gain and wide bandwidth for millimeter-wave application,” IEEE Trans. Antennas Propag., vol. 63, no. 3, pp. 966-977, March 2015.

[22] S. Liao and Q. Xue, “Dual polarized planar aperture antenna on ltcc for 60-ghz

antenna-in-package applications,” *IEEE Trans. Antennas Propag.*, vol. 65, no. 1, pp. 63-70, Jan. 2017.

[23] D. J. Bisharat, S. Liao and Q. Xue, “Circularly polarized planar aperture antenna for millimeter-wave applications,” *IEEE Trans. Antennas Propag.*, vol. 63, no. 12, pp. 5316-5324, Dec. 2015.

[24] D. J. Bisharat, S. Liao and Q. Xue, “High gain and low cost differentially fed circularly polarized planar aperture antenna for broadband millimeter-wave applications,” *IEEE Trans. Antennas Propag.*, vol. 64, no. 1, pp. 33-42, Jan. 2016.

[25] N. Ghassemi, K. Wu, S. Claude, X. Zhang and J. Bornemann, “Low-cost and high-efficient w-band substrate integrated waveguide antenna array made of printed circuit board process,” *IEEE Trans. Antennas Propag.*, vol. 60, no. 3, pp. 1648-1653, March 2012.

[26] Y. Hsu, T. Huang, H. Lin and Y. Lin, “Dual-polarized quasi yagi-uda antennas with endfire radiation for millimeter-wave mimo terminals,” *IEEE Trans. Antennas Propag.*, vol. 65, no. 12, pp. 6282-6289, Dec. 2017.

[27] S. V. Hum and J. Perruisseau-Carrier, “Reconfigurable reflectarrays and array lenses for dynamic antenna beam control: A review.” *IEEE Trans. Antennas Propag* 62.1: 183-198, 2013.

[28] Z. H. Jiang, T. Yue and W. Hong. “Low-profile and wideband dual-circularly polarized reflect-arrays based on rotated metal-backed dual-polarized aperture-coupled patch elements.” *IEEE Trans. Antennas Propag*, vol. 68, no. 3, pp. 2108-2117, March 2020.

[29] N. Payam, F. Yang, and Atef Z. Elsherbeni. *Reflectarray Antennas: Theory, Designs and Applications*. John Wiley & Sons, 2018.

[30] S. Qu, Q. Chen, M. Xia and X. Y. Zhang, “Single-layer dual-band reflectarray with single linear polarization,” *IEEE Trans. Antennas Propag*, vol. 62, no. 1, pp. 199-205, Jan. 2014.

[31] Fan Yang, and Rahmat-Samii Yahya, eds. *Surface electromagnetics: with applications in antenna, microwave, and optical engineering*. Cambridge University Press, 2019.

[32] Nayeri, Payam, Fan Yang, and Atef Z. Elsherbeni. “Beam-Scanning reflectarray

antennas: a technical overview and state of the art,” IEEE Antennas and Propag. Mag. 57.4 : 32-47,2015.

[33] H. T. Chen, A. J. Taylor, N. Yu, “A review of metasurfaces: physics and applications,”. Reports on progress in physics, 79(7): 076401,2016.

[33] R. Deng, Y. Mao, S. Xu and F. Yang, “A single-layer dual-band circularly polarized reflectarray with high aperture efficiency,” IEEE Trans. Antennas Propag., vol. 63, no. 7, pp. 3317-3320, July 2015.

[34] E. Martinez-de-Rioja, J. A. Encinar, M. Barba, R. Florencio, R. R. Boix and V. Losada. “Dual polarized reflectarray transmit antenna for operation in Ku-and Ka-bands with independent feeds.” IEEE Trans. Antennas Propag. 65.6: 3241-3246,2017.

[35] X. Meng, *et al.* “Dual-polarized reflectarray for generating dual beams with two different orbital angular momentum modes based on independent feeds in C-and X-bands.” Opt. express 26.18: 23185-23195, 2018.

[36] T. Smith, *et al.* “Design, manufacturing, and testing of a 20/30-GHz dual-band circularly polarized reflectarray antenna.” IEEE Antennas Wireless Propag. Lett. 12: 1480-1483,2013.

[37] S. Mener, *et al.* “Dual circularly polarized reflectarray with independent control of polarizations.” IEEE Trans. Antennas Propag. 63.4 : 1877-1881,2015.

[38] R. Deng, *et al.* “An FSS-backed 20/30-GHz dual-band circularly polarized reflectarray with suppressed mutual coupling and enhanced performance.” IEEE Trans. Antennas Propag.. 65.2 : 926-931,2016.

[39] Pilz, D., and W. Menzel. “Folded reflectarray antenna.” Electron. Letters 34.9: 832-833,1998.

[40] G. V. Trentini, “Partially reflecting sheet array,” IRE Trans. Antennas Propag., vol. AP-4,no.4,pp.666–671,Oct.1956.

[41] R. M. Hashmi and K. P. Esselle, “A class of extremely wideband resonant cavity antennas with large directivity-bandwidth products,” IEEE Trans. Antennas Propag., vol. 64, no. 2, pp. 830–835, Feb. 2016.

- [42] Y. Ge, K. P. Esselle, and T. S. Bird, "The use of simple thin partially reflective surfaces with positive reflection phase gradients to design wideband, low-profile EBG resonator antennas," *IEEE Trans. Antennas Propag.*, vol. 60, no. 2, pp. 743–750, Feb. 2012.
- [43] Guérin N, Enoch S, Tayeb G, *et al.* A metallic Fabry-Perot directive antenna. *IEEE Trans. Antennas Propag.*, 2006, 54(1): 220-224.
- [44] Z. Liu and W. Lu, "Low-profile design of broadband high gain circularly polarized fabry-perot resonator antenna and its array with linearly polarized feed" *IEEE Access*, vol. 5, pp. 7164-7172, 2017.
- [45] K. Dutta, D. Guha, and C. Kumar, "Theory of controlled aperture field for advanced superstrate design of a resonance cavity antenna with improved radiations properties," *IEEE Trans. Antennas Propag.*, vol. 65, no. 3, pp. 1399–1403, Mar. 2017
- [46] A. A. Baba, R. M. Hashmi, K. P. Esselle and A. R. Weily, "Compact high-gain antenna with simple all-dielectric partially reflecting surface," *IEEE Trans. Antennas Propag.*, vol. 66, no. 8, pp. 4343-4348, Aug. 2018.
- [47] R. M. Hashmi and K. P. Esselle, "A class of extremely wideband resonant cavity antennas with large directivity-bandwidth products," *IEEE Trans. Antennas Propag.*, vol. 64, no. 2, pp. 830–835, Feb. 2016.
- [48] N. Guerin, S. Enoch, G. Tayeb, P. Sabouroux, P. Vincent and H. Legay, "A metallic Fabry-Perot directive antenna," *IEEE Trans. Antennas Propag.*, vol. 54, no. 1, pp. 220-224, Jan. 2006.
- [49] W. Liu, Z.N. Chen, T.S.P See, *et al.* "SIW-slot-fed thin beam-squint-free Fabry-Pérot cavity antenna with low backlobe levels," *IEEE Antennas Wireless Propag. Lett.*, 2014, 13: 552-554.
- [50] S. A. Hosseini, F. Capolino and F. De Flaviis, "A new formula for the pattern bandwidth of fabry-pérot cavity antennas covered by thin frequency selective surfaces," *IEEE Trans. Antennas Propag.*, vol. 59, no. 7, pp. 2724-2727, July 2011.
- [51] Gu Y Y, Zhang W X, Ge Z C. "Two improved Fabry-Perot resonator printed

antennas using EBG superstrate and AMC substrate.” *Journal of Electromagnetic Waves and Applications*, 21(6): 719-728, 2007.

[52] K. Konstantinidis, K. P. Feresidis, and P. S. Hall, “Multilayer partially reflective surfaces for broadband Fabry–Pérot cavity antennas,” *IEEE Trans. Antennas Propag.*, vol. 62, no. 7, pp. 3474–3481, Jul. 2014.

[53] M. A. Al-Tarifi, D. E. Anagnostou, A. K. Amert, and K. W. Whites, “Bandwidth enhancement of the resonant cavity antenna by using two dielectric superstrates,” *IEEE Trans. Antennas Propag.*, vol. 61, no. 4, pp. 1898–1908, Apr. 2013.

[54] N. Wang, J. Li, G. Wei, L. Talbi, Q. Zeng and J. Xu, “Wideband fabry–perot resonator antenna with two layers of dielectric superstrates,” *IEEE Antennas Wireless Propag. Lett.*, vol. 14, pp. 229-232, 2015.

[55] F. Wu and K. M. Luk, “Wideband high-gain open resonator antenna using a spherically modified, second-order cavity,” *IEEE Trans. Antennas Propag.*, vol. 65, no. 4, pp. 2112–2116, Apr. 2017.

[56] A. R. Weily, K. P. Esselle, T. S. Bird, and B. C. Sanders, “Dual resonator 1-D EBG antenna with slot array feed for improved radiation bandwidth,” *IET Microwave, Antennas and Propagation.*, vol. 1, no. 1, pp. 198–203, Feb. 2007.

[57] Ishimaru A. *Electromagnetic wave propagation, radiation, and scattering: from fundamentals to applications*[M]. John Wiley & Sons, 2017.

[58] Dia’aaldin, J. Bisharat, and Daniel F. Sievenpiper. “Guiding waves along an infinitesimal line between impedance surfaces.” *Physical review letters* 119.10: 106802, 2017.

[59] K. Mak, K. So, H. Lai and K. Luk, “A magnetoelectric dipole leaky-wave antenna for millimeter-wave application.” *IEEE Trans. Antennas Propag.* 65.12: 6395-6402, 2017.

[60] Y. Li, Q. Xue, E. K. Yung and Y. Long, “The periodic half-width microstrip leaky-wave antenna with a backward to forward scanning capability.” *IEEE Trans. Antennas Propag.* 58.3: 963-966, 2009.

[61] D. Guan, Q. Zhang, P. You, Z. Yang, Y. Zhou and S. Yong, “Scanning rate enhancement of leaky-wave antennas using slow-wave substrate integrated waveguide structure.” *IEEE Trans. Antennas Propag.* 66.7: 3747-3751, 2018.

[62] J. Y. Yin *et al.* “Frequency-controlled broad-angle beam scanning of patch array

- fed by spoof surface plasmon polaritons.” IEEE Trans. Antennas Propag. 64.12: 5181-5189, 2016.
- [63] B. H. Fong, J. S. Colburn, J. J. Ottusch, J. L. Visher and D. F. Sievenpiper. “Scalar and tensor holographic artificial impedance surfaces.” IEEE Trans. Antennas Propag. 58.10: 3212-3221, 2010.
- [64] G. Minatti *et al.*, Modulated Metasurface Antennas for Space: Synthesis, Analysis and Realizations. IEEE Trans. Antennas Propag., 63(4):1288-1300, 2015.
- [65] W. Hong *et al.*, “Multibeam antenna technologies for 5g wireless communications,” IEEE Trans. Antennas Propag., vol. 65, no. 12, pp. 6231-6249, Dec. 2017.
- [66] S. Rao, L. Shafai, and S. Sharma, “Handbook of reflector antennas and feed systems,” in Applications of Reflectors, vol. 3. Norwood, MA, USA: Artech House, Jun. 2013, pp. 13–76.
- [67] Y. J. Cheng, W. Hong, and K. Wu, “Millimeter-wave substrate integrated waveguide multibeam antenna based on the parabolic reflector principle,” IEEE Trans. Antennas Propag., vol. 56, no. 9, pp. 3055-3058, Sept. 2008.
- [68] J. Lian, Y. Ban, Z. Chen, B. Fu and C. Xiao, “SIW folded Cassegrain lens for millimeter-wave multibeam application,” IEEE Antennas Wireless Propag. Lett., vol. 17, no. 4, pp. 583-586, April 2018.
- [69] J. Huang, “Bandwidth study of microstrip reflectarray and a novel phased reflectarray concept,” IEEE Antennas Propagation Society Int. Symp. Dig., Newport Beach, CA, June 1995, pp. 582–585.
- [70] H. Kamoda, T. Iwasaki, J. Tsumochi, T. Kuki, and O. Hashimoto, “60- GHz electronically reconfigurable large reflectarray using single bit phase shifters,” IEEE Trans. Antennas Propag., vol. 59, no. 7, pp. 2524–2531, 2011.
- [71] O. Bayraktar, O. Civi, and T. Akin, “Beam switching reflectarray monolithically integrated with RF MEMS switches,” IEEE Trans. Antennas Propag., vol. 60, no. 2, pp. 854–862, 2012.
- [72] Y. J. Cheng *et al.*, “ Substrate integrated waveguide (siw) rotman lens and its ka-band multibeam array antenna applications,” IEEE Trans. Antennas Propag., vol. 56, no. 8, pp. 2504-2513, Aug. 2008.
- [73] L. Schulwitz and A. Mortazawi, “A new low loss rotman lens design using a graded dielectric substrate,” IEEE Trans. Microw. Theory Tech., vol. 56, no. 12, pp. 2734-2741, Dec. 2008.

- [74] W. Lee, J. Kim and Y. J. Yoon. "Compact two-layer Rotman lensfed microstrip antenna array at 24 GHz." IEEE Trans. Antennas Propag. 59.2: 460-466, 2010.
- [75] C. Pfeiffer and A. Grbic, "A Printed, Broadband Luneburg Lens Antenna," IEEE Trans. Antennas Propag., vol. 58, no. 9, pp. 3055-3059, Sept. 2010.
- [76] M. Liang, W. Ng, K. Chang, K. Gbele, M. E. Gehm and H. Xin, "A 3-D Luneburg Lens Antenna Fabricated by Polymer Jetting Rapid Prototyping," IEEE Trans. Antennas Propag., vol. 62, no. 4, pp. 1799-1807, April 2014.
- [77] C. Mateo-Segura, A. Dyke, H. Dyke, S. Haq and Y. Hao, "Flat Luneburg Lens via Transformation Optics for Directive Antenna Applications," IEEE Trans. Antennas Propag., vol. 62, no. 4, pp. 1945-1953, April 2014.
- [78] H. Mosallaei and Y. Rahmat-Samii, "Nonuniform Luneburg and two-shell lens antennas: radiation characteristics and design optimization," IEEE Trans. Antennas Propag., vol. 49, no. 1, pp. 60-69, Jan 2001.
- [79] H. Xu, G. Wang, Z. Tao and T. Cai, "An octave-bandwidth half maxwell fish-eye lens antenna using three-dimensional gradient-index fractal metamaterials," IEEE Trans. Antennas Propag., vol. 62, no. 9, pp. 4823-4828, Sept. 2014.
- [80] T. L. Marzetta, "Noncooperative cellular wireless with unlimited numbers of base station antennas," IEEE Transactions on Wire. Commun., vol. 9, no. 11, pp. 3590-3600, November 2010.
- [81] J. Zhu, B. Peng and S. Li, "Cavity-backed high-gain switch beam antenna array for 60-GHz applications," IET Microw. Antennas Propag., vol. 11, no. 12, pp. 1776-1781, 22 9 2017.
- [82] P. Chen *et al.*, "A multibeam antenna based on substrate integrated waveguide technology for mimo wireless communications," IEEE Trans. Antennas Propag., vol. 57, no. 6, pp. 1813-1821, June 2009.
- [83] J. Lian, Y. Ban, Q. Yang, B. Fu, Z. Yu and L. Sun, "Planar millimeter-wave 2-d beam-scanning multibeam array antenna fed by compact siw beam-forming network," IEEE Trans. Antennas Propag., vol. 66, no. 3, pp. 1299-1310, March 2018.
- [84] W. Yang, Y. Yang, W. Che, C. Fan and Q. Xue, "94-ghz compact 2-d multibeam ltcc antenna based on multifolded siw beam-forming network," IEEE Trans. Antennas Propag., vol. 65, no. 8, pp. 4328-4333, Aug. 2017.
- [85] W. Hong, A. Goudelev, K. Baek, V. Arkhipenkov and J. Lee, "24-element antenna-in-package for stationary 60-ghz communication scenarios," IEEE Antennas Wireless Propag. Lett. , vol. 10, pp. 738-741, 2011.

- [86] Ullah U, Mahyuddin N, Arifin Z, et al. "Antenna in LTCC technologies: a review and the current state of the art,". IEEE Antennas and Propagation Magazine, 57(2): 241-260,2015.
- [87] K. F. Brakora, J. Halloran, and K. Sarabandi, "Design of 3-D monolithic MMW antennas using ceramic stereolithography," IEEE Trans. Antennas Propag., vol. 55, no. 3, pp. 790–797, Mar. 2007.
- [88] N. T. Nguyen, N. Delhote, M. Ettorre, D. Baillargeat, L. Coq, and R. Sauleau, "Design and characterization of 60-GHz integrated lens antennas fabricated through ceramic stereolithography," IEEE Trans. Antennas Propag., vol. 58, no. 8, pp. 2757–2762, Aug. 2010.
- [89] S. Qu, H. Yi, C. Chan, and K. Ng, "Low-cost discrete dielectric terahertz lens antenna using 3D printing," in Proc. IEEE Conf. Antennas Meas. Appl., Antibes Juan-les-Pins, France, Nov. 2014, pp. 1–3.
- [90] B. Zhang, Y. Guo, H. Zirath and Y. P. Zhang, "Investigation on 3-d-printing technologies for millimeter-wave and terahertz applications," Proceedings of the IEEE, vol. 105, no. 4, pp. 723-736, April 2017, doi: 10.1109/JPROC.2016.2639520.

Chapter II 3-D Printed Mm-wave and Sub-THz Polarization Manipulation and Beam-shaping Lenses, Prisms and Reflectarrays

2.1 Introduction

Shaping the beam of electromagnetic (EM) waves has attracted considerable attention and remarkable achievements have been achieved recently. Many interesting and exciting devices which focus light, [1-3] steer beams, [4-6] or generate orbital angular momenta, [7-9] have been demonstrated from optics to microwave. Among the wide spectrum, mm-wave and low THz frequency bands are now widely exploited for next-generation communications. In 2013, a sub-THz single-input-single-output (SISO) wireless communications link using three channels operating near 237.5 GHz for a transmission distance of 20 m with a speed of 100 Gb/s was reported [10], demonstrating the huge potential for future ultrahigh-speed wireless communications. With the rise of the metasurface, controlling the amplitude, phase, and polarization of mm-wave/THz waves has become a popular area. Over the last decade, many mm-wave/THz polarization manipulation and beam-shaping devices have been demonstrated, including antennas [11-14], reflectarrays [15-20], metasurfaces [21-26], and cloaking [27-28]. Although these interesting and exciting designs show good performance and pave the way to an efficient THz system, they require relatively costly fabrication processes, such as micro-fabrication. On the other hand, 3-D printing, also known as additive manufacturing, offers a new and economical way to construct THz devices. Since 3-D printing builds up the devices in an additive way rather than a subtractive manner (such as micro-machining or spark erosion [29], [30]), it is cost-effective, eco-friendly, and capable of producing complicated structures in a simple way [31]. To date, many THz/ Sub-THz devices have been fabricated using 3-D printing technology. Scenarios of interest include different kinds of lenses [32-34], beam splitters [35],[36], and phase plates [37],[38], to name a few. In this chapter, we present beam-shaping lenses, prisms and reflectarrays operating at

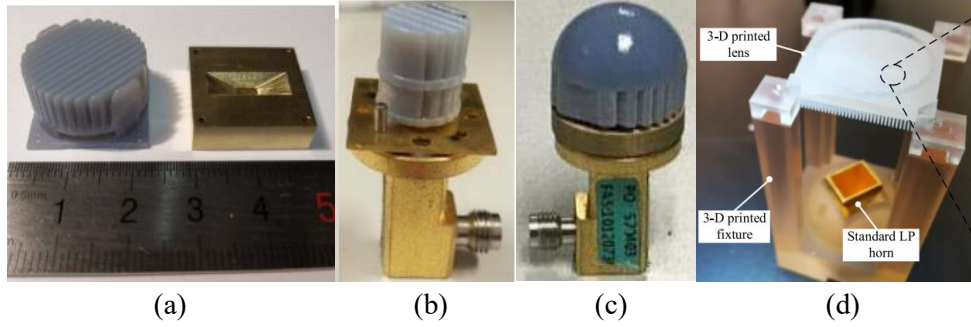


Fig. 2.1 (a) Hyperbolic lens with a polarizer ^[42]. (b) Dielectric polarizer ^[43]. (c) Dielectric polarizer and lens operating at mm-wave band ^[44]. (d) Dielectric polarizer and lens operating at THz band ^[45].

30-GHz, 0.14-THz, and 24 GHz/75-GHz respectively using 3-D printing. Specifically, Chapter 2.2 presents a kind of linear-to-circular polarization conversion lens, a Wollaston-Prism-Liked CP lens and a Rochon-Prism-Liked CP lens. Chapter 2.3 presents and discusses polarization beam splitters, including a Rochon prism and a Fresnel Rochon prism, while Chapter 2.4 demonstrates a new all-dielectric broadband dual-band reflectarray with a large frequency-ratio.

2.2 3-D Printed Planar Dielectric Linear-to-Circular Polarization Conversion and Beam-Shaping Lenses

In the mm-wave band, quarter-wave phase (QWP) plate-based lenses combining polarization conversion and beam shaping are particularly desirable. This is because the high directivity of the lens compensates for the high path loss at mm-wave frequencies [39] and a CP antenna prevents performance degradation caused by misalignment between the transmitting and receiving antennas [40], [41]. Many lens antennas with a CP source have been demonstrated. Recently, broadband circularly polarized antenna using an artificial anisotropic polarizer operating in the 60-GHz frequency band was demonstrated [42]; a hyperbolic lens is used to collimate the beams, and an artificial anisotropic polarizer is used to convert LP to CP, as shown in Fig. 2.1 (a). Wang. *et al.* [43] demonstrated a circularly polarized antenna using a dielectric polarizer, as shown in Fig. 2.1 (b). With the help of the polarizer, the directivity of the radiation pattern is also enhanced. A CP lens antenna with LP feeding was also demonstrated [44], which is formed by a cylindrical polarizer stacked with a hemispherical dielectric lens. The cylindrical polarizer, composed of dielectric grating and air slabs, converts the incident wave from LP into CP and a

hemispherical dielectric lens is used to improve the antenna gain, as shown in Fig. 2.1 (c). Later, Wu. *et al.* [45] demonstrated a terahertz CP lens antenna, in which the transmit-array is used to replace the conventional lens, as shown in Fig. 2.1 (d). Although these CP lenses have wide CP bandwidth and high gain, they are implemented by geometrically placing a lens or transmit-array above a QWP-plate. Moreover, traditional lenses [44] and dielectric transmitarrays with different unit-cell heights [45] make the design non-planar. Therefore, a geometrically planar and compact lens with both CP conversion and beam collimation/shaping is highly desirable for mm-wave applications. In this chapter, we propose a lens which achieves linear-to-circular polarization conversion and beam collimation in the transmission mode simultaneously with a planar configuration, which is different from counterparts which place a lens on top of a polarizer.

2.2.1 Unit cells of the lens

The building block of the lens is a new linear-to-circular polarization conversion unit cell (UC) with a basic structure shown in Fig. 2.2, which is simulated and optimized in ANSYS HFSS. It is composed of a dielectric grating, a supporting plate, and an anti-reflection (AR) coating, which are stacked in order. Polylactic acid (PLA) with a relative permittivity of 2.5 and a loss tangent of about 0.02 at 30-GHz is used in the design. To reduce the impact of fabrication tolerance, we choose a period of 0.8-wavelength at 30-GHz for proof-of-concept. In the simulation, periodic boundary conditions (PBCs) are set along the x and y -directions and Floquet ports are used as the excitation. Since the unit is designed with periodic boundaries, it is equal to a unit in an array with infinite uniform units with mutual coupling between adjacent cells considered. This means the performance (LP-to-CP conversion and phase delay) of each unit in the lens is different from those of the corresponding unit in an array with infinite uniform units, because of the change of the boundaries. Nevertheless, the performance differences are small and acceptable for lens design. This is because the units forming the lens slowly change to form the lens, namely two adjacent units are very similar in structure, which leads to similar boundaries for units in a lens and in an array with infinite uniform units.

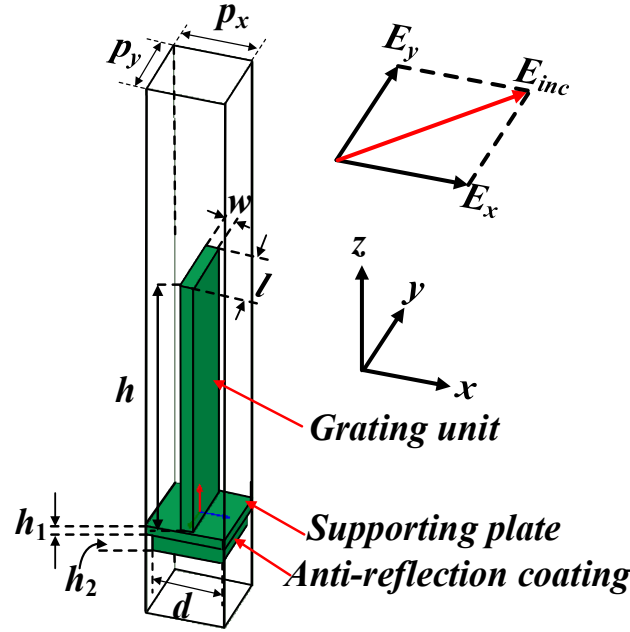


Fig. 2.2 Configuration of the UC. ($P_x=8$ mm, $P_y=8$ mm, $h=28$ mm, $h_1=1$ mm, $h_2=1.9$ mm, $d=7.2$ mm).

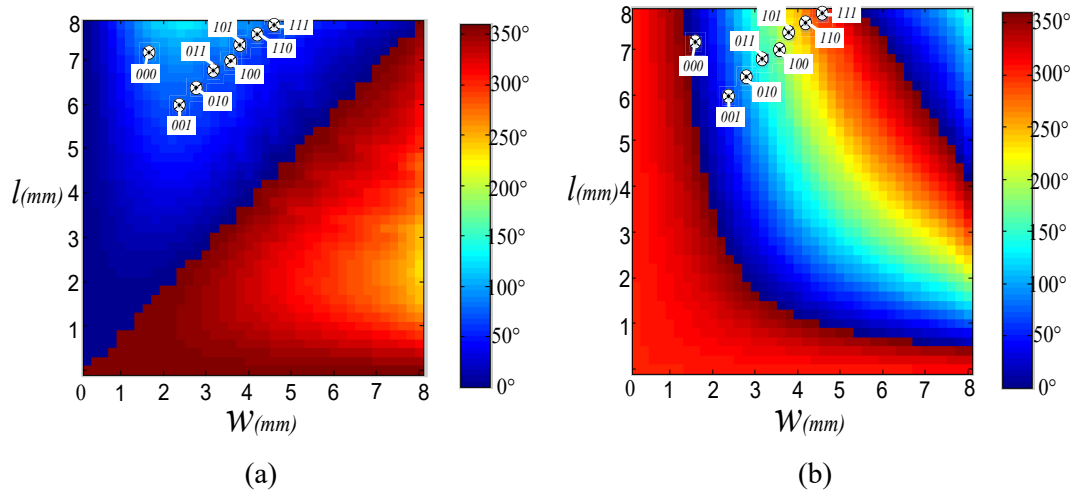


Fig. 2.3 (a) The simulated transmission phase difference between x -pol and y -pol incident waves as a function of (w, l) at 30-GHz. (b) The simulated transmission phase as a function of (w, l) at 30-GHz.

TABLE 2.1. THE DESIGNED 3-BIT UCs USING DIFFERENT SCALES OF QWP

3-bit UC	000	001	010	011	100	101	110	111
Phase response	0°	45°	90°	135°	180°	225°	270°	315°
Geometry (w, l) (mm)	(1.4, 7.4)	(2.25, 6.2)	(2.7, 6.4)	(3.1, 6.8)	(3.45, 7.1)	(3.8, 7.5)	(4.1, 7.8)	(4.5, 8)

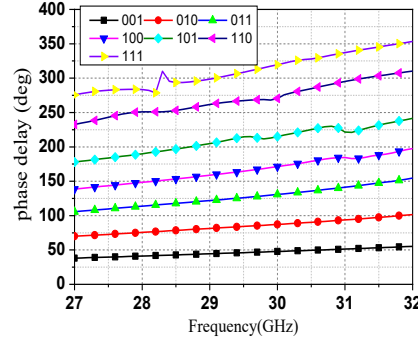


Fig. 2.4. Transmission phase delay of the 3-bit UCs (compared with 000 unit).

The incident electric field passing through the polarizer is decomposed into two orthogonal components, E_x and E_y , as shown in Fig. 2.2. Since the unit is anisotropic along x and y - directions, E_x and E_y propagate through it with different phase velocities. By adjusting the geometric values (w, l) of the polarizer, the required 90° phase difference between E_x and E_y can be realized, which results in a CP wave. Different from conventional circular polarizers [42-45] using uniform QWP units, the proposed 3-bit QWP units exhibit different transmission phase. In other words, different geometric values (w, l) can realize 90° phase difference between E_x and E_y but with different overall unit transmission phases. Therefore, by properly choosing the geometric values (w, l), the QWP units can have the same amplitude of transmission coefficient but with different phase delays. Using low dielectric constant filament can generally have wider axial bandwidth. However, to make sure a 90° phase difference between the x -polarized and y -polarized incident wave, the thickness of the UC is increased as well. A thick UC will deteriorate the performance of the lens and make the design huge. We choose eight-level phase discretization with the transmission phase of 0° , 45° , 90° , 135° , 180° , 225° , 270° , and 315° . For better representation, they are marked as “000”, “001”, “010”, “011”, “100”, “101”, “110”, and “111”. In order to provide 360° transmission phase delay and minimize the thickness, the height of 28 mm is adopted for all the units. Therefore, only the length and width of the units are optimized. The 3-bit units (w, l) should satisfy two conditions: (1) Each unit should provide a 90-degree phase difference between x -pol and y -pol incident waves. (2) Eight units should provide the 0 to 2π full transmission phase circle. Therefore, our design strategy is as follows: first, we obtain two phase masks, a transmission phase difference between x -pol and y -pol incident waves as a function of (w, l) and a transmission phase as a function of (w, l), as shown in Figs. 2.3 (a) and (b), respectively. Next, according to Fig. 2.3 (a), we can locate the region that we of interest, *i.e.* the phase difference around 90-degrees. Then, in the same

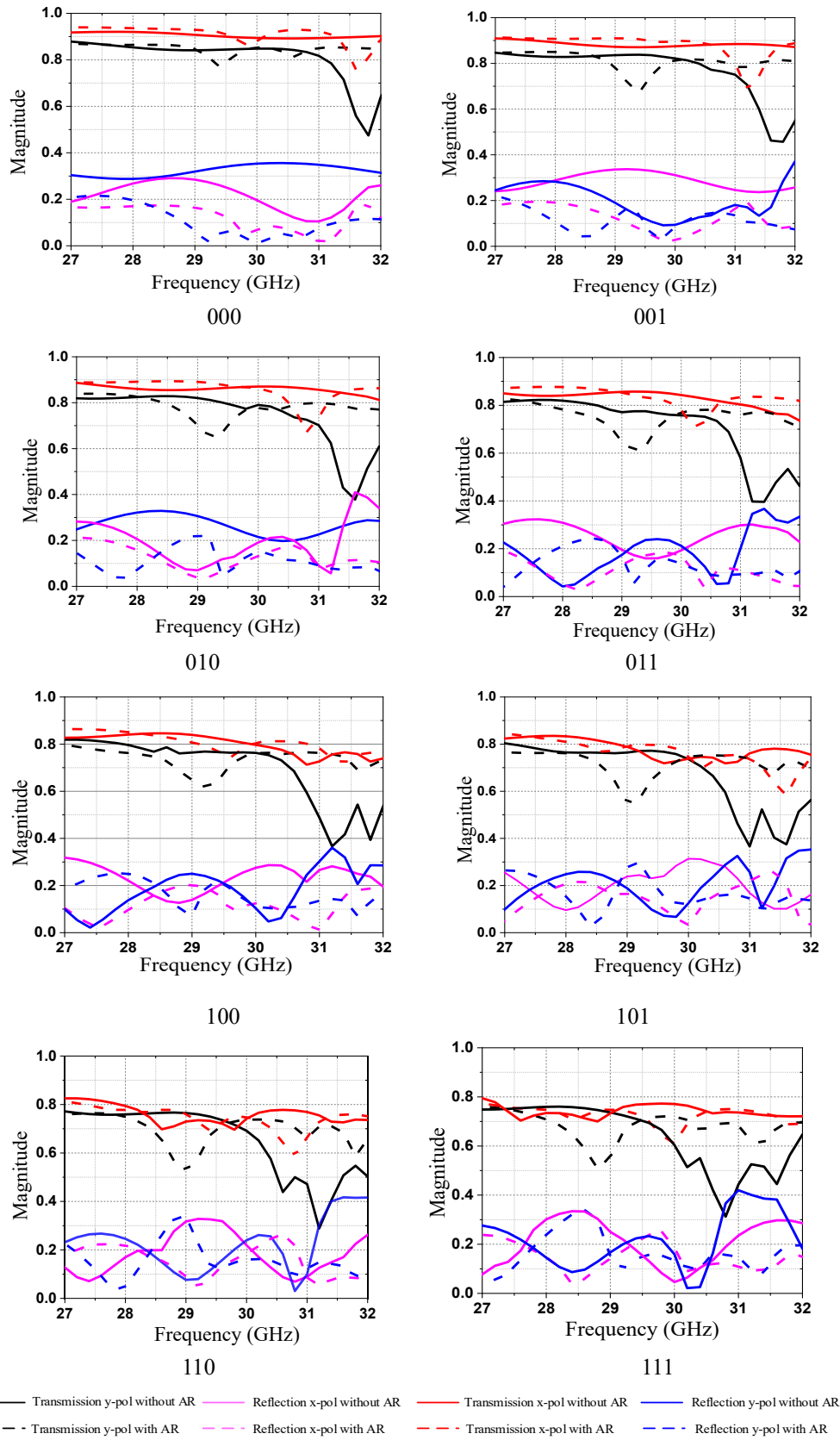


Fig. 2.5. Transmission and reflection magnitudes of the eight units with and without AR coating.

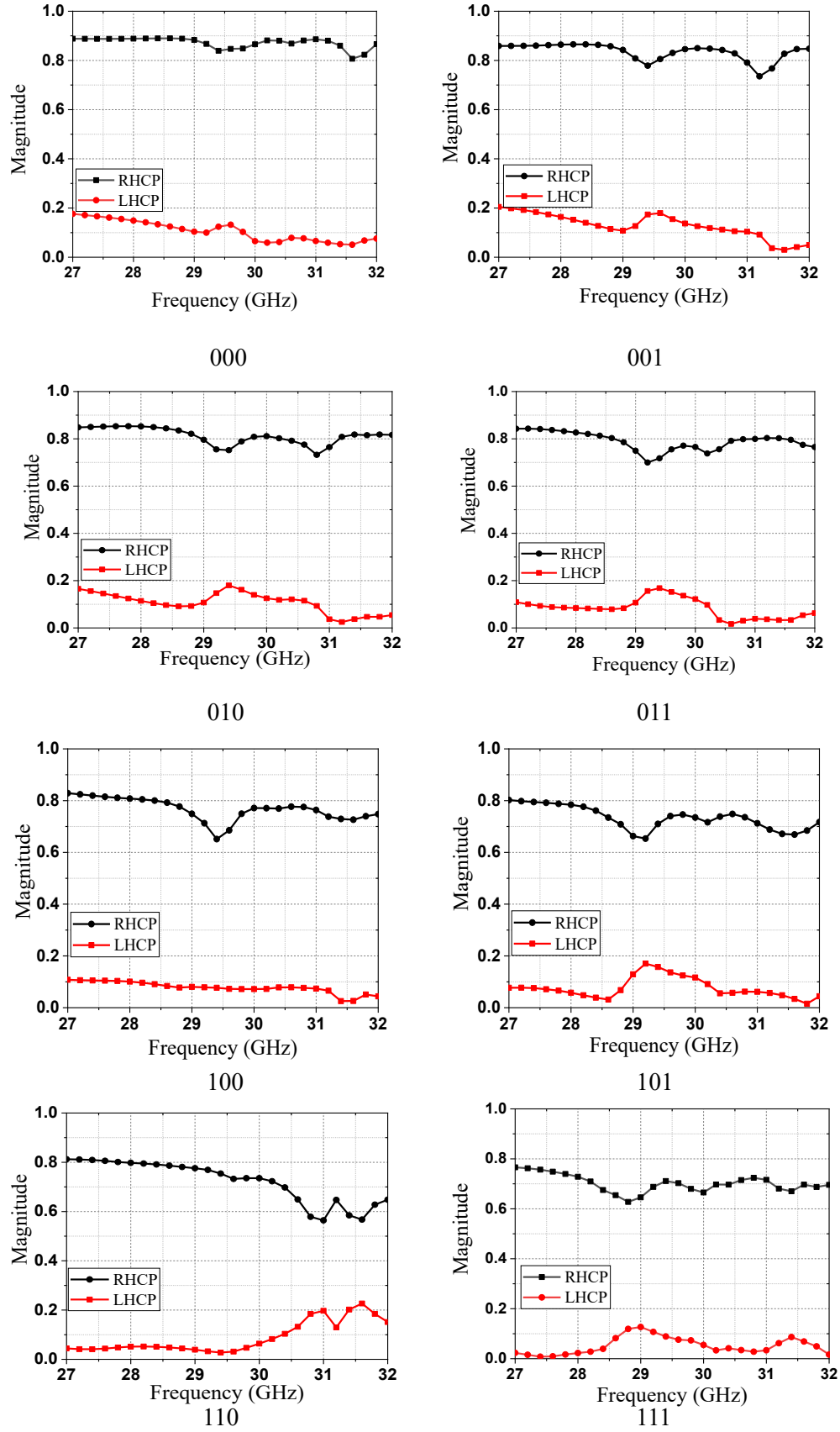


Fig. 2.6. Magnitudes of the transmitted RHCP and LHCP of eight UCs.

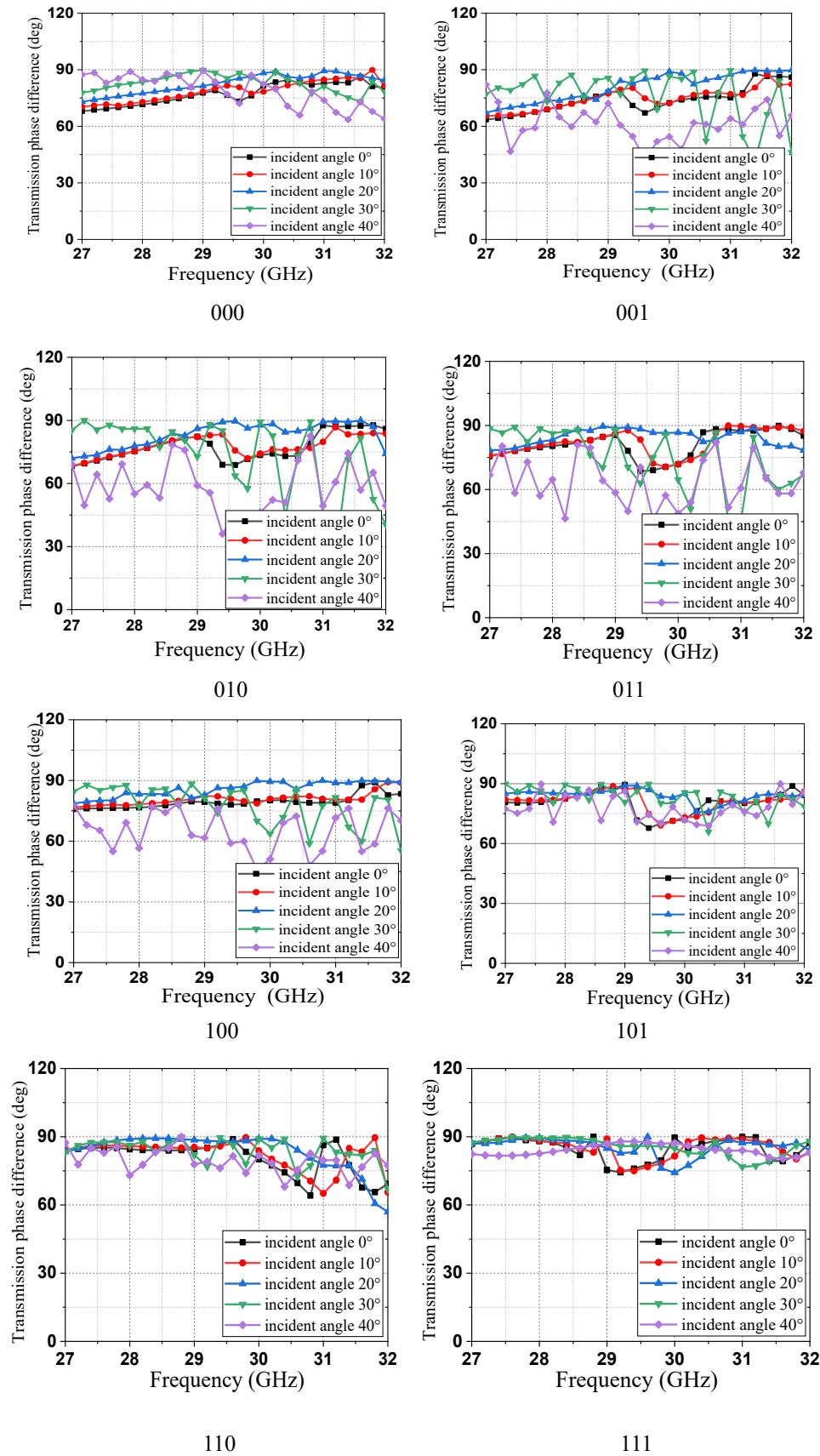


Fig. 2.7. Transmission phase difference of the TE and TM modes at different incident angles of the eight UCs.

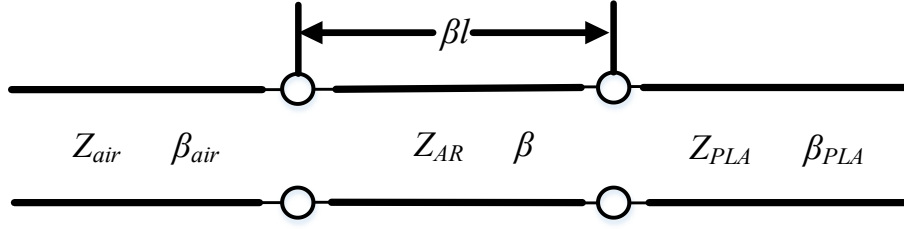


Fig. 2.8. Transmission line model of the AR coating.

region in Fig. 2.3 (b), we can select the 3-bit units that provide 0 to 2π full transmission phase circle. It is also worth mentioning that, as shown in Fig. 2.3, the proposed units are not a unique solution. The designed 3-bit sequence is shown in Table 2.1. Their transmission phase delay versus frequency curves are shown in Fig. 2.4. The transmission magnitudes of the x-pol and y-pol incident waves and the transmission magnitudes of the RHCP and LHCP (cross-pol) conversion of the eight units are given in Figs. 2.5 and 2.6, respectively. The figures indicate that the transmission loss is gradually increased due to the relatively high dielectric loss of the printing material. Fig. 2.7 shows the transmission phase difference of the TE and TM modes of the eight units under different incidence angles from normal to 40-degrees. It is observed that the performance of the units is insensitive up to 20-degrees.

The AR coatings located between two media (*i.e.* air and PLA material) with different wave impedances are equivalent to a segment of transmission line with characteristic impedance Z_{AR} , connected between two transmission lines with different characteristic impedances Z_{air} and Z_{PLA} , as shown in Fig. 2.8. The reflection coefficient of the network is given by [46]:

$$S_{11} = \frac{\left(\sqrt{\frac{Z_{PLA}}{Z_{air}}} - \sqrt{\frac{Z_{air}}{Z_{PLA}}}\right) \cos \beta l + j \left(\sqrt{\frac{Z_{AR}}{Z_{air} Z_{PLA}}} - \sqrt{\frac{Z_{air} Z_{PLA}}{Z_{AR}}}\right) \sin \beta l}{\left(\sqrt{\frac{Z_{PLA}}{Z_{air}}} + \sqrt{\frac{Z_{air}}{Z_{PLA}}}\right) \cos \beta l + j \left(\sqrt{\frac{Z_{AR}}{Z_{air} Z_{PLA}}} + \sqrt{\frac{Z_{air} Z_{PLA}}{Z_{AR}}}\right) \sin \beta l} \quad (2-1)$$

For an ideal AR coating, S_{11} must be zero, *i.e.*, the numerator of the above expression must be zero:

$$\left(\sqrt{\frac{Z_{PLA}}{Z_{air}}} - \sqrt{\frac{Z_{air}}{Z_{PLA}}}\right) \cos \beta l + j \left(\sqrt{\frac{Z_{AR}}{Z_{air} Z_{PLA}}} - \sqrt{\frac{Z_{air} Z_{PLA}}{Z_{AR}}}\right) \sin \beta l = 0 \quad (2-2)$$

The real and imaginary parts must be zero separately. The condition for the real part to be zero is:

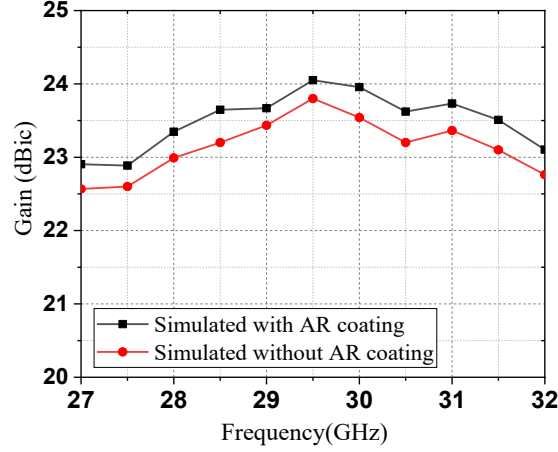


Fig. 2.9. Simulated lens peak gains with and without the AR coating.

$$\cos(\beta l) = 0, \text{ i.e. } l = (2n + 1) \frac{\lambda_0}{4} \quad (2-3)$$

where λ_0 is the centre frequency of the AR coating. Under this condition, $\sin \beta l = 1$, the condition of the imaginary part being zero becomes

$$Z_{AR} = \sqrt{Z_{air} Z_{PLA}} \quad (2-4)$$

Therefore, the thickness (h) and permittivity (ϵ_{AR}) of the AR structure required for zero reflectivity are:

$$h = \frac{\lambda_{AR}}{4} \quad \text{and} \quad \epsilon_{AR} = \sqrt{\epsilon_{air} \epsilon_{PLA}} \quad (2-5)$$

where λ_{AR} is the wavelength in the AR structure. Therefore, $\epsilon_{AR} \approx 1.58$, and $h \approx 2.0$ mm. In the design, considering that there are reflections at the boundary between the air/supporting plate, the supporting plate/polarizer and the polarizer/air, the thickness and the length of the AR coating are optimized with the goal of minimum reflection of the whole unit. The final optimized size of the AR coating is $7.2 \times 7.2 \times 1.9 \text{ mm}^3$.

The transmission and reflection magnitudes of the eight units with and without AR coating are shown in Fig. 2.9 for comparison. The figure shows that by using the AR coating, the reflection magnitude can be improved, especially for the 000, 001, 010 and 011 units, and the transmission magnitudes are significantly improved above 30-GHz. Adding the AR coating introduces a transmission minimum point at about 29-GHz for the y -polarized incident wave. Nevertheless, according to the transmitted magnitude of the RHCP shown in Fig. 2.6 and the gain comparisons with/without AR coating of the lens shown in Fig. 2.9, after adding the AR coating, the RHCP gain of the lens does not show a significant drop at this point but the average gain improves by 0.3-0.4 dB.

2.2.2 LP-to-CP conversion lens

Based on the proposed 3-bit UCs, a planar QWP lens with 169 (13×13) units in a square aperture operating at 30-GHz is designed. The configuration of the QWP-lens is shown in Fig. 2.10. The overall size of the lens is 110mm×110mm×90mm. A WR-28 waveguide feed the lens and was arranged 45° with respect to the ox -axis. The feed is linearly polarized. Its matching and gain are given in Fig. 2.11. Because the CP lens is designed based on the phase curves under the normal incidence for simplicity, using a relatively large focal to diameter (F/D) ratio reduced the effects of incident angle on lens performance. Furthermore, considering the tradeoff between the illumination efficiency and spillover efficiency, the F/D about 0.81 is adopted. The desired phase compensation at lens aperture should compensate for the spatial phase delay from the feed phase center [47]:

$$\varphi(x, y) = \frac{2\pi}{\lambda_0} (\sqrt{x^2 + y^2 + f^2} - f) + \varphi_0 \quad (2-6)$$

where f represents the focal length, λ_0 represents wavelength in free space, φ_0 represents the initial phase at the original point. The compensating phase at the lens aperture is shown in Fig. 2.12 (a) and it is then discretized using the 3-bit units, as shown in Fig. 2.12 (b). The phase center of the feed at 30-GHz is initially placed at the focal point of the lens. Next, since the thickness of the lens and the phase center vary with frequency and direction, the position of the feed along z -direction is optimized slightly to obtain the highest and the most stable gain in the entire frequency band.

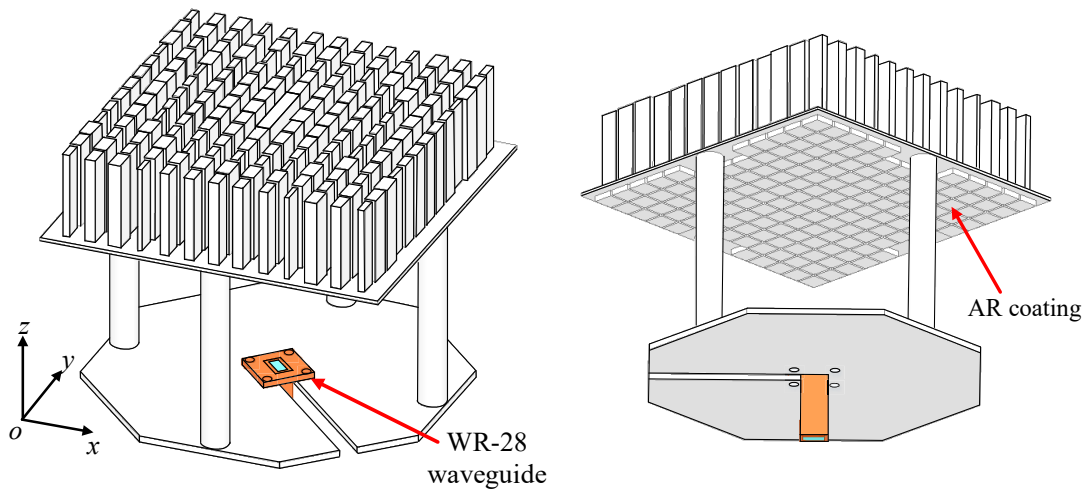


Fig. 2.10. The configurations of the CP lens with WR-28 waveguide feed.

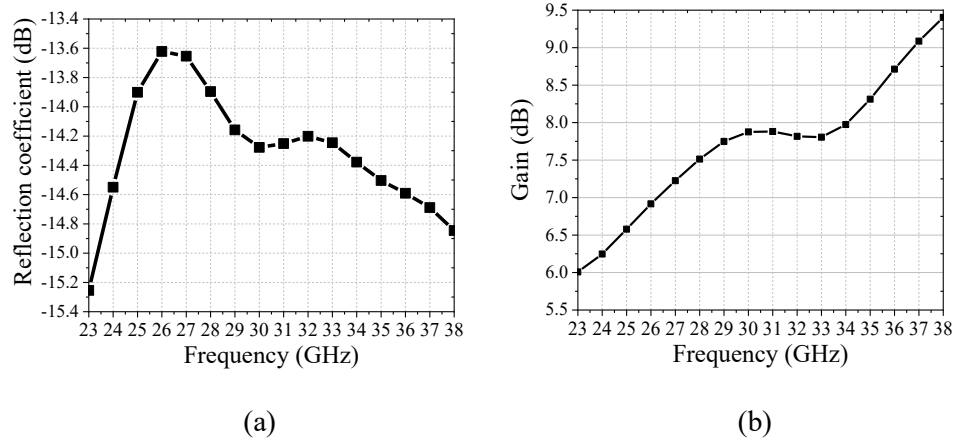


Fig. 2.11. (a) Reflection coefficient of the feed. (b) Gain of the feed.

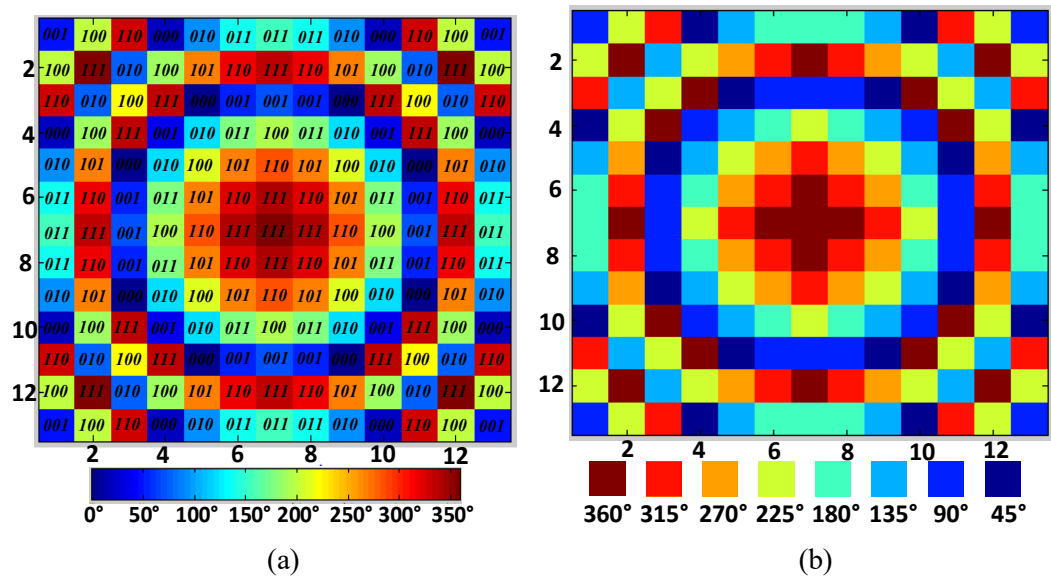


Fig. 2.12. (a) Compensating phase at the lens aperture and the corresponding UCs. (b) The discretized phase distribution at the aperture.

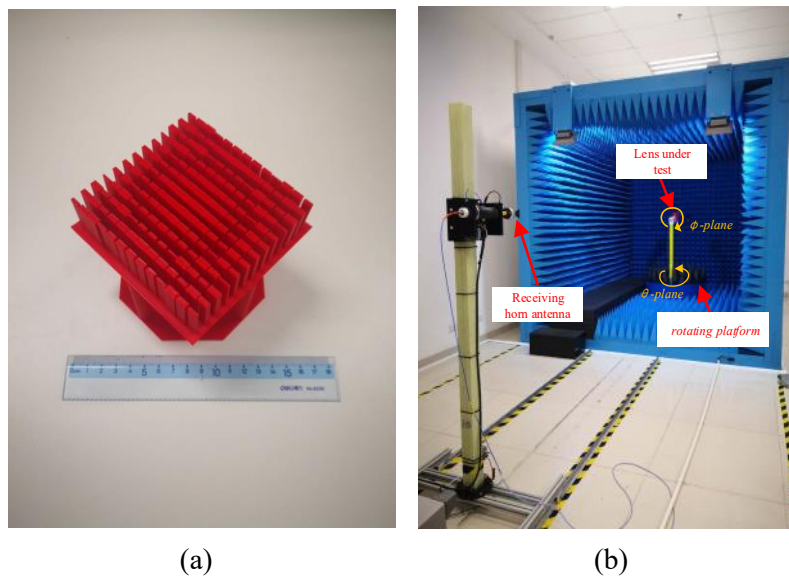


Fig.2.13. (a) Lens prototype. (b) Mm-wave far-field measurement system.

The designed lens is fabricated using a commercial Raise3d Pro2 printer. The fabricated lens prototype is shown in Fig. 2.13 (a). The lens is measured using a far-field mm-wave antenna measurement system, as shown in Fig. 2.13 (b). The antenna is fixed on the rotator using adhesive tape. A standard gain horn located at the far-field is used for the receiving antenna. The distance between the antenna and horn is around 10 m. The measured 3-D radiation patterns and the 2-D simulated and measured radiation patterns at 27, 28, 29, and 30-GHz are shown in Figs. 2.14 (a), (b) and (c), respectively. The simulated and measured results agree well. A pencil beam with high directivity can be observed and the sidelobe levels of the beams are kept well below -15 dB. The simulated and measured RHCP gains and the axial ratio of the lens are shown in Fig. 2.15. The 3-dB axial ratio bandwidth is from 25 to >33-GHz. The RHCP gains are from 22.8 to 24 dBic for the simulation and from 21.5 to 22.6 dBic for the measurement from 28 to 32-GHz. It is worth mentioning that there is 2 dB loss in the lossy filament.

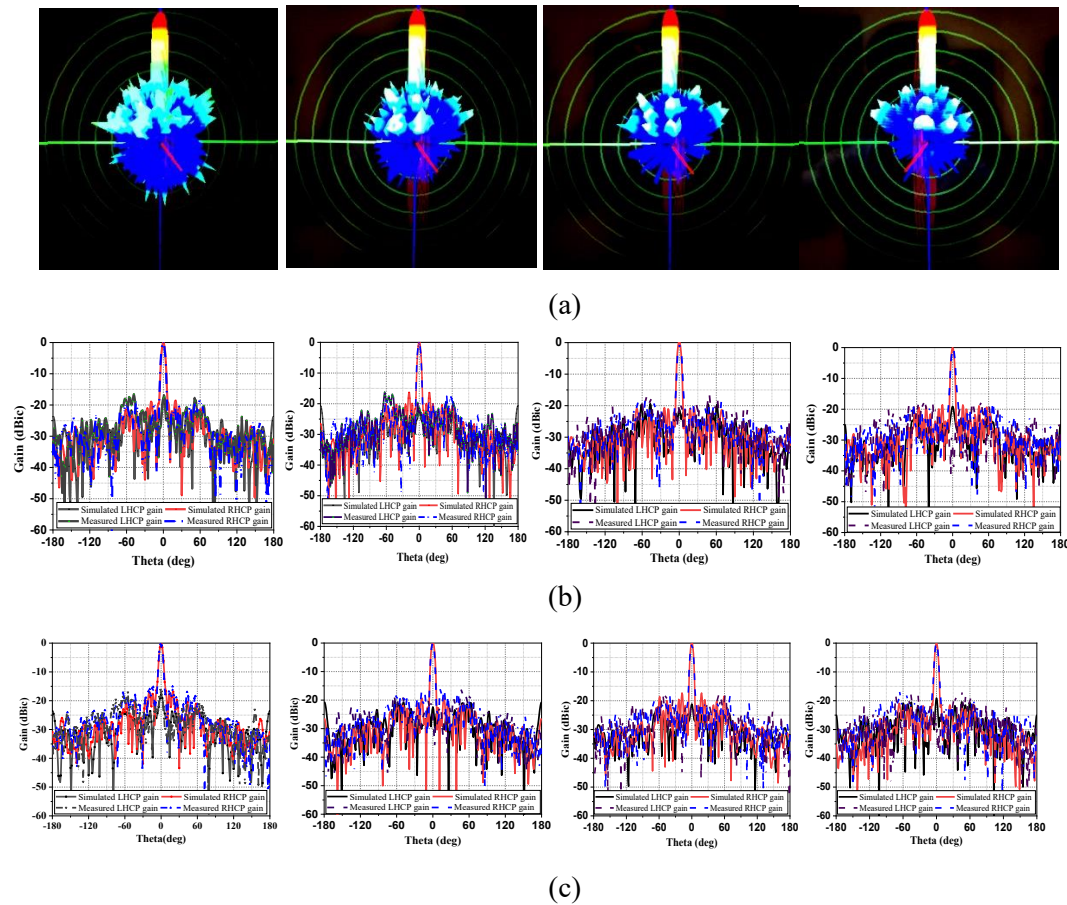


Fig. 2.14. (a) Measured 3D RHCP radiation patterns: pencil beams. (b) Simulated and measured radiation patterns in xoz -plane. (c) Simulated and measured radiation patterns in yoz -plane.

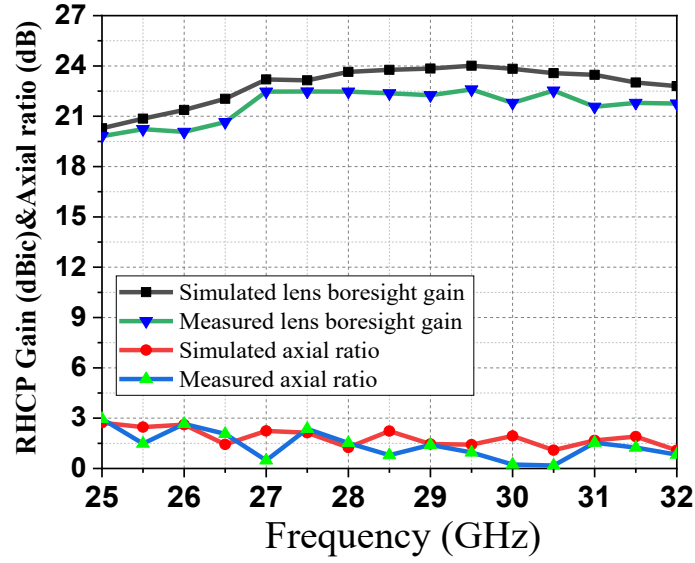


Fig. 2.15. Simulated and measured RHCP gain and axial ratio.

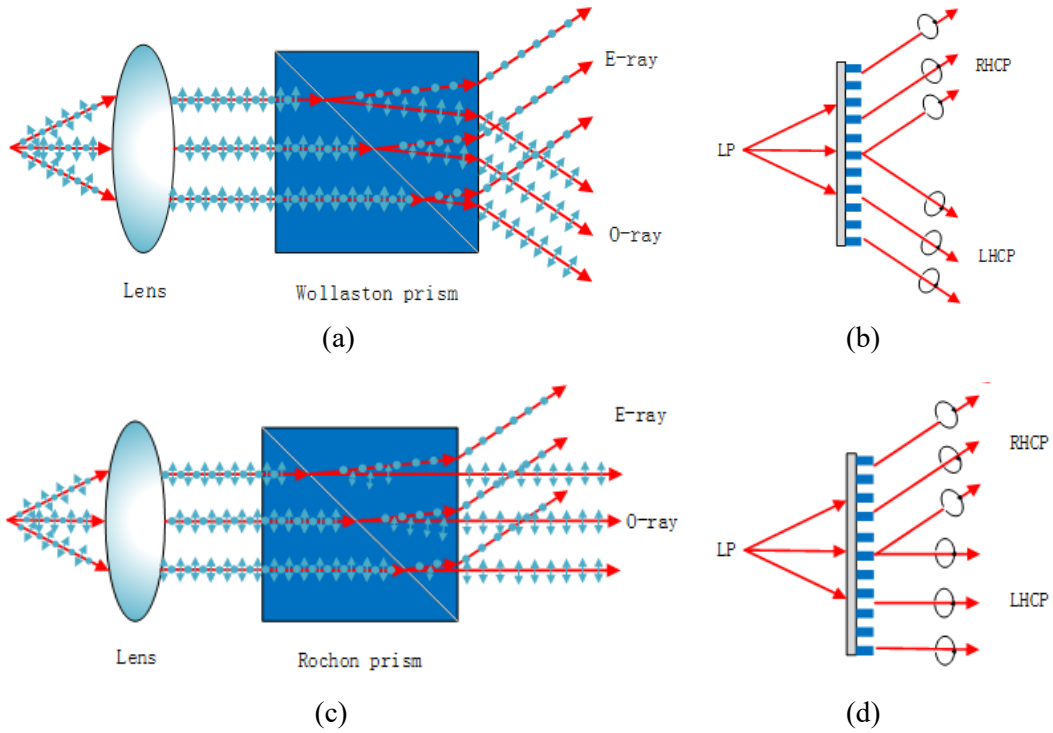


Fig. 2.16. (a) Wollaston prism which deflects the collimated extraordinary and ordinary waves. (b) Rochon prism which deflects only the collimated extraordinary wave. (c) Proposed design which collimates and symmetrically deflects both RHCP and LHCP waves. (d) Proposed design which collimates waves and deflects only the RHCP waves. (The extraordinary wave corresponds to the case of the electric field polarized perpendicular to the plane of incidence. The ordinary wave corresponds to the case of the magnetic field polarized perpendicular to the plane of incidence [48]).

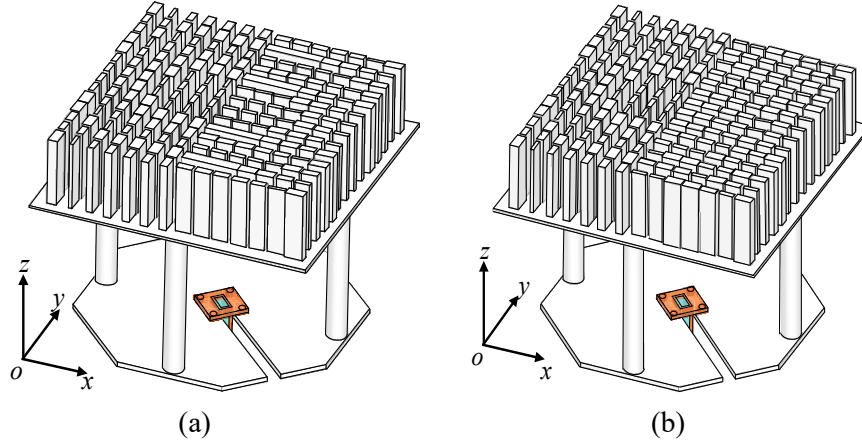


Fig. 2.17. (a) Wollaston-prism-like circularly polarized beam-shaping lens. (b) Rochon-prism-like circularly polarized beam-shaping lens.

2.2.3 Wollaston-prism-like and Rochon-prism-like planar circularly polarized beam-shaping lenses

We extended the 3-bit units to form Wollaston-prism-like and Rochon-prism-like planar circularly polarized beam-shaping lenses. A Wollaston prism and Rochon prism split the beam into two beams with perpendicular polarizations. The split beams leave the Wollaston prism at a symmetrical divergence angle (Fig. 2.16 (a)), while the Rochon prism (Fig. 2.15 (b)) refracts only the extraordinary (ordinary) wave but allows the ordinary (extraordinary) wave to propagate undeviated. However, conventional polarization beam splitters are based on naturally anisotropic materials, which require a large thickness to generate enough walk-off distance between the two orthogonal polarizations owing to the intrinsically small birefringence. Moreover, for practical optical systems, an additional lens must be placed in front of the prisms to collimate the beams, which makes the system complicated and bulky. The demonstrated beam splitting lens, on the other hand, collimates the beams and manipulates the orthogonal polarizations simultaneously with a low-profile planar form. This significantly eases these disadvantages aforementioned, as shown in Fig. 2.16 (c) and (d).

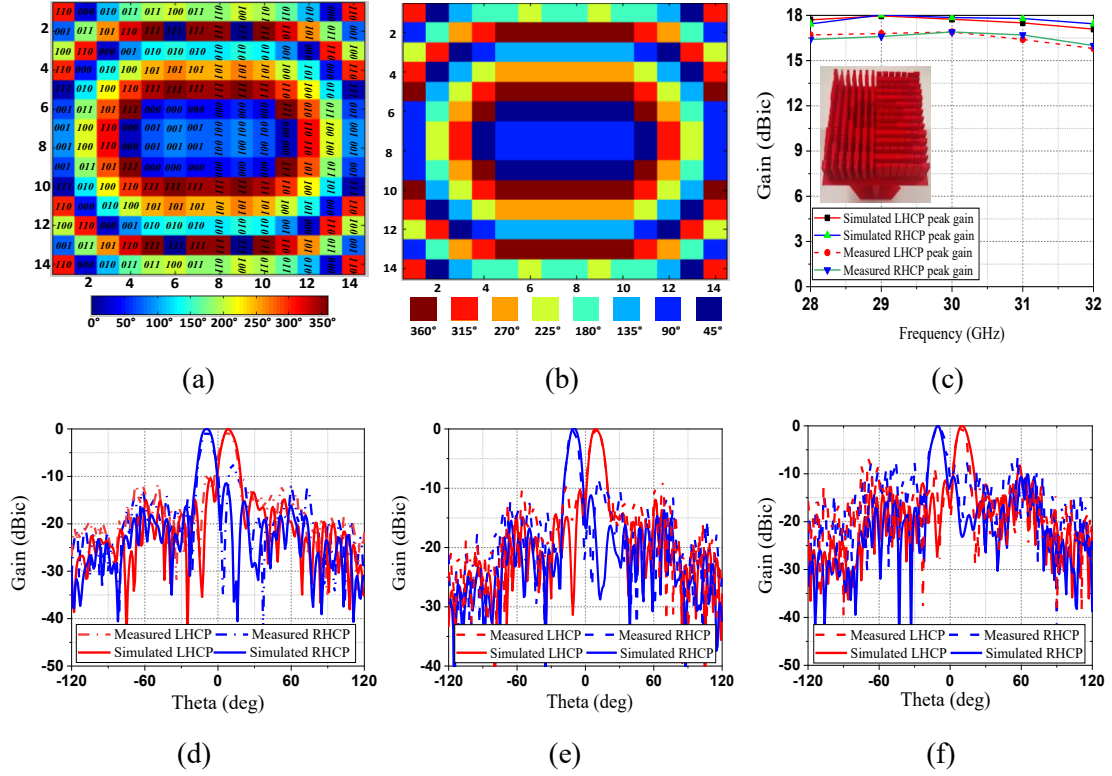


Fig. 2.18. (a) Compensating phase at the lens aperture and the corresponding code. (b) The discretized phase distribution at the aperture after using 3-bit units. Simulated and measured peak gains of Wollaston-prism-like circularly polarized beam-shaping lens (The inset shows the printed prototype). Simulated and measured radiation patterns of Wollaston-prism-like circularly polarized beam shaping lens at (a) 28-GHz, (b) 30-GHz and (c) 32-GHz.

The configuration of the Wollaston-prism-like circularly polarized beam-shaping lens is shown in Fig. 2.17 (a). The units used here are the same as those used in Section 2.2.1. 14×14 units are adopted in the design. The units in the left half of the lens are arranged orthogonally to those in the right half to generate two orthogonal circular polarization beams with equal power. To split the beam for the two circular polarizations, an additional gradient phase φ_{xn} is added to the compensating phase of the lens on each column along the x-direction, where $\varphi_{x1}=0^\circ$, $\varphi_{x2}=-45^\circ$, $\varphi_{x3}=-90^\circ$, $\varphi_{x4}=-135^\circ$, $\varphi_{x5}=-180^\circ$, $\varphi_{x6}=-225^\circ$, $\varphi_{x7}=-270^\circ$, $\varphi_{x8}=-270^\circ$, $\varphi_{x9}=-225^\circ$, $\varphi_{x10}=-180^\circ$, $\varphi_{x11}=-135^\circ$, $\varphi_{x12}=-90^\circ$, $\varphi_{x13}=-45^\circ$, and $\varphi_{x14}=0^\circ$. The compensating phase at the lens aperture, shown in Fig. 2.17 (a), is discretized by the units, as shown in Fig. 2.17 (b). For normal incidence, the angle of the tilted beam can be calculated as [49]:

$$\theta = \sin^{-1} \frac{\lambda}{2\pi} \frac{d\varphi}{dx} \quad (2-7)$$

where $d\varphi/dx$ is the phase gradient along the ox -direction. The simulated and measured lens radiation patterns at 28, 30 and 32-GHz are shown in Figs. 2.17 (d)-(f). The figure shows that LHCP and RHCP are symmetrically split with a deflecting angle of

9.2 degrees (28 GHz), 10 degrees (30 GHz), and 10.2 degrees (32 GHz). The maximum angular deviation is less than 1 degree compared to the central frequency (30 GHz). The simulated and measured peak RHCP/LHCP gains, as well as the lens prototype, are shown in Fig. 2.17 (c). The simulated peak gains span from 16.2 to 18 dBic and measured peak gains range from 15.8 to 16.9 dBic over the operating band.

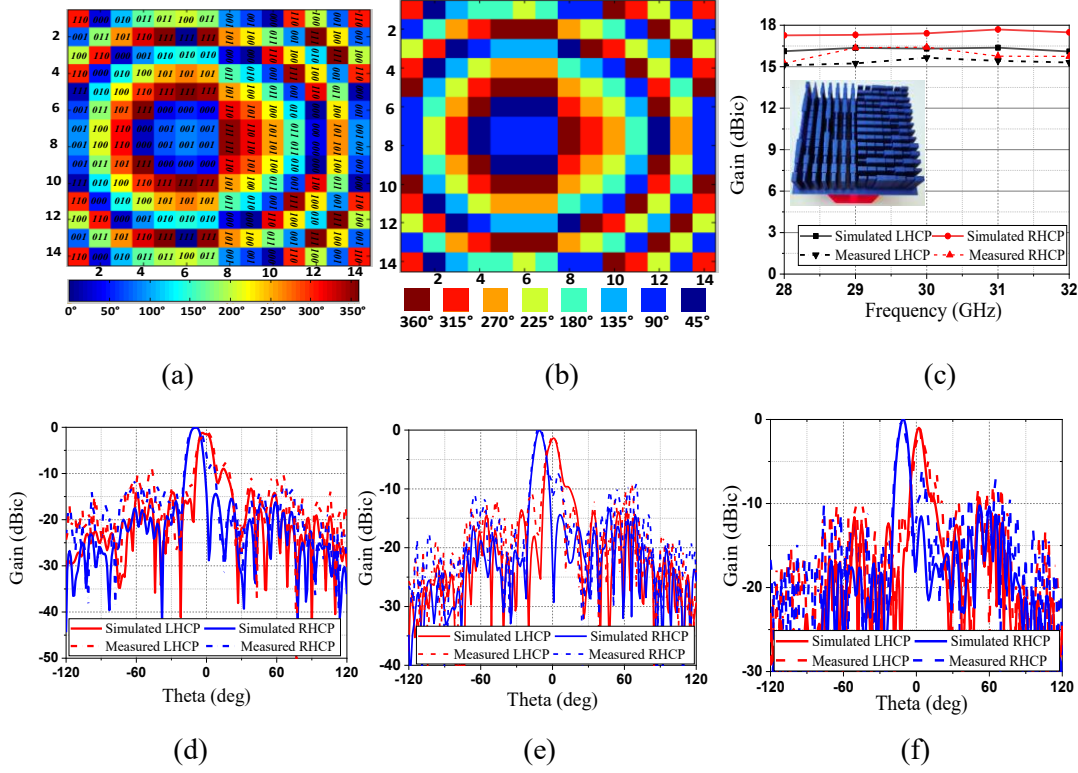


Fig. 2.19. (a) Compensating phase at the lens aperture and the corresponding code. (b) The discretized phase distribution at the aperture using 3-bit units. Simulated and measured peak gains of the Rochon-prism-like circularly polarized beam shaping lens (The inset shows the printed prototype). Simulated and measured radiation patterns of Rochon-prism-like circularly polarized beam shaping lens at (a) 28-GHz (b) 30-GHz and (c) 32-GHz.

B. Rochon-Prism-Like Planar Circularly Polarized Beam-Shaping Lens Design.

The configuration of the Rochon-prism-like circularly polarized beam-shaping lens is shown in Fig. 2.17 (b). Similar to the Wollaston-prism-like lens, it consists of 14×14 units with the orientation in the left half orthogonal to those in the right half. In order to refract only one circular polarization while allowing the other to propagate undeviated, the gradient phases which are added to the compensating phase of the lens on each column along x -direction are $\varphi_{x1}=0^\circ$, $\varphi_{x2}=-45^\circ$, $\varphi_{x3}=-90^\circ$, $\varphi_{x4}=-135^\circ$, $\varphi_{x5}=-180^\circ$, $\varphi_{x6}=-225^\circ$, $\varphi_{x7}=-270^\circ$, $\varphi_{x8}=0^\circ$, $\varphi_{x9}=0^\circ$, $\varphi_{x10}=0^\circ$, $\varphi_{x11}=0^\circ$, $\varphi_{x12}=0^\circ$, $\varphi_{x13}=0^\circ$, $\varphi_{x14}=0^\circ$.

Next, the compensating phase, shown in Fig. 2.19 (a) is discretized by the 3-bit units, Fig. 2.19 (b). The normalized simulated and measured lens radiation patterns at 28, 30 and 32-GHz are shown in Fig. 2.19(d)-(f). The RHCP beam is tilted with an angle of 9.6 degrees (28 GHz), 10.8 degrees (30 GHz) and 11 degrees (32 GHz). The simulated and measured peak RHCP/LHCP gains, as well as the lens prototype, are shown in Fig. 2.19 (c). The simulated peak gains range from 17.3 to 17.8 dBic for RHCP and from 16.1 to 16.4 dBic for LHCP. The measured gains span from 15.3 to 16.4 dBic for RHCP and from 15.2 to 15.7 dBic for LHCP from 28 to 32 GHz. The beam-splitting lenses are not limited dual beams with different circular polarizations. They can be extended to one beam with circular polarization and the other beam with linear polarization by planting half of the units with QWP and the other half with half-wave plate (HWP). It is also worth mentioning that for the unit located in the edge of the lens (incident wave are more oblique), we can design other units that have phase difference closer to 90-degrees to obtain better overall performance of the lens.

TABLE 2.2
COMPARISON OF DIFFERENT KINDS OF CP LENS ANTENNAS

Ref.	Antenna type	Shape	Fabrication technique	Thickness (mm)	Working bands (GHz)	3dB AR bandwidth	Peak gain (dBic)
[44]	CP lens	Non-planar	3-D printing	16.5 (5.61 λ_g)	60-GHz	29%	21.4
[45]	CP lens	Non-planar	3-D printing	4.2 (6.85 λ_g)	300-GHz	18.8%	30.8
[52]	CP patch source +lens	Non-planar	PCB+ machining technique	7 (1.05 λ_g)	30-GHz	4%	13.4
[53]	CP patch source +lens	Non-planar	PCB+ machining technique	81.908 (12.8 λ_g)	30-GHz	2.6%	25.9 (directivity)
[54]	CP leaky wave source +lens	Non-planar	PCB+ machining technique	N.A.	180-GHz	35%	35.8
[55]	CP transmitarray	Planar	PCB	1.13 (0.19 λ_g)	30-GHz	24.2%	22..8
[56]	CP transmitarray	Planar	PCB	1 (0.12 λ_g)	10-GHz	3.5%	21.9
[57]	CP transmitarray	Planar	PCB	12.7 mm (0.59 λ_g)	14-GHz	12.6%	24.5
This work	CP lens	Planar	3-D printing	30.9 mm (4.88 λ_g)	30-GHz	>27%	22.6

Table 2.2 compares the proposed work with other circularly polarized lens antennas. Integrating a lens with a circularly polarized source is a common approach to achieve a high gain CP antenna. The CP source can be a conventional circularly polarized helix antenna [50] or patch [51-53]. However, the CP source

increases the design complexity and the patch-based CP antennas usually suffer from narrow impedance and AR bandwidth. Therefore, lenses which can convert LP to the CP radiation are preferable. By using low-cost 3-D printing, CP-lenses working at 60 GHz [44] and 300 GHz [45] with wide axial ratio bandwidth and high gain are proposed. Both CP lenses are realized by stacking a separate circular polarizer to change the polarization with a hemisphere lens or transmit-array on top to collimate the CP beams. Taking advantage of the 3-bit polarizer, our design can be regarded as a truly CP lens, which seamlessly merges two features, the polarization conversion and the beam collimation in a single component. Therefore, considering the dielectric wavelength (λ_g), the thickness of the proposed lens (30.9 mm, $4.88 \lambda_g$ at 30 GHz) is less than those of the designs in [44] (16.5mm, $5.61 \lambda_g$ at 60-GHz) and [45] (4.2 mm, $6.85 \lambda_g$ at 300-GHz). Compared with other ultrathin transmit-array using PCB technology [55-57], the proposed 3-D printed lens has a lower cost and wider AR bandwidth because polarization conversion and phase requirements are not based on resonance.

TABLE 2.3

COMPARISON OF DIFFERENT KINDS OF POLARIZATION BEAM SPLITTER DESIGN

Ref.	Antenna type	Fabrication technique	Thickness	Working band	Beam splitting principle
[5]	LP beam splitting	PCB	3mm ($0.16 \lambda_g$)	10-GHz	anisotropic gradient-index metamaterials
[58]	LP beam splitting	PCB	25.6 mm ($1.42 \lambda_g$)	10-GHz	anisotropic gradient-index metamaterials
[59]	CP beam splitting	PCB	1.9mm ($0.13 \lambda_g$)	10-GHz	PB phase
[60]	CP beam splitting	PCB	9mm ($0.13 \lambda_g$)	12-GHz	PB phase
[61]	CP beam splitting	Micro-fabrication	420nm ($0.54 \lambda_0$)	780nm	Propagation phase + PB phase
[62]	CP beam splitting	PCB	2.07 mm ($0.07 \lambda_0$)	10-GHz	Propagation phase + PB phase
This work	CP beam splitting	3-D printing	30.9 mm ($4.88 \lambda_g$)	30-GHz	Propagation phase + QWP

Table 2.3 compares the proposed circularly polarized beam-splitting lens with other related designs. Anisotropic gradient-index metamaterials can be used to manipulate orthogonal linearly-polarized beams independently with large deflecting angles [5], [58]. As for the circular polarization, using the Pancharatnam-Berry (PB)

phase to realize beam splitting is a common approach [59], [60]. However, PB-based beam splitters can symmetrically split only the LHCP and the RHCP beams as the Wollaston prism does for linearly polarized beams. Recently, by combining the propagation phase and the PB phase, the designs in [61], [62] are capable of independently manipulating the angles of LHCP/RHCP beams. However, they are unable to collimate the beams. More importantly, since these designs still use the PB phase, their beam manipulations are limited to circular polarizations. In contrast, the proposed design can be extended to a beam-splitting lens, with one beam of circular polarization and the other with linear polarization. Note that though the presented designs achieve the function similar to the Wollaston and Rochon prism, they do not really distinguish two polarization components. In fact, they only split the available power by half and converting those two halves into different polarizations, and sending them out in different directions.

2.3 0.14 THz 3-D Printed All-Dielectric Low-Cost Low-Profile Lens-Integrated Fresnel Rochon Prism

Polarization beam splitters (PBSs), essential components controlling different polarized waves independently, have been found to be very important in the THz/sub-THz regime. To achieve polarization manipulation, a popular approach is to use metamaterial to independently modulate the phase of different polarizations, such as the gradient phase [5], [58], or the Pancharatnam-Berry (PB) phase [63-65]. Another approach is based on prisms of birefringent materials, such as Rochon, Wollaston, and Glan-Taylor prisms [68]. Generally, these prisms consist of two orthogonal prisms of birefringent material, typically a uniaxial material such as calcite. Two prisms are cemented together on their base to form two right triangle prisms with perpendicular optic axes. Outgoing beams diverge from the prism as ordinary and extraordinary waves due to the different refraction indices, with the angle of divergence determined by the prism's wedge angle and the wavelength of the wave. Unlike the Wollaston prism, which splits two polarized beams with symmetrical angles, the Rochon prism splits the beam into two polarized beams with perpendicular polarizations but refracts only the extraordinary (ordinary) wave and allows the ordinary (extraordinary) wave to pass through undeflected, as shown in Fig. 2.20, which is often crucial for keeping the alignment of the subsequent components. However, the conventional Rochon

prism is designed and realized using naturally anisotropic materials, which require a large thickness to generate enough walk-off distance between the two orthogonal polarizations owing to the intrinsically small birefringence [66]. Moreover, the accurate cementing of the prisms requires additional effort and this further increases the fabrication cost. Therefore, in this chapter, by combining 3-D printing and the Fresnel prism principle, a low-profile lens-integrated Fresnel-Rochon prism operating at 0.14 THz is proposed and demonstrated to overcome these challenges.

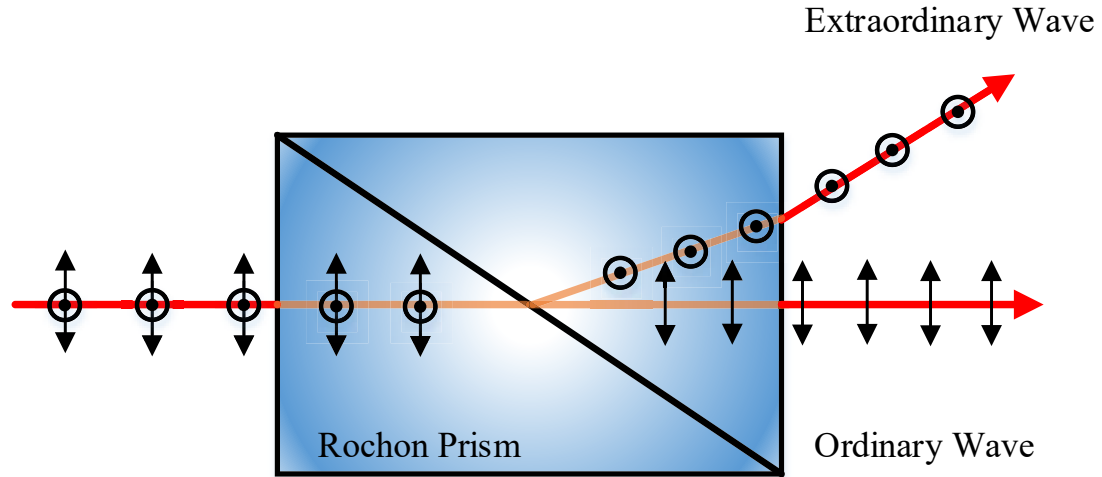


Fig. 2.20. Conventional Rochon prism realized by cementing two birefringent calcite-based prisms together.

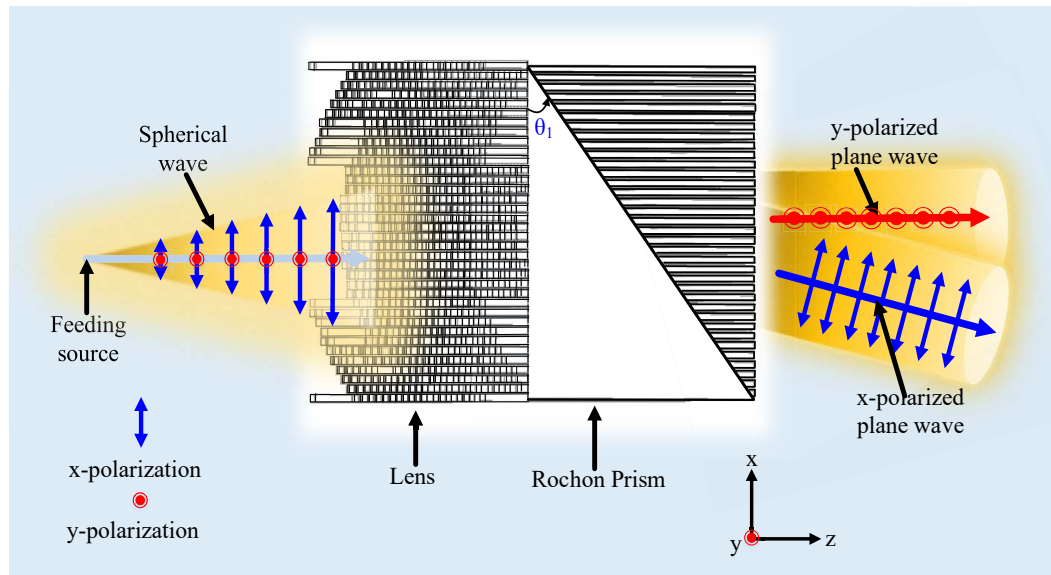


Fig. 2.21. Geometry of proposed 3-D printed lens-integrated Rochon prism ($\theta_1=45.0^\circ$).

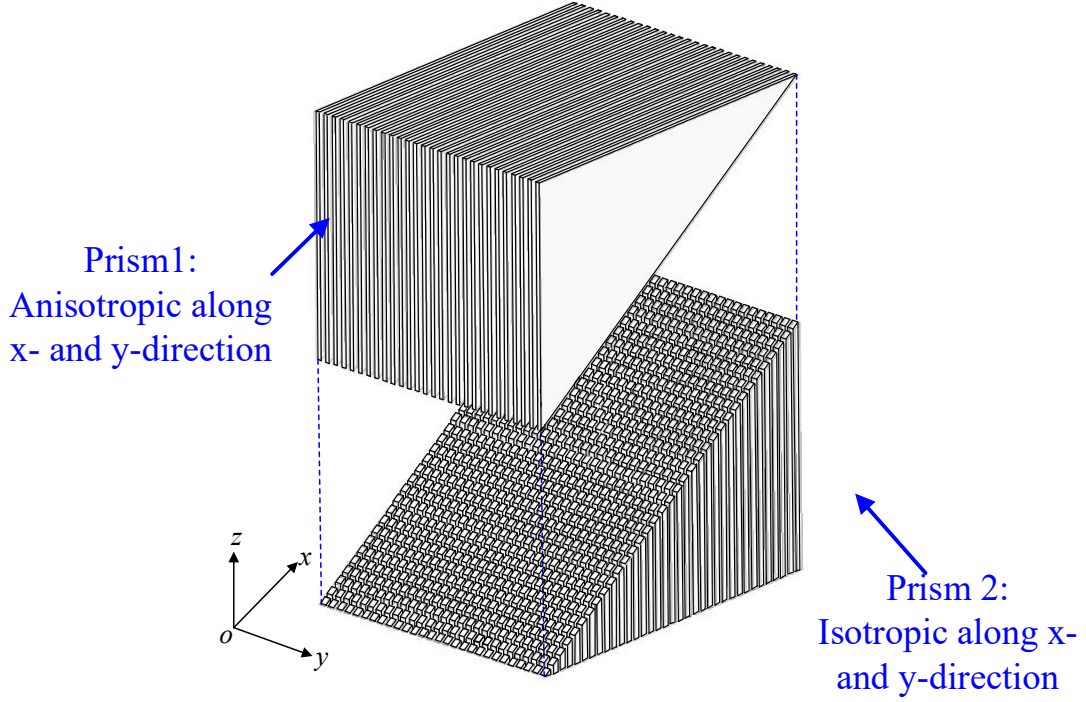


Fig. 2.22. Proposed Rochon prism consisting of prism 1 made of gratings with a rectangular cross-section and prism 2 gratings with a square cross-section.

2.3.1 3-D printed Rochon prism design

The geometry of the proposed 3-D printed lens-integrated Rochon prism is shown in Fig. 2.21. Polylactic acid (PLA) is used as the printing material with a relative permittivity of 2.5 and a loss tangent of 0.025 at 0.14 THz. The Rochon prism and lens are combined for ease of measurement. The Rochon prism is composed of two different prisms: prism 1 made of gratings with a rectangular cross-section ($n_{1x} > n_{1y}$) and prism 2 made of gratings with a square cross-section ($n_{2x} = n_{2y} = n_{1y}$), where the n_{1x} , n_{2x} , and n_{1y} , n_{2y} are the effective refractive indices of prism 1 and 2 along x- and y-directions, respectively, as shown in Fig. 2.22. In this way, the x-polarized incident wave is refracted at the boundary between the two prisms and refracted once more at the boundary between prism 2 and the air. Therefore, the outgoing beam is deflected at an angle with respect to the optical axis. As for the y-polarized incident wave, since the refractive indexes of the two prisms along y-direction are the same, the outgoing beam is undeflected, as illustrated in Fig. 2.23. The deflected angle can be calculated using the following equations [67]:

$$n_{1x} \sin \theta_1 = n_{2x} \sin \theta_2 \quad (2-8)$$

$$n_{2x} \sin(\theta_2 - \theta_1) = n_{air} \sin \theta_3 \quad (2-9)$$

where θ_1 is the wedge angle of the prism. In order to engineer the refractive indices of the dielectric gratings, the grating unit is simulated in ANSYS HFSS using periodic boundaries, as shown in Fig. 2.24. According to equations (2-8) and (2-9), the deflection angle of the Rochon prism is determined by the wedge angle of the prism and the refractive index of the material. Here, it is interesting to see the maximum deflection angle of the Rochon prism that can be achieved (the wedge angle is fixed at 45° and the relative permittivity of the printing material is 2.5) by careful selection of the dimensions of the units (w and l in Fig. 2.24) forming prism 1 and 2. First, two transmission phase masks, namely, the transmission phases along x - and y -direction through the unit (shown in Fig. 2.24) as a function of (w , l) at 0.14 THz are obtained in ANSYS HFSS, as shown in Fig. 2.25. Then, the effective refractive indices are retrieved based on the transmission phases (Γ) and frequency (f) using equation [68],[69]:

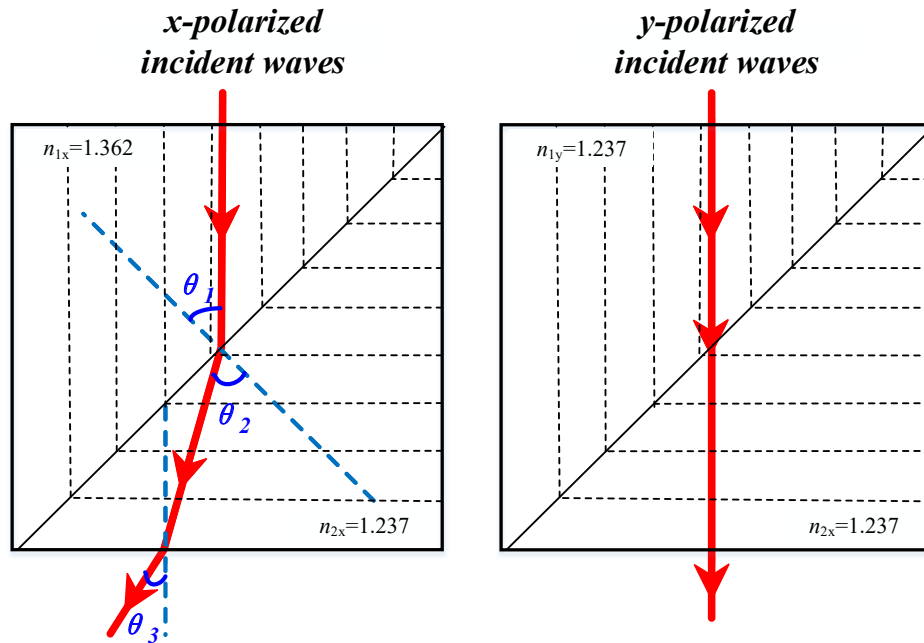


Fig. 2.23. Polarization splitting principle of the proposed Rochon prism ($\theta_1=45.0^\circ$, $\theta_2=51.16^\circ$, $\theta_3=7.65^\circ$).

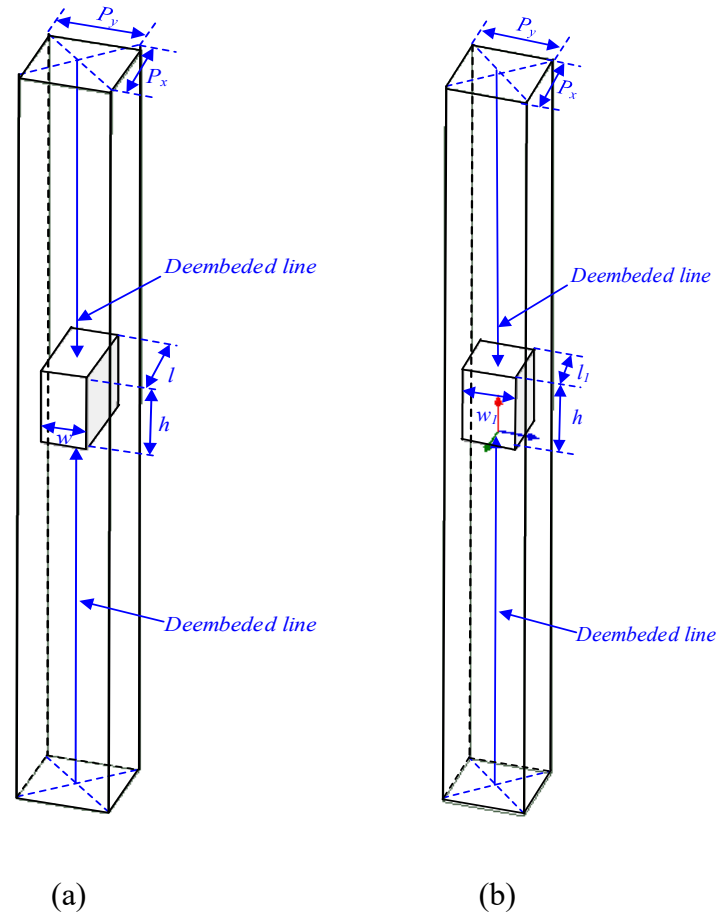


Fig. 2.24. Simulated grating unit model for refractive index retrieval in HFSS. (a) Grating unit with rectangular cross-section. (b) Grating unit with square cross-section. ($P_x=1$ mm, $P_y=1$ mm, $l=1$ mm, $w=0.5$ mm, $l_l=0.657$ mm, $w_l=0.657$ mm, $h=1$ mm)

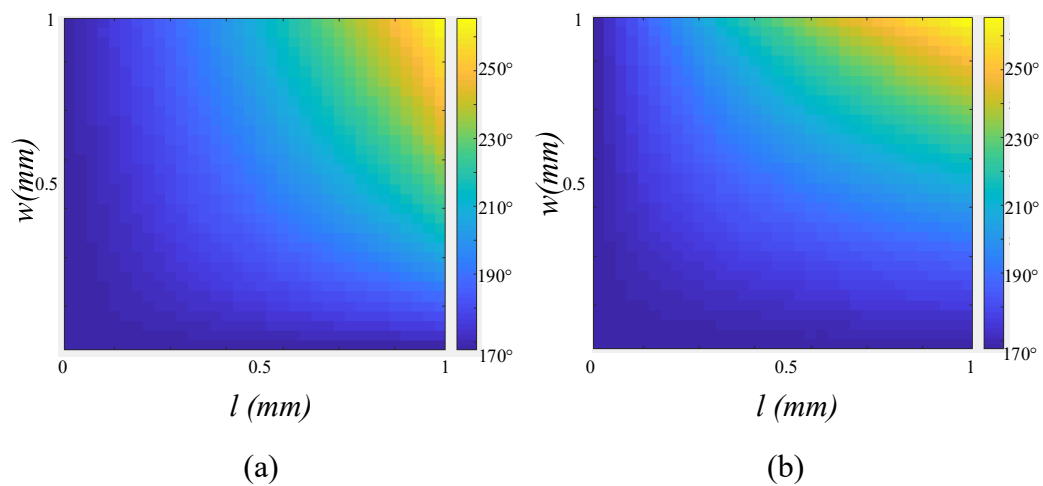


Fig. 2.25. (a) Transmission phase through unit along x-direction as function of (w, l) . (b) Transmission phase through unit along y-direction as function of (w, l) .

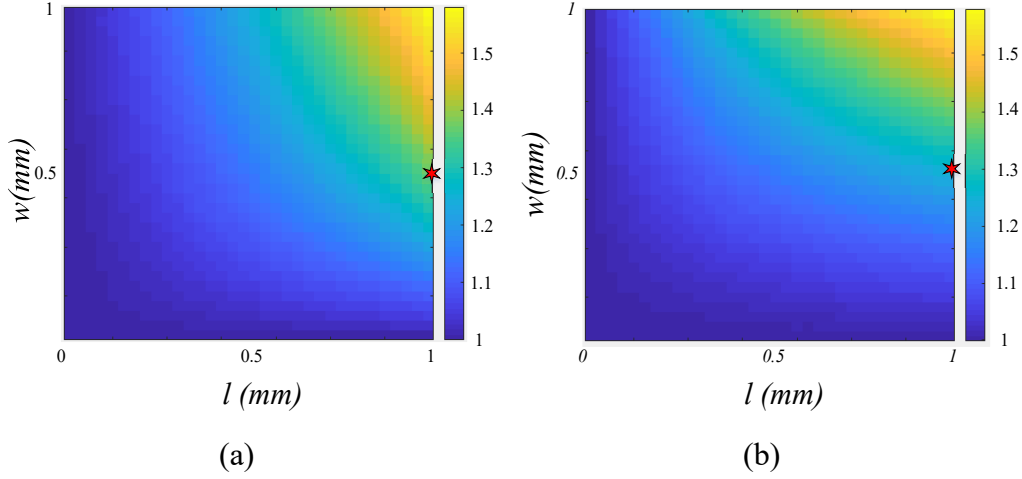


Fig. 2.26. (a) Effective refractive index tensor along x -direction as function of (w, l) . (b) Effective refractive index tensor along y -direction as function of (w, l) .

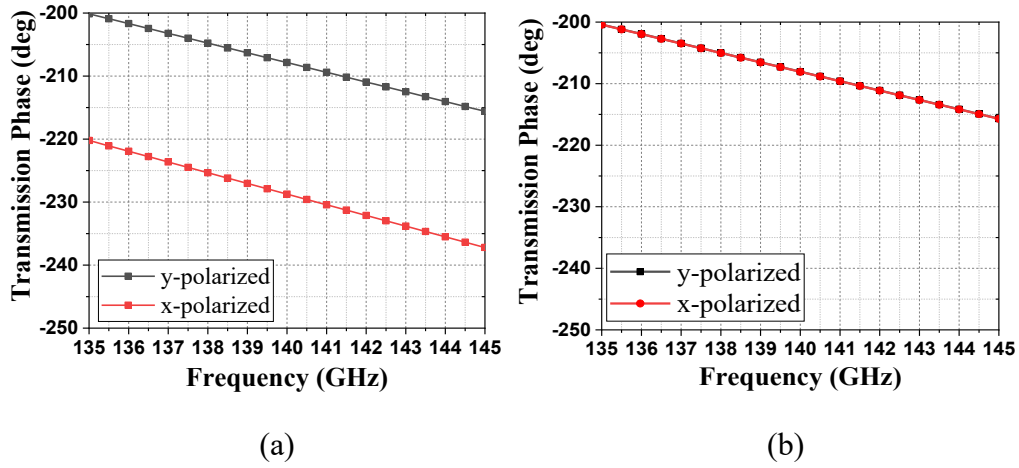


Fig. 2.27. Transmission phases of the gratings in Fig. 2.23. (a) Grating with rectangular cross-section. (b) Grating with square cross-section.

$$n_{eff} = \frac{\Gamma c}{2\pi f h} \quad (2-10)$$

where c is the speed of the light and h (1 mm) is the thickness of the gratings adopted in the model, Γ is the transmission phase. Note that the use of the effective medium to determine the relative permittivity of the composite material is only a theoretical approach under the assumption that the composite is statistically homogeneous, i.e. if we take small elements of the material then these will all have the same physical properties as the whole sample provided that the elements are sufficiently large compared with the periodicity to ensure that they are representative [70]. In the meantime, the periodicity should be smaller than the wavelength. The smaller, the better. The corresponding effective refractive index tensor along x - and y -direction as function of (w, l) are shown in Fig. 2.26. Substitute n_{1x} and n_{2x} (n_{1y}) in equations (2-8)

and (2-9) with the obtained effective refractive index tensor as function of (w , l) and compare all the deflection angles. It is found that the calculated maximum deflection angle is 7.63° under the condition that $l=1\text{mm}$ and $w=0.5\text{mm}$ for the unit forming prism 1 and $l=w=0.657\text{mm}$ for the unit forming prism 2, respectively. Therefore, the length and width of the dielectric grating unit forming prism 1 are adopted as 1 mm (along x -direction) and 0.5 mm (along y -direction) while the length and width of dielectric grating unit forming prism 2 are adopted as 0.657mm (l_1) and 0.657mm (w_1), respectively. The corresponding transmission phases (Γ) through the two units (shown in Fig. 2.24) along x - and y -direction are given in Fig. 2.27. The retrieved effective refractive indexes are 1.362 (n_{1x}) and 1.237 (n_{1y}) for prism 1 and 1.237 (n_{2x}) and 1.237 (n_{2y}) for prism 2 at 0.14 THz, respectively. Therefore, the calculated deflection angle is 7.63° (θ_3) for the x -polarized incident wave and 0° (undeflected) for the y -polarized incident wave, respectively.

2.3.2 3-D Printed Fresnel Rochon Prism design

As Section 2.3.1 has shown, the deflection angle of the Rochon prism is determined by the refractive index and the wedge angle of the prism. Because of the low refractive index of the 3-D printing material, the prism must to be sufficiently thick to generate a large deflection angle, which makes the prism bulky. In addition, a thick prism means low efficiency since considerable energy is dissipated in lossy printing material. To overcome these challenges, based on the Rochon prism proposed in Section 2.3.1, a Fresnel-Rochon prism is further proposed. To clarify the concept, Fig. 2.27 shows the comparisons between the conventional prism and the Fresnel prism as well as the Rochon prism and the proposed Fresnel-Rochon prism. As shown in Fig. 2.27 (a), when the Fresnel principle is applied to a flat-faced prism, the thickness and weight of the prism can be greatly reduced. Each small, uniformly thick prism has the same deflecting angle, which is unaltered by the change in thickness and weight [74]. Borrowing this concept, the 3-D printed Fresnel Rochon prism is proposed, which can replace the conventional bulky Rochon prism with the polarization splitting and deflection angles remaining unaltered, as shown in Fig. 2.28 (b).

The most important aspect is the determination of the thickness of each Fresnel-Rochon prism unit. For each unit, from the left to the right edge, the transmission phase should achieve a full phase-cycle (namely, $2n\pi$, where n is an integer) such that

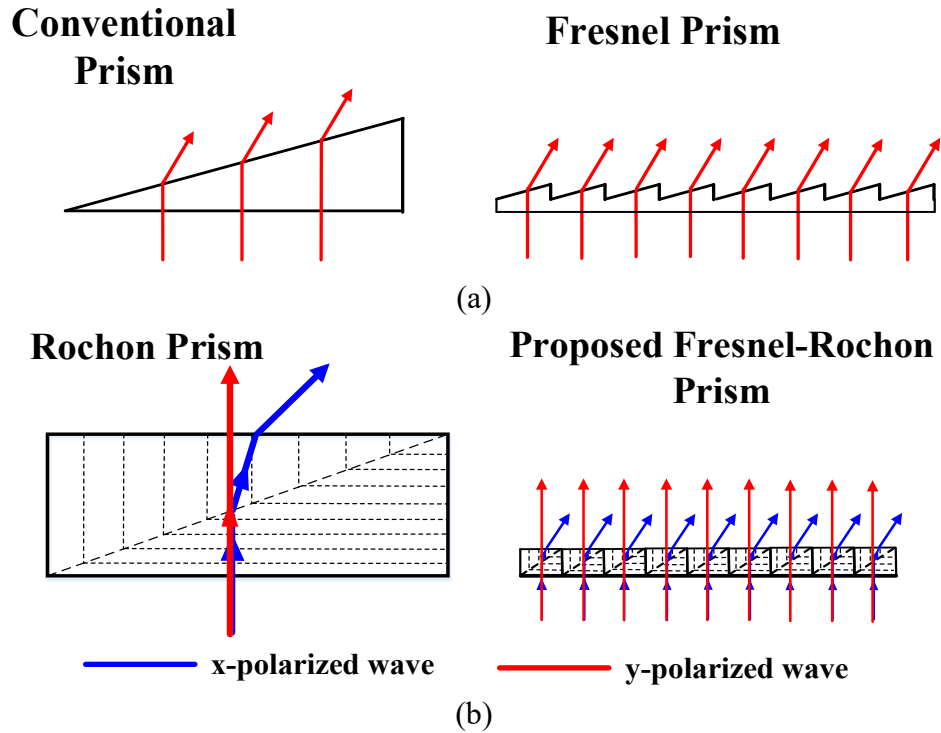


Fig. 2.28. (a) Comparison of the conventional flat-faced prism and Fresnel prism. (b) Comparison of Rochon prism and proposed Fresnel-Rochon prism under x-polarized and y-polarized incident waves illumination.

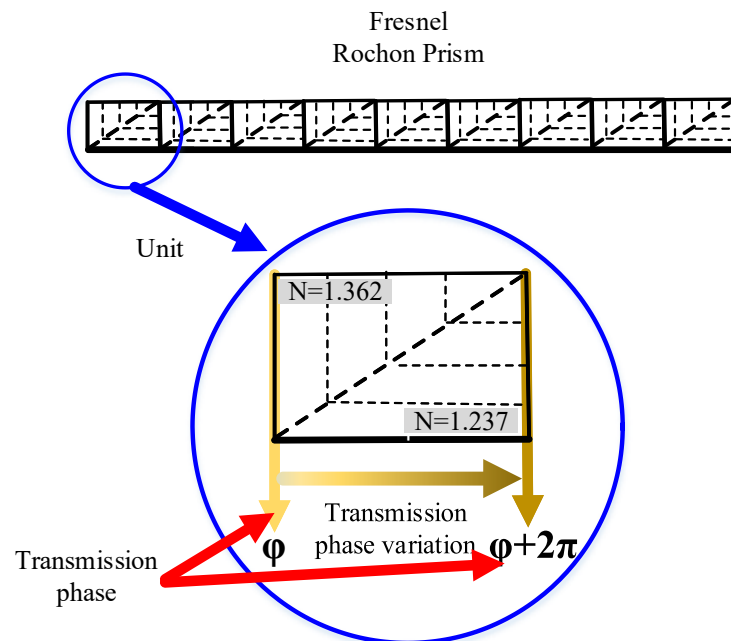


Fig. 2.29. Transmission phase analysis of proposed Fresnel-Rochon prism unit.

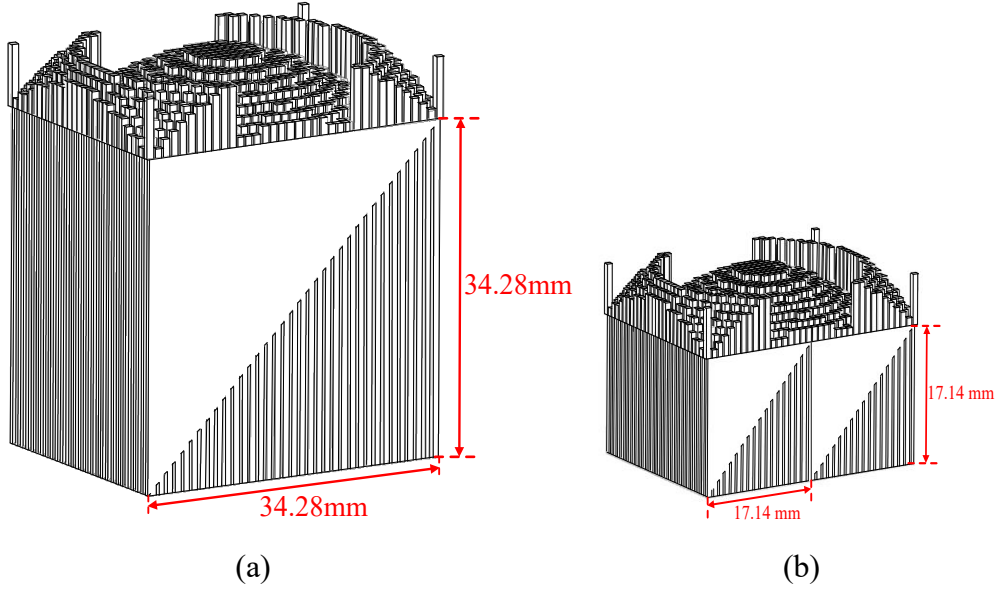


Fig. 2.30. (a) Rochon prism with the wedge angle of 45° . (b) Corresponding Fresnel-Rochon prism.

abrupt phase change is avoided at the boundary between two adjacent prism units, as shown in Fig. 2.29. To achieve the lowest height, n is adopted as 1 in the design. Therefore, the minimal thickness (h_m) of each unit is calculated to be 17.14 mm using Equation [71]:

$$h_m = \lambda / (n_{1x} - n_{2x}) \quad (2-11)$$

where λ is the wavelength in free space. To demonstrate, a Fresnel-Rochon prism with the same wedge angle as the Rochon prism proposed in Section 2.3.1 (45°) is designed. The thickness of the Rochon prism in Section 2.3.1 is 34.28 mm. By applying the Fresnel principle, the thickness of the Fresnel-Rochon prism is 17.14mm, as shown in Fig. 2.30.

The design guidelines for the proposed Fresnel-Rochon prism are summarized as follow:

- a. Determine the operational wavelength (frequency) and the deflection angle (θ_3) according to the requirements of the application.
- b. Determine the most appropriate wedge angle (θ_1) of the prism based on the deflection angle (θ_3) required;
- c. Determining the desired refractive indices of the prism 1 (n_{1x} , n_{1y}) and prism 2 (n_{2x} , n_{2y}), according to the relationships in Eqs. (2-8) and (2-9) and the wedge angle (θ_1);
- d. Obtain the desired transmission phase value (Γ) using (2-10) for each direction (“ox” and “oy”) of both prism 1 and 2 based on the selected “ h ” (in Fig. 2.24) (i.e., for

each of the four effective refractive indices $n_{1x}, n_{1y}, n_{2x}, n_{2y}$;

e. Select the periodicity (P_x and P_y in Fig. 2.24) of the dielectric gratings. The periodicity should be less than one wavelength at least and the smaller, the better. Select an initial length (l in Fig. 2.24) and width (w in Fig. 2.24) for the gratings. Then, optimize them to achieve the desired transmission phase value (Γ obtained in step d) for each direction (“ox” and “oy”) of both prism 1 and 2.

f. Determine the height of the Fresnel prism by using (2-11) to select the minimum height (h_m) of each prism unit.

The discrete lens printed on top of the Rochon prism is used to collimate the waves radiated from a horn antenna for ease of measurement. The phasing element of the discrete lens is realized by a square dielectric post with height of h_p and a length of l_p (0.8mm). The period of the square post is adopted as 1 mm. The transmission phase versus the element height is shown in Fig. 2.31 (a). The full phase-cycle (2π) can be achieved by tuning h_p from 2 to 8 mm. The compensating phase mask at the lens aperture is shown in Fig. 2.31 (b), which is calculated according to equation (2-6).

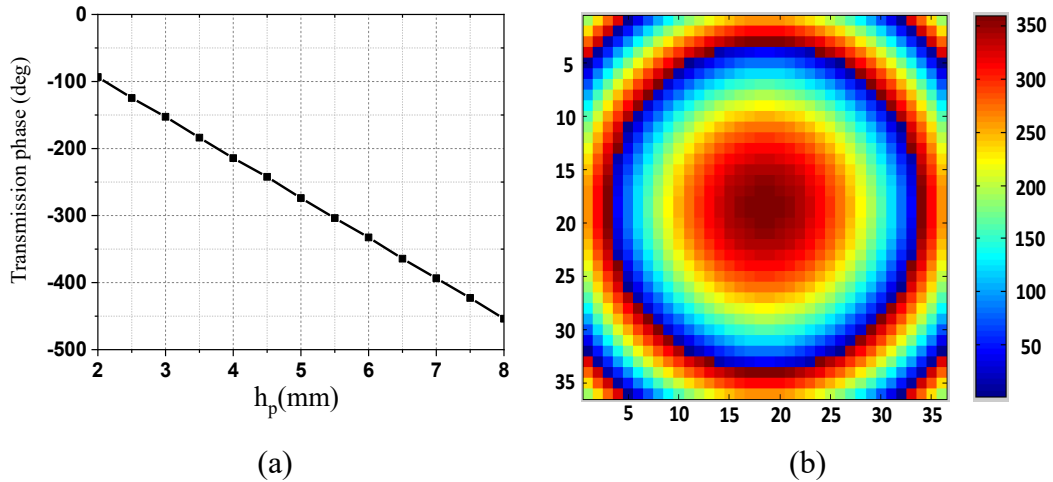


Fig. 2.31. (a) Transmission phases of different thicknesses of phasing element (h_p). (b) Compensating phase mask at lens aperture.

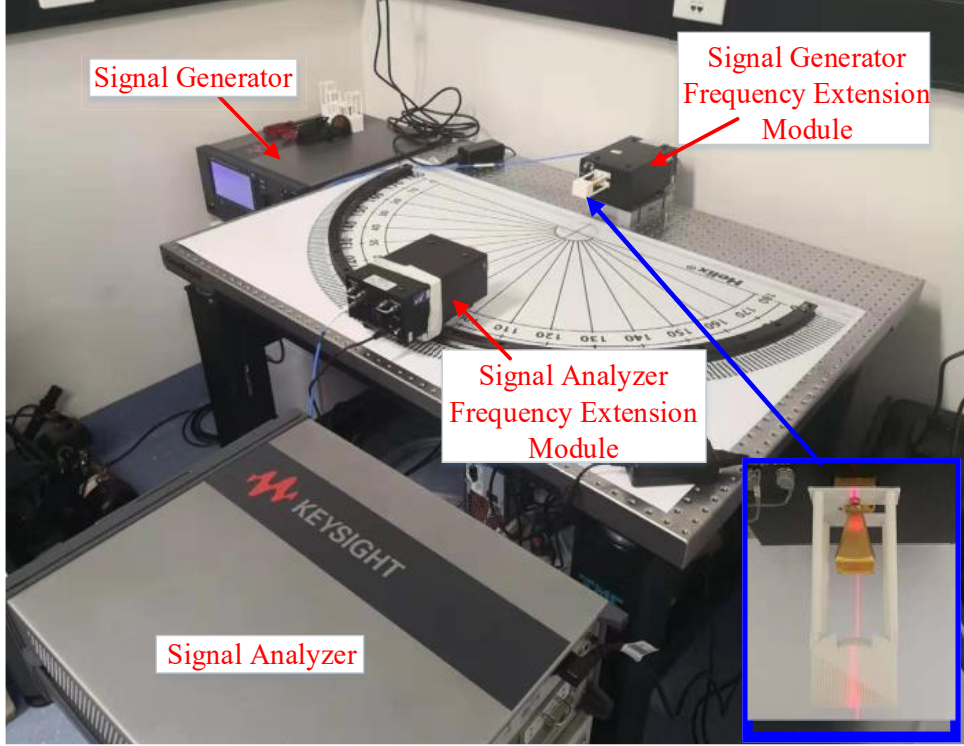


Fig. 2.32. Sub-terahertz radiation measurement system.

The lens-integrated Rochon prism prototype is printed using a commercially available printer (Raised Pro2). The estimated cost is less than \$50. The radiation performance is measured using a far-field sub-terahertz measurement system shown in Fig. 2.32. The signal from the signal generator is up-converted to 0.14 THz through the signal generator frequency extension module (Keysight E8257DV). Then, the signal is fed to the lens-integrated Rochon prism by a standard gain horn (Quinstar QWH-DPRR00). On the other side, the other standard horn is used as the receive antenna at far-field. The receiving horn antenna is connected to a signal analyzer through a signal analyzer frequency extension module (Keysight N9029NV). For the gain measurement, two identical standard gain horns are employed for making the direct gain comparison method to obtain the gain value. The lens-integrated Rochon prism gain (G_{prism}) can be obtained by [72]:

$$(G_{prism})_{dB} = (G_{gain_horn})_{dB} + 10 \log_{10} \left(\frac{P_{prism}}{P_{gain_horn}} \right) \quad (2-12)$$

where G_{gain_horn} is the gain of the standard gain horn, P_{gain_horn} is the received power from the standard gain horn, P_{Prism} is the received power from the lens-integrated prism.

The prototypes of the Rochon and Fresnel-Rochon prisms are shown in Fig. 2.33.

The calculated deflecting angles of both prisms based on (2-8) and (2-9) are 7.63° and 0° at 0.14 THz for x- and y-polarized incident waves, respectively. The simulated and measured radiation patterns of the Rochon prism and the Fresnel-Rochon prism are shown in Figs. 2.34 and 2.35, respectively. The simulated deflecting angles of the Rochon prism for the x- and y-polarized incident waves are 7° (0.138 THz) 7° (0.14 THz) 6.9° (0.142 THz) and 0° (0.138 THz) 0° (0.14 THz), 0° (0.142 THz), respectively. The simulated deflecting angles of the Fresnel-Rochon prism for the x- and y-polarized incident waves are 7.2° (0.138 THz) 7.1° (0.14 THz) 7° (0.142 THz) and 0° (0.138 THz) 0° (0.14 THz), 0° (0.142 THz), respectively. The measured deflecting angles are 7° for both Rochon prism and Fresnel-Rochon prism under x-polarized wave illumination and 0° under y-polarized wave illumination at 0.138 THz, 0.14 THz and 0.142 THz, respectively.

The simulated and measured gain of the Rochon prism and the Fresnel-Rochon prism are shown in Fig. 2.36. The measured peak gain of the Rochon prism is 20.7 dBi and 22.6 dBi for x- and y-polarized incident waves, respectively. The measured peak gain of the proposed Fresnel-Rochon prism is 23.8dBi and 24.2dBi for x- and y-polarized incident waves, respectively. Over the frequency band from 0.138 THz to 0.14 THz, the gains of the Fresnel-Rochon prism show 3 dB (x-polarization) and 2.5 dB (y-polarization) gain improvement on average compared with the Rochon prism.

So far, many commonly-used optical polarizing beam splitters consist of two appropriately-oriented birefringent calcites cemented together. When the frequency is down to the THz region, much more expensive birefringent material is required to form these beam splitters. In contrast, all-dielectric prisms are proposed here to replace the natural birefringent material. Because of the low-cost of the printing

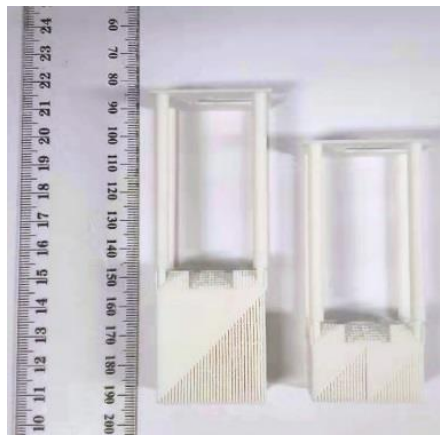


Fig. 2.33. Printed prototypes (Left: Rochon prism. Right: Fresnel Rochon prism).

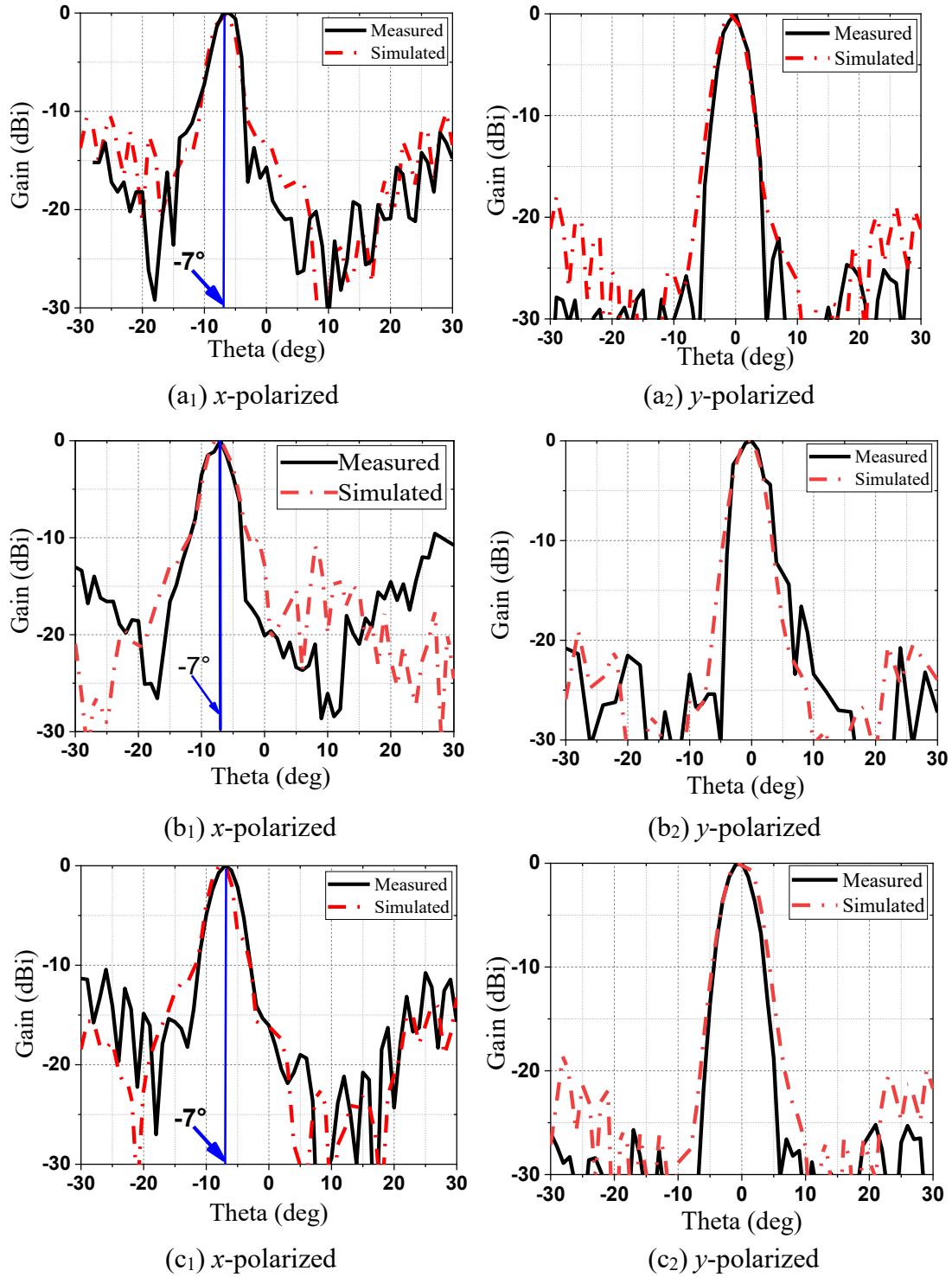


Fig. 2.34. Simulated and measured radiation patterns under x -polarized and y -polarized incident wave illumination of Rochon prism at (a) 0.138 THz. (b) 0.14 THz. (c) 0.142 THz.

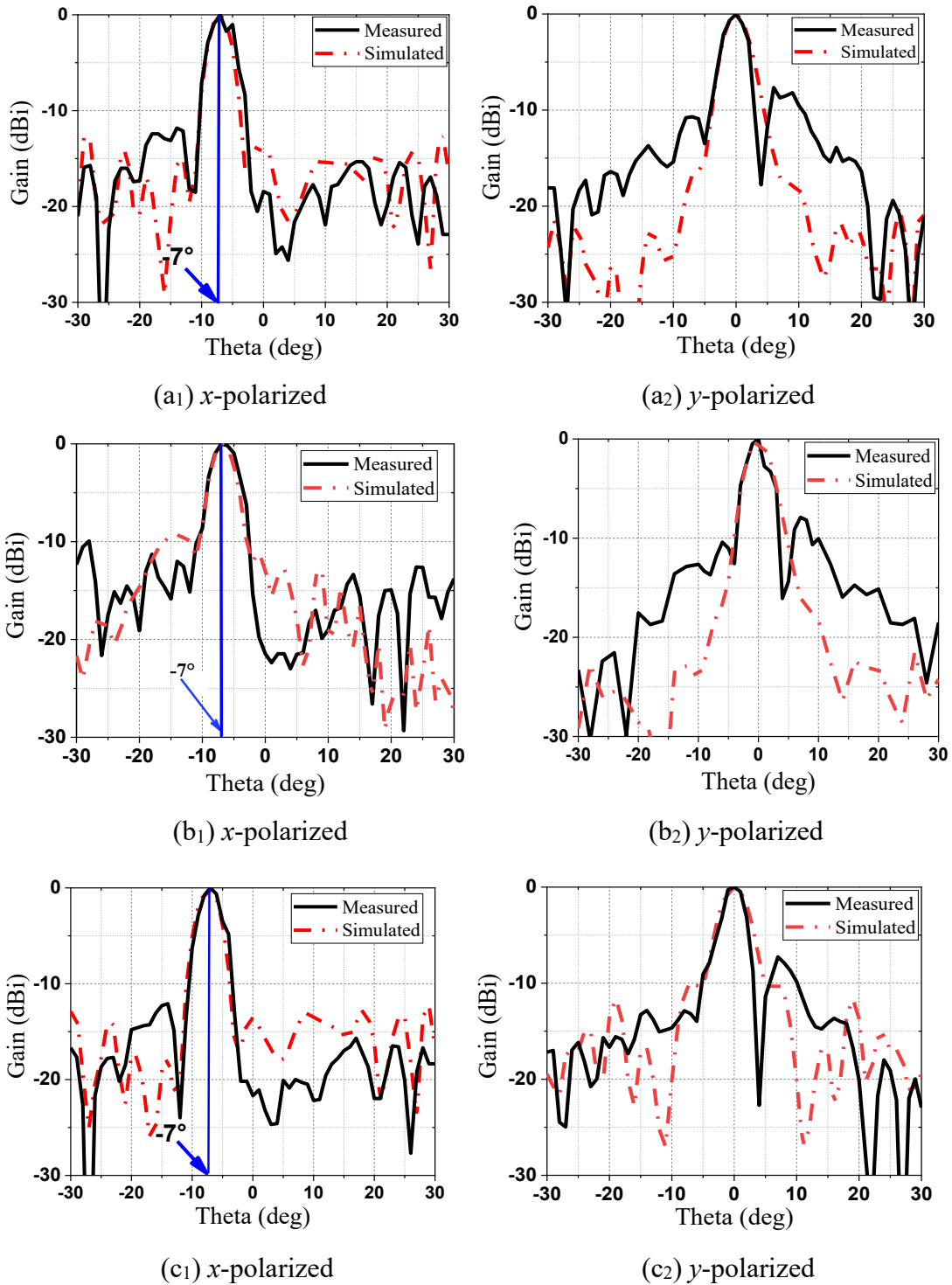


Fig. 2.35. Simulated and measured radiation patterns under x-polarized and y-polarized incident wave illumination of Fresnel-Rochon prism at (a) 0.138 THz. (b) 0.14 THz. (c) 0.142 THz.

material, the fabrication cost of these polarization beam splitters can be significantly reduced. Moreover, taking advantage of 3-D printing, these prisms can be directly fabricated without the cementing procedure and there is less waste. One of the challenges of the 3-D printed polarization beam splitter is the low refractive index and the lossy printing material. To overcome these issues, the Fresnel principle is applied to the Rochon prism with twofold benefits: first, the thickness of the Rochon prism can be significantly reduced to a fixed height, regardless of the thickness of the original Rochon prism. second, with reduced thickness, less energy is dissipated into the lossy printing material. Furthermore, by using more advanced 3-D printers, the proposed Fresnel-Rochon prism can be realized in the optical region and the proposed design principle can be applied to other polarization beam splitters, such as Wollaston prisms. It is also worth mentioning that the Fresnel-principle is frequency-dependent, as given in Eq. (2-11). Thus, the operating bandwidth of the proposed Fresnel Rochon prism will be smaller than Rochon prism though the thickness is significantly reduced.

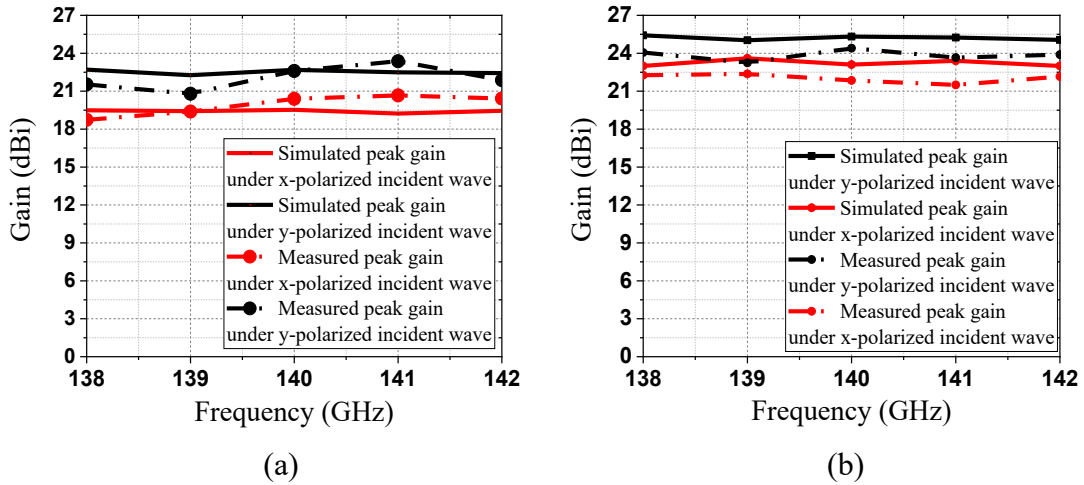


Fig. 2.36. (a) Simulated and measured peak gains of the lens-integrated Rochon prism under x -polarized and y -polarized incident waves. (b) Simulated and measured peak gains of the lens-integrated Fresnel Rochon prism under x -polarized and y -polarized incident waves.

2.4 Low-Cost 3-D Printed All-Dielectric Dual-Band Broadband Reflectarray with a Large Frequency-Ratio

As wireless systems are now exploiting a wide frequency spectrum from sub-6 GHz to the low terahertz (THz) region, dual-band/multi-band reflectarrays with a large frequency ratio are becoming more and more popular [74-78]. To achieve a large frequency ratio, one approach is to utilize a stack of two phasing element layers, with each operating at one frequency band. For example, a microstrip concentric dual split-loop element operating in the K-band is put on the top of an L-band element [74] with a frequency-selective-surface (FSS) as a spacer. Because of the stacked layers, blockage effects degrade the efficiency and gain of the lower reflectarray. To overcome this problem, Deng *et al.* proposed the Phoenix element [79] to realize a single-layer dual-band reflectarray, albeit with a restricted frequency-ratio of up to 2. Dielectric-based reflectarrays are also widely used to avoid conductor loss, since loss in the resonant metallic phasing elements increases to a degree at THz frequencies and above [80]. For example, dielectric slabs with variable heights are commonly used as the phasing element [81-88]. However, these designs operate in a single frequency band because dielectric slabs can achieve only a 2π phase change over one frequency band. In the THz and optical bands, many reported reflectarrays use low loss and high dielectric materials (such as high-resistivity silicon (HR Si) and titanium dioxide) as dielectric resonators (DR) sitting on a gold ground [89-91]. Currently, most dielectric-based reflectarrays are constructed from dielectric slabs (perforated holes), or DR as the phasing element and the metal plane as ground. To the best of our knowledge, an all-dielectric dual-band reflectarray with a large frequency-ratio has not been previously reported.

In this section, we propose a kind of all-dielectric dual-band reflectarray that adopts a dielectric mirror as the ground and air as the phasing element. In this way, the conventional metal ground is removed. Therefore, the design is a truly dielectric-only reflectarray with the benefit of direct 3-D printing. Unlike full metal ground, the dielectric mirror shows bandgap characteristics only in the pre-designed frequency. Out of the bandgap, electromagnetic (EM) wave can pass through it with little hindrance. This feature makes the dual-band property of the dielectric-based reflectarray possible. With careful selection of the bandgap feature of the dielectric

mirror structure, the dual-band frequency-ratio is scalable and can be very large. Furthermore, since phase tuning is realized using an air layer with linear phase response, the reflectarray is broadband and shows stable performance. In addition, there is no mutual interference between dual-band in regard to phase, and the compensating phase of the two bands can be therefore considered independently. A prototype operating at K-band and V-band is printed and measured to verify the concept and its basic configuration is given in Fig. 2.37.

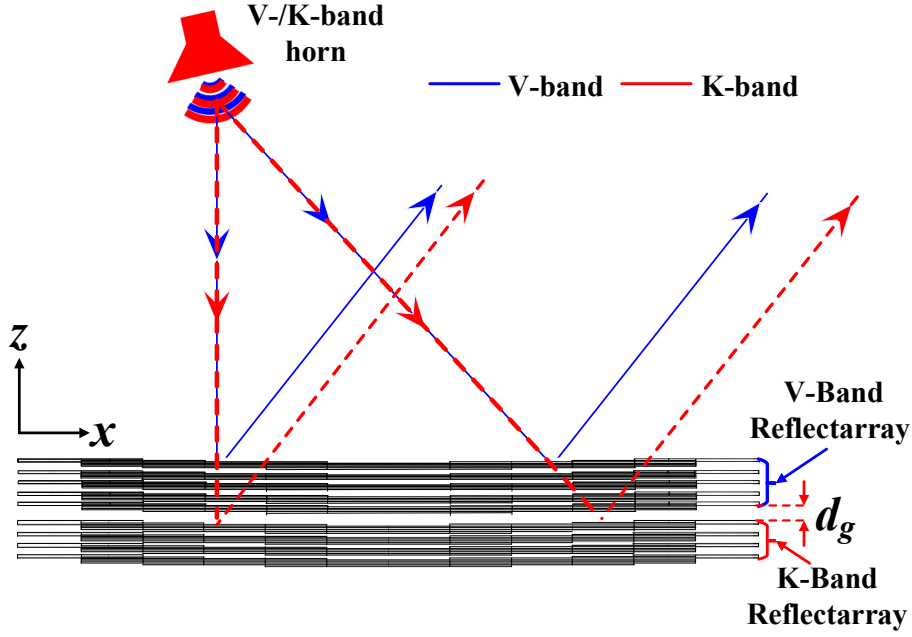


Fig. 2.37. Configuration of the proposed dual-band all-dielectric reflectarray. ($d_g=4.8$ mm).

2.4.1 Dielectric mirror

The basic building block of the reflectarray is based on dielectric mirror structure, which is formed by periodically stacking dielectric layers and air layers, as shown in Fig. 2.38 (a). At low frequencies, i.e. the wavelength is much longer than the periodicity, the wave propagates through the structure as if the structure is homogenous with the corresponding effective refractive index. As the frequency increases, multiple partial reflections from the boundaries between two materials with different refractive indices become important and all these partially-reflected waves interfere with each other and give rise to significant overall reflection. Eventually, when the cut-off frequency is reached, the wave is completely reflected backward. This cut-off frequency and the bandgap can be found using eigenmode analysis in

ANSYS HFSS assuming infinite periodicities, as shown in Figs. 2.38 (b) and (c). Note that although multiple bandgaps can be achieved using the dielectric mirror structure, only the lowest bandgap is used in the design. The location of the bandgap can be adjusted by tuning the length of the periodicity. The larger the periodicity, the lower frequency of the first bandgap. This means that the bandgap of the dielectric mirror, and therefore the operating frequencies of the reflectarray, can be easily controlled. The band-width of the bandgap can also be controlled as the bandgap region increases with the index difference ($n_1 - n_2$) [66].

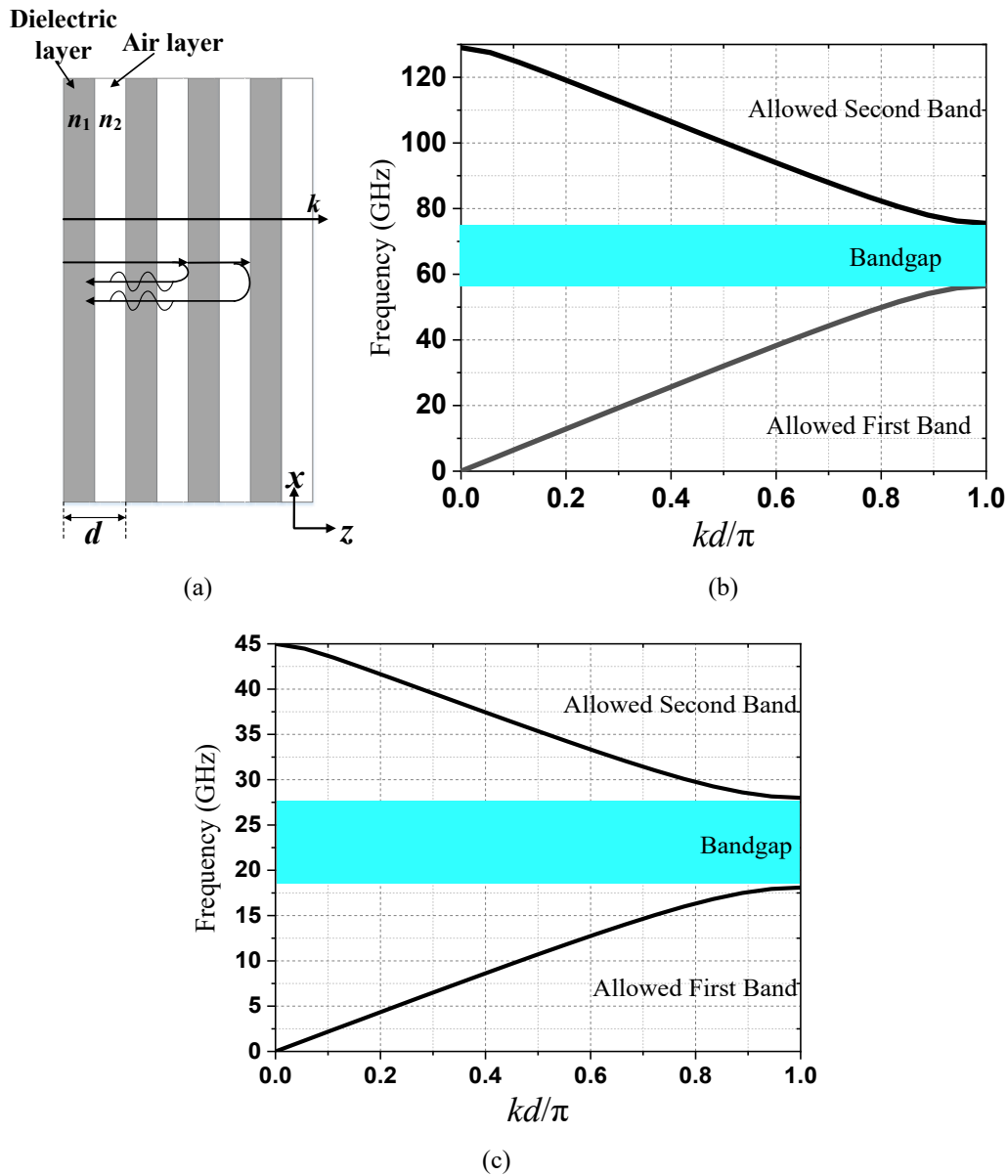


Fig. 2.38. (a) Basic configuration of the dielectric mirror structure. (k is the propagation constant inside the medium). (b) Dispersion curve of the proposed V-band dielectric mirror structure. (c) Dispersion curve of the proposed K-band dielectric mirror structure.

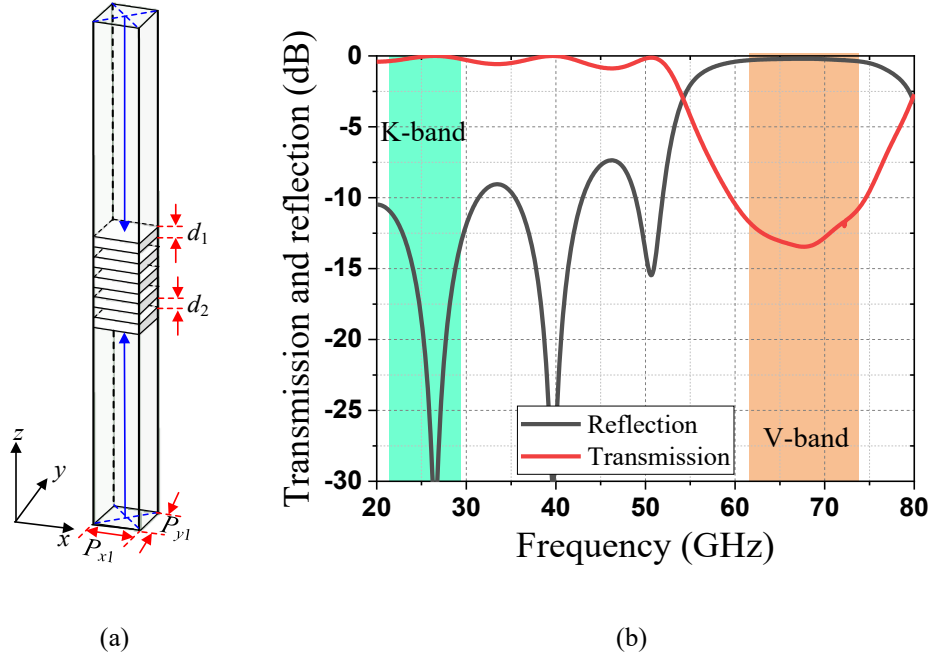


Fig. 2.39. (a) Simulation model of dielectric mirror structure in ANSYS HFSS for V-band reflectarray. (b) Transmission and reflection coefficients of the structure. ($d_1=0.8$ mm, $d_2=1$ mm, $P_{x1}=P_{y1}=3.5$ mm).

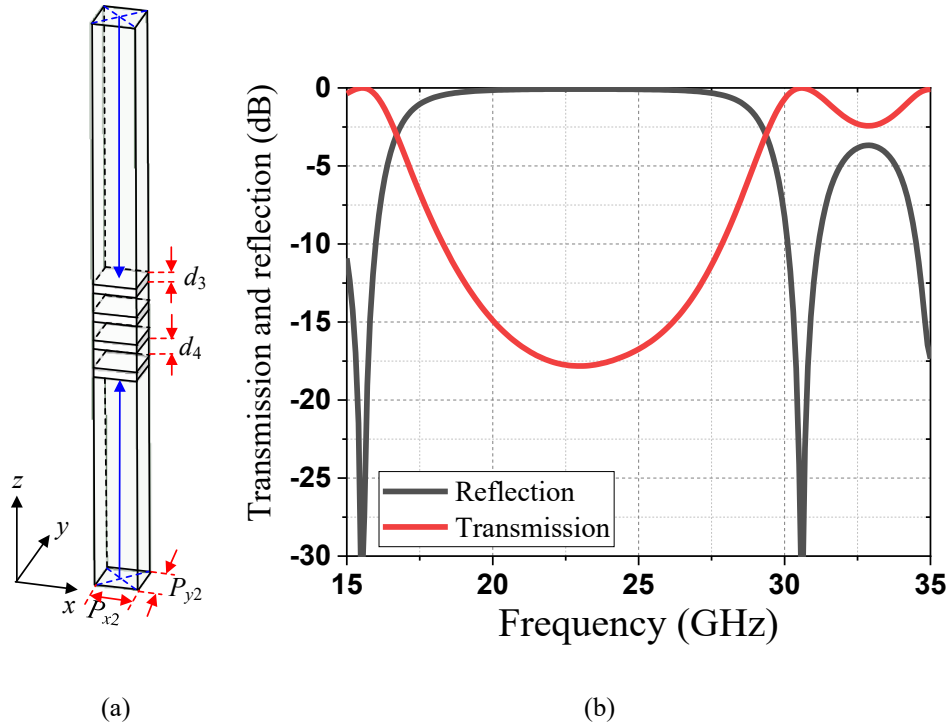


Fig. 2.40. (a) Simulation model of dielectric mirror structure in ANSYS HFSS for K-band reflectarray. (b) Transmission and reflection coefficients of the structure. ($d_3=1.5$ mm, $d_4=3.5$ mm, $P_{x2}=P_{y2}=7.5$ mm).

Ideally, the dielectric stack of the dielectric mirror structure is infinite. However, sufficient reflection can be achieved by using the multiple periodicities of the dielectric stack. In the design, the reflectarray in the high-band is achieved by stacking five dielectric layers in order using polylactic acid (PLA) with a relative permittivity of 2.5, a loss tangent of 0.025, and thickness of 0.8 mm. The distance between two adjacent dielectric layers (air layer) is 1 mm. While the reflectarray in the low-band is achieved by stacking four-dielectric layers (PREPERM® 3-D ABS) with a relative permittivity of 4, a loss tangent of 0.004, and a thickness of 1.5 mm in order. The distance between two adjacent dielectric layers is 3.5 mm. The simulation model of the V-band dielectric mirror structure and its corresponding transmission and reflection coefficients are shown in Fig. 2.39. From 60 GHz to 75 GHz, the reflection coefficient is better than 0.3 dB, demonstrating that the EM wave is reflected by the dielectric mirror in V-band, while the transmission coefficient is better than 10 dB from 20 GHz to 30 GHz, indicating that EM wave can transmit through it in the K-band. The simulation model of the K-band dielectric mirror structure and its corresponding transmission and reflection coefficients are shown in Fig. 2.40. From 18 GHz to 27.5 GHz, the reflection coefficient is better than 10 dB, demonstrating that the EM wave is reflected by the dielectric mirror in the K-band.

As dielectric mirror structures are used for the building blocks of the reflectarray, it is important to investigate the performance of the dielectric mirror structures under oblique incident waves. The simulated reflection coefficients of the dielectric mirror structures under oblique incident angles up to 40-degree are shown in Fig. 2.41. The figure reveals that the bandgaps of the V-band and K-band are very stable and the operating bandgaps shift slightly to the higher frequency when the incident angle increases.

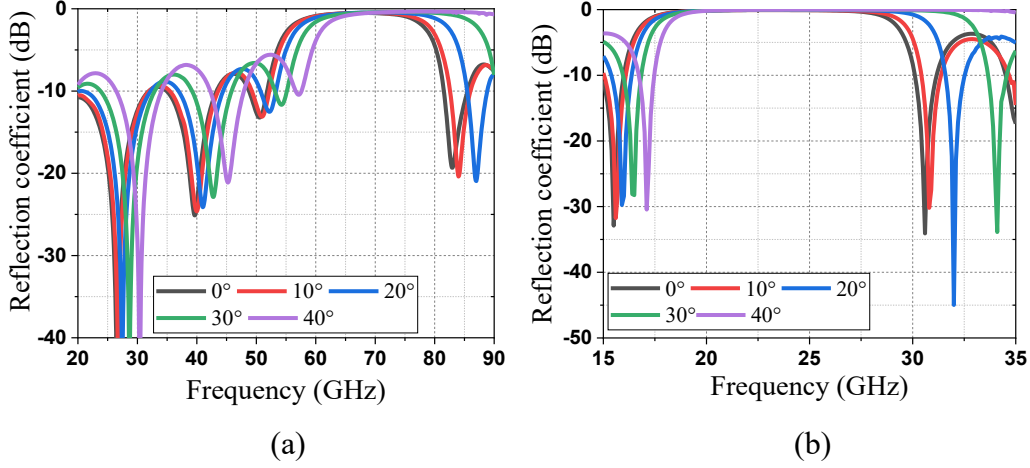


Fig. 2.41. (a) The reflection coefficients of V-band dielectric mirror structure under oblique incident angles. (b) The reflection coefficients of the K-band dielectric mirror structure under oblique incident angles.

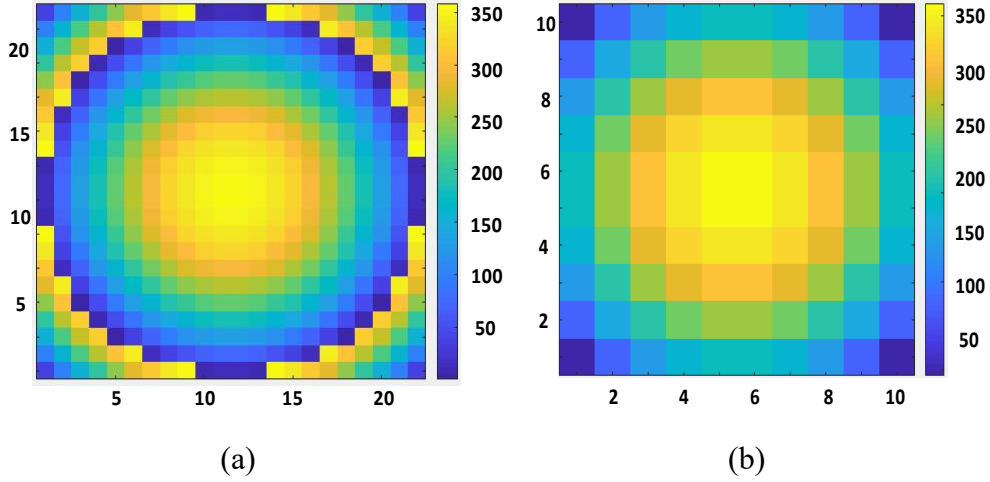


Fig. 2.42. (a) Compensating phase in V-band. (b) Compensating phase in K-band.

2.4.2 Reflectarray design

The array of the proposed dielectric mirror structure was built in a stepped configuration to form the reflectarray. In this way, the air was used as the wideband phasing element, which is different from conventional designs using dielectric slabs [83-86]. The phase compensation on the aperture was calculated according to equation (2-6). The aperture size is 77 mm \times 77 mm and the focal length is set as 150 mm. 22 \times 22 and 10 \times 10 phasing elements are used for the high-band and low-band reflectarray, respectively. Generally, for conventional multi-layered reflectarrays, the upper phasing element affects the bottom phasing element due to mutual coupling.

Therefore, a high-performance FSS structure must be used to avoid mutual coupling between the two frequency bands [74],[75]. For the proposed design, because all the phasing elements of the upper reflectarray are the same (only positions along z -direction are different), they do not impose change on the compensating phase of the reflectarray on the bottom. Therefore, the compensating phase of the dual-band can be considered independently. The calculated compensating phase masks of the high-band and low-band reflectarray are shown in Fig. 2.42.

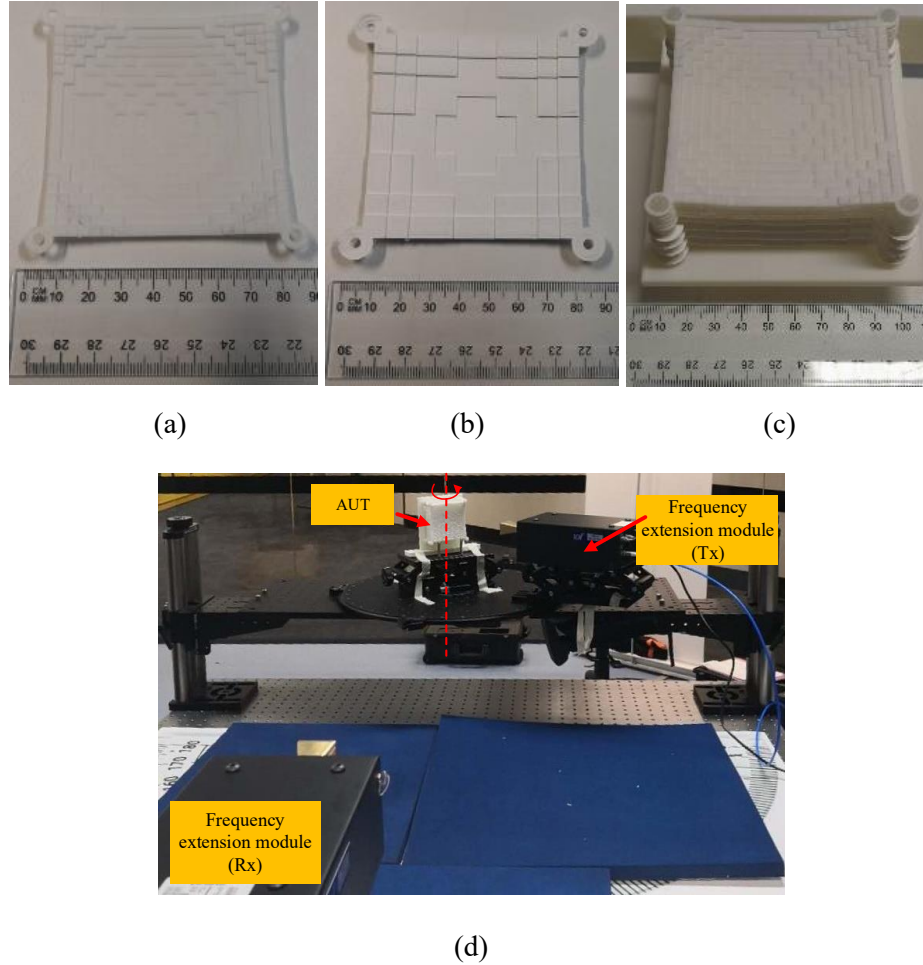


Fig. 2.43. (a) Top view of the V-band structure. (b) Top view of the K-band structure. (c) Assembled view. (d) Measurement system.

The prototype of the reflectarray is fabricated using a generic 3-D printer Flashforge Guider II, as shown in Figs. 2.43 (a)-(b). The V-band and K-band reflectarrays are composed of five and four dielectric layers, respectively, and they are then assembled, as shown in Fig. 2.43 (c). The fabrication cost is less than \$30. The radiation performance is measured using a far-field measurement system, as shown in Fig. 2.43 (d). To avoid the blocking effect, the inclination angle of the feed horn antenna is

offset -20-degree, and the reflection direction is therefore 20° . The radiation patterns in V-band (66-GHz & 70-GHz) and K-band (24 GHz&27-GHz) are shown in Figs. 2.44 and 2.45, respectively. The measured gains are shown in Fig. 2.46. The peak gain is 30.7 dBi for the V-band and 23.2 dBi for the K-band. Because air is used as the phasing elements with linear phase response, the reflectarray shows broadband performance with a 1-dB gain bandwidth of 32% (from 21 to 29 GHz) for the K-band and 15.7% (from 64 to 75 GHz) for the V-band.

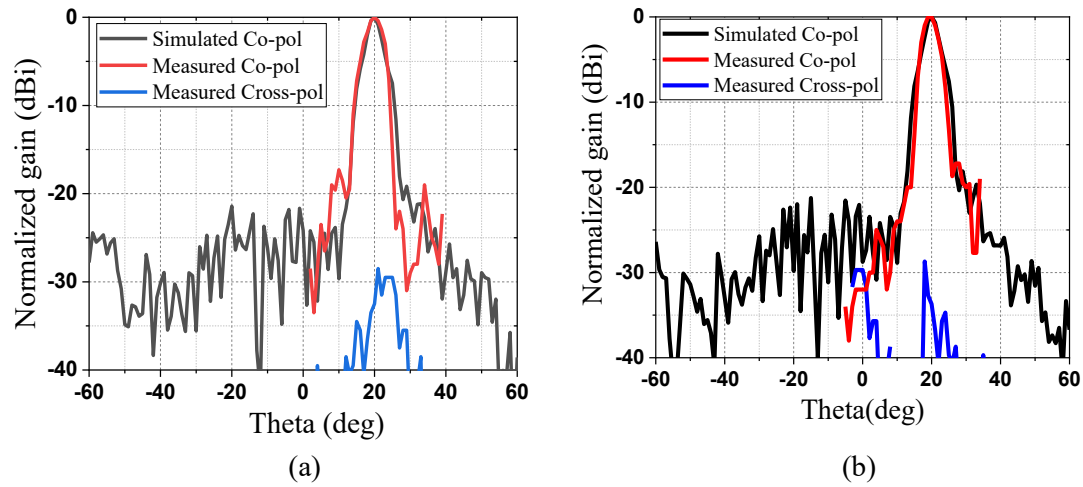


Fig. 2.44. Simulated and measured radiation patterns. (a) 66 GHz. (b) 70 GHz.

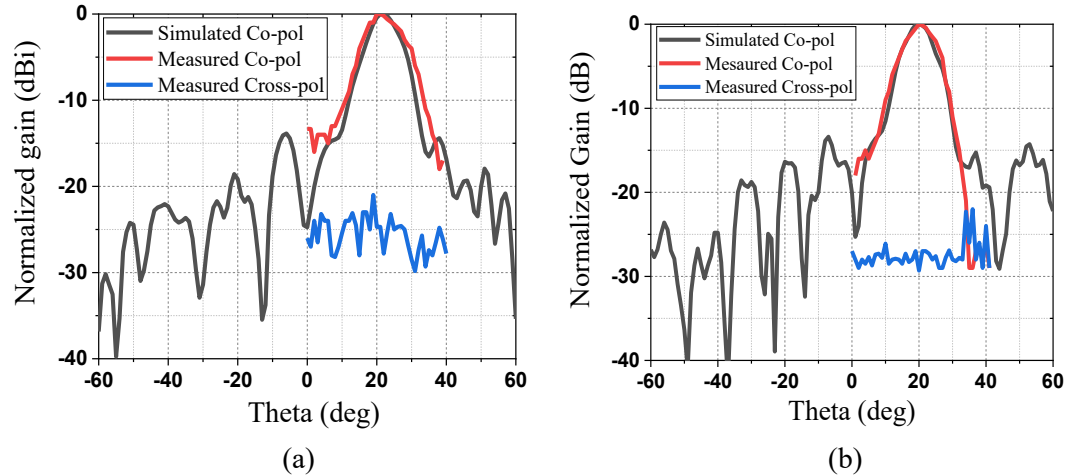


Fig. 2.45. Simulated and measured radiation patterns. (a) 24 GHz. (b) 27 GHz.

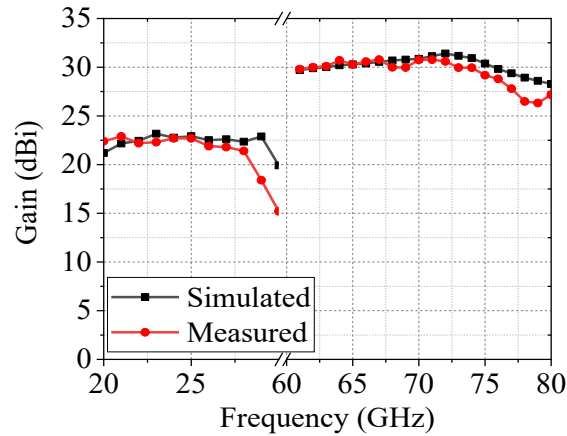


Fig. 2.46. Simulated and measured antenna gain.

TABLE 2.4 COMPARISON OF DIFFERENT KINDS OF DUAL-BAND REFLECTARRAY ANTENNAS

Ref.	Configurations	Operating Frequency	Mutual interference	Gain (dBi/dBic)	1-dB Gain Bandwidth [%]	Frequency-ratio	Fabrication
[74]	Single layer phasing element + full Ground	29.8/20	Strong	40/35.8	-/-	1.49	PCB
[75]	Multi-layer phasing element + FSS	30.2/20.4	Weak	40.2/36.7	10.1/7.2	1.48	PCB
[76]	Multi-layer phasing element + FSS	29.8/20	Medium	38.5/36.4 (directivity)	-/-	1.49	PCB
[77]	Single layer phasing element + full Ground	30/20	Medium	38.9/36.7	6.3/6.9	1.5	PCB
[78]	Multi-layer phasing element	29.7/19.7	Strong	38.5/35.1	-/-	1.5	PCB
[79]	Single layer phasing element + full Ground	20/10	Weak	36.1/30.3	9.1/14	2	PCB
[92]	Single layer phasing element + full Ground	13.5/9	Weak	23.4/17.8	7.3/5.5	1.5	PCB
[93]	DR+ full ground	10/5.68	Weak	23/19	24/14	1.76	N.A.
This work	Dielectric mirror + air	65/24 GHz	Weak	30.7/23.2	15.7/32	2.7	3-D printing

Table 2.4 compares the proposed reflectarray with other dual-band reflectarrays. As the table shows, most dual-band reflectarray antennas are based on metallic resonators either printed in a single layer or arranged in multiple layers. Additional effort is required to reduce the mutual coupling between different resonant cells, such as using FSS or designing sophisticated resonators [74-76]. [93] proposed a dual-band

dielectric reflectarrays by cutting notch on the dielectric resonator. However, the notched structure is complicated to fabricate. In addition, because the metallic structure and DR are based on resonance, the bandwidths of the designs are medium. In fact, dielectric-based reflectarrays are always implemented by planting dielectric slabs or DR on full metal ground. In contrast, for the proposed design, no metal is required, which makes the design an all-dielectric one. Since the 2π phase circle is achieved without being based on resonance, the reflectarray achieves broadband and stable performance over dual-band. Furthermore, the dielectric mirror structure functions as not only the metal ground to reflect EM wave but also as the FSS (it reflects EM wave on high-band and allows EM wave on low-band to pass). Thus, the dual-band feature with a large frequency-ratio is easily achieved. Because the upper phasing element has no mutual interference with the bottom phasing element inherently regarding phase, the compensating phase of dual bands can be considered independently. Moreover, compared with state-of-the-art designs using PCB technology or micro-fabrication, the proposed all-dielectric design enjoys the benefit of 3-D printing with low cost, light weight, and easy to fabricate. It is worth mentioning that the order of the reflectarray in the upper and bottom can be swept. However, it must ensure that the bandgap of the upper dielectric mirror will not affect the lower reflectarray.

2.5 Conclusion

In summary, a series of new mm-wave and THz beam-shaping lenses, prisms and reflectarrays is proposed using the low-cost 3-D printing. All these devices feature high gain with low profile. Some are also capable of collimating beams and manipulating polarizations simultaneously. These devices can be potentially used in different kinds of point-to-point communication applications.

2.6 References

- [1] D. Tang, C. Wang, C. Z. Zhao, *et al.* "Ultrabroadband superoscillatory lens composed by plasmonic metasurfaces for subdiffraction light focusing," *Laser & Photonics Reviews*, 9(6): 713-719, 2015.
- [2] Z. Zhang, D. Wen, C. Zhang, *et al.* Multifunctional light sword meta-surface lens.

- ACS photon., 5(5): 1794-1799, 2018.
- [3] R. Rajasekharan, C. Bay, Q. Dai, *et al.*, “Electrically reconfigurable nanophotonic hybrid grating lens array,” Appl. Phys. Lett 96 (23), 233108, 2010.
- [4] K. Won, A. Palani, H. Butt, *et al.* “Electrically Switchable Diffraction Grating Using a Hybrid Liquid Crystal and Carbon Nanotube Based Nanophotonic Device,” Adv. Opt. Mater 1 (5), 368-373, 2013.
- [5] T. Cai *et al.*, “Ultra-Thin polarization beam splitter using 2-D transmissive phase gradient metasurface,” IEEE Trans. Antennas Propag., vol. 63, no. 12, pp. 5629-5636, Dec. 2015.
- [6] Z. Wei, Y. Cao, X. Su, *et al.* “Highly efficient beam steering with a transparent metasurface,” Opt. Exp, 21(9): 10739-10745, 2013.
- [7] Y. Li, X. Li, L. Chen, *et al.*, “Orbital angular momentum multiplexing and demultiplexing by a single metasurface,” Adv. Opt. Mater., 5(2): 1600502. 2017.
- [8] S. Yu, L. Li, G. Shi, *et al.*, “Generating multiple orbital angular momentum vortex beams using a metasurface in radio frequency domain,” Appl. Phys. Lett., 108(24): 241901, 2016.
- [9] C. Zhang, L. Deng, J. Zhu, *et al.* “Control of the spin angular momentum and orbital angular momentum of a reflected wave by multifunctional graphene metasurfaces,”. Materials, 11(7): 1054. 2018.
- [10] S. Koenig *et al.*, “Wireless sub-THz communication system with high data rate,” Nature Photon., vol. 7, pp. 977–981, Oct. 2013.
- [11] K. Fan, Z. Hao, Q. Yuan and W. Hong, “Development of a high gain 325–500 GHz antenna using quasi-planar reflectors,” IEEE Trans. Antennas Propag, vol. 65, no. 7, pp. 3384-3391, July 2017.
- [12] Y. Liu *et al.*, “Millimeterwave and terahertz waveguide-fed circularly polarized antipodal curvedly tapered slot antennas,” IEEE Trans. Antennas Propag, vol. 64, no. 5, pp. 1607-1614, May 2016.
- [13] N. Zhu and R. W. Ziolkowski, “Photoconductive THz antenna designs with high radiation efficiency, high directivity, and high aperture efficiency,” IEEE Trans. THz Sci. Technol., vol. 3, no. 6, pp. 721-730, Nov. 2013.
- [14] Y. Huang, L. Wu, M. Tang and J. Mao, “ Design of a beam reconfigurable THz antenna with graphene-based switchable high-impedance surface,” IEEE Trans. on Nanotech., vol. 11, no. 4, pp. 836-842, July 2012.
- [15] P. Nayeri *et al.*, “3D printed dielectric reflectarrays: low-cost high-gain antennas

at sub-millimeter waves,” IEEE Trans. Antennas Propag, vol. 62, no. 4, pp. 2000-2008, April 2014.

[16] X. You, R.T. Ako, W. S. L. Lee, *et al.* “Terahertz reflectarray with enhanced bandwidth,” Adv. Opt. Mater., 1900791, 2019.

[17] T. Niu, W. Withayachumnankul, *et al.* Experimental demonstration of reflectarray antennas at terahertz frequencies. Opt. Exp, 21(3): 2875-2889, 2013.

[18] Z. Hao, J. Wang, Q. Yuan and W. Hong, “Development of a low-cost THz metallic lens antenna,” IEEE Antennas Wireless Propag. Lett. , vol. 16, pp. 1751-1754, 2017.

[19] D. Headland, W. Withayachumnankul, R. Yamada, *et al.* “Terahertz multi-beam antenna using photonic crystal waveguide and Luneburg lens,” APL Photonics, 3(12): 126105, 2018.

[20] Z. Miao, Z. Hao, Y. Wang, B. Jin, J. Wu and W. Hong, “A 400-ghz high-gain quartz-based single layered folded reflectarray antenna for terahertz applications,” IEEE Trans. THz Sci. Technol., vol. 9, no. 1, pp. 78-88, Jan. 2019.

[21] S.-W. Qu, H. Yi, B. J. Chen, K. B. Ng, and C. H. Chan, “Terahertz reflecting and transmitting metasurfaces,” Proc. IEEE, vol. 105, no. 6, pp. 1166–1184, Jun. 2017.

[22] H. Yi, S.-W. Qu, B.-J. Chen, X. Bai, K. B. Ng, and C. H. Chan, “Flat terahertz reflective focusing metasurface with scanning ability,” Sci. Rep., vol. 7, Jun, Art. no. 3478, 2017.

[23] S. Liu, L. Zhang, Q.L. Yang, *et al.* “Frequency-dependent dual-functional coding metasurfaces at terahertz frequencies,” Adv. Opt. Mater, 4(12): 1965-1973, 2016.

[24] L. Zhang, R. Y. Wu, G.D. Bai, *et al.* “Transmission-reflection-integrated multifunctional coding metasurface for full - space controls of electromagnetic waves,” Adv. Funct. Mater, 28(33): 1802205, 2018.

[25] G. D. Bai, Q. Ma, S. Iqbal, *et al.* “Multitasking shared aperture enabled with multiband digital coding metasurface,” Adv. Opt. Mater, 6(21): 1800657, 2018.

[26] L.H. Gao, Q. Cheng, J. Yang, *et al.* “Broadband diffusion of terahertz waves by multi-bit coding metasurfaces,” Light Sci. Appl., 4(9): e324, 2015.

[27] D. Liang, J. Gu, J. Han, *et al.* “Robust large dimension terahertz cloaking,” Adv. Mater., 24(7): 916-921, 2012.

[28] F. Zhou, Y. Bao, W. Cao, *et al.* “Hiding a realistic object using a broadband terahertz invisibility cloak”. Sci. Rep, 1: 78, 2011.

- [29] T. Niu, W. Withayachumnankul, *et al.* “Terahertz reflectarray as a polarizing beam splitter”, *Opt. Exp*, 22(13): 16148-16160, 2014.
- [30] X. Shang, M. Ke, Y. Wang, and M. J. Lancaster, “WR-3 band waveguides and filters fabricated using SU8 photoresist micromachining technology,” *IEEE Trans. THz Sci. Technol.*, vol. 2, no. 6, pp. 629–637, Nov. 2012.
- [31] B. Zhang, Y.X. Guo, H. Zirath, *et al.* “Investigation on 3-D-printing technologies for millimeter-wave and terahertz applications,” *Proc. IEEE*, 105(4): 723-736, 2017.
- [32] S. Qu, H. Yi, C. Chan, and K. Ng, “Low-cost discrete dielectric terahertz lens antenna using 3D printing,” in *Proc. IEEE Conf. Antennas Meas. Appl.*, Antibes Juan-les-Pins, France, Nov., pp. 1–3, 2014.
- [33] J. Suszek, A. Siemion, M. S. Bieda, *et al.* “3-D-printed flat optics for THz linear scanners,” *IEEE Trans. THz Sci. Technol.*, 5(2): 314-316, 2015.
- [34] H. Xin, M. Liang “3-D-printed microwave and THz devices using polymer jetting techniques,” *Proc. IEEE*, 105(4): 737-755, 2017.
- [35] A.I. Hernandez-Serrano, E. Castro-Camus, “Quasi-Wollaston-prism for terahertz frequencies fabricated by 3D printing,” *Journal of Infrared, Millimeter, and Terahertz Waves*, 38(5): 567-573, 2017.
- [36] R. Mendis, M. Nagai, W. Zhang, *et al.* “Artificial dielectric polarizing-beamsplitter and isolator for the terahertz region,” *Sci. Rep*, 7(1): 5909, 2017.
- [37] A.I. Hernandez-Serrano, E. Castro-Camus, D. Lopez-Mago, “q-plate for the generation of terahertz cylindrical vector beams fabricated by 3D printing,” *Journal of Infrared, Millimeter, and Terahertz Waves*, 38(8): 938-944, 2017.
- [38] Gospodaric J, Kuzmenko A, Pimenov A, *et al.* “3D-printed phase waveplates for THz beam shaping,” *Appl. Phys. Lett*, 112(22): 221104, 2018.
- [39] T. S. Rappaport *et al.*, “Millimeter wave mobile communications for 5G cellular: It will work!,” *IEEE Access*, vol. 1, pp. 335-349, 2013.
- [40] Nasimuddin, X. Qing and Z. N. Chen, “Compact circularly polarized symmetric-slit microstrip antennas,” *IEEE Antennas and Propagation Magazine*, vol. 53, no. 4, pp. 63-75, Aug. 2011.
- [41] S. Gao, Q. Luo, and F. Zhu, *Circularly Polarized Antennas*. Hoboken, NJ, USA: Wiley, Nov. 2013.
- [42] C. Ding and K. Luk, “A Wideband High-Gain Circularly-Polarized Antenna Using Artificial Anisotropic Polarizer,” *IEEE Trans. Antennas Propag.* vol. 67, no. 10, pp. 6645-6649, Oct. 2019.

- [43] K. X. Wang and H. Wong, "A wideband millimeter-wave circularly polarized antenna with 3-D printed polarizer," *IEEE Trans. Antennas Propag.*, vol. 65, no. 3, pp. 1038-1046, March 2017.
- [44] K. X. Wang and H. Wong, "Design of a wideband circularly polarized millimeter-wave antenna with an extended hemispherical lens," *IEEE Trans. Antennas Propag.*, vol. 66, no. 8, pp. 4303-4308, Aug. 2018.
- [45] G. Wu, Y. S. Zeng, K. F. Chan, S. Qu and C. H. Chan, "High-gain circularly polarized lens antenna for terahertz applications," *IEEE Antennas Wireless Propag. Lett.* Early access.
- [46] K. Zhang, D. Li, K. Chang, *et al.* *Electromagnetic theory for microwaves and optoelectronics*[M]. Berlin: Springer, 1998.
- [47] P. Nayeri, F. Yang, and A.Z. Elsherbeni. *Reflectarray antennas: theory, designs, and applications*. John Wiley & Sons, 2018.
- [48] C. C. Montarou, T.K. Gaylord, "Analysis and design of modified Wollaston prisms," *Applied optics*, 38(31): 6604-6616, 1999.
- [49] Z. Li, *et al.* "Graphene plasmonic metasurfaces to steer infrared light". *Sci. Rep.* 5, 12423; doi: 10.1038/srep12423, 2015.
- [50] M. F. Farooqui and A. Shamim, "3-D inkjet-printed helical antenna with integrated lens," *IEEE Antennas Wireless Propag. Lett.*, vol. 16, no. 8, pp. 800–803, Aug. 2016.
- [51] L. Xue and V. Fusco, "Polarisation insensitive planar dielectric slab waveguide extended hemi-elliptical lens," *IET Microw., Antennas Propag.*, vol. 2, no. 4, pp. 312–315, Jun. 2008.
- [52] Z. Shi, S. Yang, S.-W. Qu, and Y. Chen, "Circularly polarised planar Luneberg lens antenna for mm-Wave wireless communication," *Electron. Lett.*, vol. 52, no. 15, pp. 1281–1282, 2016.
- [53] X. Wu, G.V. Eleftheriades, T.E. van Deventer-Perkins. "Design and characterization of single-and multiple-beam mm-wave circularly polarized substrate lens antennas for wireless communications," *IEEE Transactions on Micro. Theory. Tech.*, 49(3): 431-441, 2001.
- [54] M. A. Campo, D. Blanco, G. Carluccio, O. Litschke, S. Bruni and N. Llombart. "Circularly polarized lens antenna for Tbps wireless communications," 2018 48th European Microwave Conference (EuMC). IEEE, 2018: 1147-1150.
- [55] L. Di Palma, A. Clemente, L. Dussopt, R. Sauleau, P. Potier and P. Pouliguen,

- “Circularly Polarized Transmitarray With Sequential Rotation in Ka-Band,” IEEE Trans. Antennas Propag, vol. 63, no. 11, pp. 5118-5124, Nov. 2015.
- [56] J. Yu, L. Chen, X. Shi, “A multilayer dipole-type element for circularly polarized transmitarray applications,” IEEE Antennas Wireless Propag. Lett, 15: 1877-1880, 2016.
- [57] C. Tian, Y. Jiao and G. Zhao, “Circularly polarized transmitarray antenna using low-profile dual-linearly-polarized elements,” IEEE Antennas Wireless Propag. Lett, vol. 16, pp. 465-468, 2017.
- [58] H. F. Ma, G. Z. Wang, W. X. Jiang, and T. J. Cui, “Independent control of differently-polarized waves using anisotropic gradient-index metamaterials,” Sci. Rep., vol. 4, p. 6337, 2014.
- [59] W. Luo, S. Xiao, Q. He, S. Sun, L. Zhou, “Photonic spin hall effect with nearly 100% efficiency,” Adv. Opt. Mater. 3, 1102– 1108, 2015.
- [60] C. Liu *et al.* “Fully controllable pancharatnam-berry metasurface array with high conversion efficiency and broad bandwidth. Sci. Rep. 6, 34819; doi: 10.1038/srep34819 2016.
- [61] B. Wang, F. Dong, H. Feng, *et al.* “Rochon-Prism-like planar circularly polarized beam splitters based on dielectric metasurfaces,”. ACS Photon.5, 1660–1664 , 2017.
- [62] Y. Yuan, K. Zhang, X. M. Ding, B. Ratni, S. N. Burokur, Q. Wu, “Complementary transmissive ultra-thin meta-deflectors for broadband polarization-independent refractions in the microwave region”, Photon. Res., vol. 7, no. 1, pp. 80-88, 2019.
- [63] W.S. Lee, *et al.* “Metasurface Beam Splitter: Broadband Terahertz Circular - Polarization Beam splitter” Adv. Opt. Mater, 6, 1700852, 2018.
- [64] H.X Xu, G. Hu, L. Han, *et al.* Chirality-Assisted High-Efficiency Metasurfaces with Independent Control of Phase, Amplitude, and Polarization. Adv. Opt. Mater, 7(4): 1801479, 2019.
- [65] Xu H X, Ma S, Ling X, *et al.* Deterministic approach to achieve broadband polarization-independent diffusive scatterings based on metasurfaces. ACS Photo., , 5(5): 1691-1702, 2017
- [66] S.O. Kasap, R.K. Sinha, *Optoelectronics and photonics: principles and practices*. New Jersey: Prentice Hall, 2001.
- [67] B. Max, and E. Wolf. *Principles of optics: electromagnetic theory of propagation, interference and diffraction of light*. Elsevier, 2013.

- [68] A.B. Numan, J. F. Frigon, J.J. Laurin “Printed w-band multibeam antenna with luneburg lens-based beamforming network.” *IEEE Trans. Antennas Propag.*, 66(10): 5614-5619, 2018.
- [69] S. Gao, *et al.*, “All-dielectric metasurfaces for simultaneously realizing polarization rotation and wavefront shaping of visible light.” *Nanoscale* 11.9: 4083-4090, 2019
- [70] D. K. Hale, “The physical properties of composite materials”, *Journal of materials science*, 11(11): 2105-2141, 1976.
- [71] S. Veronneau-Troutman, “Fresnel prisms and their effects on visual acuity and binocularity,” *Trans. Amer. Ophthalmolog. Soc.*, vol. 76, pp. 610–653, 1978.
- [72] V. A. Soifer, V. Kotlar, and L. Doskolovich. *Iterative Methods for Diffractive Optical Elements Computation*. Boca Raton, FL, USA: CRC Press, 1997.
- [73] A. Balanis, *Antenna theory: analysis and design*. John wiley & sons, 2016.
- [74] T. Smith, U. Gothelf, O. S. Kim, and O. Breinbjerg, “Design, manufacturing, and testing of a 20/30-GHz dual-band circularly polarized reflectarray antenna,” *IEEE Antennas Wireless Propag. Lett.*, vol. 12, pp. 1480–1483, Nov. 2013.
- [75] R. Deng, F. Yang, S. Xu and M. Li, “An FSS-Backed 20/30-GHz dual-band circularly polarized reflectarray with suppressed mutual coupling and enhanced performance,” *IEEE Trans. Antennas Propag.*, vol. 65, no. 2, pp. 926-931, Feb. 2017.
- [76] T. Smith, U. Gothelf, O. S. Kim, and O. Breinbjerg, “An FSS backed 20/30 GHz circularly polarized reflectarray for a shared aperture L- and Ka-band satellite communication antenna,” *IEEE Trans. Antennas Propag.*, vol. 62, no. 2, pp. 661–668, Feb. 2014.
- [77] R. Deng, Y. Mao, S. Xu and F. Yang, “A single-layer dual-band circularly polarized reflectarray with high aperture efficiency,” *IEEE Trans. Antennas Propag.*, vol. 63, no. 7, pp. 3317-3320, July 2015.
- [78] J. M. Baracco, P. Ratajczak, P. Brachat, and G. Toso, “A dual frequency Ka-band printed Fresnel reflector for ground terminal applications,” *IEEE Trans. Antennas Propag.*, vol. 63, no. 10, pp. 4352–4366, Oct. 2015.
- [79] R. Deng, S. Xu, F. Yang and M. Li, “Single-layer dual-band reflectarray antennas with wide frequency ratios and high aperture efficiencies using phoenix elements,” *IEEE Trans. Antennas Propag.*, vol. 65, no. 2, pp. 612-622, Feb. 2017.
- [80] R. Ako, A. Upadhyay, W. Withayachumnankul, *et al.* “Dielectrics for terahertz metasurfaces: material selection and fabrication techniques. *Advanced Optical*

Materials, 2020.

- [81] P. Nayeri *et al.*, “3D printed dielectric reflectarrays: low-Cost high-gain antennas at sub-millimeter waves,” IEEE Trans. Antennas Propag., vol. 62, no. 4, pp. 2000-2008, April 2014.
- [82] Y. He, Z. Gao, D. Jia, W. Zhang, B. Du and Z. N. Chen, “ Dielectric metamaterial-based impedance-matched elements for broadband reflectarray,” IEEE Trans. Antennas Propag., vol. 65, no. 12, pp. 7019-7028, Dec. 2017.
- [83] M. K. T. Al-Nuaimi, Y. He and W. Hong, “Design of inhomogeneous all-dielectric electromagnetic-wave diffusive reflectarray metasurface,” IEEE Antennas Wireless Propag. Lett., vol. 18, no. 4, pp. 732-736, April 2019.
- [84] M. D. Wu *et al.*, “Design and measurement of a 220 GHz wideband 3-D printed dielectric reflectarray,” IEEE Antennas Wireless Propag. Lett., vol. 17, no. 11, pp. 2094-2098, Nov. 2018.
- [85] F. Ahmadi, K. Forooraghi, Z. Atlasbaf and B. Virdee, “Dual linear-polarized dielectric resonator reflectarray antenna,” IEEE Antennas Wireless Propag. Lett., vol. 12, pp. 635-638, 2013.
- [86] S. Zhang, “Three-dimensional printed millimetre wave dielectric resonator reflectarray,” IET Microw. Antennas Propag., vol. 11, no. 14, pp. 2005-2009.
- [87] P. Nayeri *et al.*, “High gain dielectric reflectarray antennas for THz applications,” 2013 IEEE Antennas and Propagation Society International Symposium (APSURSI), Orlando, FL, 2013, pp. 1124-1125, doi: 10.1109/APS.2013.6711222.
- [88] Y. Sun and K. W. Leung, “Millimeter-wave substrate-based dielectric reflectarray,” IEEE Antennas Wireless Propag. Lett., vol. 17, no. 12, pp. 2329-2333, Dec. 2018.
- [89] D. Headland, *et al.* “Dielectric resonator reflectarray as high-efficiency nonuniform terahertz metasurface”. ACS Photonics, 3(6): 1019-1026, 2016.
- [90] Z. Shi, *et al.* “Single-layer metasurface with controllable multiwavelength functions,” Nano letters, 18(4): 2420-2427, 2018.
- [91] W. Chen, *et al.* “A broadband achromatic polarization-insensitive metalens consisting of anisotropic nanostructures,” Nature communications, 10(1): 1-7, 2019.
- [92] S.-W. Qu, Q.-Y. Chen, M.-Y. Xia, and X. Y. Zhang, “Single-layer dual band reflectarray with single linear polarization,” IEEE Trans. Antennas Propag., vol. 62, no. 1, pp. 199–205, Jan. 2014.
- [93] M. G. N. Alsath, M. Kanagasabai and S. Arunkumar, “Dual-band dielectric

resonator reflectarray for C/X-bands,” IEEE Antennas Wireless Propag. Lett., vol. 11, pp. 1253-1256, 2012.

Chapter III High Gain LTCC Antenna-in-Package for 60-GHz Applications

3.1 Introduction

To better integrate the antenna into the transceiver, a simple and efficient solution is antenna-in-packages (AIPs) [1-3]. In fact, with the rise of mm-wave communication, AIPs have become a top research subject. For example, 60 GHz AIPs with aperture-coupled patch antennas and 16-element arrays are proposed in [4], which are realized in a multilayer organic package structure. An air cavity is used to improve the antenna bandwidth and efficiency. The peak gain can reach 8 dBi for the antenna and 17 dBi for the array. Zhang et al. demonstrated that the grid array antenna can achieve high gain, broad bandwidth with a simple feeding scheme [5]–[10], which is a good choice for fixed-beam array applications. Liao and Xue [11] developed a dual-polarized AIP aperture antenna with wide bandwidth and high isolation. The antenna can achieve 12 dBi gain with an aperture size of $12 \times 12 \times 1.128 \text{ mm}^3$. To achieve a higher effective isotropic radiated power (EIRP) for the transmitter and higher signal-to-noise ratio (SNR) for the receiver, researchers from Samsung implemented an AIP phased array consisting of 24 circular stacked antennas on LTCC for stationary 60 GHz communication [12]. The array features more than 9 GHz bandwidth, 45° beam-steering ranges, and more than 14.5 dBi gain at boresight. Later, IBM also demonstrated phase array AIP designs based on multilayer organic or LTCC technologies [13]. These interesting and exciting designs enrich the AIP antenna community and pave the way for future miniaturized and efficient mm-wave systems. A state-of-the-art array antenna technology developed for highly integrated mm-wave radios for short-range and multigigabit-per-second wireless communications can be found in [14]. On the other hand, the 60 GHz band has the lossy channel with the excess loss of up to approximately 15 dB/km due to oxygen absorption. Therefore, improving antenna gain is indispensable to compensate for the significant propagation loss caused by the oxygen absorption and also ensure that a sufficient margin exists to overcome other losses, such as rain-induced fading. High gain aperture antennas, such

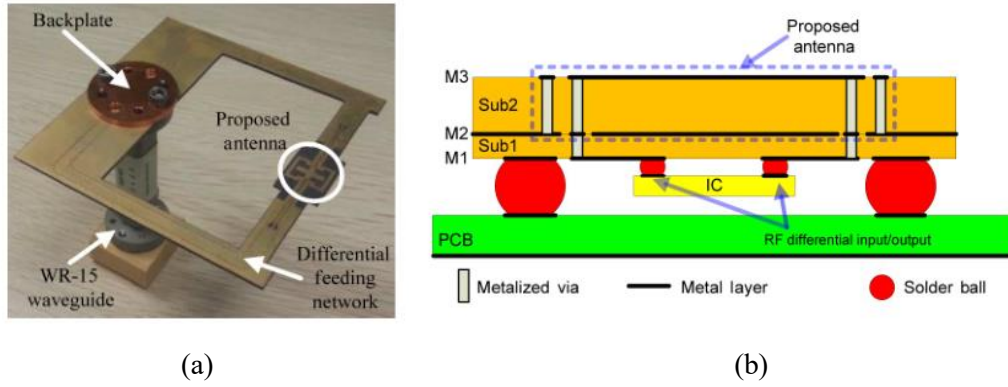


Fig. 3.1 (a) PAA ^[15]. (b) PAA integrated into the front-end of transceiver ^[15].

as horn and parabolic reflector antennas, are widely used for various mm-wave applications. However, the high profile and large size of conventional aperture antennas have hindered them more widespread consumer-level applications. Recently, differential-fed planar aperture antennas (PAAs) with high gain and wide bandwidth have been proposed [15], as shown in Fig. 3.1. By using differential feeding, the antenna has the advantages of wide impedance bandwidth, low cross-polarization, stable and symmetric radiation patterns. However, these antennas are difficult to extend to the array configurations. To overcome these problems, this section presents a new LTCC single-ended-fed planar antenna (SPAA) with wide bandwidth, high gain, and compact size.

3.2 Single-Ended-Fed High-Gain LTCC Planar Aperture Antenna for 60 GHz Antenna-in-Package Applications

The basic configuration of the proposed SPAA is shown in Fig. 3.2. In the design, there are 11 LTCC layers (defined as d_1 – d_{11}) and 12 metal layers (defined as m_1 – m_{12}). Ferro A6M with a relative permittivity of 5.9 and the loss tangent of 0.002 is used as the dielectric material. The thickness of each layer is 0.094 mm. Generally, the proposed SPAA consists of three parts: a metalized open cavity as the antenna aperture, the balanced-fed patch as the aperture feeding, and the SIW-to-signal-probe transition. The open cavity occupies six-layers (d_1 – d_6) with metalized vias as sidewalls and the ground (m_7) as its bottom. The height of the cavity is 0.566 mm, which roughly corresponds to a quarter of the dielectric wavelength at 60 GHz. The

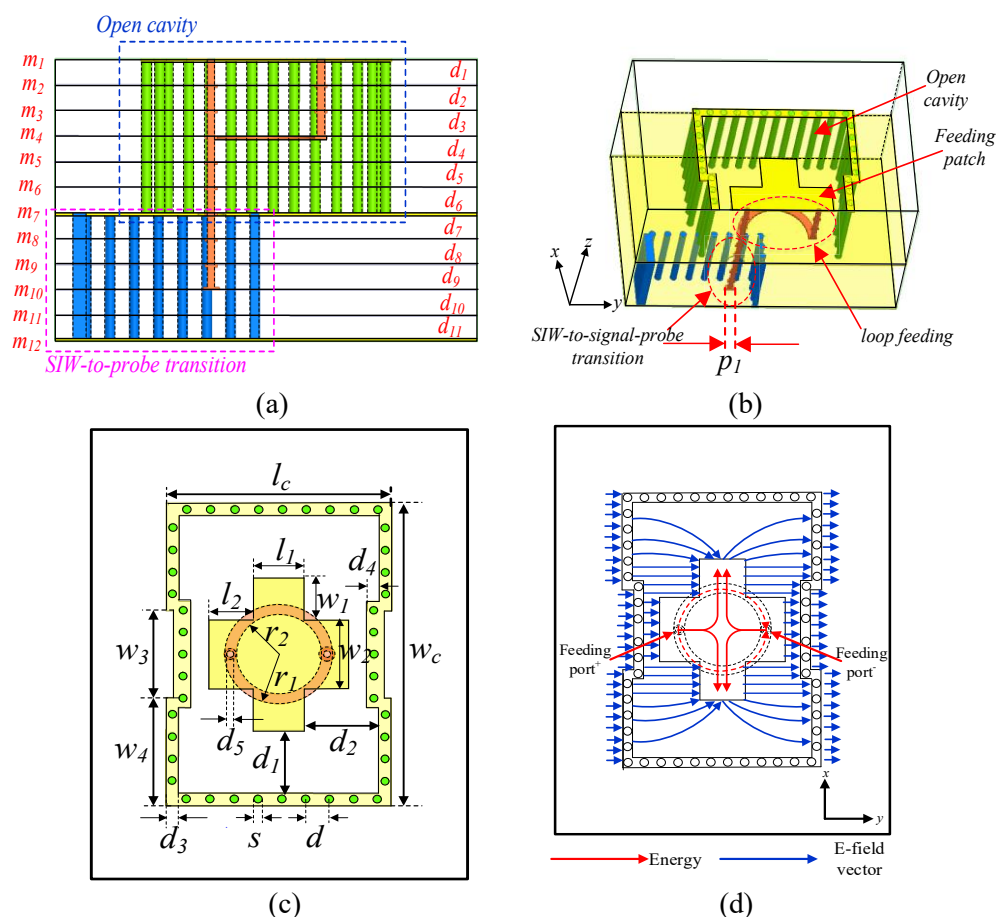


Fig. 3.2. (a) Side view. (b) 3-D view (only positive side of the xz -plane is shown here due to the symmetry). (c) Top view. (d) Working principle demonstration (top view).

diameter of the cavity via is adopted as 0.15 mm, and the distance between the adjacent vias is 0.45 mm. To excite the patch with a balanced signal, a loop-shaped balun structure beneath the patch is carefully designed and optimized, as shown in Figs. 3.2 (b) and (c). Based on this feeding scheme, the signal from the SIW-to-signal-probe transition is divided into two. One directly feeds the patch through the vertical signal via while the other goes through the loop with a 180° phase delay to feed the patch. To achieve the 180° phase delay, the length of the loop should satisfy the equation:

$$\pi(\frac{r_1+r_2}{2})=(n+\frac{1}{2})\lambda_g \quad (3-1)$$

where r_1 and r_2 are the outer and inner radii of the loop, respectively, λ_g is the dielectric wavelength, and n is an integer and equal to 1 in the design. On the other hand, the top patch should be excited with equal power from the two

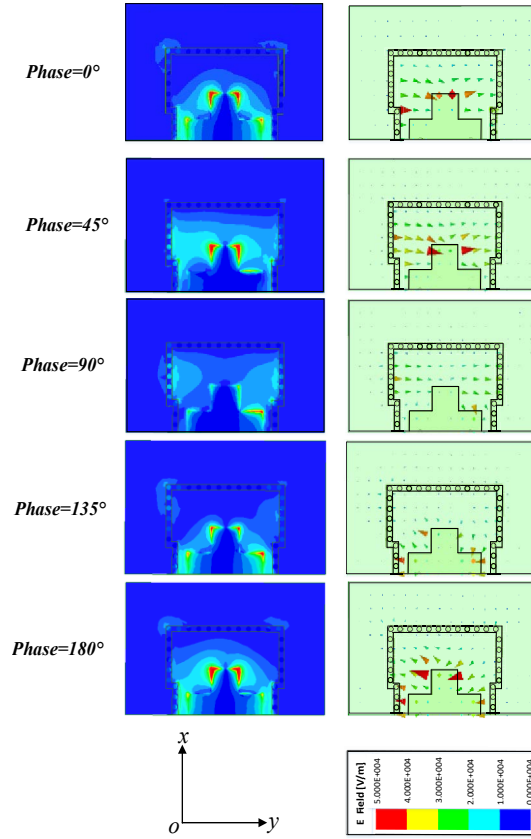


Fig. 3.3. Simulated E-field distribution on the surface of the proposed SPAA at 60 GHz for different phases. Because of the symmetrical boundary, only half of the overall structure is shown here.

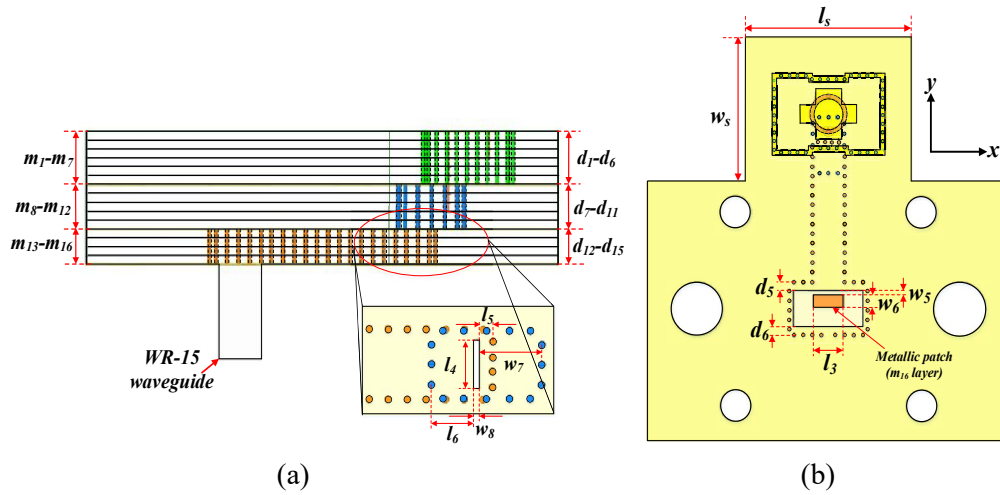


Fig. 3.4 (a) Top view of the SPAA antenna element. (b) Side view of the proposed SPAA element.

ports so that the E-fields are equally distributed on the two sides of the aperture. Therefore, the width of the loop, i.e., r_1-r_2 , is carefully optimized to obtain equal power division and thus the main beam of the antenna can be fixed on its boresight

without tilting. As another crucial part, the SIW-to-signal-probe transition is designed and also carefully optimized, as shown in Fig. 3.2 (b). Since the signal via with a diameter of 0.15 mm penetrates multiple layers (d_1 – d_9), pads with a diameter of 0.25 mm are adopted to ensure that the vias of the signal probe on each layer are fully connected. To achieve good matching of this transition, the bottom pad of the signal probe is enlarged to 0.3 mm so that it can introduce some perturbations in capacitance to cancel out the inductance introduced by the long probe [16]. The operating principle of the SPAA is illustrated in Fig. 3.2 (d). By taking advantage of the loop-shaped balun, the energy can propagate on the patch, splitting into two parts along $\pm y$ -directions in the form of a traveling wave. By careful optimization of the patch size, a very uniform E-field distribution can be realized on the aperture, leading to high aperture efficiency and, thus the gain. Note that the dielectric margins outside the edges of the cavity also contribute to the antenna radiation, which helps to increase the antenna's actual radiating aperture and the gain. A more intuitive understanding can be achieved by observing the E-field distributions on the surface of the proposed SPAA at different phases, as shown in Fig. 3.3. Because of the symmetrical boundary, only half of the overall structure is shown here. A uniform and symmetrical E-field distribution at the antenna aperture can be roughly observed at the left side of Fig. 3.3. The strengths of the E-fields are generally equal at the two sides of the patch. The right-side field in Fig. 3.3 that the surface vectors of the E-field distributions along the $+y$ -direction are gradually weakened and then change to the other direction when the phase is escalated from 0° to 180° , indicating good linear polarization. The symmetric E-field distributions along the y -direction also demonstrated that the loop-shaped balun works very well.

The top and side views of the overall structure of the proposed SPAA element are shown in Fig. 3.4, respectively. The width of the SIW line is adapted to 1.7 mm so that only the dominant mode can propagate. The energy in the lower SIW line (d_{12} – d_{15}) is coupled to the upper SIW line (d_7 – d_{11}) through the slot, as shown in Fig. 3.4 (a). The SPAA element is directly fed by a WR-15 waveguide. To obtain good impedance matching between the SIW and the waveguide a rectangular patch is printed between

the WR-15 and the SIW on the m_{16} layer as the impedance transformer, as shown in Fig.3.4 (b). The prototype was simulated and optimized in ANSYS HFSS. Because of the symmetry, the perfect magnetic conductor symmetrical boundary on the yz plane is set in simulation to save simulation time and improve accuracy. The goal of optimization was maximization of the broadside gain, simultaneously maintaining wide impedance and gain bandwidths. The optimized geometrical parameters of the prototype are shown in Table 3.1.

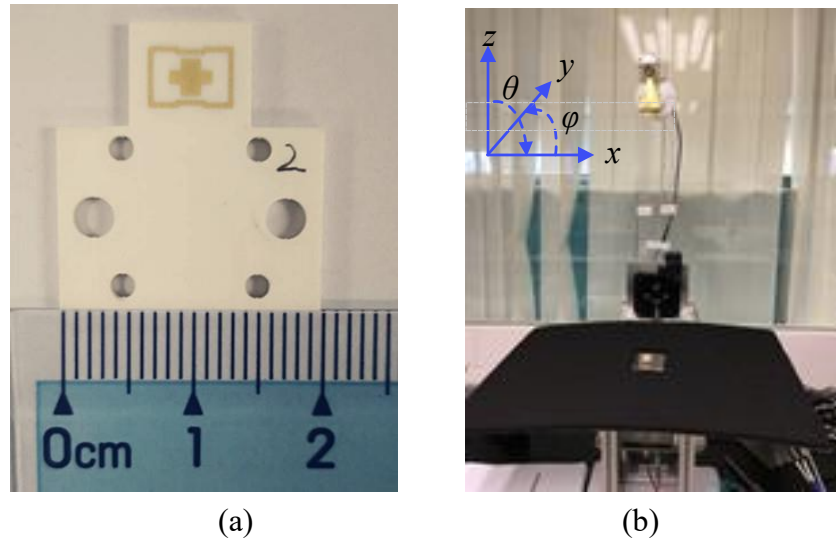


Fig. 3.5. (a) Prototype of the SPAA element. (b) Antenna under test.

An antenna prototype is fabricated and measured to demonstrate the idea, as shown in Fig. 3.5(a). The antenna radiation performance is measured by using an in-house far-field mm-wave antenna measurement system, as shown in Fig. 3.5(b). Due to system limitation, only radiation patterns of the upper sphere [the polar angle $\theta \in (-90^\circ, 90^\circ)$] are measured and given in Fig. 3.6. As the figure shows, the measured radiation patterns agree well with the simulated ones. The radiation patterns are stable over the operating frequency band with a front-to-back ratio of 20 dB and cross-polarization below -20 dB. The S-parameters and boresight gains of the SPAA element are given in Fig. 3.7. The simulated -10 dB impedance bandwidth is from 56.7 to 65 GHz while the measured one shows slight deterioration. The measured -8 dB impedance bandwidth is from 56.4 to 65 GHz. The maximum gain which can be

achieve is 11.5 dBi at 62 GHz. The aperture efficiency (ε_{ap}) of the antenna can be calculated as follows [17]:

$$\varepsilon_{ap} = \frac{G\lambda^2}{4\pi A_p} \quad (3-2)$$

where G and A_p are the gain and the aperture size of the antenna, respectively. λ is the free-space wavelength. If we regard the cavity size as the antenna physical radiating area, the calculated aperture efficiency at 62 GHz is as high as 107.5%. This is clearly not true and indicates that the margins of the substrate also contribute to the antenna gain. If we consider the ground size $l_s \times w_s$ as the physical aperture, then the calculated aperture efficiency drops to 50%. Since the actual physical aperture of the proposed antenna is hard to pinpoint, we can only speculate that the actual aperture efficiency of the proposed antenna is no less than 50%.

TABLE 3.1 DIMENSIONS OF THE SPAA ANTENNA AND ARRAY

Parameters	l_s	l_c	l_1	l_2	l_3	l_4	l_5	l_6
value(mm)	7.5	6.17	0.95	0.83	1.61	1.2	0.34	1.08
Parameters	l_7	l_8	w_s	w_c	w_f	w_1	w_2	w_3
value(mm)	1.18	1.26	7.5	4.24	1.75	0.85	1.4	1.77
Parameters	w_4	w_5	w_6	w_7	w_8	w_9	w_{10}	w_{11}
value(mm)	2.2	0.23	0.63	1.63	0.15	0.184	0.61	0.49
Parameters	w_{12}	dx	dy	d_1	d_2	d_3	d_4	d_5
value (mm)	0.43	5.9	5	1.27	1.4	0.24	0.23	0.45
Parameters	d_6	d_7	d_8	d_9	d_{10}	d	s	r_1
value (mm)	0.42	0.66	0.47	0.84	0.81	0.15	0.45	1.01
Parameters	r_2	P_1						
value (mm)	0.81	0.3						

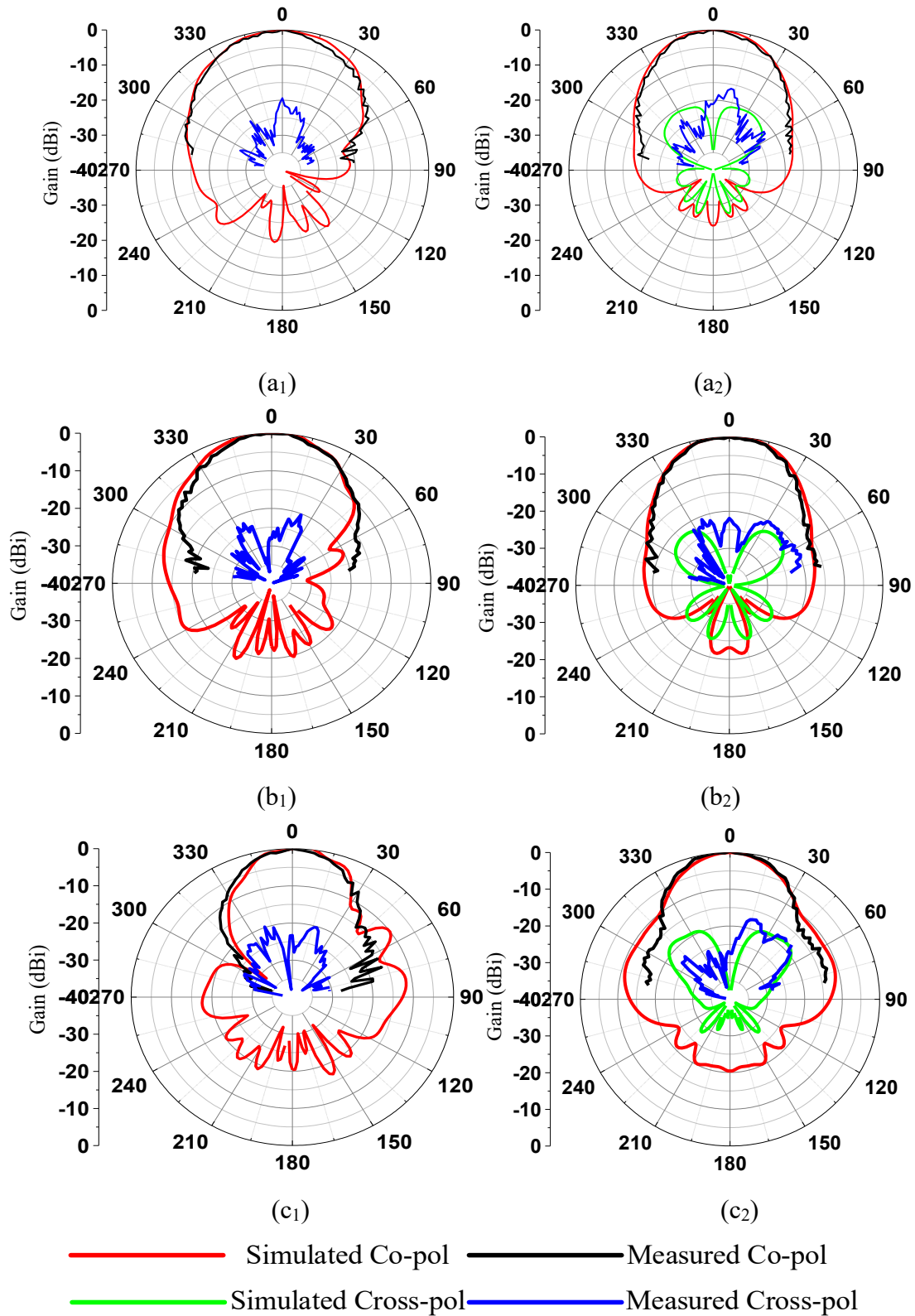


Fig. 3.6. Simulated and measured radiation patterns of the SPAA element. (a₁) yoz plane at 58 GHz. (a₂) xoz plane at 58 GHz. (b₁) yoz plane at 60 GHz. (b₂) xoz plane at 60 GHz. (c₁) yoz plane at 63 GHz. (c₂) xoz plane at 63 GHz.

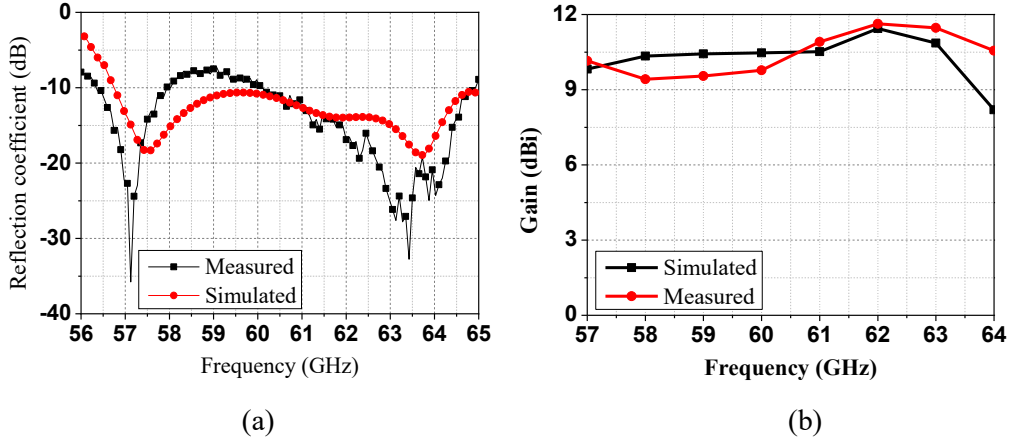


Fig. 3.7. Simulated and measured return loss of the SPAA element. Simulated and measured SPAA boresight gains.

Based on the proposed SPAA element, a 4×4 array antenna with an SIW feeding network is designed and demonstrated. The side view of the array is shown in Fig. 3.8. Basically, the array consists of three regions, namely, the 16 SPAA elements in the upper layers 1–6 (Region I), the 2×4 feeding cavities with SIW-to-probe transitions in the middle layers 7–11 (Region II), and the 1-to-8 SIW-based power divider in layers 12–15 with the WR-15 waveguide (Region III). The configuration of the Region I is shown in Fig. 3-9 (a). The patch feeding and the top metal of the cavity are printed on the upper part of the m_1 layer. The cavity vias are penetrated from d_1 to d_6 , and the metallic ground is located on the m_7 layer. The parameters of the elements are kept the same as those in Section II. The distances are 5.9 and 5 mm between the adjacent SPAA element in the $+x$ and $+y$ directions. As Fig. 3.9 (b) shows, the Region II consists of five layers, including the 2×4 2-element subarrays with feeding cavities and SIW-to-probe transition. The bottom pad of the probe is located at m_{10} layer, and the vias of the cavity are positioned from d_7 to d_{11} . The feeding cavities are excited by coupling slots (dashed line in Fig. 3.9 (b)) etched on the m_{12} layer. The 1-to-8 power divider, which is used to couple the energy to the subarrays through the slots, occupies the lower four layers (Region III), as shown in Fig. 3.9 (c). The array is directly fed by the WR-15 waveguide. To obtain good impedance matching between the SIW and the waveguide, a rectangular patch is printed between the WR-15 and the SIW in the m_{16} layer as the impedance transformer. The detailed dimensions of the array are shown in Table 3.1.

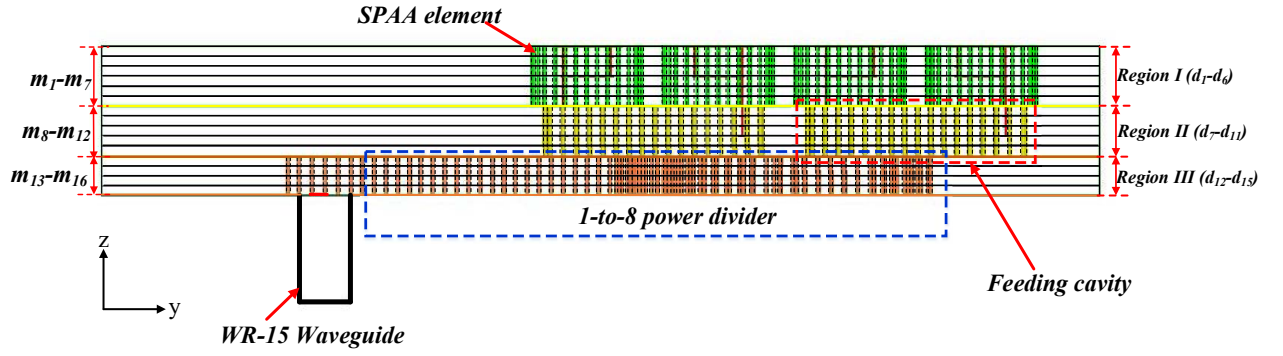


Fig. 3.8. Side view of the SPAA array.

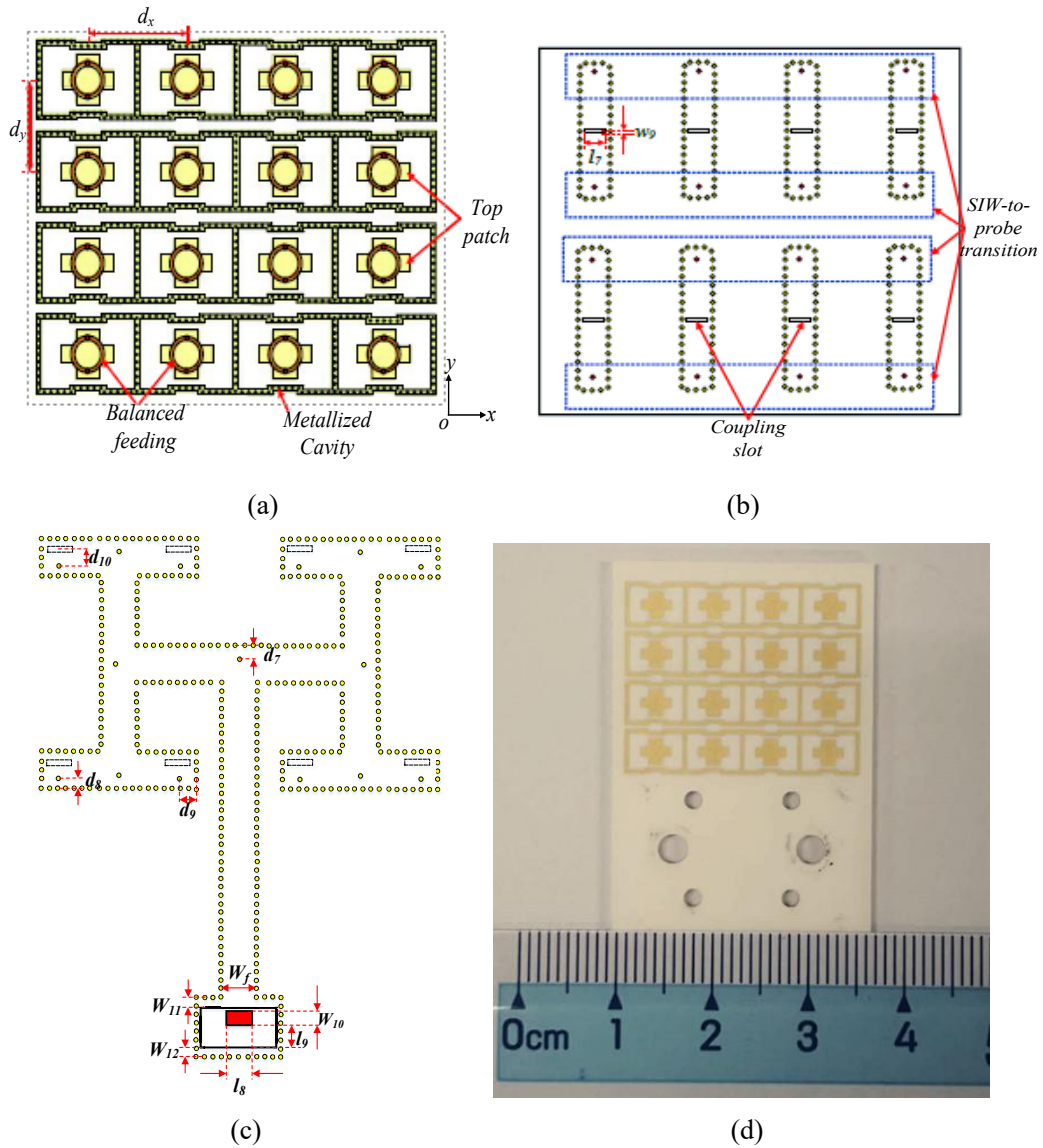


Fig. 3.9. (a) Top view of Region I. (b) Top view of Region I. (c) Top view of Region I. (d) Array prototype.

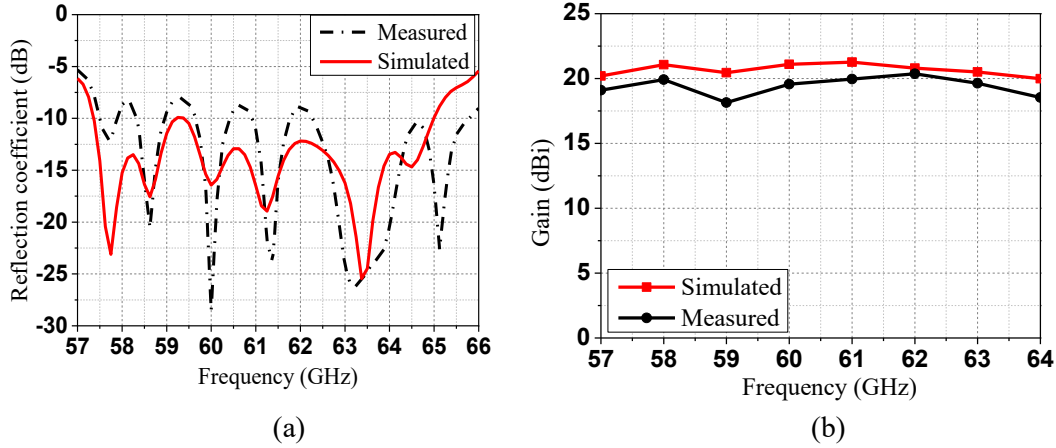


Fig. 3.10. (a) Simulated and measured return loss of the SPAA array. (b) Simulated and measured gains of the array.

The array prototype is fabricated and measured to verify the idea, as shown in Fig. 9 (d). The simulated and measured return losses are shown in Fig. 3.10 (a). The simulated -10 dB impedance bandwidth is from 57.4 to 65.1 GHz, and the measured -8 dB impedance bandwidth is from 57.5 to 65.7 GHz. The simulated and measured radiation patterns at 58, 60, and 63 GHz are depicted in Fig. 3.11, respectively. The radiation patterns are stable over the operating frequency band. Due to the loop shaped balun feeding, the patterns are generally symmetrical with the main beam fixed at the boresight. The measured cross polarizations are all below -30 dB, and the simulated ones are less than -60 dB, and they are not shown in Fig. 3.11. The simulated and measured gains at boresight are shown in Fig. 3.10 (b). The simulated gains are escalated from 19.98 to 21.3 dBi, and measured gains are escalated from 18.2 to 20.4 dBi. The discrepancies between the simulated and measured results can possibly be attributed to fabrication tolerance and other uncertainties, such as the relative permittivity and the thickness of the substrate variation, the metalized losses, and surface roughness.

In summary, a new SPAA and array have been proposed and demonstrated. Using loop-shaped balun feeding, the energy propagates on the patch in a traveling wave and illuminates the aperture with uniform E-field distributions. Therefore, the antenna and array can achieve wide bandwidth, high gain, and a low profile with a relatively simple structure. Prototypes have been designed and fabricated using the LTCC process to verify the idea. Nevertheless, differential feeding antennas generally

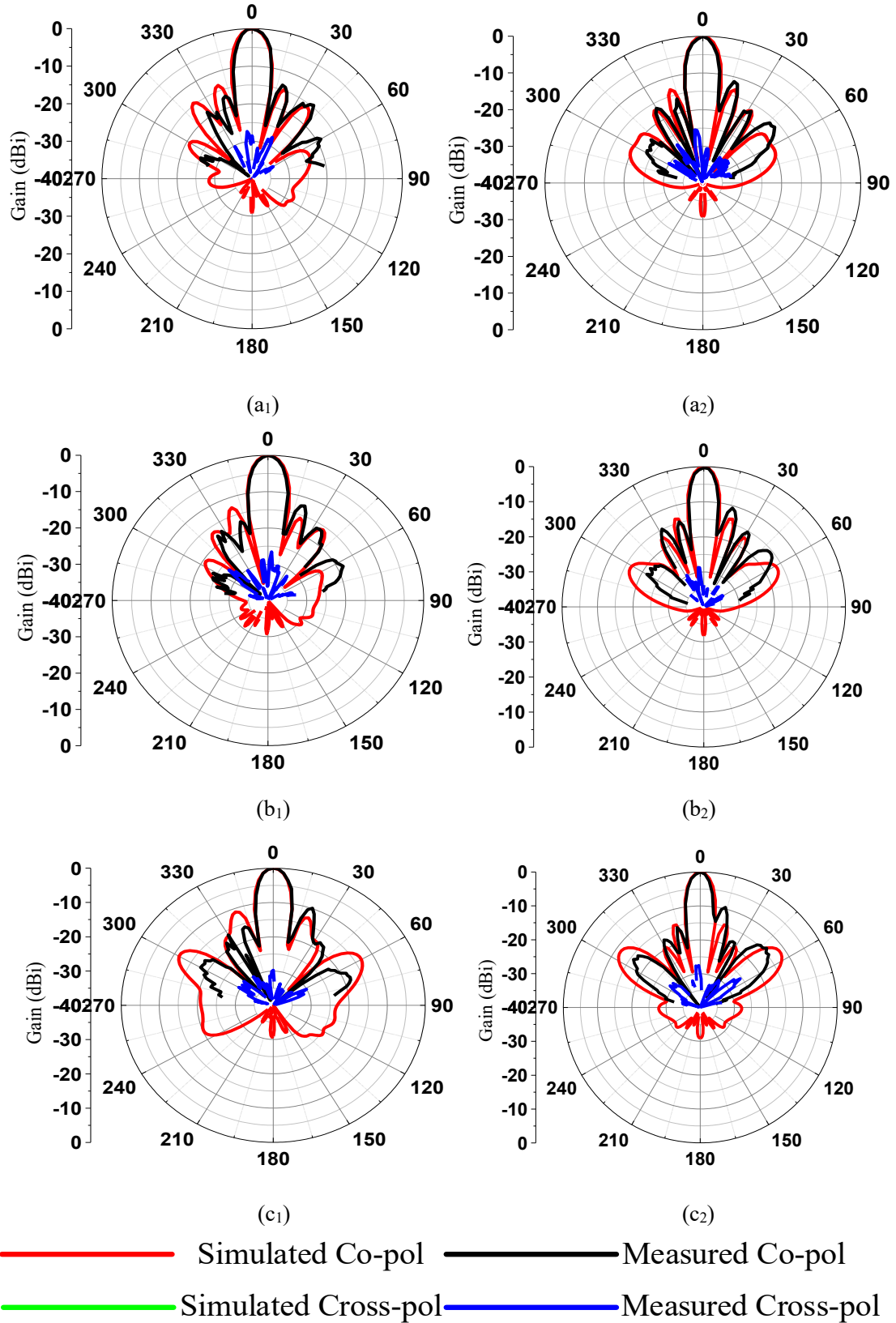


Fig. 3. 11. Simulated and measured array radiation patterns. (a₁) yoz plane at 58 GHz. (a₂) xoz plane at 58 GHz. (b₁) yoz plane at 60 GHz. (b₂) xoz plane at 60 GHz. (c₁) yoz plane at 63 GHz. (c₂) xoz plane at 63 GHz

require a differential feeding network, which may increase the design complexity and increase the loss. Therefore, in the next section, we present a low-profile wideband and high-gain patch antenna array using shorting via connecting the upper patch and ground to achieve the function of a virtual ac ground plane of differential feeding. This enables the antenna element to achieve good radiation performances, including stable gain (variation less than 1 dB) and a symmetrical beam with low cross-polarization over the entire frequency band. The performances of the antenna element are comparable to those of the differential-driven patch antenna while the complex differential feeding network is not required.

3.3 Low-Profile Wideband and High-Gain LTCC Patch Antenna Array for 60 GHz Applications

The basic configuration of the proposed LTCC 60 GHz patch antenna is shown in Fig. 3.12. Ferro A6M with a relative permittivity of 5.9 and a loss tangent of 0.002 is used as the dielectric material. The thicknesses of each tape layer and metal layer are 0.096 and 0.01 mm, respectively. To suppress the surface wave propagating along the substrate, the proposed patch antenna is enclosed by a square cavity of ground via holes. The size of the cavity is adopted as $2.5 \text{ mm} \times 2.5 \text{ mm}$ and the ground of the cavity is located at m_5 layer. The ground via holes penetrated from the d_1 to d_4 layers. The diameter of the ground via hole is 0.15 mm and via hole pitch is set at 0.45 mm. The signal probe penetrates from d_2 to d_8 with a diameter of 0.1 mm. The metal pad with a diameter of 0.2 mm is adopted to ensure that the signal probe via holes in each layer are fully connected. In the design, the bottom pad of the signal probe at the m_9 layer is enlarged to 0.3 mm so that the increased capacitance can cancel out the inductance of the long signal probe to obtain good matching. As the antenna occupies only the upper four tape layers with a height of 0.384 mm, a coupled feeding mechanism is adopted here to broaden the impedance of the antenna. As shown in Fig. 3.12, two rectangular patches, denoted as a coupled patch and a driven patch, are designed, and printed on the m_1 and m_2 layers, respectively. The driven patch is

directly connected to and fed by the signal probe, while the coupled patch is excited by the driven patch, a distance of 0.096mm away. The capacitance, introduced by the driven patch incorporated with the coupled patch, suppresses some of the inductance generated by the signal probe and the driven patch, which acts as a series-resonant element with a resonant frequency close to that of the patch. Therefore, the bandwidth of the antenna is significantly broadened.

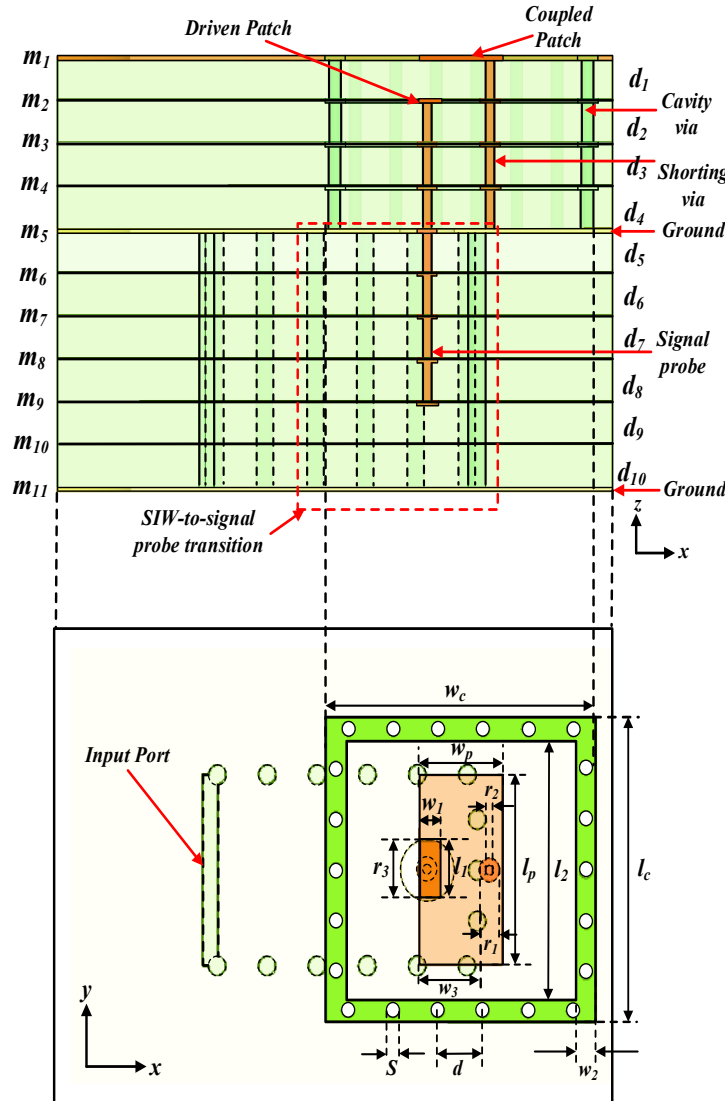


Fig. 3.12. Side view and top view of the antenna element.

Fig. 3.13 shows the return loss of the antenna with and without the coupled feeding scheme, and it is seen that the -10 dB impedance bandwidth is from only 60 to 64 GHz for direct feeding. For the antenna with coupled feeding, the -10 dB impedance bandwidth covers from 57 to >70 GHz. Basically, the bandwidth of the

antenna is determined by the antenna height, the relative permittivity of the substrate, and the feeding mechanism. The thickness of the feeding layer has a limited effect on the antenna bandwidth. However, if we decrease the thickness of the feeding network or the thickness of the SIW, we need to reoptimize the matching between the SIW and the vertical feeding probe. A low SIW thickness means a low characteristic impedance for SIW, which is hard to match within a wide bandwidth.

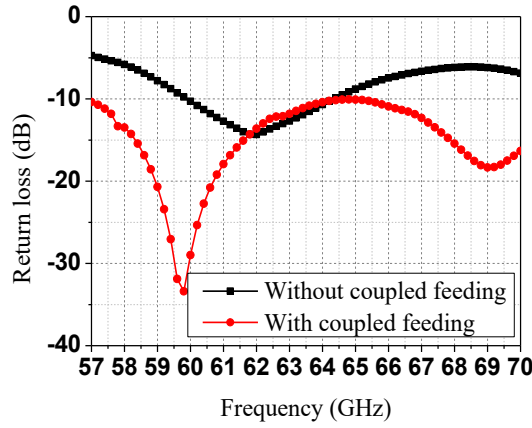


Fig. 3.13. Return loss of the antenna element with and without coupled feeding.

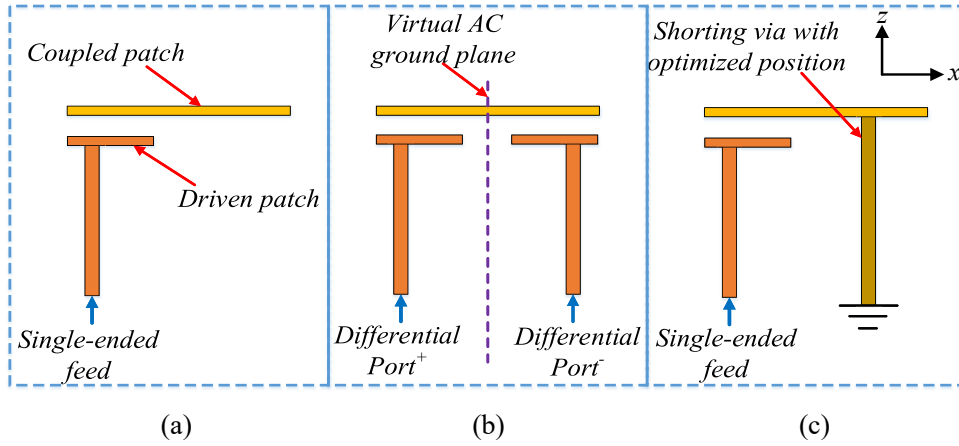


Fig. 3.14. Schematic comparison of (a) single-ended feed, (b) differential feed, and (c) single-ended feed with shorting via.

The shorting via that connects the top patch and the ground is used to simultaneously improve the radiation patterns and stabilize the gain of the antenna within a wide frequency band. Fig. 3.14 depicts the schematic comparison of the single-ended feed antenna, differential feed antenna, and the single-ended feed antenna with shorting via.

For the differential feeding, the virtual ac ground plane is located between the two feeds in the middle of the patch because the currents on the two feeds possess the same magnitude and contra phase [18]. However, for the single-ended feed patch antenna with the shorting via, the magnitudes of the currents in the feed and in the shorting via are not equal. Therefore, the position of the shorting via along ox -direction is carefully optimized to guarantee that a quasi-virtual ac ground plane exists in the middle of the patch, and thus ensures the good radiation performances of the antenna.

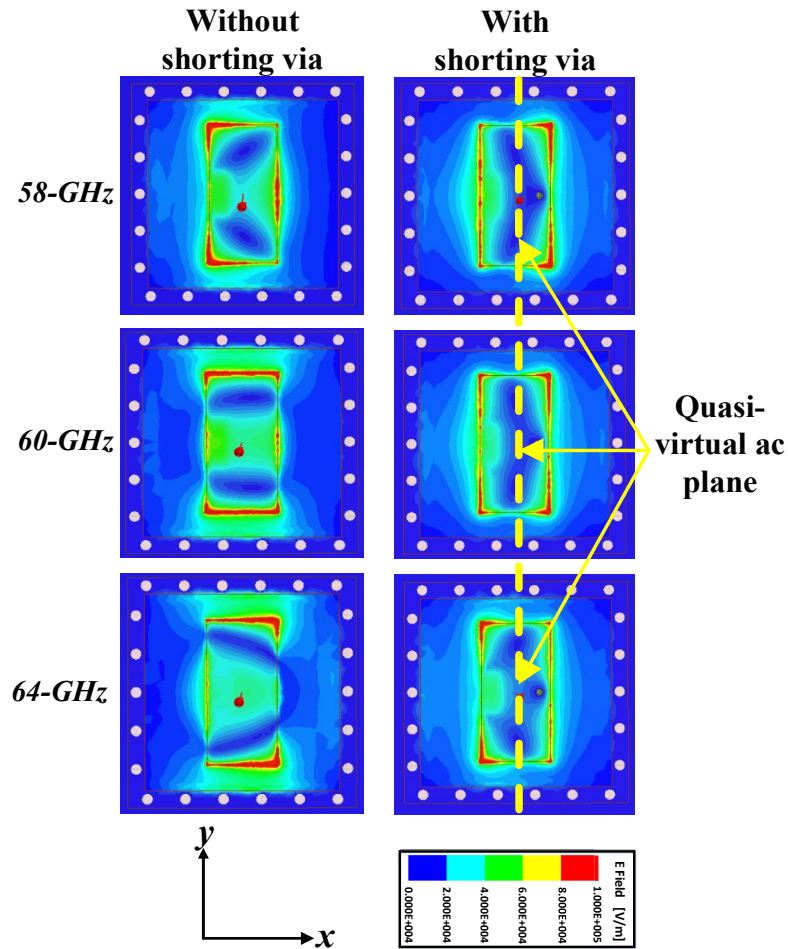


Fig. 3.15. Surface E-field distributions at the antenna aperture with and without shorting via at 58, 60, and 64 GHz.

To better reveal the function of the shorting via, the surface E-field distributions at the antenna aperture with and without shorting via are shown in Fig. 3.15. IN the scenario that the shoring via is not applied to the antenna, it is observed that the E-

fields are not uniformly distributed at the aperture. Moreover, the E-fields are concentrated at the edges of the short sides of the top patch, especially at high frequencies (60 and 64 GHz); this gives rise to the increase of antenna cross-polarization. For the antenna with shorting via, the uniform E-fields distributions on the two sides of the long edges of the patch can be roughly observed. Moreover, the shorting via induces the currents from the patch to the ground and forces the E-fields of the YOZ plane in the middle of the patch to near zero, as can be clearly observed on the right-hand side figure of Fig. 3.15. The existence of this plane demonstrates that the proposed shorting via achieves the functions of the virtual ac ground plane in the differential feeding to some extent. Therefore, the proposed design can achieve good radiation performances, comparable to that of those of differential feeding while the complex differential feeding network is not required for array design.

The radiation patterns of the antennas with and without shorting via are given in Fig. 3.16 for easy comparison. The antenna without shorting via shows a decrease in co-polarizations and an increase in the cross-polarizations when the frequency moves to the higher band. The antenna with shorting via shows stable radiation patterns with their main beam fixed at boresight and the cross-polarizations are kept at a low level. Fig. 3.17 depicts the antenna boresight gains with and without shorting via. The figure shows that the boresight gain is very stable from 57 to 64 GHz for the antenna with shorting via, while the boresight gain quickly drops for the antenna without shorting via. Compared with previous designs [19]–[21], the proposed antenna demonstrates superior performance: namely, the gains are much more stable with variation less than 1 dB and the cross-polarizations are better over the entire wide operating bandwidth. On the other hand, compared with the differential antennas, the design not only enjoys the merits of the differentially-fed antenna but also avoids the implementation of a differential feeding network, which is complicated for array configuration. As the proposed design is implemented by using more sophisticated multilayer fabrication technology than PCB fabrication, the simpler the structure, the fewer the uncertainties.

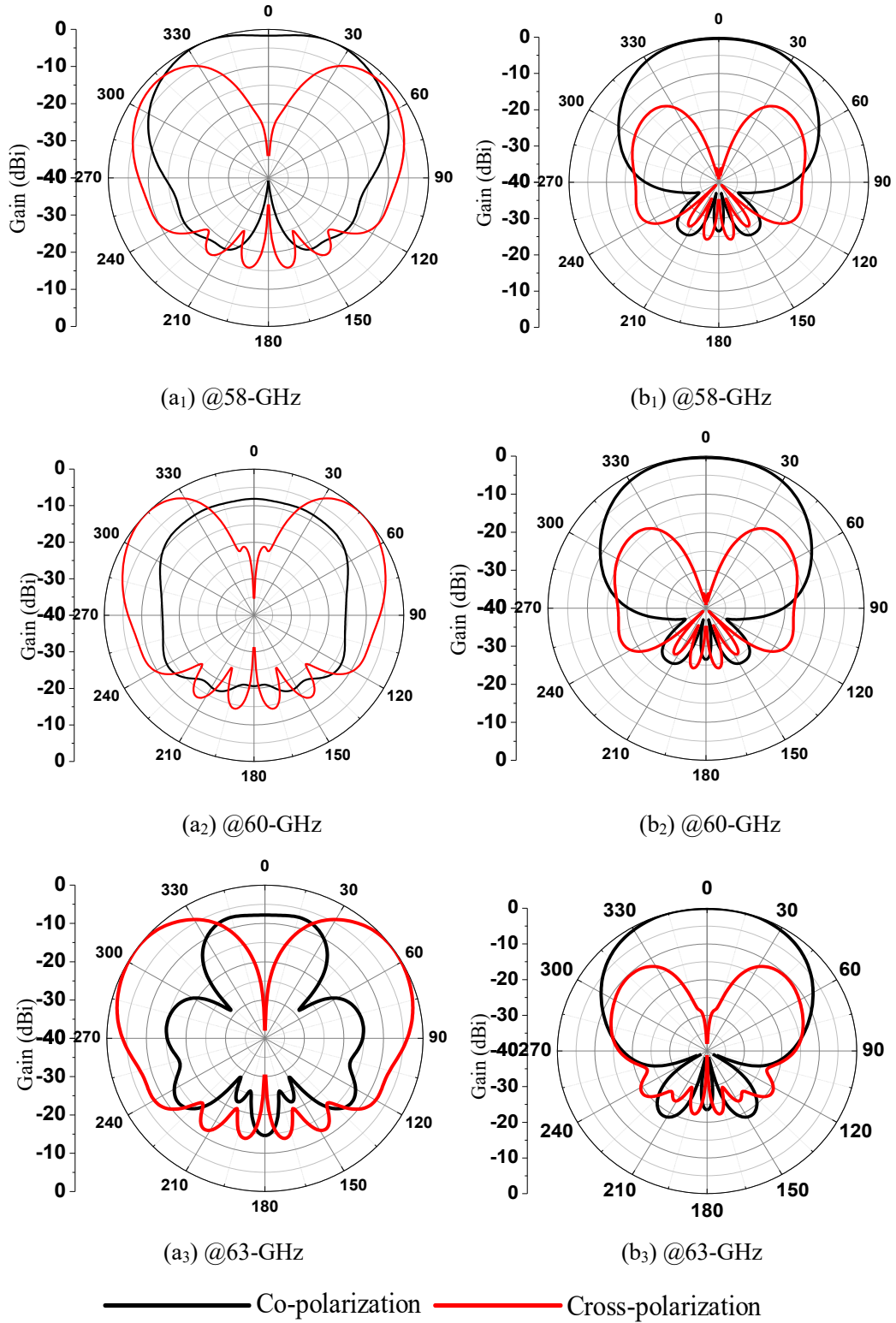


Fig. 3.16. Radiation patterns at YOZ plane with/without shorting via at 58, 60, and 63 GHz, respectively. (a₁) Without shorting via at 58 GHz. (a₂) With shorting via at 58 GHz. (b₁) Without shorting via at 60 GHz. (b₂) With shorting via at 60 GHz. (a₃) Without shorting via at 63 GHz. (b₃) With shorting via at 63 GHz.

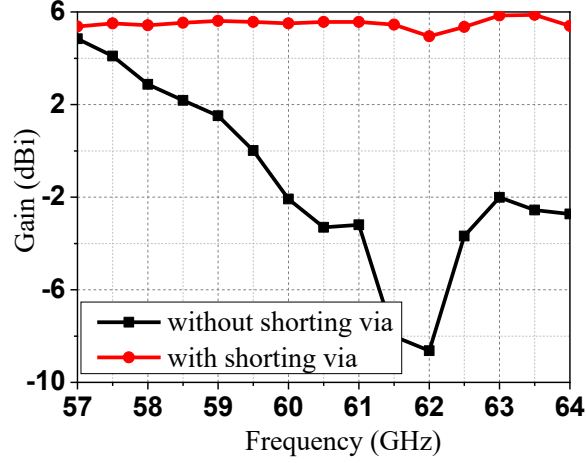


Fig. 3.17. Simulated antenna boresight gains with and without shorting via.

Based on the proposed antenna element, a 4×4 antenna array is designed and measured. Considering that the loss of the SIW is smaller than that of the microstrip line at 60 GHz, we adopted the SIW to realize the feeding network. The side view of the array is shown in Fig. 3.18. Basically, the array consists of three parts: a 16-element upper radiation part (Region I, layers 1–4), the 2×4 vertical coupled 1–2 power dividers in the middle (Region II, layers 5–10), and the lower 1–8 SIW-based power dividers with WR-15 waveguide input (Region III, layers 11–15).

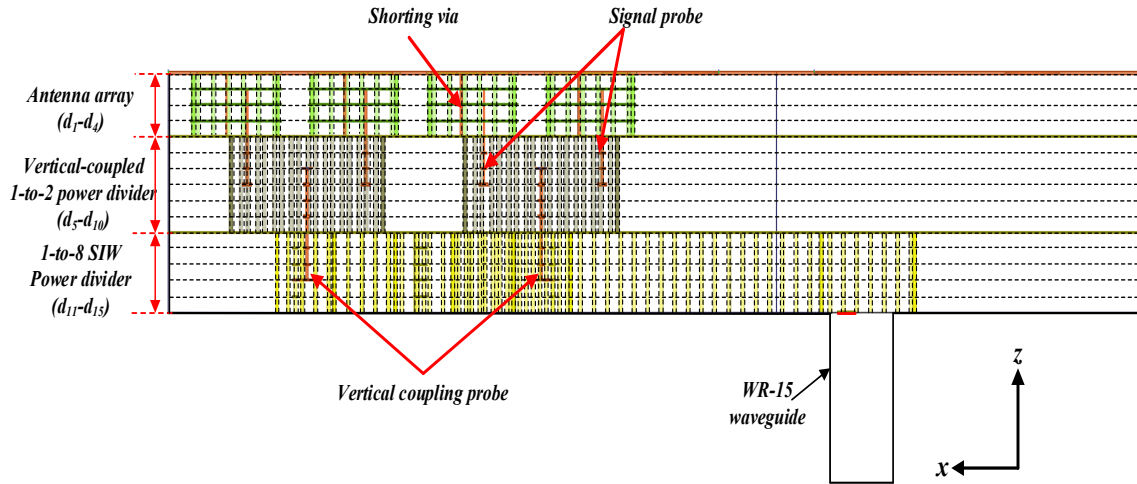
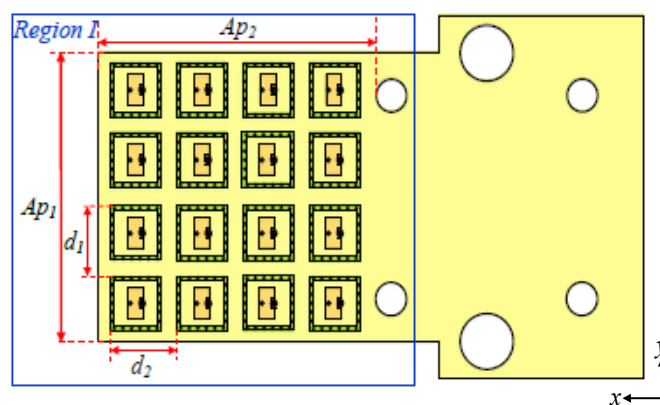
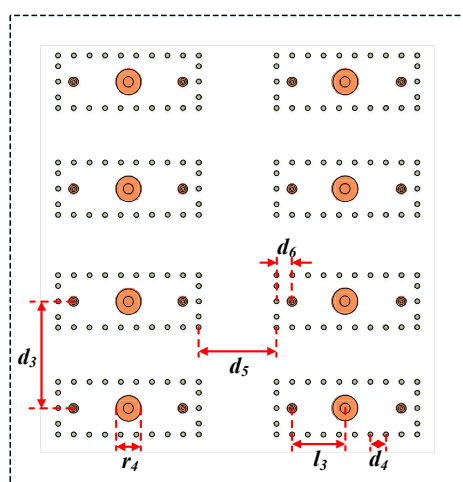


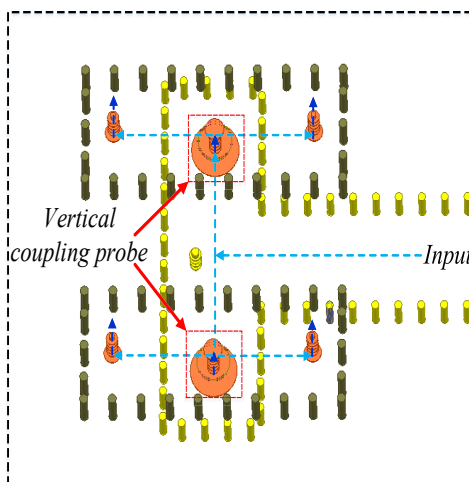
Fig. 3.18. Side view of the antenna array



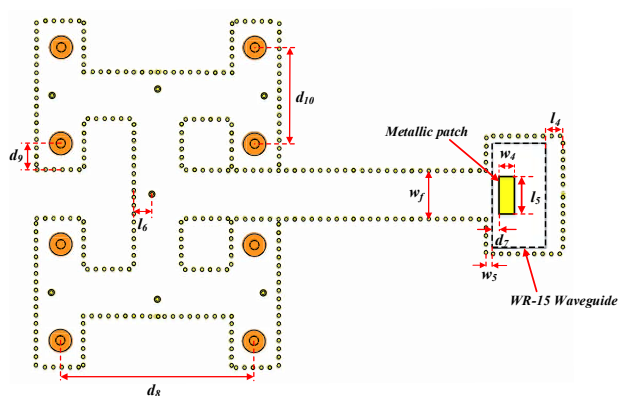
(a)



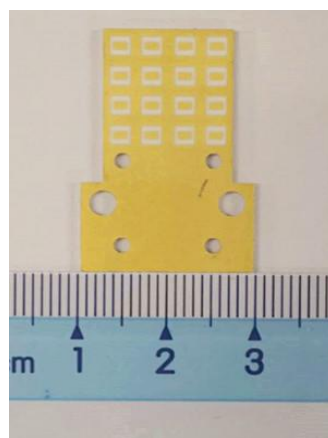
(b)



(c)



(d)



(e)

Fig. 3.19. (a) Top view of the array. (b) Top view of the 2 4 vertical coupled 1–2 power dividers (Region II). (c) 3-D view of the vertical coupled 1–2 power dividers. (d) Top view of the 1–8 power divider with the WR-15 feed. (e) Array prototype.

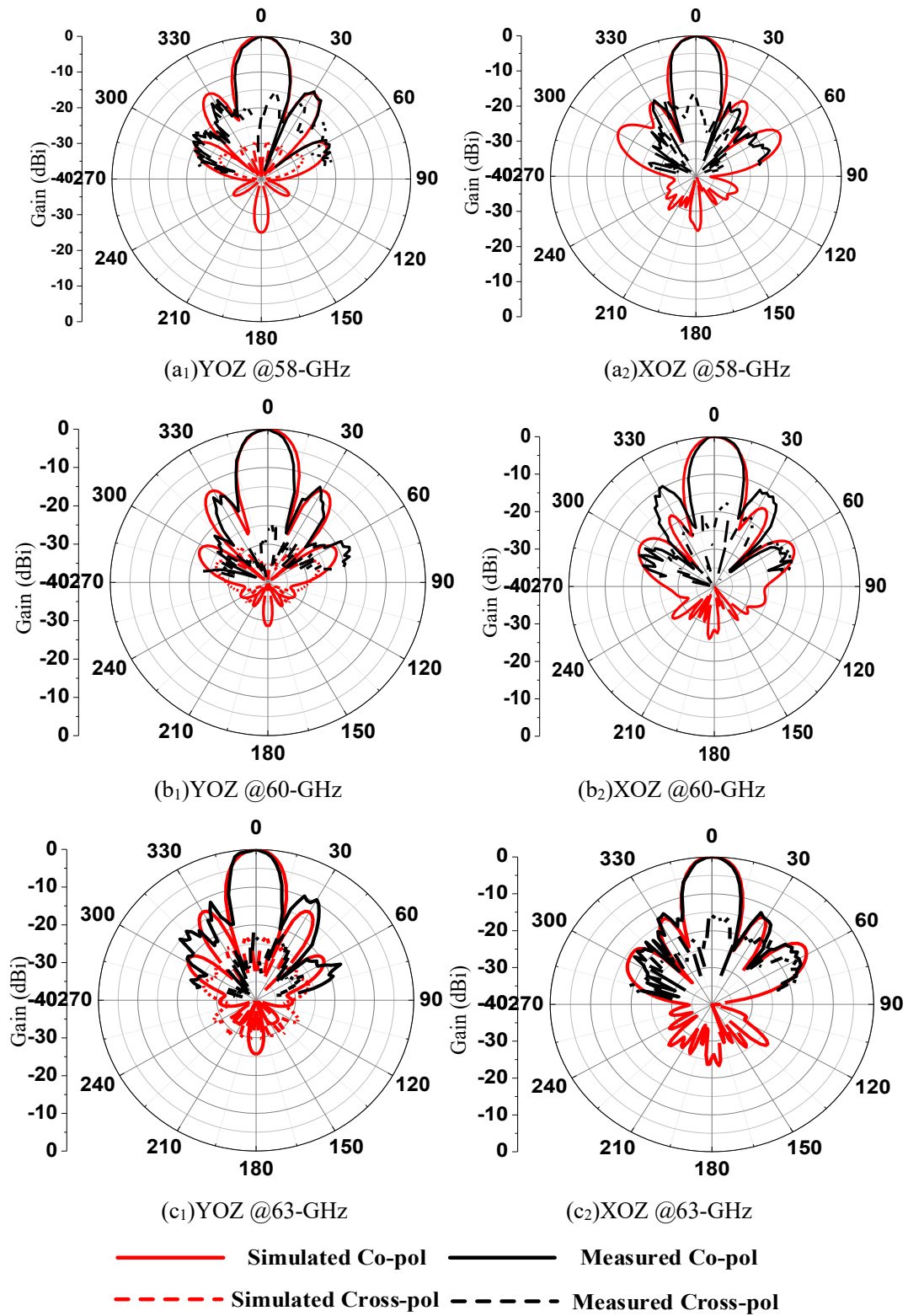


Fig. 3.20. Simulated and measured radiation patterns of the array. (a₁) YOZ plane at 58 GHz. (a₂) XOZ plane at 58 GHz. (b₁) YOZ plane at 60 GHz. (b₂) XOZ plane at 60 GHz. (c₁) YOZ plane at 63 GHz. (c₂) XOZ plane at 63 GHz.

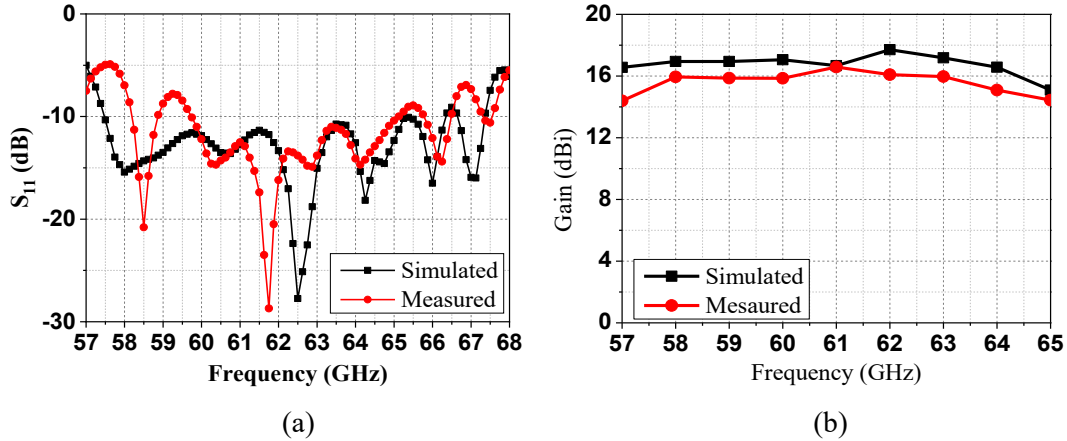


Fig. 3.21. (a) Simulated and measured S-parameters. (b) Simulated and measured gain.

The top view of the Region I is shown in Fig. 3.19. The distances between the adjacent elements are 3.5 mm along both x- and y-directions. The parameters of the elements are kept the same as those in previous section. The margins outside the cavity on the top surface of the antenna are covered with metal to suppress the surface wave. Each element is excited by the signal probe, the bottom of which is inserted into the lower SIW. The top view of the 2×4 vertical coupled 1–2 power dividers, which occupy the d_5 – d_{10} layers, is shown in Fig. 3.19 (a). The 3-D view of the SIW power dividers, together with the vertical coupling probe, is depicted in Fig. 3.19 (b). The vertical coupling probes, which penetrate from d_7 to d_{13} layers, are used to smoothly induce energy from the lower SIW to the upper SIW. To achieve good impedance matching, the two metallic pads at both ends of the vertical coupling probe are enlarged to increase the capacitance to compensate the inductance of the probes. The top view of the 1–8 SIW power divider with WR-15 waveguide feed (Region III) is shown in Fig. 3.19 (c). The 1–8 power divider occupies the lower five layers. The width of the SIW line is adopted to 1.7 mm so that only the dominant mode propagates. To obtain good matching between the WR-15 waveguide and the SIW, a rectangular patch with a length of 1.34 (l_5) mm and a width of 0.57 mm (w_4) is printed in the m_{16} layer, as shown in Fig. 3.19 (d). The detailed dimensions of the array are shown in Table 3.2.

The array prototype is fabricated and measured to verify the idea, as shown in Fig. 3.19(e). The radiation performance of the array is measured, as shown in Fig. 3.20. As the figure indicates, the measured radiation patterns are consistent with the simulated

ones. The radiation patterns are stable over the operating frequency band, with the front-to-back ratio being better than 25 dB. The simulated cross-polarizations are below -20 dB and the measured ones are below -15 dB. The S_{11} of the array are shown in Fig. 3.21 (a), measured using Anritsu Vector Network Analyzer MS4646B. The simulated -10 dB impedance bandwidth is from 57.5 to 66.2 GHz. The measured results show some deterioration below 60 GHz, and the -8 dB impedance bandwidth is from 58.1 to 66.4 GHz. The simulated and measured boresight gains of the array are depicted in Fig. 3.21 (b). The maximum gain is 17.8 dBi for simulation and 16.7 dBi for measurement. The discrepancy between the simulated and measured results mainly derive from two factors. On the one hand, in the antenna fabrication, the surface roughness of the metallic layer is greater than that in the simulation and the LTCC substrate might shrink slightly. In addition, there are some fabrication deviations, which cannot be accurately predicted in the simulation. On the other hand, there are small misalignments between the AUT/transmit horn (calibration) and the receiving antenna during the measurement, in addition to some possible influences from the measurement system, such as adapters and cables.

TABLE 3.2 DIMENSIONS OF THE ARRAY

Parmeter	l_c	l_p	l_1	l_2	l_3	l_4	l_5	l_6
value (mm)	2.7	1.68	0.5	2.3	1.76	0.63	1.34	0.55
Parmeter	w_c	w_p	w_1	w_2	w_3	w_4	w_5	d
value (mm)	2.7	0.83	0.217	0.2	0.62	0.57	0.24	0.45
Parmeter	d_1	d_2	d_3	d_4	d_5	d_6	d_7	d_8
value (mm)	3.5	3.5	3.47	0.5	2.44	0.49	0.24	6.94
Parmeter	d_9	r_1	r_2	r_3	r_4	s	w_f	Ap_1
value (mm)	0.95	0.1	0.3	0.58	0.816	0.15	1.7	14.4
Parmeter	Ap_2							
value (mm)	13.5							

3.4 Conclusion

In summary, this section has reported the development of an LTCC antenna-in-package for 60-GHz applications. In Section 3.2, we proposed a single-ended-fed planar aperture antenna, which inherits the merits of the differential-fed antenna with low cross-polarization and high aperture efficiency. Because the aperture is excited by

a travelling wave, the antenna exhibits wide impedance bandwidth. The antenna element is easily extended to an array to achieve high gain. In Section 3.3, we proposed a kind of patch antenna with coupled feeding and shorting pin configuration. This antenna can achieve good radiation performance comparable to that of differential-fed antennas while a complicated feeding network is not required. Both designs can be used for 60-GHz communication applications. Ideally, the antenna array can be scaled to arbitrary frequencies. However, due to the fabrication tolerance of the LTCC. The array configuration can be potentially scaled up to 140 GHz.

3.5 References

- [1] Y. P. Zhang, "Integration of microstrip antenna on ceramic ball grid array package," *Electron. Lett.*, vol. 38, no. 1, pp. 14–16, 2002.
- [2] Y. P. Zhang, "Finite-difference time-domain analysis of an integrated circuit ceramic ball grid array package antenna for single-chip wireless transceivers," *IEEE Trans. Antennas Propag.*, vol. 52, pp. 435–442, Feb. 2004.
- [3] Y. P. Zhang, "Integrated ceramic ball grid array package antenna," *IEEE Trans. Antennas Propag.*, vol. 52, pp. 2538–2544, 2004.
- [4] S. B. Yeap, Z. N. Chen, and X. Qing, "Gain-enhanced 60-GHz LTCC antenna array with open air cavities," *IEEE Trans. Antennas Propag.*, vol. 59, no. 9, pp. 3470–3473, Sep. 2011.
- [5] Zhang Y P, Sun M, Chua K M, *et al.* Antenna-in-package in LTCC for 60-GHz radio[C]//2007 International workshop on Antenna Technology: Small and Smart Antennas Metamaterials and Applications. IEEE: 279-282, 2007.
- [6] Y. P. Zhang, M. Sun, D. Liu, and Y. Lu, "Dual grid array antennas in a thin-profile package for flip-chip interconnection to highly integrated 60-GHz radios," *IEEE Trans. Antennas Propag.*, vol. 59, no. 4, pp. 1191–1199, Apr. 2011.
- [7] M. Sun, Y. P. Zhang, D. Liu, K. M. Chua, and L. L. Wai, "A ball grid array package with a microstrip grid array antenna for a singlechip 60-GHz receiver," *IEEE Trans. Antennas Propag.*, vol. 59, no. 6, pp. 2134–2140, Jun. 2011.
- [8] B. Zhang and Y. P. Zhang, "Grid array antennas with subarrays and multiple feeds for 60-GHz radios," *IEEE Trans. Antennas Propag.*, vol. 60, no. 5, pp. 2270–2275, May 2012.
- [9] Y. P. Zhang, "Integration of microstrip antenna on cavity-down ceramic ball grid array package." *Electronics Letters*, 38(22): 1307-1308, 2002.

- [10] J. J. Wang, Y. P. Zhang,, K.M. Chua, *et al.* “Circuit model of microstrip patch antenna on ceramic land grid array package for antenna-chip codesign of highly integrated RF transceivers.” IEEE Trans. Antennas Propag., 53(12): 3877-3883, 2005.
- [11] S. Liao and Q. Xue, “Dual polarized planar aperture antenna on LTCC for 60-GHz antenna-in-package applications,” IEEE Trans. Antennas Propag., vol. 65, no. 1, pp. 63–70, Jan. 2017.
- [12] D. G. Kam, D. Liu, A. Natarajan, S. Reynolds, H. C. Chen, and B. Floyd, “LTCC packages with embedded phased-array antennas for 60 GHz communications,” IEEE Microw. Wireless Compon. Lett., vol. 21, no. 3, pp. 142–144, Mar. 2011.
- [13] J. Grzyb, D. Liu, U. Pfeiffer, and B. Gaucher, “Wideband cavity-backed folded dipole superstrate antenna for 60 GHz applications,” in Proc. IEEE AP-S Int. Symp., Jul. pp. 3939–3942, 2006.
- [14] A. E. I. Lamminen, J. Saily, and A. R. Vimpri, “60-GHz patch antennas and arrays on LTCC with embedded-cavity substrates,” IEEE Transactions on Antennas and Propagation, vol. 56, no. 9, pp. 2865-2874, Sept. 2008.
- [15] S. Liao, P. Wu, K. M. Shum, and Q. Xue, “Differentially fed planar aperture antenna with high gain and wide bandwidth for millimeter-wave application,” IEEE Trans. Antennas Propag., vol. 63, no. 3, pp. 966–977, Mar. 2015.
- [16] W. C. Yang, H. Wang, W. Q. Che, Y. Huang, and J. Wang, “Highgain and low-loss millimeter-wave LTCC antenna array using artificial magnetic conductor structure,” IEEE Trans. Antennas Propag., vol. 63, no. 1, pp. 390–395, Jan. 2015.
- [17] W. L. Stutzman and G. A. Thiele, Antenna Theory and Design. 3rd ed. Hoboken, NJ, USA: Wiley, 2012.
- [18] Y. P. Zhang and J. J. Wang, “Theory and analysis of differentially-driven microstrip antennas,” IEEE Trans. Antennas Propag., vol. 54, no. 4, pp. 1092–1099, Apr. 2006.
- [19] K.-S. Chin, W. Jiang, W. Che, C.-C. Chang, and H. Jin, “Wideband LTCC 60-GHz antenna array with a dual-resonant slot and patch structure,” IEEE Trans. Antennas Propag., vol. 62, no. 1, pp. 174–182, Jan. 2014.
- [20] H. Chu, Y.-X. Guo, and Z. Wang, “60-GHz LTCC wideband vertical off-center dipole antenna and arrays,” IEEE Trans. Antennas Propag., vol. 61, no. 1, pp. 153–161, Jan. 2013.
- [21] D. Wang, K. B. Ng, C. H. Chan, and H. Wong, “A novel wideband differentially-fed higher-order mode millimeter-wave patch antenna,” IEEE Trans. Antennas

Propag., vol. 63, no. 2, pp. 466–473, Feb. 2015.

Chapter IV Dual-Band Mm-Wave Polarization Manipulation and Beam-shaping Devices

4.1 Introduction

The main focus of previous sections has been single-band beam shaping devices. However, most scenarios of communication require dual-band or multi-band channels. For example, in satellite communication, antennas are required to operate at two distinct frequency bands for two-way communication via the satellite with forward links (hub uplink and consumer downlink) and return links (consumer uplink and hub downlink). Moreover, for the mm-wave channel communication, due to the high path loss, shadowing, and blockages [1-3], mm-wave signals suffer from severe propagation attenuation and vulnerability to obstacles. Since they can only propagate only a few miles and do not generally penetrate solid materials, mm-wave links are highly intermittent [4]. This is a real challenge for mobile applications as a mobile user may frequently experience blockages caused by buildings, vehicles, humans, or urban furniture. Consequently, it is difficult to guarantee reliable communication in the mm-wave frequency range. To overcome the high path loss and blockage problems, one straightforward approach is the dense deployment of mm-wave infrastructure to increase line-of-sight (LOS) reliability. A more practical and reasonable way is to tightly integrate an mm-wave network with an existing sub-6 GHz network [5-7]. Unlike the mm-wave signals, signals in the sub-6 GHz spectrum can travel many miles and easily penetrate solid obstacles. Therefore, the sub-6 GHz band can be used for the provision of relatively reliable communications and consistent user experience, while the mm-wave band provides high-capacity enhancement. In this regard, dual-band and multi-band beam-shaping devices are highly desirable for future communication applications. Therefore, this section mainly focuses on an investigation of dual-band beam-shaping devices. Section 4.2 introduces a dual-band high gain antenna by folding a reflectarray into the Fabry-Perot cavity. Section 4.3 explores a large frequency-ratio, high aperture reuse

efficiency, dual-band antenna for mm-wave, and sub-6 GHz communication applications.

4.2 Folding Reflectarray Into Fabry-Perot Cavity Makes Dual-Band Dual Polarized High Gain Antenna

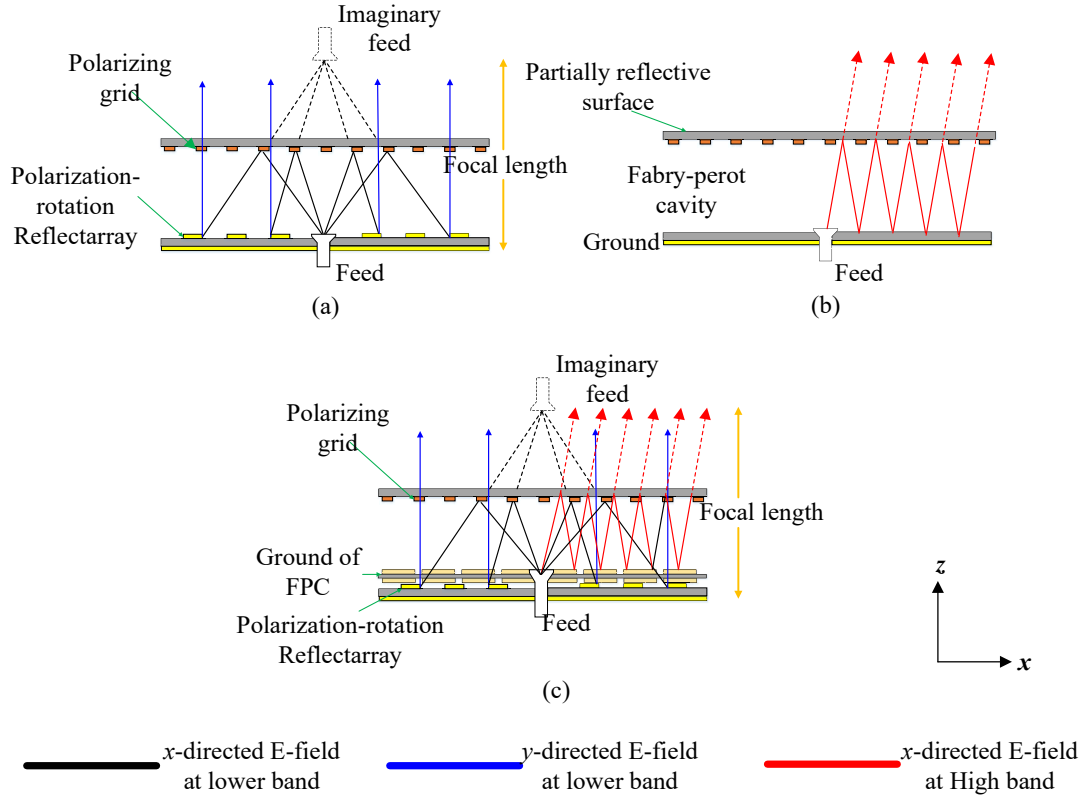


Fig. 4.1. (a) Configurations of folded reflectarray. (b) Configurations of FPC antenna. (c) Folding the reflectarray into the FPC.

The configurations and principles of the proposed Fabry-Perot cavity (FPC) and folded reflectarray (FR) hybrid design are shown in Fig. 4.1. The basic idea is based on “cavity reuse”, i.e. the FR and Fabry-Perot resonance occupy the same cavity. To achieve this, firstly, the grid polarizer of the FR should also work as the partially reflective surface (PRS) of the FPC. Secondly, an frequency selective surface (FSS) is inserted on top of the reflectarray as the ground of the FPC. This is to guarantee that the phases of the reflected waves inside the FPC are not affected by the phasing elements of the reflectarray. Then, for the FR band, EM waves with an x -directed E-

field are transmitted from the feed to the grid. They are reflected by the grid toward the reflectarray. The reflectarray collimates the EM waves and twists their polarizations by 90° . Finally, the waves pass the grid and are radiated into free space with high gain (y -directed E-field). For the FPC band, the EM waves with x -directed E-field are reflected inside the cavity. Each reflection interferes constructively in the broadside direction, leading to a high directive beam (x -directed E-field).

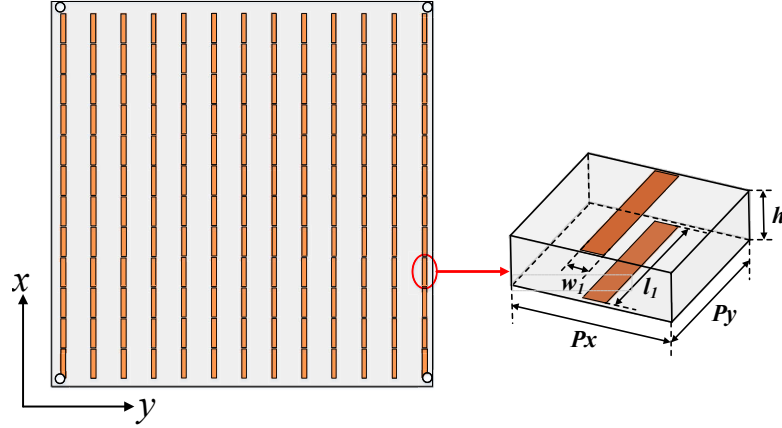


Fig. 4.2. Configuration of the grid polarizer of the reflectarray /PRS of the FPC ($P_x=10\text{mm}$, $P_y=10\text{mm}$, $w_l=9.6\text{mm}$, $l_l=1.5\text{mm}$, $h=0.787\text{mm}$).

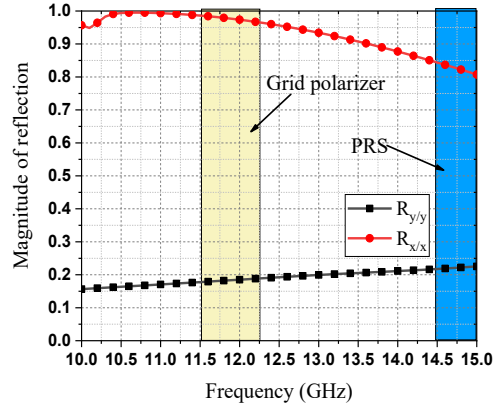


Fig. 4.3. Reflection magnitudes of the grid polarizer for x - and y -polarization normal incident waves.

4.2.1 Antenna design

A. Grid Polarizer (Reflectarray) /PRS (FPC) Design

To fold the reflectarray into the FPC, the fundamental requirement is that the grid polarizer of the reflectarray should also work as the PRS of the FPC. In the design, the grid polarizer is implemented using a double-screen grid with a length of 9.6mm and a width of 1.5mm with Rogers 5880 ($\epsilon_r=2.2$, $\tan\delta=0.0009$,

thickness=0.787mm) substrate as spacer, as shown in Fig. 4.2. The length of the grid is about half of the dielectric wavelength in the operating band (12-GHz in the design) and the width is much smaller than the operating wavelength. Therefore, the grid polarizer reflects the incident waves (x -directed E-field) because of the half-wavelength resonance and allows incident waves (y -directed E-field) to pass with little reflection. As Fig. 4.3 shows, the grid polarizer also partially reflects the x -directed E-field incident waves (with the magnitudes ranging from 0.8 to 0.85) from 14.5 to 15 GHz, which is the FPC band in the design, demonstrating that it can be used as the PRS of the FPC. The reflection phase of the x -directed E-field incident waves (ϕ_{prs}) is shown in Fig. 4.4. The reflection phase ranges from 134 to 138° from 14.5 GHz to 15 GHz, which is obtained in HFSS using master/slave boundary conditions.

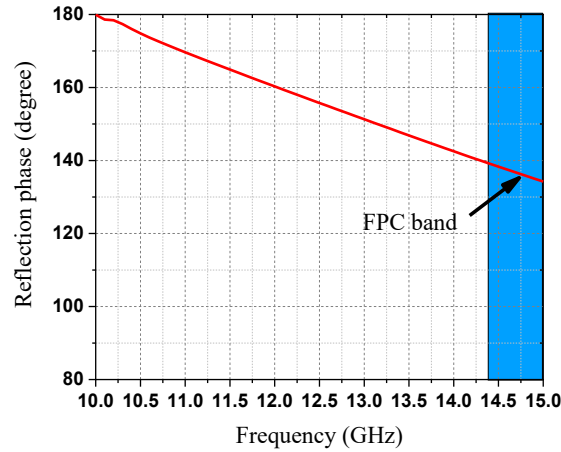


Fig. 4.4. Reflection phase of the grid polarizer under x -polarized incident wave.

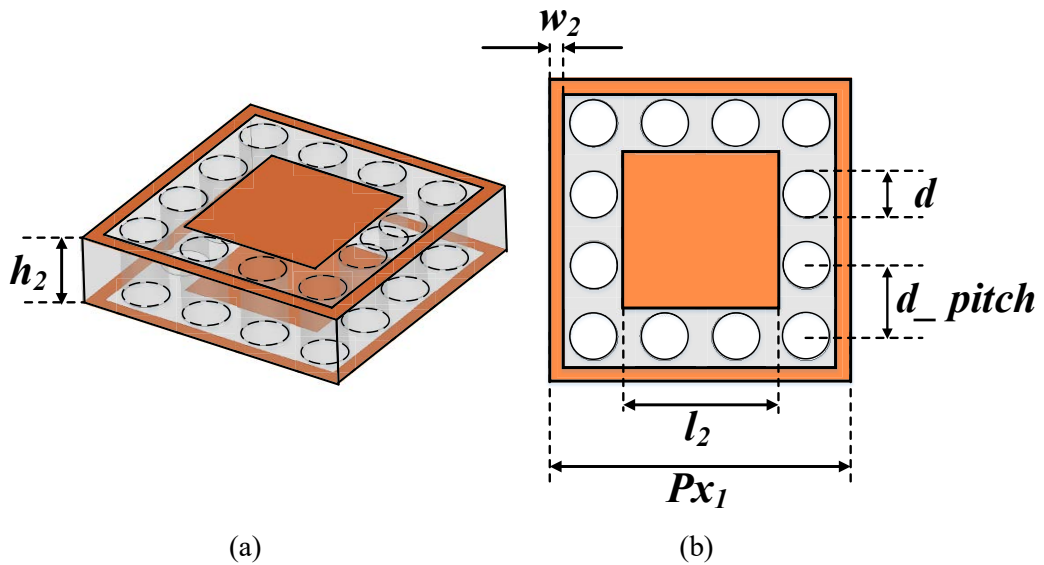


Fig. 4.5. FSS structure with perforated holes. (a) 3-D view. (b) Top view. (P_{x1} =12.7mm, P_{x2} =12.7mm, w_2 =0.65mm, l_2 =6.6mm, d =1.8mm, d_{pitch} =3mm, h_2 =3.175mm).

B. Ground of the FPC

In most cases, the ground of the FPC is purely metallic, or an artificial magnetic conductor is used to reduce the thickness of the FPC. Here, considering that the ground should reflect the EM waves in the high-band while allowing those in the low-band to pass through to realize the FR, the ground is formed of an FSS using Arlon AD800 substrate ($\epsilon_r=2.2$, $\tan\delta=0.0009$, thickness=3.175mm) as a spacer, as shown in Fig. 4.5. The reflection/transmission curves of the proposed FSS are shown in Fig. 4.6. In the simulation, it is found that, when using a low relative permittivity substrate to form the spacer, the FSS shows better transmission/reflection responses. Since the substrate with $\epsilon_r=2.2$ is the lowest relative permittivity substrate commonly used, the substrate is perforated with air holes to reduce its effective relative permittivity. As Fig. 4.6 reveals, the FSS shows better transmission in the low-band when perforated air holes are used. For the high-band (14.5 to 15 GHz), the FSS reflects the incident waves, which can be used as the ground of the FPC band, while for the lower band (11.7 to 12.2GHz), the EM-waves can pass through the FSS and then impinged on the reflectarray. The reflection phase of the FSS is given in Fig. 4.7, which shows that the reflection phase of the FPC band is from -135 to -144° . The thickness of the FPC cavity (h_{cavity}) should satisfy the Fabry-Perot resonant condition, given by [8-10]:

$$\frac{-4\pi h_{\text{cavity}}}{\lambda_0} + \varphi_{\text{PRS}} + \varphi_{\text{FSS}} = 2n\pi \quad (4-1)$$

where φ_{PRS} and φ_{FSS} are the reflection phases of the PRS and FSS ground, respectively, λ_0 is the free space wavelength at the centre frequency and n is an integer. Generally, multiple cavity heights satisfy Eq. (4-1). In the design, the thickness is adopted in accordance with half of the focal length of the FR.

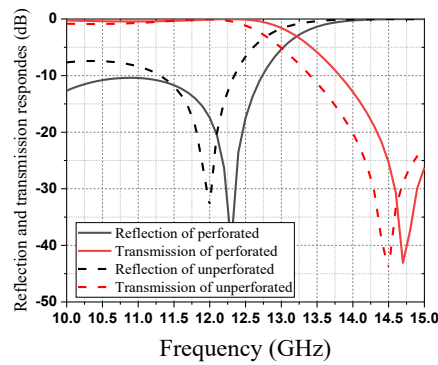


Fig. 4.6. Simulated transmission and reflection responses with and without perforated holes.

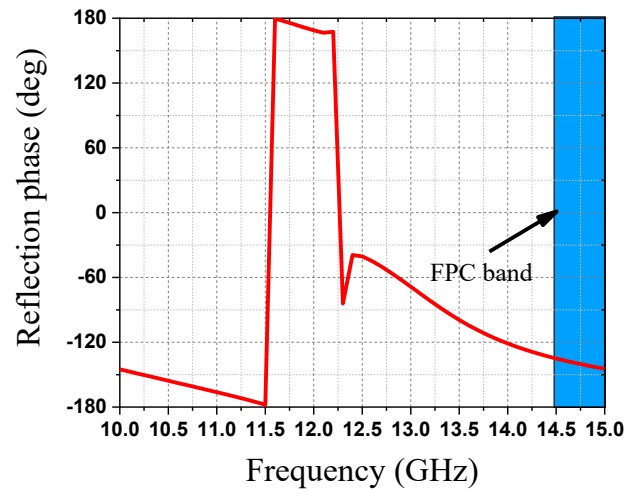


Fig. 4.7. Reflection phase of the FSS.

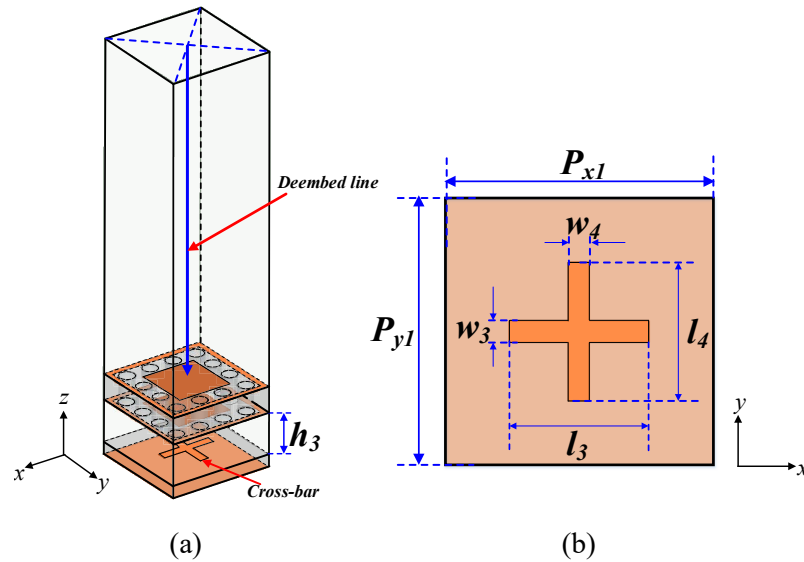


Fig. 4.8. Simulated model of the phasing element in HFSS. (b) Top view of the cross-bar. ($P_{x1}=12.7\text{mm}$, $P_{x2}=12.7\text{mm}$, $w_3=1\text{mm}$, $w_4=1\text{mm}$, $h_3=5\text{mm}$).

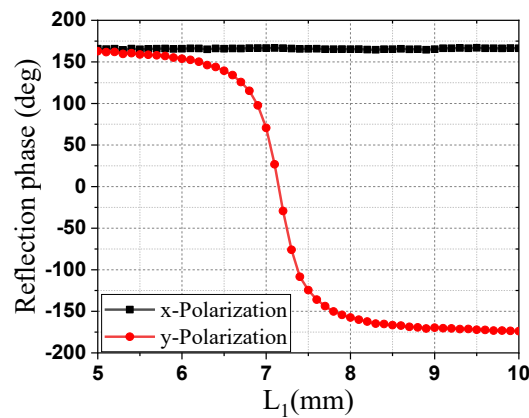


Fig. 4.9. Reflection phase of x-directed and y-directed polarizations incident waves by varying the length of L_4 .









Reflection phase (deg)	0	45	90	135	180	225	270	315
Geometry								
(l_3, l_4)	(4.0,6.84)	(6.45,6.92)	(6.68,7.04)	(6.76,7.40)	(6.84,4.0)	(6.92,6.45)	(7.04,6.68)	(7.40,6.68)

Fig. 4.10. Eight level phasing unit of the FR.

C.FR Design

The high gain of the lower band is achieved based on the FR principle. As stated previously, the reflectarray should be able to twist the incident wave's polarization by 90° and simultaneously collimate the incident waves. To twist the polarization, each phasing element should be capable of providing a 180° phase difference between the x -directed and y -directed E-field incident waves. To collimate the waves, the phasing elements as a whole should provide a 360° phase circle. Here, a cross-bar is used as the phasing element, as shown in Fig. 4.8. In phase curve retraction, the FSS is included in the model. The reflection phases for x -directed and y -directed E-field incident waves at 12.8 GHz with different values of l_4 are shown in Fig. 4.9. As the figure shows, the 342° reflection phase of y -directed E-field incident waves can be obtained by changing the length of l_4 from 5 to 10 mm while the reflection phases of x -directed E-field incident wave are nearly constant. Therefore, we can adopt eight-level phasing elements that satisfy the above conditions, as shown in Fig. 4. 10, to implement the reflectarray. The focal length of 60mm is adopted in the design. The aperture compensating phase should compensate for the spatial phase delay from the feed phase center, given by [11]:

$$\varphi(x, y) = \frac{2\pi}{\lambda_0} (\sqrt{x^2 + y^2 + f^2} - f) + \varphi_0 \quad (4-2)$$

where f represents the focal length, λ_0 represents the wavelength in free space, φ_0 represents the initial phase at the original point. In the design, 100 phasing elements are used with a total aperture size of 127mm×127mm.

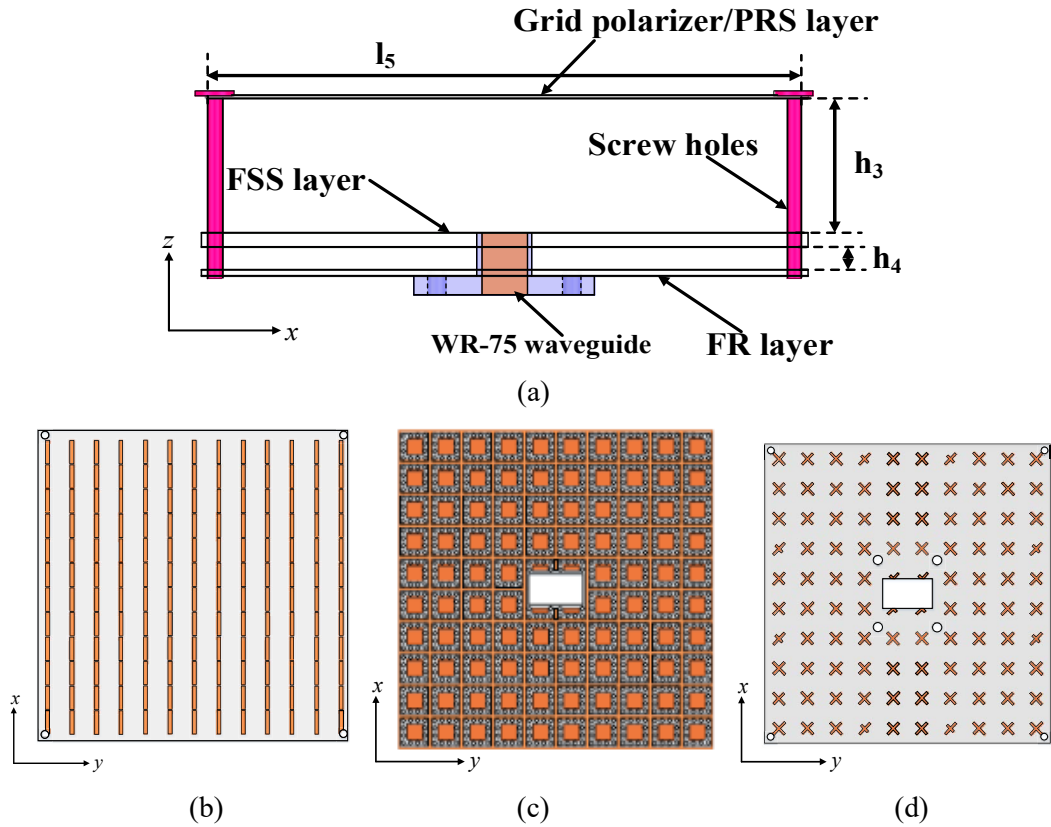


Fig. 4.11. (a) Side view of the antenna ($h_3=30.7$ mm, $h_4=5$ mm, $l_5=127$ mm). (b) Top view of grid polarizer/PRS. (c) Top view of the FSS. (d) Top view of the reflectarray.

4.2.2 Design guidelines

For demonstration purposes, the antenna is designed to cover the dual frequency bands of 11.7-12.2 GHz and 14.5-14.8 GHz, which are downlink and uplink bands for the broadcast satellite service (BSS), respectively. Without loss of generality, we set FPC resonance for the higher band (f_h), and FR for the lower band (f_l). The design guidelines are as follow:

1. Grid polarizer (FR) /PRS (FPC) design.

Design the grid polarizer/PRS according to the required bands. The grid polarizer can be implemented by using conventional periodical rectangular patches or meandering line structures [12,13]. Once the structure is determined, detailed dimensions should be further optimized to meet two requirements: (1) the grid polarizer reflects only one polarization but allows the orthogonal polarization to pass at f_l ; (2) it also partially reflects the incident waves at f_h . Using double-layered structure can provide wider operating bandwidth than single-layered structure.

2. FSS design

The FSS should be optimized to reflect the EM-waves of the FPC band and allow EM-waves of the FR band to pass. Double screen FSSs are recommended as they can provide wider bandwidth and better out-of-band performance than the single-layer FSS [14-16].

3. Feed design

Here, the WR75 waveguide is used as the feed as it can cover both bands. Other approaches, such as dual-band patch antenna with U-shaped slots [17,18] or wideband patch antenna using parasitic patches [19], can be also used as the feed.

4. Cavity height selection

Basically, the cavity height is half the focal length. However, it can be further optimized to balance the highest and the most stable gain of the reflectarray and ensure that the Fabry-Perot resonant condition is also satisfied at the required frequency.

5. Reflectarray design

The reflectarray should be able to twist the incident wave's polarization by 90° and simultaneously collimate the incident waves. Generally, different kinds of phasing elements can achieve this goal apart from the cross-bar used in the proposed design, such as split-ring resonators [20] and patches with different phase delay lines [21]. In the simulation, the FSS should be included for phase response retrieval.

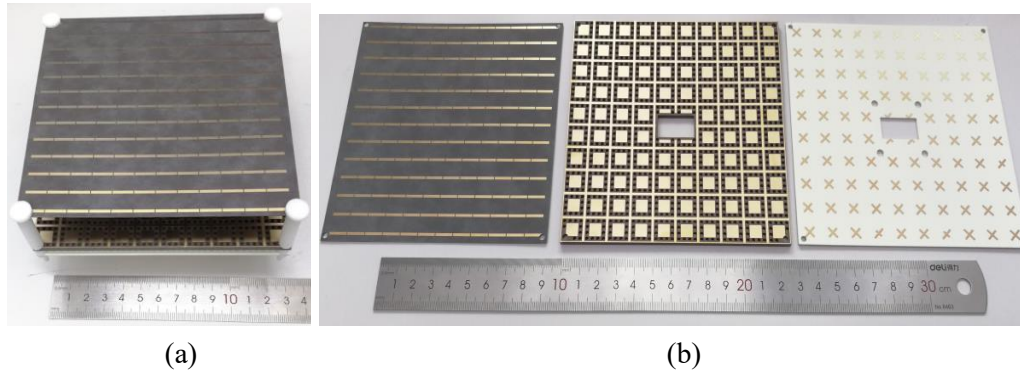


Fig. 4.12. Antenna prototype. (a) Assembling view. (b) Top view of each layer.

4.2.3 Fabrication, measurement, and discussion

The side view of the antenna and the top view of each layer are shown in Fig. 4.11. A WR 75 waveguide is used as the feed. The antenna prototype is fabricated and assembled, as shown in Fig. 4. 12. The radiation performance is measured in a

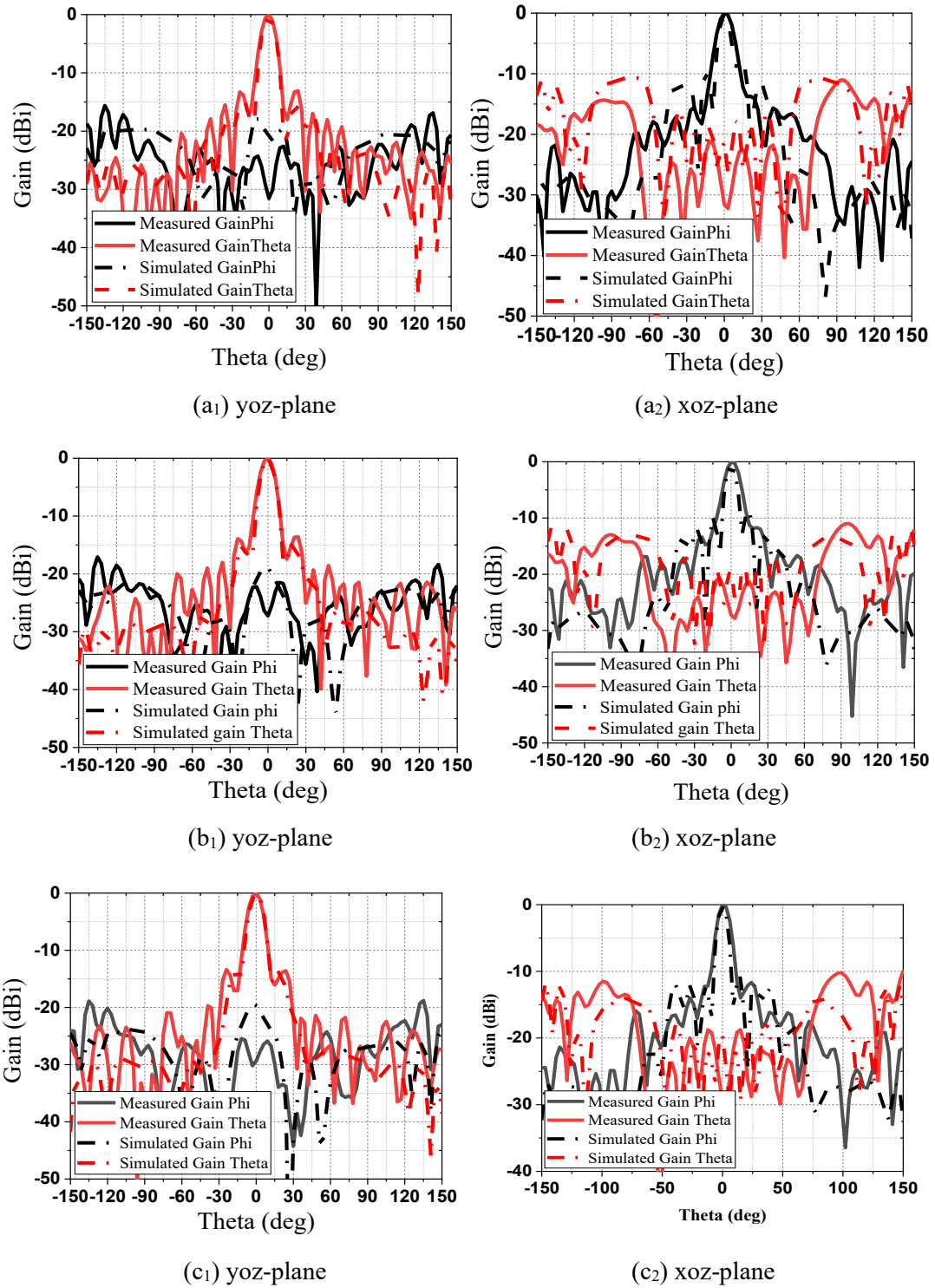


Fig.4.13. Simulated and measured antenna gain at (a) 11.8 GHz. (b) 11.9 GHz. (c) 12.1 GHz.

Satimo StarLab antenna radiation measurement system. The antenna radiation patterns in the low-band (11.8, 11.9 and 12.1 GHz) and high-band (14.6, 14.7 and 14.8 GHz) are given in Figs. 4.13 and 4.14, respectively. The antenna gain versus frequency is plotted in Fig. 4.15. The peak gains achieved are 18.1-dBi at 12 GHz

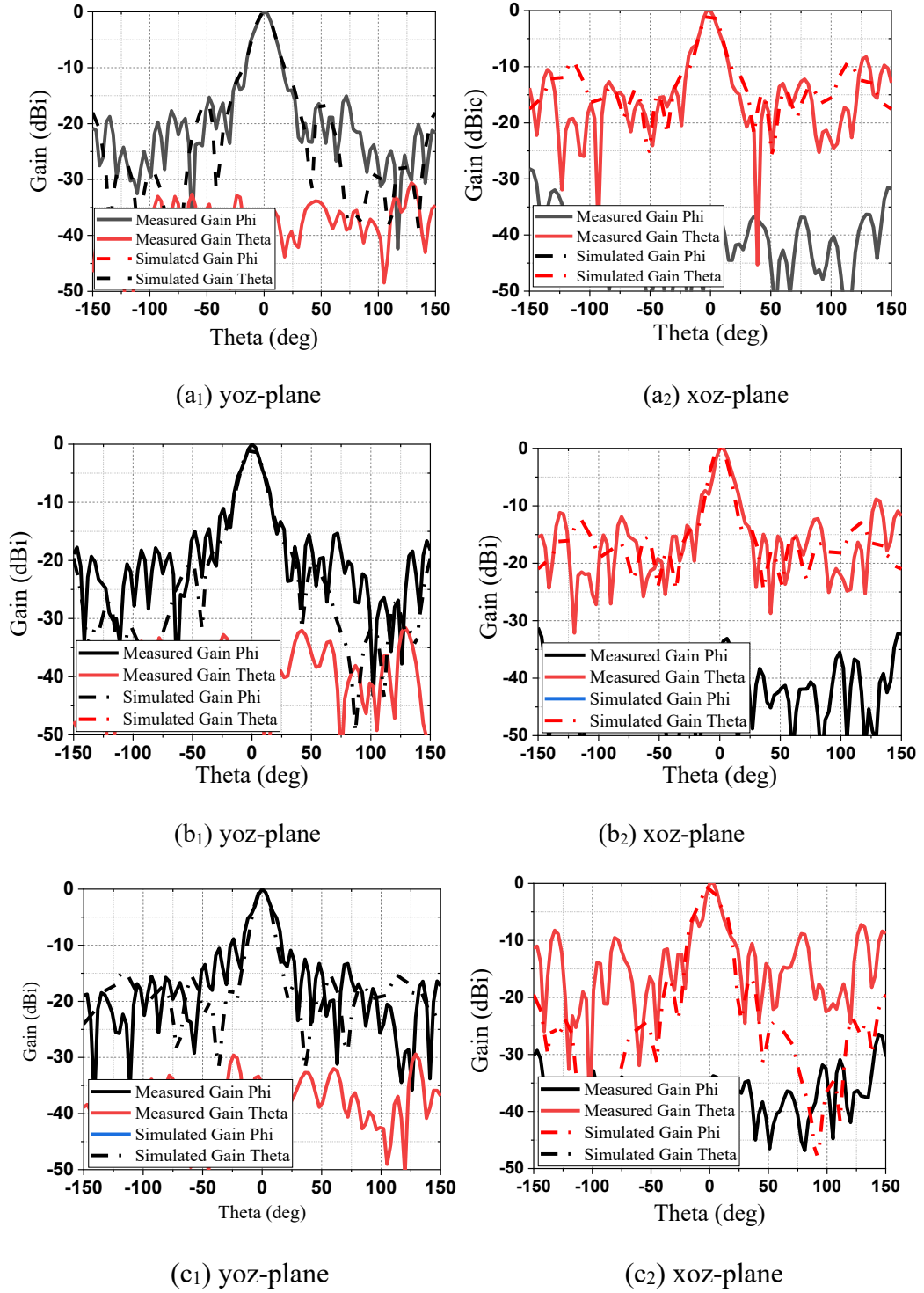


Fig.4.14. Simulated and measured antenna gain at (a) 14.5 GHz. (b) 14.6 GHz. (c) 14.7 GHz

for the lower band and 18.1 dBi at 14.7 GHz for the higher band, respectively.

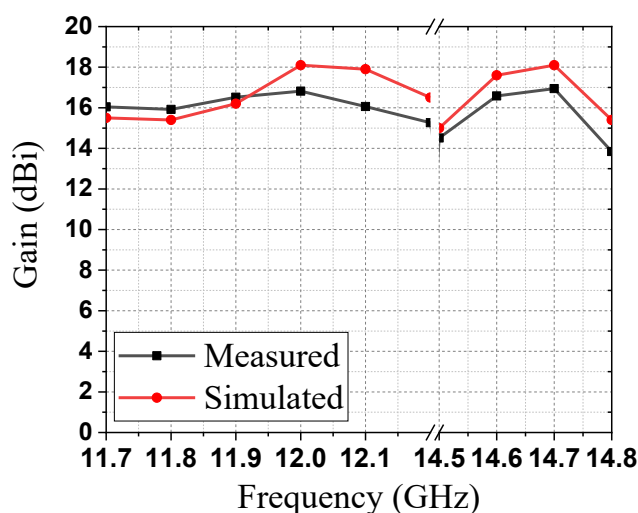


Fig. 4.15. Simulated and measured gain.

Compared with traditional reflectarray configuration, FR has the advantages of eliminating the blockage effects of the feed and a height reduced by half. Nevertheless, FR can only be used to achieve high directive radiation over one polarization [22-31] due to the polarizing grid. Fabry-Perot resonance is widely used to achieve high directive radiation, but a Fabry-Perot antenna with dual-polarized radiation using a single linearly-polarized feed has not been reported to date. Most state-of-the-art studies to realize dual-band dual-polarized radiation use a dual-polarized primary source [32-36]. Here, by combining the FR and the FPC resonance, a new dual-band dual-polarized high gain antenna with a single linearly-polarized feed is proposed. The design inherits the merits of the FR and overcome the limitation of the FR of achieving high directive radiation over only one polarization. Because the reflectarray is folded into the FPC, the size is not increased much. Using high-performance FSS, the interference between two operating bands can be minimized even if the two operating frequency bands are close to each other. Moreover, the operating frequency bands are scalable to the other frequency band to meet the requirement of different communication systems.

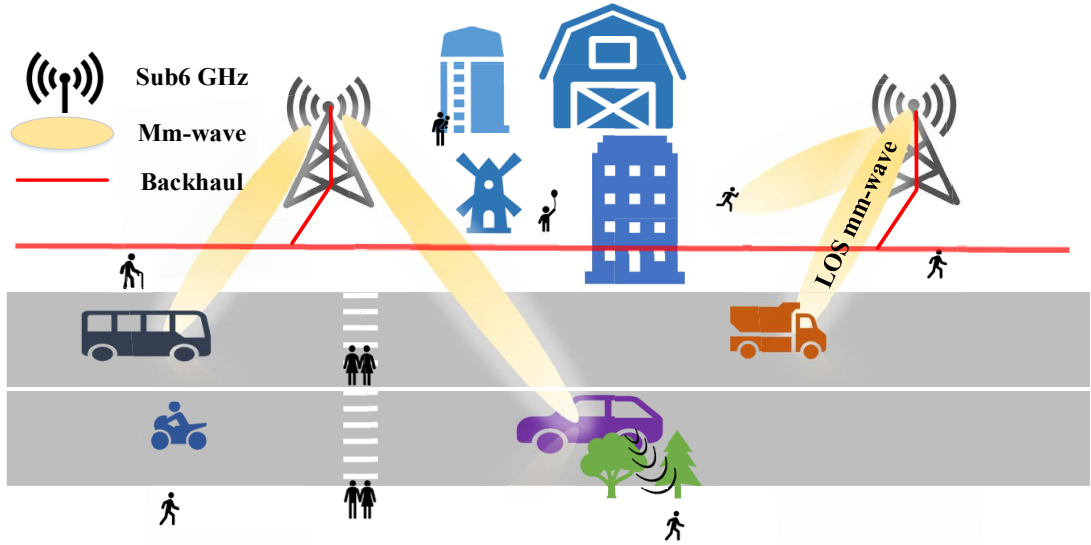


Fig. 4.16. Mm-wave/sub-6 GHz Integrated 5G network.

4.3 Large Frequency-Ratio, High Aperture Reuse Efficiency, Dual-Band Antenna for Millimetre-Wave and Sub-6 GHz Applications

As stated previously, due to high path loss, shadowing, and blockages, mm-wave signals suffer from severe propagation attenuation and are vulnerable to obstacles. Consequently, it is difficult to guarantee reliable communication in the mm-wave frequency range. To resolve this issue, a practical and reasonable method is to tightly integrate an mm-wave network with an existing sub-6 GHz network. The sub-6 GHz band can be used to provide more reliable communications and a consistent user experience. As shown in Fig. 4.16, the mm-wave spectrum can be used for LOS communication with high data-rate transmission, while the sub-6 GHz spectrum is used for long-distance and non-LOS communications.

To cover both the sub-6 GHz and mm-wave frequency bands, from the antenna point of view, using two antennas operating at different frequency bands is the most straightforward approach. However, the disadvantage is the low aperture reuse efficiency [37]. Therefore, using a single shared-aperture antenna with a large frequency-ratio that can simultaneously cover mm-wave and sub-6 GHz may be a better choice. However, this is challenging due to the realization of the large frequency-ratio and isolation. To meet this challenge, Zhang *et al.* proposed a kind of 60-GHz SIW slot array antenna, which simultaneously functions as the radiator of

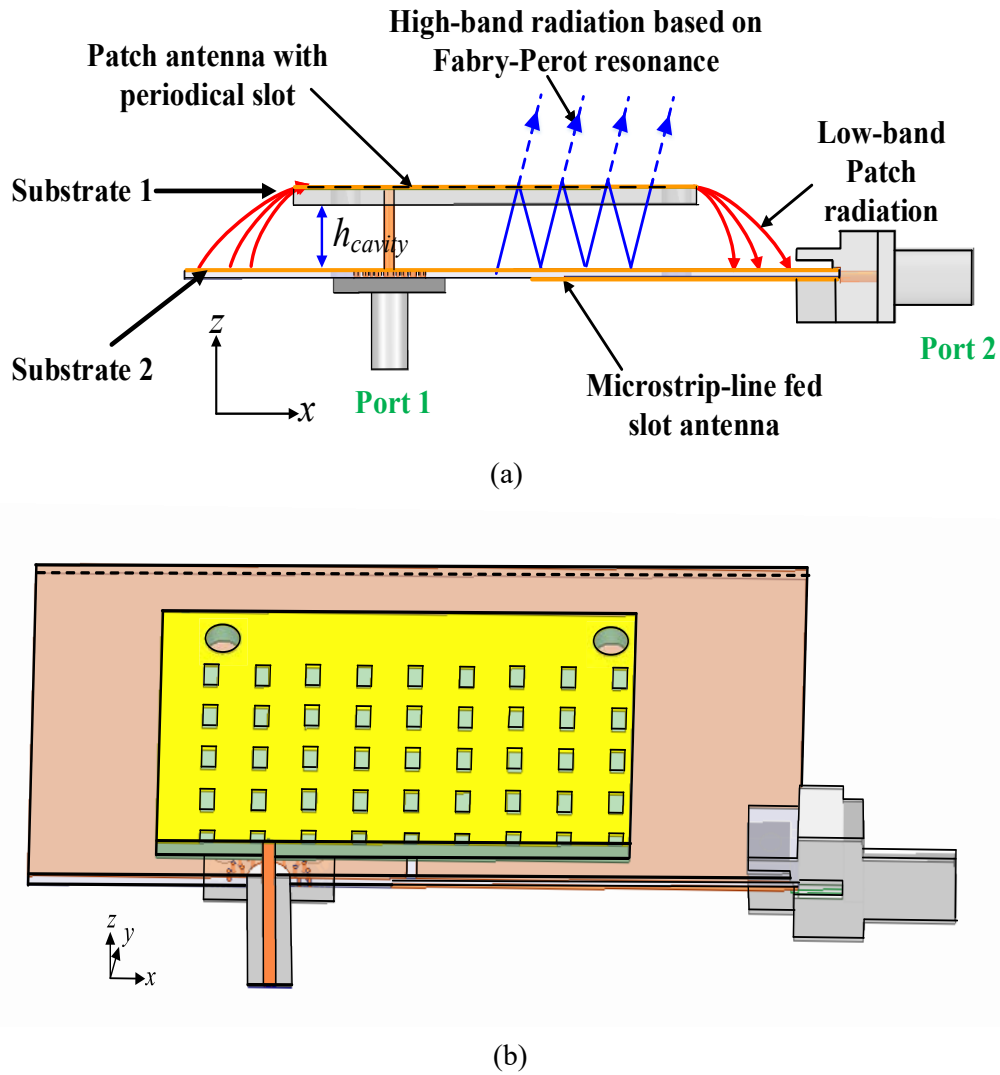


Fig. 4.17. Structure of the proposed dual-band large frequency-ratio antenna. (a) Side view and working principle (not scaled in z -direction). (b) 3-D view. (because of symmetry, only half is shown here).

a patch antenna operating at 3.5 GHz [38]. By taking advantage of the high-pass nature of SIW technology to reject the lower frequency signal and using a low pass filter to suppress the higher frequency signal, extremely high isolation can be achieved. Apart from the large frequency-ratio and isolation, considering the high attenuation of the mm-wave signal, the high gain in the mm-wave frequency band is another indispensable feature of this kind of antenna. Generally, using an array formed of multiple antenna elements can achieve high gain, albeit with a rather bulky feeding network. The other approach is using one antenna with high directivity. Considering its ease of integration, the Fabry-Perot cavity antenna is attractive because it can achieve high gain without a complicated feeding network.

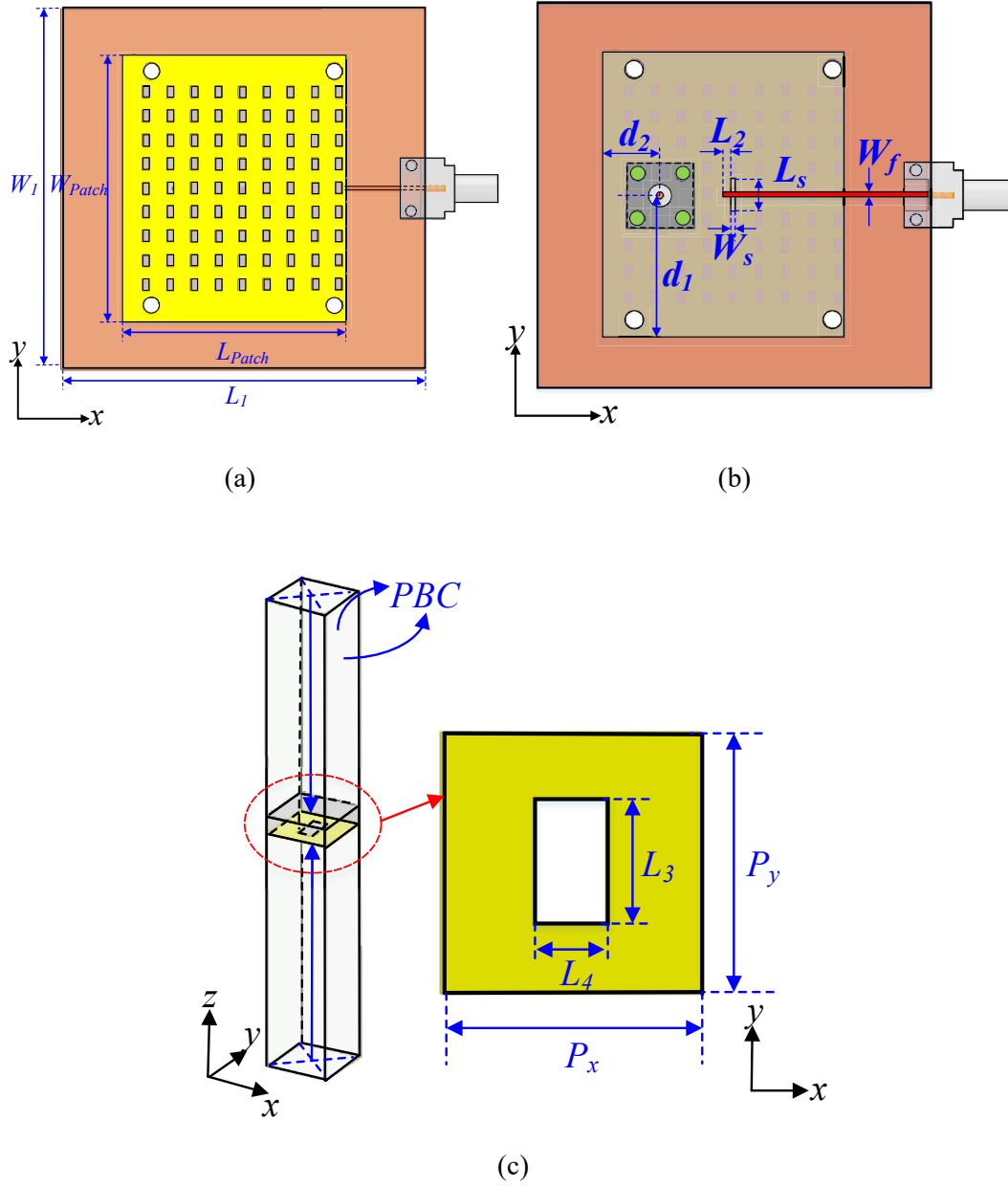


Fig. 4.18. Configurations of the antenna. (a) Top view. (b) Bottom view. (c) Unit of the periodical slot forming PRS.

By employing a partially reflective-surface (PRS) on top of a fully reflective surface with a low-directivity primary source, high directivity radiation can be achieved as long as the height of the cavity satisfies the resonant condition. This section proposes a dual-band, large frequency-ratio, high aperture reuse efficiency, and high gain antenna by integrating Fabry-Perot (FP) resonance into a patch antenna. To achieve high aperture reuse efficiency, the patch with periodical slots acts as the

radiator for the 2.4-GHz frequency band and simultaneously functions as the partially reflective surface (PRS) of the FP resonant antenna operating at 28 GHz. The reflection magnitude of the PRS can be easily adjusted by adjusting the dimensions of the periodical slots. Moreover, the slots operating at 28 GHz have little influence on the radiation of the patch, since its size is much smaller than the wavelength at 2.4 GHz. In addition to aperture reuse, the design also has the benefit of cavity reuse, i.e. the patch and FP resonance occupy the same cavity, and the antenna therefore maintains a low profile. Because of the FP resonance, the antenna achieves a high gain of 16 dBi at 28 GHz. Note that the frequency bands and the ratio adopted in the design are only for demonstration. The design has the potential to be configured to other frequencies based on the same principles.

4.3.1 Antenna design

The basic configuration of the proposed dual-band large frequency-ratio antenna is shown in Fig. 4.17. The frequency bands of 2.4 GHz (low-band) and 28 GHz (high-band) are adopted for demonstration. For low-band radiation, a patch located as the top of substrate 1 (Rogers 4003 with a relative permittivity of 3.55, loss tangent of 0.0027, and a thickness of 1.524 mm) is used as the radiator while the ground of the patch antenna is located at the top of substrate 2 (Rogers 4003 with a thickness of 0.813 mm). For the high-band radiation, a microstrip line-fed slot antenna implemented on substrate 2 is used as the primary source, where the microstrip line is located at the bottom and the slot is cut on the top full ground. Thus, Port 1 is used for the patch mode excitation and Port 2 is used for the FP resonant mode excitation. To achieve high aperture reuse efficiency, the PRS is implemented by cutting periodical slots in the patch, as shown in Figs. 4.18 (a) and (b). Therefore, the patch antenna and the FPC antenna share the same aperture, resulting in high aperture-reuse efficiency. Since the patch antenna can be regarded as a special cavity [39], it shares the same cavity with FP resonance, leading to a small height.

A. FPC antenna operating in high-band

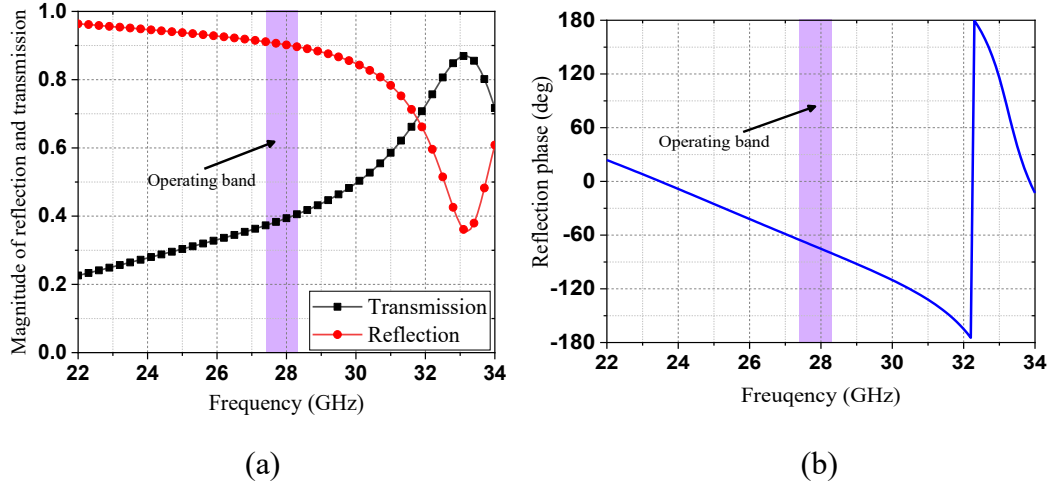


Fig. 4.19. (a) Transmission and reflection magnitudes of the PRS. (b) Reflection phase.

The geometry of the periodical slot is shown in Fig. 4.18 (c). The partial reflection of PRS is achieved based on slot resonance. When the slot length is half of the dielectric wavelength at the resonant point, most of the energy can transmit through the slot. When the frequency deviates from the resonant point, the reflection magnitude gradually increases. As shown in Fig. 4.19 (a), at resonant point (33 GHz), a transmission magnitude of up to 0.88 is achieved. For frequencies lower than 33 GHz, the reflection magnitude gradually increases when the frequency decreases. Therefore, the reflection magnitude of the PRS at the desired frequency (28 GHz in the proposed design) can be easily tuned by adjusting the resonance of the slot. The relation between the directivity (D) of the FP resonator antenna and the reflection magnitude ($|\Gamma|$) of the PRS layer can be expressed as [40]:

$$D = 10 \log \frac{1 + |\Gamma|}{1 - |\Gamma|} \quad (4-3)$$

The higher the reflection of the PRS, the higher the gain the FPC antenna can achieve. Therefore, the reflection magnitude of PRS is designed to be 0.9 at 28 GHz to provide sufficient reflection, as shown in Fig. 4.19 (a). The reflection phase of the PRS is given in Fig. 4.19 (b), and is important for determining the thickness of the FPC, and therefore the height of the 2.4 GHz patch antenna. The thickness of the FPC (h_{cavity}) should satisfy the Fabry-Perot resonant condition, given by:

$$\frac{-4\pi h_{cavity}}{\lambda_0} + \varphi_{PRS} + \varphi_{Ground} = 2n\pi \quad (4-4)$$

where φ_{PRS} and φ_{Ground} are the reflection phases of the PRS and ground, respectively, λ_0 is the free space wavelength at the centre frequency and n is an integer. Although multiple cavity heights can satisfy the Eq. (4-4), the thickness of the design is adopted as 1.76 mm to minimize antenna height.

A slot antenna is used as the feed of the Fabry-Perot radiation. The slot is located at the centre of the FPC by cutting the top full metal of substrate 2 (ground of the 2.4-GHz patch). Since the slot is sufficiently small compared with the wavelength at 2.4 GHz, it does not affect the radiation performance of the patch antenna. The slot is fed by a microstrip line, which is directly connected to the SMK connector as an input, as shown in Fig. 4.18 (a). The dimensions of the antenna is shown in Table 4.1.

B. Patch antenna operating in low-band

Once the geometry of PRS and the thickness of FPC are determined, the patch antenna operating at 2.4 GHz can be designed. The patch is printed at the top of substrate 1, the length of which is about half that of the dielectric wavelength at 2.4 GHz. The ground of the patch antenna is located at the top of substrate 2, as shown in Fig. 4.17 (a). Because of periodical slot cutting on the patch, it is important to compare the performance of the proposed patch antenna with one with full metal. Figs. 4.20 and 4.21

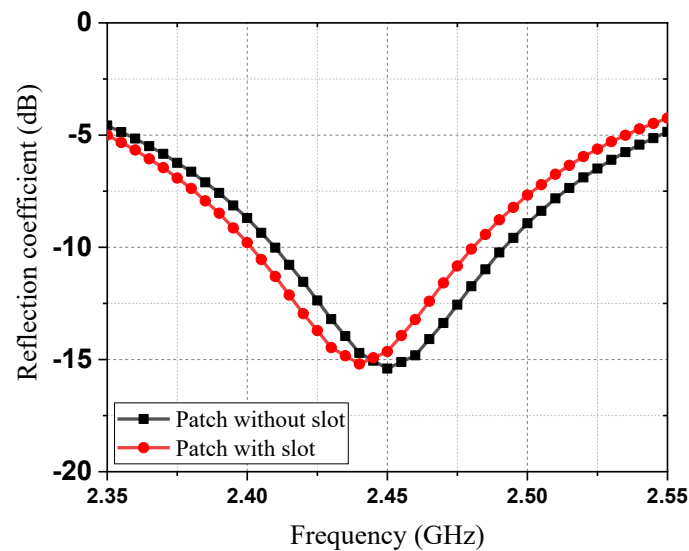


Fig. 4.20. Simulated reflection coefficients with and without slot on patch.

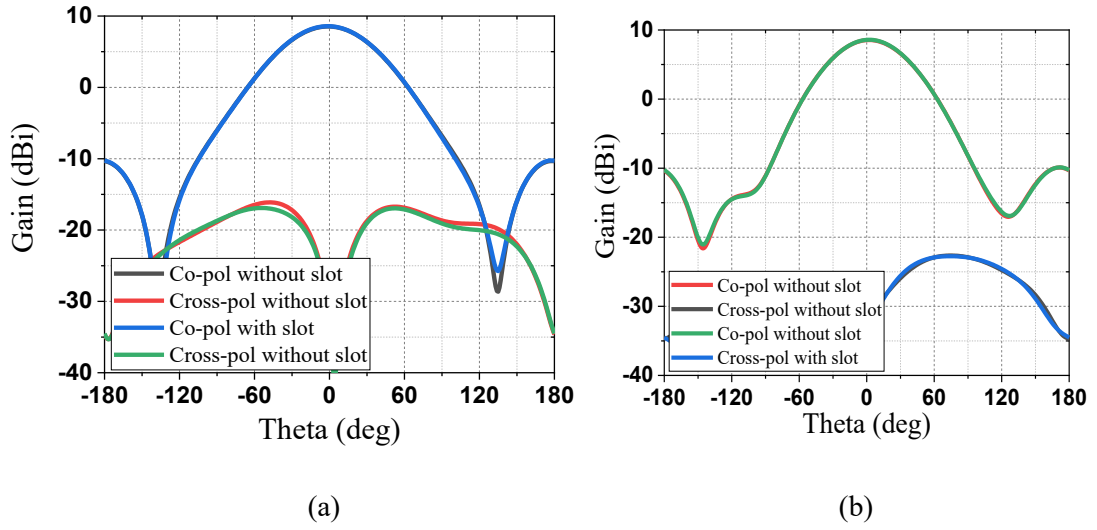


Fig. 4.21. Simulated radiation patterns with/without slot on patch at 2.4 GHz. (a) yoz-plane. (b) xoz-plane.

TABLE 4.1 DIMENSIONS OF THE ANTENNA.

Parameter	W_{patch}	W_s	W_f	W_1	L_{patch}	L_s	L_f
value (mm)	55.4	0.96	0.87	74.97	46.17	6.12	39.8
Parameter	L_1	L_2	L_3	L_4	P_x	P_y	h_{cavity}
value (mm)	75.4	1.45	2.42	1.37	5	5	1.76
Parameter	d_1	d_2					
value (mm)	27.7	10.88					

compare the impedance matching and radiation patterns of the patch antenna with and without slots. The figure show that impedance matching of the patch antenna with slots only slightly shifts by 10 MHz to the lower frequency band while the radiation performance of the patch with and without slots are almost the same. This is because the length and width of the periodical slots operating at 28 GHz are much smaller than those of slots operating at 2.4 GHz, and slots have little influence on the radiation of the patch antenna. The proposed configuration is particularly suitable for the large frequency-ratio antenna design since the larger the frequency-ratio, the smaller the influence of the slots on the performance of the patch antenna.

4.3.2 Measurement and discussion

To demonstrate, an antenna prototype was fabricated and measured, as shown in Fig. 4.22. The S-parameters of the two bands are given in Fig. 4.23. For the sub-6 GHz band, the -10-dB reflection coefficients are from 2.40 GHz to 2.48 GHz for the simulation and 2.40 GHz to 2.47 GHz for the measurement. For the mm-wave band, the -10-dB reflection coefficients are from 27.7 GHz to 28.1 GHz for the simulation and 27.7 GHz to 28.3 GHz for the measurement. The simulated and measured radiation patterns at 2.42 GHz and 28 GHz are shown in Fig. 4.24 and 4.25, respectively. The peak gain for the two bands is given in Fig. 4.26, and reaches 8.0 dBi and 16 dBi for the 2.4 GHz band and 28 GHz band, respectively. Table 4.2 compares the key characteristics of the proposed design with other dual-band large frequency-ratio antennas operating in the microwave and millimetre-wave bands simultaneously. Using two antennas is a straightforward way to achieve dual-band features with easy of configuration [17-19], but the designs suffer from low aperture reuse efficiency. To achieve high gain in the mm-wave frequency band with high aperture reuse efficiency, the use of an array densely distributed on the aperture is proposed in [11]. However, the feeding network on the antenna aperture causes the aperture reuse efficiency to be reduced. In the present work, by simply cutting slots in the patch, high gain in the mm-wave band is achieved without the need for an array feeding network and the antenna achieves high aperture reuse efficiency. Since the patch and the FP resonant occupy the same cavity, the antenna remains relatively thin. It is also worth mentioning that slot array antennas can be used instead of the slot element to achieve multi-beam or beam steering for mm-wave band, which will be a valuable future work.

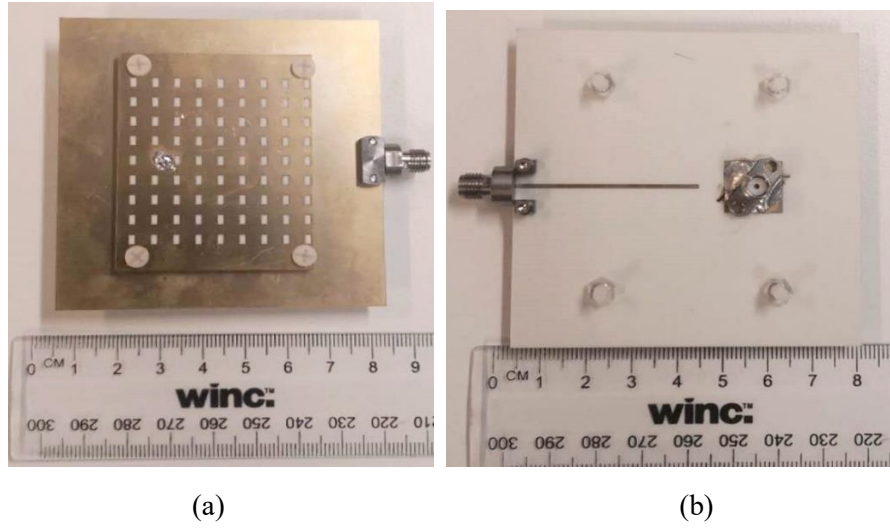


Fig.4.22. Fabricated prototype. (a) Top view. (b) Bottom view.

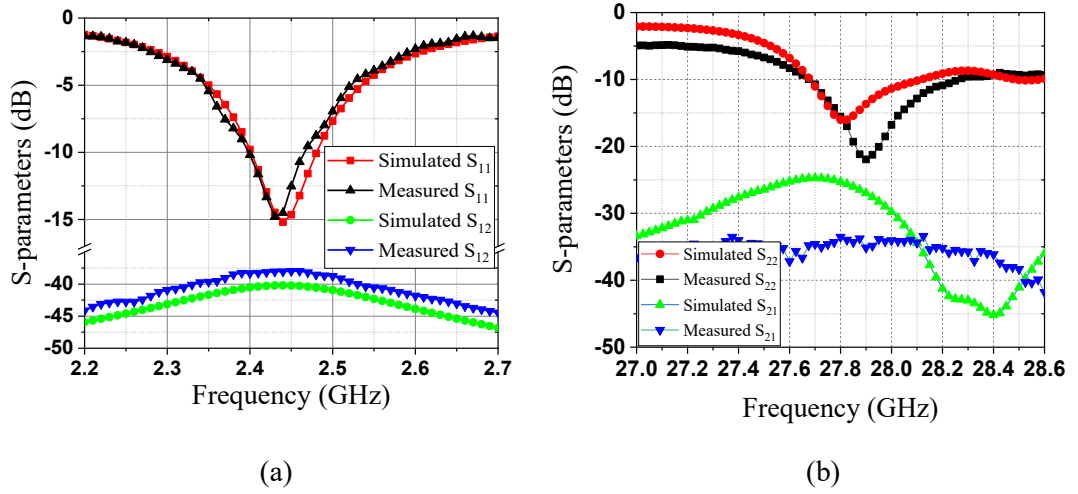


Fig. 4.23. Simulated and measured S-parameters. (a) Sub-6 GHz band. (b) mm-wave band.

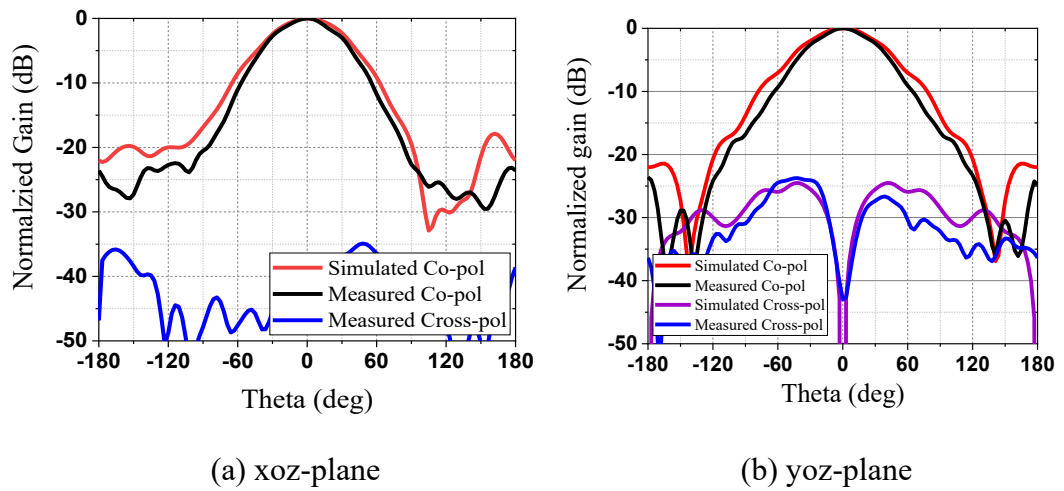


Fig. 4.24. Simulated and measured radiation patterns at 2.42 GHz.

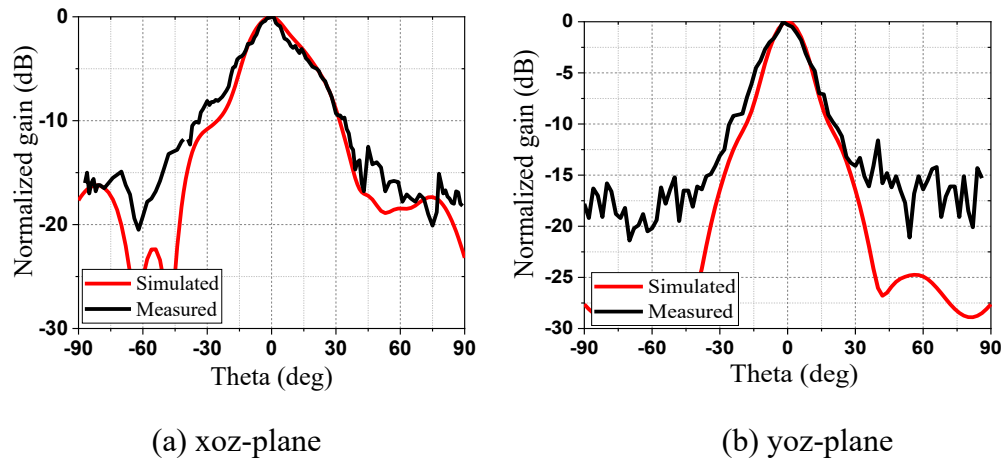


Fig. 4.25. Simulated and measured radiation patterns at 28 GHz.

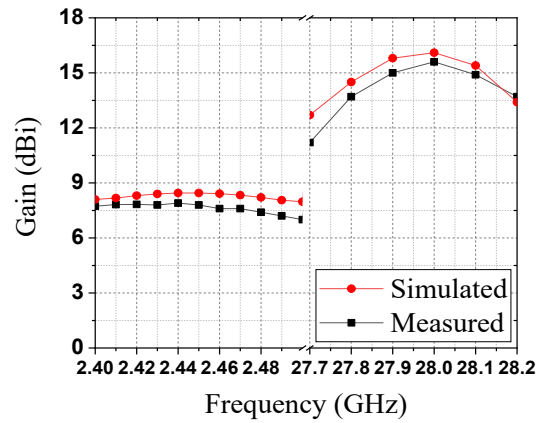


Fig.4.26 Simulated and measured antenna gain.

TABLE 4.2

COMPARISON OF DIFFERENT KIND OF DUAL-BAND ANTENNA FOR MICROWAVE AND MILLIMETRE-WAVE
APPLICATIONS

Ref.	Freq (GHz), Frequency- ratio	Peak gain	Array (Sub-6 GHz/mm- wave)	Thickness normalized to the wavelength @ lower frequency band	Reuse ratio efficiency
[37]	3.5/60, 17	7.3/24	No/Yes	0.02	High
[41]	2.4/24, 10	7.3/11.5	No/No	0.2	High
[42]	5/60, 12	3.4/16	No/Yes	0.92	0
[43]	4/60, 15	4/7	No/No	0.01	0
[44]	5.8/30, 5.2	4.5/9.37	No/No	0.02	0
[45]	2.4/24, 10	6.8/18.2	No/No	0.16	Low
[46]	5.2/24, 4.6	3.93/6.2	No/No	0.026	High
This work	2.4/28, 11.7	8.0/16	No/No	0.03	High

4.4. Conclusion

In summary, dual-band high gain antennas are outlined in this section. The first design is achieved by folding the reflectarray into the FPC. High gain radiation over two bands is achieved by exploiting the collimating reflectarray and FPC resonant principles. The design inherits the merits of the FR but overcome the limitation of the FR of only achieving high directive radiation over one polarization due to the polarizing grid. In addition, the design can enrich the FPC antenna community because the state-of-the-art attempt to realized dual-band dual-polarized radiation use a dual-polarized primary source. Next, a dual-band antenna with a large frequency-ratio of 11.7 (2.4 GHz/28 GHz) and high aperture reuse efficiency is proposed, which integrates FP resonance in a patch antenna for sub-6 GHz and mm-wave applications. The patch with periodical slots acts as the radiator for the 2.4 GHz frequency band and simultaneously functions as the PRS of the FPC antenna operating at 28 GHz. Thus, the FPC antenna and the patch antenna share the same cavity and the aperture. Because of FP resonance, the antenna can achieve a high gain of 16 dBi in the 28 GHz band without a feeding network. The antenna configuration has the potential to be scaled to other frequency bands with an even larger frequency-ratio.

4.5 References

- [1] Rappaport, Theodore S., *et al.* “Millimeter wave mobile communications for 5G cellular: It will work!.” IEEE access: 335-349, 2013.
- [2] I. A. Hemadeh, K. Satyanarayana, M. El-Hajjar and L. Hanzo, “Millimeter-wave communications: physical channel models, design considerations, antenna constructions, and link-budget,” IEEE Commun. Surv. Tutor., vol. 20, no. 2, pp. 870-913, 2018.
- [3] Y. Niu, C. Gao, Y. Li, *et al.* Exploiting multi-hop relaying to overcome blockage in directional mmwave small cells. Journal of communications and networks, 18(3): 364-374, 2016.
- [4] M. Riza Akdeniz *et al.*, “Millimeter wave channel modeling and cellular capacity evaluation,” IEEE JSAC, vol. 32, no. 6, June 2014, pp. 1164–79.

- [5] H. Zhao *et al.*, “28 GHz millimeter wave cellular communication measurements for reflection and penetration loss in and around buildings in new york city,” Proc. IEEE ICC, June 2013, pp. 5163–67
- [6] M. Zhang *et al.*, “Will TCP work in mmWave 5G cellular networks?,” IEEE Commun. Mag., 57(1): 65-71, 2019.
- [7] M. M. Kassem *et al.*, “Future wireless spectrum below 6 GHz: A UK Perspective,” Proc. IEEE DySPAN, Sept. 2015, pp. 59–70.
- [8] H. Shokri-Ghadikolaei *et al.*, “Millimeter wave cellular networks: A MAC layer perspective,” IEEE Trans. Commun., vol. 63, no. 10, Oct. pp. 3437–58, 2015.
- [9] J. Deng, O. Tirkkonen, R. Freij-Hollanti, T. Chen and N. Nikaein, “Resource allocation and interference management for opportunistic relaying in integrated mmWave/sub-6 GHz 5G networks,” IEEE Commun. Mag. 55.6: 94-101, 2017.
- [8] G. V. Trentini, “Partially reflecting sheet array,” IRE Trans. Antennas Propag., vol. AP-4, no. 4, pp. 666–671, Oct. 1956.
- [9] R. M. Hashmi and K. P. Esselle, “A class of extremely wideband resonant cavity antennas with large directivity-bandwidth products,” IEEE Trans. Antennas Propag., vol. 64, no. 2, pp. 830–835, Feb. 2016.
- [10] Y. Ge, K. P. Esselle, and T. S. Bird, “The use of simple thin partially reflective surfaces with positive reflection phase gradients to design wideband, low-profile EBG resonator antennas,” IEEE Trans. Antennas Propag., vol. 60, no. 2, pp. 743–750, Feb. 2012.
- [11] N. Payam, F. Yang, and Atef Z. Elsherbeni. *Reflectarray Antennas: Theory, Designs and Applications*. John Wiley & Sons, 2018.
- [12] L. Young, L. Robinson and C. Hacking, “Meander-line polarizer,” IEEE Trans. Antennas Propag. 21.3: 376-378, 1973.
- [13] E. Arnaud, R. Chantalat, M. Koubeissi, T. Monediere, E. Rodes and M. Thevenot, “Global design of an EBG antenna and meander-line polarizer for circular polarization,” IEEE Antennas Wireless Propag. Lett. , vol. 9, pp. 215-218, 2010.
- [14] J. Zhu, Y. Yang, S. Li, S. Liao and Q. Xue, “Dual-Band dual circularly polarized antenna array using FSS-integrated polarization rotation AMC ground for vehicle satellite communications,” IEEE Transactions on Veh. Technol., vol. 68, no.

11, pp. 10742-10751, Nov. 2019.

[15] J. Huang, T.-K. Wu, S.-W. Lee, "Tri-band frequency selective surface with circular ring elements", IEEE Trans. Antennas Propag., vol. 42, no. 2, pp. 166-175, Feb. 1994.

[16] R. Orr *et al.*, "Circular polarization frequency selective surface operating in KU and KA band", IEEE Trans. Antennas Propag., vol. 63, no. 11, pp. 5194-5197, Nov. 2015.

[17] K. Lee, S. L. S. Yang and A. A. Kishk, "Dual- and multiband U-Slot patch antennas," in IEEE Antennas Wireless Propag. Lett. , vol. 7, pp. 645-647, 2008.

[18] Kin-Fai Tong, Kwai-Man Luk, Kai-Fong Lee and R. Q. Lee, "A broad-band U-slot rectangular patch antenna on a microwave substrate," IEEE Trans. Antennas Propag., vol. 48, no. 6, pp. 954-960, June 2000.

[19] C. Wood, "Improved bandwidth of microstrip antennas using parasitic elements," in IEE Proceedings H - Microwaves, Optics and Antennas, vol. 127, no. 4, pp. 231-234, August 1980.

[20] N. Misran, R. Cahill and V. F. Fusco "Concentric split ring element for dual frequency reflectarray antennas,". Electronics Letters, 39(25): 1,2003.

[21] E. Carrasco, M. Barba and J. A. Encinar, "Reflectarray element based on aperture-coupled patches with slots and lines of variable length," IEEE Trans. Antennas Propag., vol. 55, no. 3, pp. 820-825, March 2007.

[22] J. Ren and W. Menzel, "Dual-frequency folded reflectarray antenna." IEEE Antennas Wireless Propag. Lett. 12: 1216-1219, 2013.

[23] X. Liu, Y. Ge, X. Chen and L. Chen, "Design of folded reflectarray antennas using pancharatnam-berry phase reflectors." IEEE Access 6: 28818-28824, 2018.

[24] W. Zhang, D. Fu and A. Wang, "A compound printed air-fed array antenna," 2007 International Conference on Electromagnetics in Advanced Applications, Torino, 2007, pp. 1054-1057,

[25] Z. Miao, Z. Hao, Y. Wang, B. Jin, J. Wu and W. Hong. "A 400-GHz high-gain quartz-based single layered folded reflectarray antenna for terahertz applications." IEEE Trans. THz Sci. Technol.9.1: 78-88,2018.

[26] Y. Hu, W. Hong and Z. H. Jiang, "A multibeam folded reflectarray antenna With

wide coverage and integrated primary sources for millimeter-wave massive MIMO applications,” *IEEE Trans. Antennas Propag.* 66.12: 6875-6882, 2018.

[27] Y. Cao, W. Che, W. Yang, C. Fan and Q. Xue “Novel wideband polarization rotating metasurface element and its application for wideband folded reflectarray.” *IEEE Trans. Antennas Propag.* vol. 68, no. 3, pp. 2118-2127, March 2020.

[28] J. Yang, *et al.* “Shaping Bessel beams using source-integrated folded reflectarray.” *Optics letters* 43.21: 5222-5225, 2018.

[29] S. Qu, H. Zhang, W. Wu, P. Li, S. Yang and Z. Nie, “Wideband folded reflectarray using novel elements with high orthogonal polarization isolation *IEEE Trans. Antennas Propag.* 64.7: 3195-3200, 2016.

[30] Pilz, D., and W. Menzel. “Folded reflectarray antenna,” *Electron. Lett.* 34.9 (1998): 832-833.

[31] A. Freni, A. Mazzinghi and G. Carluccio, “Folded reflectarray with spherical polarizer,” *IEEE Trans. Antennas Propag.* vol. 68, no. 5, pp. 3613-3624, May 2020.

[32] G. Tan, X. Yang H. Xue, Z.Lu “A dual-polarized Fabry-Perot cavity antenna at Ka band with broadband and high gain.” *Progress In Electromagnetics Research* 60: 179-186, 2015.

[33] P. Xie, G. Wang, H. Li and J. Liang, “A dual-polarized two-dimensional beam-steering Fabry-Pérot cavity antenna with a reconfigurable partially reflecting surface.” *IEEE Antennas Wireless Propag. Lett.* 16: 2370-2374, 2017.

[34] P. Qin, L. Ji, S. Chen and Y. J. Guo “Dual-polarized wideband Fabry-Perot antenna with quad-layer partially reflective surface.” *IEEE Antennas Wireless Propag. Lett.* 17.4: 551-554, 2018.

[35] M. Mi, S. Zhang and B. Sun, “A dual-polarized fabry-perot cavity antenna with high gain,” 2017 Sixth Asia-Pacific Conference on Antennas and Propagation (APCAP), Xi'an, 2017, pp. 1-3.

[36] F. Meng, Y. Liu and S. K. Sharma, “A dual-polarized broadband resonant cavity antenna,” 2018 12th International Symposium on Antennas, Propagation and EM Theory (ISAPE), Hangzhou, China, 2018, pp. 1-2.

[37] Y. R. Ding and Y. J. Cheng, “A tri-band shared-aperture antenna for (2.4, 5.2) GHz Wi-Fi application with MIMO function and 60 GHz Wi-Gig application with

beam-scanning function,” *IEEE Trans. Antennas Propag.*, vol. 68, no. 3, pp. 1973–1981, March 2020.

[38] J. F. Zhang, Y. J. Cheng, Y. R. Ding, and C. X. Bai, “A dual-band shared-aperture antenna with large frequency ratio, high aperture reuse efficiency, and high channel isolation,” *IEEE Trans. Antennas Propag.*, vol. 67, no. 2, pp. 853–860, Feb. 2019.

[39] Y. T. Lo, D. Solomon, and W. F. Richards, “Theory and experiment microstrip antennas,” *IEEE Trans. Antennas Propag.*, vol. AP-27, no. 2, pp. 137–145, Mar. 1979.

[40] R. Lian, Z. Tang and Y. Yin, “Design of a broadband polarization-reconfigurable Fabry–Perot resonator antenna,” *IEEE Antennas Wireless Propag. Lett.*, vol. 17, no. 1, pp. 122–125, Jan. 2018.

[41] L. Y. Feng and K. W. Leung, “Dual-frequency folded-parallel-plate antenna with large frequency ratio,” *IEEE Trans. Antennas Propag.*, vol. 64, no. 1, pp. 340–345, Jan. 2016.

[42] L. Zhang, K. Y. See, B. Zhang, and Y. P. Zhang, “Integration of dual-band monopole and microstrip grid array for single-chip tri-band application,” *IEEE Trans. Antennas Propag.*, vol. 61, no. 1, pp. 439–443, Jan. 2013.

[43] D. Wang and C. H. Chan, “Multiband antenna for WiFi and WiGig communications,” *IEEE Antennas Wireless Propag. Lett.*, vol. 15, pp. 309–312, 2016.

[44] B. J. Xiang, S. Y. Zheng, H. Wong, Y. M. Pan, K. X. Wang, and M. H. Xia, “A flexible dual-band antenna with large frequency ratio and different radiation properties over the two bands,” *IEEE Trans. Antennas Propag.*, vol. 66, no. 2, pp. 657–667, Feb. 2018.

[45] L. Y. Feng and K. W. Leung, “Dual-fed hollow dielectric antenna for dual-frequency operation with large frequency ratio,” *IEEE Trans. Antennas Propag.*, vol. 65, no. 6, pp. 3308–3313, Jun. 2017.

[46] Y.-X. Sun and K. W. Leung, “Substrate-integrated two-port dual-frequency antenna,” *IEEE Trans. Antennas Propag.*, vol. 64, no. 8, pp. 3692–3697, Aug. 2016.

Chapter V Conclusion and Future Work

5.1 Conclusion

Millimetre-wave (mm-wave) and terahertz (THz) technologies have created a new era of many emerging research areas, such as high-resolution imaging, high-speed big data communications, and ubiquitous sensing. To meet different requirement, there is great significance in the development of mm-wave and THz beam-shaping devices, including antennas, reflectarrays, and polarization beam splitters. The thesis first summarized the state-of-the-art works in Chapter I and then developed a series of mm-wave and THz beam-shaping devices using 3-D printing, LTCC, and PCB technology.

The main focus of Chapter II is low-cost low-profile 3-D printed polarization manipulation and beam shaping devices. In this chapter, a circularly polarized lens operating at 30 GHz is proposed first. The lens simultaneously achieves linear to circular polarization conversion and the beam collimation in the transmission mode with a planar configuration, which is different from its counterparts which have a lens on top of the polarizer. The related content entitled “3-D Printed Planar Dielectric Linear-to-Circular Polarization Conversion and Beam Shaping Lenses Using Coding Polarizer” has been published in **IEEE Transactions on Antennas and Propagation**. Next, we propose and demonstrate a 3-D printed low-cost low-profile Fresnel-Rochon prism to replace the conventional Rochon prisms formed of two right triangle prisms. The proposed Rochon prism enjoys the benefit of simple fabrication without any further assembly procedure. Prototypes operating at 0.14 THz frequency were printed and measured to verify the idea. The related content entitled “Sub-Terahertz 3-D Printed All-Dielectric Low-Cost Low-Profile Lens-Integrated Fresnel-Rochon Prism” has been submitted to **IEEE Transactions on Terahertz Science and Technology**. Finally, a new all-dielectric broadband dual-band reflectarray with a large frequency-ratio is proposed using low-cost 3-D printing. Different from conventional reflectarrays using metallic resonant cells or dielectric slabs as phasing elements with the full metal ground, the proposed design is built with air as the phasing element and dielectric mirror structure as the ground. In this way, the metal ground is removed, which makes the design all-dielectric. By careful selection of the bandgap frequency

of the dielectric mirror, the dual-band frequency-ratio is scalable and can be very large. Compared with state-of-the-art works using printed-circuit-board (PCB) or micro-fabrication, the proposed all-dielectric design enjoys the merits of low cost, light weight, and fast prototyping with generic 3D printing. The related content entitled “Low-Cost 3-D Printed All-Dielectric Dual-Band Broadband Reflectarray with a Large Frequency-Ratio” has been submitted to **IEEE Transactions on Antennas and Propagation**.

Chapter III focuses on high gain LTCC antenna arrays for mm-wave antenna-in-package applications. First, based on the concept of planar aperture antenna, single-ended-fed planar aperture antennas (SPAAs) using LTCC process technology are proposed, which not only inherit the merits of the aperture antennas including high gain, wide bandwidth but also exhibit the advantages of low profile and compact size. The related content entitled “Single-Ended-Fed High-Gain LTCC Planar Aperture Antenna for 60 GHz Antenna-in-Package Applications” has been published on **IEEE Transactions on Antennas and Propagation**. Next, we proposed a low-profile wideband and high gain patch antenna array. We adopt a shorting pin connecting the upper patch and ground to achieve the virtual ac ground plane of differential feeding. This enables the antenna element to achieve good radiation performances including stable gain, symmetrical beam with low cross-polarization, which are comparable to those of the differential-driven patch antenna while the complex differential feeding network is not required. The related content entitled “Low-Profile Wideband and High Gain LTCC Patch Antenna Array for 60-GHz Applications” has been published on **IEEE Transactions on Antennas and Propagation**.

Chapter IV proposes dual-band beam-shaping devices by merging devices with different functions. Firstly, a new kind of dual-band dual-polarized high gain antenna with a single linearly polarized feed is proposed by folding a reflectarray into a Fabry-Perot cavity (FPC). This design inherits the merits of the folded reflectarray (FR), namely, the blockage effect is avoided and the height is reduced by half. More importantly, the design breaks the limitation of the FR of only achieving high directive radiation over one polarization due to the polarizing grid, and it can also enrich the FPC antenna community because the state-of-the-art works to realize dual-band dual-polarized radiation use dual-polarized primary source. The related content entitled “Folding Reflectarray Into Fabry-Perot Cavity Makes Dual-Band Dual Polarized High Gain Antenna with a Single Linearly Polarized Feed” has been

submitted to **IEEE Transactions on Antennas and Propagation**. To provide high capacity and reliable communication, tightly integrating millimetre-wave (mm-wave) networks with an existing sub-6 GHz network is a promising strategy. To meet the requirement of this scenario, a dual-band antenna with a large frequency-ratio of 11.7 (2.4 GHz/28 GHz) is proposed, which integrates a high-band (FPC) antenna in a low-band patch antenna. The two antennas share the same aperture with a high aperture efficiency. Because of the FP resonance, the antenna can achieve a peak gain of 16 dBi in the 28 GHz band without a feeding network. The related content entitled “Large Frequency-Ratio, High Aperture Reuse Efficiency, Dual-Band Antenna for Millimetre-Wave and Sub-6 GHz Applications” has been submitted to **IEEE Transactions on Antennas and Propagation**.

5.2 Future work

The designs and principles demonstrated in the thesis have the potential to be scaled to higher frequency operation and applications. However, they are mainly restricted by the tolerance and resolution of the corresponding fabrication technique. If better fabrication can be used, these designs can be scaled to much higher frequencies in the future. Thus, some studies related to this thesis may be worthy of further investigation.

1. New mm-wave and THz beam shaping devices using integrated additively manufactured electronics (AME) technique. In Chapter II, the beam-shaping devices are all-dielectric and fabricated using dielectric additive manufacturing. Since our laboratory has the dielectric and conductor one-stop printer, it would be interesting to design devices using this printer. The combination of the conductor-based structure and the dielectric structure can provide more degrees of freedom to develop devices with new functions, which cannot be achieved using the dielectric-only printing.

2. Tunable mm-wave and THz beam-shaping devices. Tunable or reconfigurable devices have wider applications but the switches commonly used in the microwave region (such as pin diodes) cannot be used in the mm-wave and THz region. Therefore, exploring phase change materials, such as graphene, to dynamically control the states of the devices may be a good approach and deserves considerable attention in future work.

Publications

- [1] **J. Zhu**, Y. Yang, S. Liao and Q. Xue, “Dual-Band Antenna Hybridizing Folded Transmitarray and Folded Reflectarray”, *IEEE Transactions on Antennas and Propagation*, accepted for publication.
- [2] **J. Zhu**, Y. Yang, S. Liao and Q. Xue, “Aperture-Shared Millimeter-Wave/Sub-6 GHz Dual-Band Antenna Hybridizing Fabry-Perot Cavity and Fresnel Zone Plate”, *IEEE Transactions on Antennas and Propagation*, early access doi: 10.1109/TAP.2021.3098559.
- [3] **J. Zhu**, Y. Yang, M. Li, et al., “Additively Manufactured Millimeter-Wave Dual-Band Single-Polarization Shared Aperture Fresnel Zone Plate Metalens Antenna”, *IEEE Transactions on Antennas and Propagation*, early access, doi: 10.1109/TAP.2021.3070224.
- [4] **J. Zhu**, Y. Yang, D. McGloin, S. Liao and Q. Xue, “3-D Printed All-Dielectric Dual-Band Broadband Reflectarray with a Large Frequency-Ratio”, *IEEE Transactions on Antennas and Propagation*, early access doi: 10.1109/TAP.2021.3076528.
- [5] **J. Zhu**, Y. Yang, D. McGloin, S. Liao and Q. Xue, “Sub-Terahertz 3-D Printed All-Dielectric Low-Cost Low-Profile Lens-Integrated Polarization Beam Splitter”, *IEEE Transactions on Terahertz Science and Technology*. vol. 11, no. 4, pp. 433-442, July 2021, doi: 10.1109/TTHZ.2021.3064209.
- [6] **J. Zhu**, Y. Yang, D. McGloin, S. Li, S. Liao and Q. Xue, “3-D Printed Planar Dielectric Linear-to-Circular Polarization Conversion and Beam Shaping Lenses Using Coding Polarizer”, *IEEE Transactions on Antennas and Propagation*, vol. 68, no. 6, pp. 4332-4343, June 2020.
- [7] **J. Zhu**, Y. Yang, C. Chu, S. Li, S. Liao and Q. Xue, “Low-Profile Wideband and High-Gain LTCC Patch Antenna Array for 60 GHz Applications”, *IEEE Transactions on Antennas and Propagation*, vol. 68, no. 4, pp. 3237-3242, April 2020.
- [8] **J. Zhu**, Y. Yang, S. Li, S. Liao and Q. Xue, “Dual-Band Dual Circularly Polarized Antenna Array Using FSS-Integrated Polarization Rotation AMC Ground for Vehicle Satellite Communications”, *IEEE Transactions on Vehicular Technology*, vol. 68, no. 11, pp. 10742-10751, Nov. 2019.
- [9] **J. Zhu**, Y. Yang, S. Li, S. Liao and Q. Xue, “Single-Ended-Fed High-Gain LTCC

Planar Aperture Antenna for 60 GHz Antenna-in-Package Applications”, *IEEE Transactions on Antennas and Propagation*, vol. 67, no. 8, pp. 5154-5162, Aug. 2019.

[10] **J. Zhu**, S. Liao, Y. Yang, S. Li, and Q. Xue, “60 GHz Dual-Circularly Polarized Planar Aperture Antenna and Array”, *IEEE Transactions on Antennas and Propagation*, vol. 66, no. 2, pp. 1014-1019, Feb. 2018.

[11] **J. Zhu**, S. Li, S. Liao, Y. Yang and H. Zhu, “60 GHz Substrate-Integrated-Waveguide-Fed Patch Antenna Array With Quadri-Polarization”, *IEEE Transactions on Antennas and Propagation*, vol. 66, no. 12, pp. 7406-7411, Dec. 2018.

[12] **J. Zhu**, S. Liao, S. Li and Q. Xue, “60-GHz Substrate Integrated Waveguide Based Monopulse Slot Antenna Arrays”, *IEEE Transactions on Antennas and Propagation*.vol. 66, no. 9, pp. 4860-4865, Sept. 2018.

Conference paper:

[1] **J. Zhu**, Y. Yang, C. Chu, S. Li, S. Liao and Q. Xue, “Mm-Wave Low-Profile Wideband Antenna Array Using Low-temperature Co-fired Ceramics (LTCC) Technique”, 2019 International Conference on Microwave and Millimeter Wave Technology (ICMMT), Guangzhou, China, 2019, pp. 1-2. **(Honorable mention award)**

[2] **J. Zhu**, Y. Yang, C. Chu, S. Li, S. Liao and Q. Xue, “60-GHz High Gain Planar Aperture Antenna Using Low-Temperature Cofired Ceramics (LTCC) Technology”, 2019 IEEE MTT-S International Wireless Symposium (IWS), Guangzhou, China, 2019, pp. 1-3.

[3] **J. Zhu**, C. Chu, L. Deng, Y. Yang and S. Li, “Mm-Wave High Gain Substrate Integrated Cavity Excited Patch Antenna Array”, 2018 Asia-Pacific Microwave Conference (APMC), Kyoto, 2018, pp. 591-593.

[4] **J. Zhu**, D. McGloin, Y. Yang and B. Liu, “0.32 THz dual circularly polarized reflectarray”, 2020 Conference on Lasers and Electro-Optics Pacific Rim (CLEO-PR), Sydney, Australia, 2020, pp. 1-2, doi: 10.1364/CLEOPR.2020.C11B_3.

Under review papers:

[1] **J. Zhu**, Y. Yang, et.al, “Dual-Band Aperture-Shared High Gain Antenna for Millimeter-Wave Multi-Beam and Sub-6 GHz Communication Applications”, *IEEE Transactions on Antennas and Propagation*, major revision.

[2] **J. Zhu**, Y. Yang, et.al, “Aperture-Shared All-Metal End-Fire High Gain Parabolic Antenna for Millimeter-Wave Multi-Beam and Sub-6 GHz Communication Applications”, *IEEE Transactions on Antennas and Propagation*, under review.

[3] **J. Zhu**, Y. Yang, et.al, “Additively Manufactured Transmissive Ultrathin Metasurfaces for Broadband Circular Polarization Decoupled Beams and Orbital Angular Momentum Generation”, *ACS Applied Materials & Interfaces*, under review.

[4] **J. Zhu**, Y. Yang, et.al, “Large Frequency-Ratio, High Aperture Reuse efficiency, Dual-Band Antenna for Millimeter-Wave and Sub-6 GHz Applications”, *IEEE Antennas and Wireless Propagation Letters*, Major revision.